

Evapotranspiration: Application, Scaling and Uncertainty

Ali Ershadi Esmaeilabadi

February 2014

A thesis submitted for the degree of Doctor of Philosophy
School of Civil & Environmental Engineering, Faculty of Engineering
University of New South Wales, Sydney, Australia



Summary

Evapotranspiration (ET) represents one of the key components of the terrestrial hydrological cycle. In this research, a number of different aspects of ET estimation are studied in order to better understand the causes of uncertainty in flux estimation and also to identify potential approaches to improve ET prediction.

First, the differences amongst commonly used ET models are evaluated and discussed. This analysis includes: i) an intercomparison of models over various land surface conditions; and ii) a study on the role of model structure and resistance parameterization on flux estimation. Results from these investigations provide guidance into making an informed choice on an ET model. It is shown that a modified form of the Priestley-Taylor model outperforms more complex Penman-Monteith and energy balance type estimation approaches. Moreover, it is identified that for Penman-Monteith type models, the resistance parameterization is more influential than model structure.

Second, the effects of spatial scaling on ET estimation are studied by undertaking an in-depth evaluation of the Surface Energy Balance System (SEBS) models response to the aggregation of input forcing: a necessary step in undertaking regional to global scale estimation of surface heat fluxes. Aggregation of input forcing showed limited effect on the land surface temperature (LST) and available energy, but reduced ET at the image scale by up to 15% and at the pixel scale by up to 50%. The main source of such errors was determined to be due to the role of the roughness parameterization.

Finally, a Bayesian technique is developed for the explicit quantification of uncertainties in process-based models. In a case study using the SEBS model, the Bayesian technique illustrated that the main reason for discrepancy between simulated and observed sensible heat fluxes was a result of errors in the local observations of the LST. This was related back to footprint difference between the in-situ LST sensor and the eddy covariance system used for independent flux estimation.

Overall, results of this research provide new insights into the process of evapotranspiration, and offer new ideas for future research aimed at improved realization of the evapotranspiration process.

Acknowledgements

Foremost, I would like to express my sincere gratitude to my supervisors A/Prof. Matthew McCabe and A/Prof. Jason Evans for their continuous dedication, motivation and support during my PhD research. Their endless sources of inspiration and guidance helped me in developing the critical thinking and reasoning skills most required for my future career. Furthermore, I would like to thank my external supervisor Prof. Jeff Walker for his encouragement and insightful comments.

I would also acknowledge my collaborators and co-authors: Dr. Gregoire Mariethoz (UNSW), Prof. Dmitri Kavetski (U of Adelaide), Prof. Eric Wood (Princeton U) and Mr. Nathaniel Chaney (Princeton U) for their thoughtful support and advice. Their contributions and insights were greatly appreciated. A special note of appreciation to Prof. Ashish Sharma, Dr. Sivakumar Bellie, Prof. Andy Baker, Dr. Fiona Johnson and Dr. Raj Mehrotra for their thoughtful direction and guidance during my annual reviews.

I would like to express my appreciation to the Victorian Government's Department of Primary Industry (DPI) and Australia's National Centre for Groundwater Research and Training (NCGRT) for financially and technically supporting my research: in particular to Dr. Andy McAllister, Dr. Mohammad Abuzar, Dr. Des Whitfield and Prof. David Lockington.

A special thanks goes to Dr. Qiaozhen Mu (U of Montana), Dr. Joshua Fisher (NASA-JPL), Dr. Diego Miralles (U of Bristol), Dr. Carlos Jimenez (Observatoire de Paris), Dr. Fuqin Li (Geoscience Australia), Mr. Robert Pipunic (U of Melbourne), Dr. Yi Liu (UNSW), Dr. Hoori Ajami (UNSW), A/Prof. Lixin Wang (Indiana U), Ms. Patty McLaughlin (UNSW) and Ms. Patricia Karwan (UNSW) for their great technical and logistic support.

This research would have not been possible without the data and tools I acquired from FLUXNET (fluxnet.ornl.gov), FLUXDATA (www.fluxdata.org), USGS EarthExplorer (earthexplorer.usgs.gov), LAADS Web – NASA (ladsweb.nascom.nasa.gov) and LPDAAC (lpdaac.usgs.gov).

Above all, I would like to express my endless appreciation and heartfelt thanks to my wife Leila for supporting me spiritually and for her belief in my abilities. I also thank my son Arash for his patience and support during my PhD, especially for his understanding and letting me focus on the writing of this thesis. My parents and parents-in-law were all extremely supportive, patient and encouraging of my decision in committing to my PhD research. I am thankful to all of them.

List of Publications

Type of publication	Publication information
Journal paper, published	Ershadi, A. , McCabe, M.F., Evans, J.P., J.P. Walker, (2013) ' <u>Effects of spatial aggregation on the multi-scale estimation of evapotranspiration</u> ', Remote Sensing of Environment, 131, 51-62, http://dx.doi.org/10.1016/j.rse.2012.12.007
Journal paper, published	Ershadi, A. , McCabe, M. F., Evans, J.P., Mariethoz, G., Kavetski, D. (2013) ' <u>A Bayesian analysis of sensible heat flux estimation: quantifying uncertainty in meteorological forcing to improve model prediction</u> ', Water Resources Research, 49(5), 2343-2358, http://dx.doi.org/10.1002/wrcr.20231
Journal paper, published	Ershadi, A. , McCabe, M.F., Evans, J.P., Chaney, N.W., Wood, E.F., ' <u>Multi-site evaluation of terrestrial evaporation models using globally distributed FLUXNET data</u> ', Agricultural and Forest Meteorology, 187(0): 46-61
Journal paper, in review	Ershadi, A. , McCabe, M.F., Evans, J.P., Wood, E.F., ' <u>Impact of model structure and parameterization on Penman-Monteith type evaporation models</u> ', Journal of Hydrology
Book chapter, published	McCabe, M.F., Miralles, D., Jimenez, C., Ershadi, A. , Fisher, J., Mu Q., Liang, M., Mueller, B., Sheffield, J., Seneviratne, S., Wood, E.F., (2013) ' <u>Global scale estimation of land surface heat fluxes from space: product assessment and intercomparison</u> ', Book chapter in 'Remote Sensing of Energy fluxes and Soil Moisture Content', Ed. George Petropoulos, Taylor & Francis CRC Press.
Conference paper, Refereed	Ershadi, A. , McCabe, M.F., Evans, J.P & Walker, J.P., (2011) ' <u>Evaluation of energy balance, combination, and complementary schemes for estimation of evaporation</u> , Proceedings of IAHS Lead Symposia, IUGG2011, Melbourne, Australia
Conference presentation	McCabe, M.F., Ershadi, A. , Chaney, N., Jimenez, C., Miralles, D., Mueller, B., Seneviratne, S., Wood, E.F., (2013) ' <u>Global estimation of evapotranspiration from the GEWEX LandFlux Initiative: model intercomparison and evaluation at the tower scale</u> ', EGU General Assembly 2013
Conference paper, not refereed	Ershadi, A. , McCabe, M.F., Evans, J.P., Walker, J.P., Pipunic, R., (2011) ' <u>Estimation of evaporation using the surface energy balance system (SEBS) and numerical models</u> ', 3 rd International Symposium on Remote Sensing of Environment, Sydney, Australia
Conference poster	Ershadi, A. , McCabe, M.F., Evans, J.P., (2011) ' <u>Estimating surface heat fluxes from remote sensing, process models and regional climate simulations</u> ', EGU General Assembly 2011
Conference poster	Ershadi, A. , McCabe, M.F., Evans, J.P., (2011) ' <u>Issues of scale in surface heat flux retrieval using multi-resolution, multi-temporal satellite imagery</u> ', Proceedings of IAHS Lead Symposia, IUGG2011, Melbourne, Australia
Conference paper, not refereed	Evans, J.P., McCabe, M.F., Mueller, B., Meng, X., Ershadi, A. , (2011) ' <u>A comparison of satellite evapotranspiration estimation efforts</u> ', WIRADA Science Symposium Proceedings, Melbourne, Australia

Conference
presentation

McCabe, M.F., **Ershadi, A.**, Evans, J.P., Liu, Y., Vinukollu, R., Wood, E.F., Jimenez, C., Kummerow, C, Mueller, B., Seneviratne, S., Rossow, W., (2010) 'Evaluating latent heat flux estimates from land surface models, a regional climate model simulation and a surface energy balance algorithm over Australia's Murray Darling Basin', 2nd Hydrology delivers Earth System Science to Society, Japan

Table of Contents

SUMMARY.....	I
ACKNOWLEDGEMENTS.....	II
LIST OF PUBLICATIONS.....	III
TABLE OF CONTENTS.....	V
LIST OF FIGURES.....	IX
LIST OF TABLES.....	XIII
NOMENCLATURE.....	XIV
1 GENERAL INTRODUCTION.....	2
1.1 Literature Review.....	4
1.1.1 Application Challenges in Evapotranspiration Estimation.....	4
1.1.2 Scale Issues in Evapotranspiration Estimation.....	8
1.1.3 Uncertainty Issues in Evapotranspiration Estimation.....	10
1.2 Objectives of the Thesis.....	11
1.3 Thesis Outline.....	11
2 MULTI-SITE EVALUATION OF TERRESTRIAL EVAPOTRANSPIRATION MODELS....	15
Abstract.....	15
2.1 Introduction.....	15
2.2 Data and Methodology.....	19
2.2.1 Forcing Data.....	19
2.2.2 Model Descriptions.....	22
2.2.3 Statistical Evaluations.....	29
2.2.4 Energy Budget Closure at Flux Tower Sites.....	30
2.3 Results.....	32
2.3.1 Performance of Models over the Entire Data Period.....	32
2.3.2 Performance of Models at Monthly Timescales.....	36
2.4 Discussion.....	38
2.4.1 SEBS Model Performance.....	38
2.4.2 AA Model Performance.....	39
2.4.3 PM Model Performance.....	40
2.4.4 PT-JPL Model Performance.....	41
2.4.5 Performance of the Ensemble Mean Method.....	42

2.4.6	Limitations of the current study	43
2.5	Conclusion	44
	Acknowledgement.....	45
3	IMPACT OF MODEL STRUCTURE AND PARAMETERIZATION ON PENMAN-MONTEITH TYPE EVAPOTRANSPIRATION MODELS	48
	Abstract.....	48
3.1	Introduction.....	49
3.2	Data and Methodology	52
3.2.1	Input Forcing and Evaluation Data	52
3.2.2	Description of Penman-Monteith Model Structures	52
3.2.3	Including Dynamic Roughness Parameterization	59
3.2.4	Developing Model Parameterization Scenarios	60
3.2.5	Energy Budget Closure at Flux Tower Sites	60
3.3	Results	61
3.3.1	Penman-Monteith Model	61
3.3.2	Shuttleworth-Wallace Model	64
3.3.3	Mu Model.....	68
3.3.4	Identification of the Best Performing Scenarios.....	70
3.4	Discussion.....	71
3.4.1	Influence of Model Structure and Parameterization.....	72
3.4.2	Review of Differences between Current and Previous Studies.....	74
3.5	Conclusion	76
	Acknowledgement.....	77
4	EFFECTS OF SPATIAL AGGREGATION ON THE MULTI-SCALE ESTIMATION OF EVAPOTRANSPIRATION	80
	Abstract.....	80
4.1	Introduction.....	80
4.2	Description of Study Area and Data Sources	83
4.2.1	Meteorological Data	84
4.2.2	Satellite Data.....	85
4.2.3	Surface Energy Balance System (SEBS) Model	86
4.3	Methodology	87
4.4	Results and Discussion	89
4.4.1	Input Aggregation: Effect of Surface Temperature and Vegetation	89
4.4.2	Effects of Flux Aggregation Approach	96
4.5	Summary and Conclusion.....	100

Acknowledgement.....	101
5 A BAYESIAN UNCERTAINTY ANALYSIS OF HEAT FLUX ESTIMATION	103
Abstract.....	103
5.1 Introduction.....	103
5.2 Field Measurements and Site Description	105
5.3 Modeling Approach	106
5.3.1 Surface Energy Balance System (SEBS)	106
5.3.2 The Bayesian Inference Technique.....	107
5.3.3 MCMC Sampling of the BIT-SEBS Posterior Distribution	109
5.3.4 BIT-SEBS Methodology for Analysing SMEX02 Tower Data	110
5.4 Results	116
5.4.1 Convergence Analysis of the MCMC Iterations.....	116
5.4.2 Bayesian Uncertainty Analysis of SEBS Inputs	118
5.4.3 Inferred Values of Meteorological Variables	122
5.5 Discussion.....	126
5.6 Conclusions.....	129
Acknowledgements	129
6 SYNTHESIS AND THESIS RECOMMENDATIONS	131
6.1 Thesis Overview and Conclusions.....	131
6.1.1 Model Intercomparison and Assessment	131
6.1.2 Influence of Model Parameterisation on Performance.....	134
6.1.3 Scaling Issues in Evapotranspiration	135
6.1.4 Uncertainty in Evapotranspiration.....	136
6.2 Recommendations and Future Work	136
6.2.1 Application of ET models	136
6.2.2 Scale	138
6.2.3 Uncertainty	139
6.2 Concluding Remarks	140
REFERENCES	142
APPENDIX A – SUPPLEMENTARY MATERIALS FOR CHAPTER 2.....	171
APPENDIX B – SUPPLEMENTARY MATERIALS FOR CHAPTER 3.....	181
APPENDIX C – SUPPLEMENTARY MATERIALS FOR CHAPTER 5.....	196
C.1 Evaluation of the Response Error Parameter r	196

C.2 Evaluation of the Significance of the Choice of Priors..... 197

List of Figures

Figure 2-1: Location of the eddy-covariance towers used to provide forcing and validation data in this study.	22
Figure 2-2: Comparison of Nash- Sutcliffe efficiency coefficient calculated for simulated latent heat flux versus observed, energy residual (ER) corrected and Bowen ratio (BR) corrected ones. GRA=Grassland, CRO=Cropland, SHR=Shrubland, ENF=Evergreen Needleleaf Forest, DBF=Deciduous Broadleaf Forest.	31
Figure 2-3: Comparison of the efficiency of the evapotranspiration models. <i>RE</i> is relative error (lower is better) and <i>NSE</i> is the Nash-Sutcliffe Efficiency coefficient (higher is better). Towers in each biome type are arranged from left to right (e.g. G1 to G4 for Grassland). EM is for ensemble mean of the models.	33
Figure 2-4: Mean per-month value of the Nash-Sutcliff Efficiency calculated for each of the four studied models at each of the 20 tower locations. The x-axis represents month of the year, while each point on the graph represents the temporally averaged per-month <i>NSE</i> calculated for all available tower record years (see Table 2-1 for details on individual tower data length). Note that the per-month <i>NSE</i> values are for half-hourly or hourly scale <i>ET</i> data, not in monthly scale. f_E is normalized fraction of monthly observed <i>ET</i> . EM is for ensemble mean of the models.	38
Figure 3-1: Performance of the PM model in adjusting the resistance parameterization. <i>RE</i> is relative error ($RE=RMSD/\text{mean}(\lambda E_{obs})$) and <i>NSE</i> is the Nash-Sutcliff efficiency. The x-axis displays the various landcover types used in the simulations, with vegetation height increasing from left-to-right (both within and between biomes).	63
Figure 3-2: Mean monthly values of the Nash-Sutcliff Efficiency (<i>NSE</i>) calculated for the PM model’s scenarios at each of the 20 tower locations. The x-axis represents month of the year, while each point on the graphs of PM ⁰ to PM ⁴ represents the temporally averaged monthly <i>NSE</i> calculated for all available tower record years (see Table 2-1 for details on individual tower data length). f_E is normalized fraction of monthly observed evapotranspiration.	64
Figure 3-3: Performance of the SW model in adjusting the resistance parameterization. <i>RE</i> is relative error ($RE=RMSD/\text{mean}(\lambda E_{obs})$) and <i>NSE</i> is the Nash-Sutcliff efficiency. The x-axis displays the various landcover types used in the simulations, with vegetation height increasing from left-to-right (both within and between biomes). The (not shown) <i>RE</i> value for SW ⁴ scenario is 3.	67
Figure 3-4: Mean monthly values of the Nash-Sutcliff Efficiency (<i>NSE</i>) calculated for the SW model’s scenarios at each of the 20 tower locations. The x-axis represents month of the year, while each point on the graph of SW ⁰ to SW ⁴ represents the temporally averaged monthly <i>NSE</i> calculated for all available tower record years (see Table 2-1 for details on individual tower data length). f_E is normalized fraction of monthly observed evapotranspiration.	68

Figure 3-5: Performance of the Mu model in adjusting the resistance parameterization. RE is relative error ($RE=RMSD/\text{mean}(\lambda E_{obs})$) and NSE is the Nash-Sutcliff efficiency. The x-axis displays the various landcover types used in the simulations, with vegetation height increasing from left-to-right (both within and between biomes). 69

Figure 3-6: Mean monthly values of the Nash-Sutcliff Efficiency (NSE) calculated for the Mu model's scenarios at each of the 20 tower locations. The x-axis represents month of the year, while each point on the graphs of Mu^0 to M^3 represents the temporally averaged monthly NSE calculated for all available tower record years (see Table 2-1 for details on individual tower data length). f_E is normalized fraction of monthly observed evapotranspiration..... 70

Figure 4-1: Location of the study area in Australia's Murray-Darling Basin (top-left), with the Murrumbidgee sub-catchment (top-middle) and the Coleambally irrigation area (top-right) also identified. Bottom panels show the Landsat band combination (7-4-2) colour composites for selected days at 120 m resolution. Green indicates vegetation and pink to magenta indicates bare soil. MIA represents the Murrumbidgee Irrigation Area, CIA the Coleambally Irrigation Area and MIL the Murrumbidgee Irrigation Limited regions. 84

Figure 4-2: Variations of net radiation (R_n in $W.m^{-2}$), air temperature (T_a in $^{\circ}C$) and wind speed (u_a in $m.s^{-1}$) for selected days. The thick grey line shows the time of the Landsat satellite overpass. 85

Figure 4-3: Flowchart of input aggregation (left) and flux aggregation (middle) scenarios. SEBS model flowchart is also shown in the right side. L. S. Param. refers to land surface parameters, including vegetation height, LAI , fractional vegetation cover, emissivity and albedo derived from reflectance bands. Numbers in each box are spatial resolution in meters. For the SEBS flowchart, Q_n is available energy as $Q_n = R_n - G_0$ 88

Figure 4-4: Spatial maps of a) the land surface temperature and b) the resulting evapotranspiration from the SEBS model using a simple averaging approach..... 90

Figure 4-5: Density (left) and cumulative density (right) plots of λE for three selected days from original 120 m data and aggregation of input forcing to coarser resolutions. 91

Figure 4-6: (a) variations of the relative spatial mean (μ_r) and (b) relative spatial standard deviation (σ_r) for T_s ($^{\circ}C$), u^* ($m.s^{-1}$), r_a ($s.m^{-1}$), H ($W.m^{-2}$), λE ($W.m^{-2}$) and Q_n ($W.m^{-2}$) across aggregated resolutions from 240 to 960 m, increasing by 120 m increments. 93

Figure 4-7: The relative error (E_r) at the pixel scale for T_s ($^{\circ}C$), u^* ($m.s^{-1}$), r_a ($s.m^{-1}$), H ($W.m^{-2}$), λE ($W.m^{-2}$) and Q_n ($W.m^{-2}$) across aggregated resolutions from 240 to 960 m, increasing by 120 m increments. Triangles represent the mean relative errors and lines above and below identify the 75th and 25th percentiles respectively for each aggregated resolution. 94

Figure 4-8: Pixel scale relative errors in (a) the aerodynamic resistance and (b) the latent heat flux due to input aggregation..... 95

Figure 4-9: Native resolution (top) and aggregated latent heat flux (λE) from Landsat using simple averaging (SA), nearest neighbour (NN), bilinear (BL) and bicubic interpolation (BC) aggregation methods to the equivalent 960 m resolution of the MODIS sensor..... 97

Figure 4-10: Errors in estimation of the total mass of evapotranspiration (in m^3) due to the aggregation of the latent heat flux for different spatial interpolation methods. Negative values mean aggregated pixels are less than the original fine resolution values. Numbers above the images for NN, BL and BC are spatial sum..... 99

Figure 5-1: Walnut Creek Basin (thick black line) and location of soybean and corn towers. The land use map of the region is shown in the background..... 106

Figure 5-2: Computational flowchart of the Bayesian inference procedure in BIT-SEBS using the slice sampling MCMC. Input data and parameters are highlighted in grey squares. 110

Figure 5-3: Time series of the land surface temperature T_s , air temperature T_a and wind speed u_a for all 12 towers (6 over soybean and 6 over corn) of the SMEX02 campaign during the daytime. Grey lines represent soybean towers and black lines the corn towers. The tower averaged precipitation is shown in the upper panel. Gaps in the data record reflect the removal of rain periods from the analysis, given the influence that these have on flux observations. 112

Figure 5-4: Time series of the standard deviation (σ) for T_s ($^{\circ}C$), T_a ($^{\circ}C$) and u_a ($m.s^{-1}$) derived from all of the SMEX02 towers at each time step during daytime. 113

Figure 5-5: Quantile-Quantile (QQ) plots of the land surface temperature T_s , air temperature T_a and wind speed u_a for all towers at 12:00 PM (local time) on day-of-year 173 and 174..... 114

Figure 5-6: The overall procedure used in BIT-SEBS to estimate input meteorological variables. Input data and parameters are shown in grey squares. The procedure is applied at each time step of each tower. 116

Figure 5-7: Traces of the posterior input meteorological variables in the Markov chain traces (left) and their corresponding cumulative mean (right; with x-axis in logarithmic scale). Results represent a single 12:00 PM time stamp for day-of-year 173 at tower WC162 (soybean). The means of all variables appear stationary after about 1,000 iterations. 117

Figure 5-8: Prior and posterior distributions of input meteorological variables for the 12:00 PM time stamp of tower WC162 (soybean) for day-of-year 173. The thin line is the prior distribution (Gaussian PDF), the histogram represents the MCMC samples

from the posterior distribution, and the thick line is a Gaussian PDF fitted to the histogram of posteriors..... 118

Figure 5-9: The overall procedure to simulate sensible heat fluxes in SEBS using both stochastic and deterministic forms. x denotes the input forcing (T_s, T_a, u_a). The procedure is applied at each time step of each tower. 119

Figure 5-10: Scatterplots of observed sensible heat flux (H_{obs} ; x-axis) versus deterministic simulated (H_{dt}) and stochastic simulated (H_{st}) for all day-time soybean (top) and corn (bottom) half-hourly tower values. Linear regression statistics of both H_{dt} and H_{st} are also shown. The quantity E_{rel} represents the relative error, defined as the *RMSD* divided by the range of observations. The 1:1 line is also shown. 120

Figure 5-11: Time series of observed sensible heat flux H_{obs} , stochastic simulated H_{st} and deterministic simulated sensible heat flux H_{dt} for 6 selected towers. For each panel, R^2 and E_{rel} are given for deterministic (Det.) and stochastic (Sto.) linear regressions. 121

Figure 5-12: Observed and Bayesian inferred values of meteorological variables for a soybean tower (left, WC162) and corn tower (right, WC152). The grey lines in the top three rows represent the observed values for the other 11 flux towers. In the bottom panels, the observed, deterministic calculated and stochastic generated sensible heat fluxes are shown. The x-axis for all panels indicate hour of the day (local time) for day-of-year 173. 124

Figure 5-13: Differences between Bayesian inferred and observed values for land surface temperature, air temperature and wind speed. Soybean towers are shown in grey and corn towers in black. Top panel shows average precipitation occurring during the field campaign..... 126

List of Tables

Table 2-1: Selected flux towers and their attributes. z_g is the site elevation (above sea level) in m, z_m is tower height in m, h_c is the canopy height in m, Y is the number of years of data and L is the processing level of data.	21
Table 2-2: List of required data and parameters for evapotranspiration models as used within this study.	29
Table 2-3: A summary of the performance of the evapotranspiration models. Biome types are defined as: GRA=Grassland, CRO=Cropland, SHR=Shrubland, ENF=Evergreen Needleleaf Forest, DBF=Deciduous Broadleaf Forest. The numbers in the parenthesis in each grid are biome averaged R^2_{avg} , RE_{avg} and NSE_{avg} (from left to right), and the numbers with bold font indicate the best performance. The numbers underneath the biome abbreviations in the first column denote the ranked order of models (SEBS, AA, PM, PT-JPL from left to right) based on their statistical performance (see Appendix A) over that particular land cover type	35
Table 3-1: The Biome-Property-Lookup-Table (BPLT) adopted from Mu et al. (2011). Land covers are defined as evergreen needleleaf forest (ENF); evergreen broadleaf forest (EBF); deciduous needleleaf forest (DNF); deciduous broadleaf forest (DBF); mixed forest (MF); woody savannahs (WL); savannahs (SV); closed shrubland (CSH); open shrubland; grassland, urban and built-up, barren or sparsely vegetated (GRA); cropland (CRO)	59
Table 3-2: Features of the 14 model/parameterisation combinations for estimating evapotranspiration.....	60
Table 3-3: NSE_{avg} values of all scenarios over various biomes. Values with bold font show the top-ranked scenarios for each biome and the underlined values show the runner-up(s). Biomes shown in the first column and are grasslands (GRA), croplands (CRO), shrublands (SHR), evergreen needleleaf forest (ENF) and deciduous broadleaf forest (DBF).	71
Table 5-1: Range of vegetation height (h_c), leaf area index (LAI) and fractional vegetation cover (f_c) during the study period.....	106

Nomenclature

A	available energy ($A = R_n - G_0$) (W.m^{-2})
A_c	available energy in the canopy (W.m^{-2})
A_s	available energy at the soil surface (W.m^{-2})
AATSR	Advanced Along Track Scanning Radiometer
AVHRR	Advanced Very High Resolution Radiometer
B	Stanton number (-)
C_c	bulk canopy conductance (m.s^{-1})
c_L	biome-specific mean potential stomatal conductance (m.s^{-1})
c_ℓ	leaf scale stomatal conductance (m.s^{-1})
c_p	specific heat capacity of air ($\text{J.kg}^{-1} \text{K}^{-1}$)
d_0	displacement height (m)
d_i	thickness of the i th soil layer (m)
d_t	total thickness of the soil layer (m)
λE	evapotranspiration (mm) or latent heat flux (W.m^{-2})
λE_{wc}	evaporation of wet canopy (W.m^{-2})
λE_p	potential evapotranspiration (W.m^{-2})
λE_p^c	potential evapotranspiration from canopy (W.m^{-2})
λE_p^s	potential evaporation from soil (W.m^{-2})
λE_s	evaporation from soil (W.m^{-2})
λE_t	canopy transpiration (W.m^{-2})
EVI	Enhanced Vegetation Index (-)
e	actual vapor pressure (Pa)
e_s	saturation vapor pressure (Pa)
F_1	weighting function (-) representing the effect of solar radiation on plant stress
F_2	weighting function (-) representing the effect of humidity on plant stress
F_3	weighting function (-) representing the effect of air temperature on plant stress
F_4	weighting function (-) representing the effect of soil moisture on plant stress
f_{APAR}	fraction of absorbed PAR (-)
f_c	fractional (green) vegetation cover (-)
f_E	normalized fraction of monthly evapotranspiration (-)
f_g	green canopy fraction (-)
f_{IPAR}	fraction of intercepted PAR (-)
f_M	plant moisture constraint (-)
f_{SM}	soil moisture constrain on soil evaporation (-)
f_T	plant temperature constraint (-)
f_{wet}	surface relative wetness (in PT-JPL and PM-Mu models) (-)
FAO	Food and Agriculture Organization
G_0	ground heat flux (W.m^{-2})
G_s^{st}	stomatal conductance (m.s^{-1})
G_s^{cu}	cuticular conductance (m.s^{-1})
g	acceleration due to gravity (m.s^{-2})

g_{bl}	leaf-scale boundary layer conductance ($\text{m}\cdot\text{s}^{-1}$)
g_{cu}	leaf cuticular conductance per LAI ($\text{m}\cdot\text{s}^{-1}$)
g_e	leaf conductance to evaporated water ($\text{m}\cdot\text{s}^{-1}$)
g_h	leaf conductance to sensible heat flux ($\text{m}\cdot\text{s}^{-1}$)
H	sensible heat flux ($\text{W}\cdot\text{m}^{-2}$)
IRGA	Infrared Gas Analyser
h_c	vegetation height (m)
h_s	a parameter associated with the water vapour deficit (-)
k_c	reduction functions for scaling of potential evapotranspiration in canopy (-)
k_s	reduction functions for scaling of potential evapotranspiration in soil (-)
k_{wc}	reduction functions for scaling of potential evapotranspiration in wet canopy (-)
K_h	eddy diffusion coefficient ($\text{m}^2\cdot\text{s}^{-1}$)
L	Obukhov length (m)
LAI	Leaf Area Index (-)
$m(T_{min})$	multiplier to limit c_L by T_{min} (-)
$m(VPD)$	multiplier to limit c_L by the effects of high VPD (-)
MODIS	Moderate Resolution Imaging Spectroradiometer
MOST	Monin-Obukhov Similarity Theory
NDVI	Normalized Differenced Vegetation Index (-)
N_{root}	number of soil layers in the rooting zone
NSE	Nash-Sutcliffe Efficiency
P	precipitation (mm)
PAR	Photosynthetically Active Radiation ($\text{W}\cdot\text{m}^{-2}$)
q	specific humidity ($\text{kg}\cdot\text{kg}^{-1}$)
q^*	specific humidity of the saturated air ($\text{kg}\cdot\text{kg}^{-1}$) at temperature T_a
Q_n	total available energy ($\text{W}\cdot\text{m}^{-2}$)
RE	Relative Error
RH	Relative Humidity (%)
RMSD	Root-Mean-Squared Difference
R_n	net radiation ($\text{W}\cdot\text{m}^{-2}$)
R_n^c	net radiation in the canopy ($\text{W}\cdot\text{m}^{-2}$)
R_n^s	net radiation in the soil surface ($\text{W}\cdot\text{m}^{-2}$)
r_a	aerodynamic resistance ($\text{s}\cdot\text{m}^{-1}$)
r_a^s	bulk aerodynamic resistance to soil evaporation ($\text{s}\cdot\text{m}^{-1}$)
r_a^t	bulk aerodynamic resistance to canopy transpiration ($\text{s}\cdot\text{m}^{-1}$)
r_a^{wc}	bulk aerodynamic resistance to wet canopy evaporation ($\text{s}\cdot\text{m}^{-1}$)
r_{corr}	correction factor for r_s to it adjust for standard meteorological condition (-)
r_{ew}	bulk external resistance at the hypothetical wet condition ($\text{s}\cdot\text{m}^{-1}$)
R_g	incident solar radiation ($\text{W}\cdot\text{m}^{-2}$)
R_{gl}	minimum solar radiation necessary for transpiration ($\text{W}\cdot\text{m}^{-2}$)
r_h^{wc}	wet canopy resistance to sensible heat flux ($\text{s}\cdot\text{m}^{-1}$)
r_r^{wc}	wet canopy resistance to radiative heat transfer ($\text{s}\cdot\text{m}^{-1}$)
r_s^{min}	minimum canopy resistance ($\text{s}\cdot\text{m}^{-1}$)
r_s^{max}	maximum or cuticular canopy resistance ($\text{s}\cdot\text{m}^{-1}$)
r_s	bulk surface resistance ($\text{s}\cdot\text{m}^{-1}$)

r_s^s	bulk surface resistance to soil evaporation ($s.m^{-1}$)
r_s^t	bulk surface resistance to canopy transpiration ($s.m^{-1}$)
r_s^{ws}	bulk surface resistance to wet canopy evaporation ($s.m^{-1}$)
<i>SAVI</i>	Soil Adjusted Vegetation Index (-)
T_a	air temperature (K)
T_{opt}	optimum temperature ($^{\circ}C$)
T_{ref}	optimal temperature for photosynthesis (K)
u_a	wind speed ($m.s^{-1}$)
u_*	friction velocity ($m.s^{-1}$)
<i>VPD</i>	Vapor Pressure Deficit (Pa)
x	input forcing
\tilde{x}	observed (measured) input data
y	model response
\tilde{y}	observed (measured) response
z	measurement height above the canopy (m)
z_{0h}	roughness height for heat transfer (m)
z_{0m}	roughness height for momentum transfer (m)
z'_{0m}	roughness length of bare soil surface (m)
α_{PT}	Priestley-Taylor coefficient (-)
β	vector of model parameters
γ	psychrometric constant ($Pa.K^{-1}$)
Δ	slope of the saturation vapor pressure versus temperature ($Pa.K^{-1}$)
θ_a	potential air temperature (K)
θ_s	potential land surface temperature (K)
θ_v	virtual potential air temperature (K)
θ_{ref}	soil moisture content thresholds for field capacity ($m^3.m^{-3}$)
θ_{wilt}	soil moisture content thresholds for wilting point ($m^3.m^{-3}$)
κ	von-Karman's constant (-)
λ	latent heat of vaporization ($J.kg^{-1}$)
μ	mean, average
σ	standard deviation
Ψ_m	stability correction function for momentum transfer
Ψ_h	stability correction function for heat transfer
ρ	density of moist air ($kg.m^{-3}$)
ω_x	Parameters of input error model
ω_y	Parameters or response error model

Chapter 1
General Introduction

1 General Introduction

Evapotranspiration (ET)¹ represents the key linking process between the hydrological and energy cycles and as such plays an important role in a variety of disciplines including land surface modelling (Chen and Dudhia 2001), global circulation models (Dolman 1993), irrigation systems (Allen 2000; Bos et al. 2008), hydrology (Sorooshian et al. 1993) and water resources management (Biswas 2004). Knowledge of this variable provides insights and understanding into the complex processes, mechanisms and mutual interactions between the land and atmosphere in terms of mass and heat transfers. Over the land surface, ET accounts for approximately 60% of the total precipitation that is returned to the atmosphere, while in arid and semi-arid regions this can be as high as 90% (Brutsaert 2005). Given the value of understanding the evaporative process in a range of disciplines, the accurate estimation of ET across a range of spatial and temporal scales is of considerable interest.

Despite the aforementioned importance of ET, detailed knowledge and characterisation of the process remains constrained by a number of outstanding issues. Some of these relate to its inherent variability in both space and time and also across climates and ecosystems. Others relate to the challenge of directly measuring the process, whether at local scales using lysimeters (Holmes 1984; Goss and Ehlers 2009), Bowen ratio towers (Todd et al. 2000), eddy covariance towers (Tanner 1967; Meyers and Baldocchi 2005; Aubinet et al. 2012) or via scintillometers (Meijninger et al. 2002) or at larger spatial scales using surface water balance (Wilson et al. 2001) and atmospheric water balance (Kustas and Brutsaert 1987) approaches.

As establishing and maintaining an in-situ measurement station is expensive, there is an economic limit to the spatial density of these systems. As a result, ET models have been developed to estimate this variable from routinely available meteorological data (Farahani et al. 2007; Allen et al. 2011a, b). There have been a number of efforts to describe the evaporative process over the years, developing from simple empirical understanding of the system (Dalton 1802; Bowen 1926; Thornthwaite and Holzman 1939) to more sophisticated approaches (Monin and Obukhov 1945; Penman 1948; Monteith 1965; Brutsaert 1982). Nowadays, the most common practical techniques to estimate ET are those that combine relevant atmospheric variables and surface parameters using a process-based or empirical model (Kalma et al. 2008; Wang and Dickinson 2012). However, these models are not without their own problems and issues and there have been a number of efforts detailing these difficulties (Ward 1971; Dickinson et al. 1991; Sellers et al. 1997; Rana and Katerji 2000). Apart from challenges arising from the data demanding nature of the models, needed parameters may be hard to determine or require local calibration (Stannard 1993; Sumner and Jacobs 2005; Leuning et al. 2008). Even in cases where data and parameters are available, extrapolating the point scale estimates to larger spatial scales remains highly uncertain (Dunin and Aston 1984; Running et al. 1987).

¹ The term evapotranspiration as used in this thesis refers to all process of vaporization including evaporation from soil, transpiration from canopy and evaporation from intercepted water in the canopy.

In response to these challenges, a number of techniques have been developed especially for the spatial estimation of ET based upon the use of satellite remote sensing retrievals (Norman et al. 1995; Bastiaanssen et al. 1998a; Su 2002; Allen et al. 2007b; Carlson 2007; Fisher et al. 2008; Mu et al. 2011). The basis for such models remains the fundamental techniques developed during the 1940's to 1980's (Monin and Obukhov 1945; Monteith 1965; Brutsaert 1982), but with the addition of modules that are able to incorporate remote sensing data as input forcing (Schmugge et al. 2002). The modules have been developed to estimate albedo, emissivity and resistance² parameters from optical bands (Ross 1976a; Becker and Li 1995; Zhao et al. 1997; Su 2002; Cleugh et al. 2007), or to estimate the land surface temperature (Li et al. 2004; Sobrino et al. 2004) and available energy (Kustas and Daughtry 1990; Kustas and Norman 1996) from thermal bands of the remote sensing images. Other models explicitly use the spatial variability context of optical and thermal bands for estimating near-surface temperature gradient (Bastiaanssen et al. 1998a; Allen et al. 2007b), or for ET estimation by developing the so-called triangular or trapezoidal spaces from a vegetation index and the land surface temperature (Carlson 2007; Petropoulos et al. 2009).

Although remote sensing models can partially address the issue of spatial representativeness, the main challenges in efficient description of the ET process remained largely unresolved. These challenges can be categorized into three general themes: application, scaling and uncertainty. These are broadly described below, with further details provided in the following chapters:

- **The Application Challenges** are mainly associated with the performance of the models in the reproduction of the measured values of ET. These are linked with the description and formulation of the governing physical process of evapotranspiration within the models. As evapotranspiration constitutes a major component of hydrological studies, the choice of the ET model can have considerable influences on the assessment, planning and management of water resources. Such influences are further highlighted in the water resources applications, in which continuous measurement and distribution of ET is important for food and environmental sustainability and security at different scales (Parry et al. 1999; Seneviratne et al. 2006; Jung et al. 2010).
- **The Scaling Challenges** are linked with the effects of spatial and temporal resolutions on i) the input variables and parameters in the models, and ii) scaling of the estimated fluxes, in particular when remote sensing data are used (see **Chapter 4**). For example, thermal remote sensing images provide estimates of the sources of energy for ET process (Price 1982; Kustas and Norman 1996) and vegetation parameters estimated from optical remote sensing data provide estimates of the aerodynamic and surface resistances against ET process (Bastiaanssen et al. 1998a; Jiang and Islam 1999). While

² Resistance parameters include aerodynamic and surface resistances. Aerodynamic resistance is the resistance against transfer of heat from the land surface to the atmosphere. Surface resistance is the bulk resistance of the soil/canopy system against the transfer of water vapor from soil pores or leaf stomata up to a level in the atmosphere.

remote sensing data are available at a range of spatial (meter to kilometre) and temporal (e.g. sub-hourly to bi-weekly) resolutions, they may or may not reflect the space and time scales of the process they are intending to represent. The spatio-temporal resolution influences on the performance of the ET models remain under-investigated, apart from a limited number of contributions (Kustas et al. 2004; McCabe and Wood 2006; Brunsell et al. 2008; Long et al. 2011; van Bussel et al. 2011). Such scaling challenges are especially important over heterogeneous surfaces, where sub-pixel variability of evaporative elements is high and can cause large ET variations within a coarse resolution pixel (Anderson et al. 2003; Kustas et al. 2003; Kustas et al. 2004; Li et al. 2008; Anderson et al. 2011).

- **The Uncertainty Challenge** relates to understanding and characterising the various components of uncertainty, present in the evaporative process. Due to the complexity of many ET models, quantifying the magnitude and distribution of errors in ET products remains challenging. Approaches that seek to discriminate the total uncertainty of ET as an integrated value of its individual error-prone components, i.e. errors in input data, model structure, model parameters and response variable(s) (van der Tol et al. 2009; Ferguson et al. 2010; Renard et al. 2010), provide an opportunity to better understand the evaporative process and its sensitivities.

Although these challenges do not necessarily exist in isolation – indeed they are often interlinked (Price 1982; Sellers et al. 1997; McCabe and Wood 2006) – they constitute the framework of this thesis and are often repeated as keywords. The following section seeks to expand on some of these themes, with details provided on the underlying issues as well as a list of specific objectives of this thesis contribution, which will be further developed in the subsequent chapters.

1.1 Literature Review

As mentioned above, three outstanding challenges were identified in the estimation and understanding of the evaporative process. Here is an expansion on these ideas: the application, scaling and uncertainty issues, together with a brief literature review of previous contributions to identify the knowledge gaps and research motivations. A more comprehensive literature review, relevant to the points raised in this section, can be found within the introductory sections of **Chapters 2 to 5**.

1.1.1 Application Challenges in Evapotranspiration Estimation

There are a number of fundamental approaches for describing the process of evapotranspiration. These can be broadly categorized into energy balance (Su 2002), combination (Penman 1948; Monteith 1965), complementary (Bouchet 1963a; Brutsaert and Stricker 1979) and radiation-based (Priestley and Taylor 1972; Fisher et al. 2008) approaches. Monin-Obukhov Similarity Theory (MOST) (Monin and Obukhov 1945; Brutsaert 1982) provides the general theoretical basis for these approaches, describing the process of heat and water vapour transfer from land to an overlying level in the atmosphere using a form of non-linear flux-gradient functions. However,

the fundamental approaches diverge in their use of the MOST functions and also employ differences, simplifications and empiricisms of the related parameterization (Brutsaert 1982, 2005).

In the energy balance approaches, the latent heat flux (or evapotranspiration) is estimated as a residual term in the general energy balance equation, i.e. $\lambda E = R_n - G_0 - H$ where λE is the latent heat flux (interchangeable with ET), R_n is net radiation, G_0 is the ground heat flux and H is the sensible heat flux (all in $\text{W}\cdot\text{m}^{-2}$). In this equation, the main difficulty is in estimation of the sensible heat flux (Su 2002), which is a function of the near-surface temperature gradient and aerodynamic resistance. Different forms of the energy balance methods have been developed, either acting on a single land element (e.g. pixel) independent of spatial variability of the land surface (Kalma and Jupp 1990; Norman et al. 1995; Su 2002) or by accounting for the spatial variability (Bastiaanssen et al. 1998a; Allen et al. 2007b). One of the more commonly used energy balance methods is the Surface Energy Balance System (SEBS) model developed by Su (2002), which has been used in a number of studies (Jia et al. 2003; McCabe and Wood 2006; van der Kwast et al. 2009) and is explored in this thesis in some additional detail in **Chapter 2**.

In the combination type of approaches, both the heat and vapour transfer concepts are combined in a form first presented by Penman (1948) for evaporation from wet surfaces, and later extended by Monteith (1965) (known as the Penman-Monteith model) for moisture limited surfaces. The Penman-Monteith model has been widely used in a number of studies and is the basis for the standard guidelines developed by the Food and Agriculture Organization (e.g. FAO-56; Allen et al. 1998). The model is used in patch scale agriculture studies (Allen 2000; Allen et al. 2005; Er-Raki et al. 2007; Jabloun and Sahli 2008), often with local calibration of parameters (Stannard 1993; Sumner and Jacobs 2005). Alternative forms of the model have also been developed with specific structure and parameterization for land surface models (Nijssen et al. 2001; Ek et al. 2003; Kumar et al. 2011), regional to global scale climate models (Dolman 1993; Evans and McCabe 2010) and also for application with remote sensing data (Cleugh et al. 2007; Mu et al. 2011).

The radiation-based and complementary approaches are both derivatives of the combination theory, albeit with differing assumptions (Brutsaert 2005). The complementary approaches are based on a balancing feedback mechanism between actual³ and potential⁴ ET: over moisture limited surfaces, the energy not used for ET can increase the temperature and humidity demand of the air and thus increase the hypothetical potential ET. This concept was first introduced by Bouchet (1963b), but further developed in a number of subsequent contributions (Brutsaert and Stricker 1979; Granger and Gray 1989; Hobbins et al. 2001; Szilagyi et al. 2009). The main advantage of the complementary approaches, especially the advection-aridity model of Brutsaert and Stricker (1979), is in relaxing the need for surface resistance and

³ Actual ET occurs from a moisture ‘stressed’ environment, which requires consideration of aerodynamic and surface resistances to describe the environmental constraints on evaporative water loss.

⁴ Potential ET is ET from a well-watered vegetation surface or open water when there is no limitation in supplying required energy for vaporization.

error-prone soil moisture data. Hence, the model relies mainly on the parameterization of the aerodynamic resistance, which often requires wind speed and roughness parameters. Such advantages of the complementary approaches motivated a number of contributions for patch to field scale ET estimation (Ali and Mawdsley 1987; Crago and Brutsaert 1992; Qualls and Gultekin 1997; Hobbins et al. 2001; Crago and Crowley 2005), but fewer studies for examining the method at larger scales (Zhang et al. 2011; Venturini et al. 2012).

The Priestley and Taylor (1972) approach is a radiation-based model formulated by reducing the Monteith (1965) model to its radiation components only (Brutsaert 2005). Hence, the aerodynamic parameters do not appear in the Priestley-Taylor model (see **Chapter 2**). The Priestley-Taylor model has been used for the estimation of potential ET over lakes and data-scarce regions (De Bruin and Keijman 1979; Xu and Singh 2002; Bormann 2011; Xystrakis and Matzarakis 2011) and to assess the influence of environmental and ecological variability on potential ET (Fisher et al. 2011). As the model only requires available energy and air temperature to calculate potential ET, its application is straightforward in data-scarce regions: a feature that motivated some studies to reduce its potential ET to actual ET (Flint and Childs 1991; Stannard 1993; Fisher et al. 2005; Fisher et al. 2008; Miralles et al. 2011).

These fundamental approaches differ (and are also similar) in a number of ways: i) the energy balance models relax the need for the surface resistance parameter, but require accurate land surface temperature and aerodynamic resistance; ii) the combination models detail the physical processes of ET, but need more data and are sensitive to surface resistance parameterization, which is often highly uncertain; iii) the complementary approaches can relax the need for both land surface temperature and surface resistance, but still need parameterization of aerodynamic resistance; and iv) the radiation-based models need the least amount of data and parameters, but are deficient in describing the physical process of ET.

Clearly there is much choice in the type and style of models available for user application. As such, there is a need for developing some guidance to provide an informed choice on the ET approach. However, the capacity for such informed model selection cannot be obtained from the majority of the literature that have a focus on evaluating a single ET model (Beven 1979; Inclán and Forkel 1995; Su et al. 2005; Mu et al. 2007; Fisher et al. 2008; Szilagyi et al. 2009; Wang and Yamanaka 2012; García et al. 2013). Rather, it comes from undertaking intercomparison studies that use a common dataset to assess model performance. Unfortunately, there are relatively few intercomparison studies that provide a basis for model selection (Crago and Brutsaert 1992; Stannard 1993; Sumner and Jacobs 2005; Cleugh et al. 2007; Vinukollu et al. 2011c). Even when these have been undertaken, there may be limitations in the variability of the modeling approaches and the diversity of the land surface conditions examined. For example, Crago and Brutsaert (1992) evaluated complementary and combination methods over a grassland site and found that the complementary approach has a better performance. However, in another study Cleugh et al. (2007) identified that a combination approach has a better performance over forest and savanna sites, when compared to an energy balance approach. Likewise, results of a

study by [Sumner and Jacobs \(2005\)](#) showed that a calibrated radiation-based approach can perform better than a combination approach in a natural pasture site. More recently, [Vinukollu et al. \(2011c\)](#) elaborated a rather more comprehensive assessment of the models and concluded on the superiority of a non-calibrated radiation-based approach!

The differences in the materials and methods of those studies, as well as variations in the recognized best performing ET approaches, reduce the capacity for identifying a suitable model for a particular biome and climate type. An effective inter-comparison study should include a range of ET models each belonging to a fundamental approach (with commonly used parameterization of the resistances), as well as a comprehensive set of data sources, attributing: i) representative geographical distribution of the towers; ii) with high-quality meteorological data required to run all models and flux observations to evaluate the performance of simulations; iii) over a range of biomes and climates representing various vegetation heights, phenology and land surface heterogeneity encompassing both moisture and energy limited climates; iv) covering long periods of records representing seasonal variability in hydro-meteorological condition of the land surface; v) with data at short temporal scales (\leq hourly) to conform to the steady-state assumption of the model's theory ([Brutsaert 1982](#); [Stull 1988](#)); vi) and with enough accompanying field or remote sensing data to represent the realistic (dynamical) development of vegetation phenology required for parameterization of the resistances.

Such comprehensive intercomparison studies are critical not only for field to basin scale hydrological applications, but also for global ET assessments: for instance, those being undertaken within the framework of the LandFlux-EVAL initiative (www.iac.ethz.ch/url/LandFlux-EVAL) ([Mueller et al. 2013](#)) and the WACMOS ET (<http://wacmoset.estellus.eu>) projects. As such, a challenge to be addressed in this thesis is to assess the performance of key models, each belonging to a fundamental approach, over a variety of land surface conditions and climate types in order to provide a basis for model selection (see **Chapter 2**).

As part of overall model selection, there are two significant issues that influence the performance of model schemes in flux estimation: resistance parameterisations and model structure.

The aerodynamic and surface resistances represent key parameters for the Penman-Monteith model. Hence, a number of previous studies have focused on the development and evaluation of resistance parameterization methods to improve the Penman-Monteith model's performance ([Thom et al. 1975](#); [Bailey and Davies 1981](#); [Ball 1987](#); [Noilhan and Planton 1989](#); [Verma 1989](#); [Rana and Katerji 1998](#); [Todorovic 1999](#)). For example, [Rana and Katerji \(1998\)](#) identified that the surface resistance parameter is the most important factor for short to medium height vegetation (e.g. grass and sorghum) in moisture limited conditions of a semi-arid climate, but this parameter has a secondary role (after R_n) for short crops with limited moisture stress. Also, [Bailey and Davies \(1981\)](#) showed that the Penman-Monteith model is sensitive to the surface resistance parameterization over soybean and maize, but less so to the aerodynamic resistance.

Likewise, the structure of the Penman-Monteith model in differentiating between the evaporating sources can influence its performance. For example, [Shuttleworth and Wallace \(1985\)](#) modified the single-source Penman-Monteith model to a two-layer scheme (with a Penman-Monteith equation in each layer), in which the mutual interactions between soil and canopy are in series. Separate to the layered structure of the soil-canopy system, other studies developed the Penman-Monteith model to a multi-source structure ([Huntingford et al. 1995](#); [Mu et al. 2011](#)) in which the evaporative sources are in parallel (i.e. with no interactions between the sources). Evaluation of the multi-layer and multi-source models ([Raupach and Finnigan 1988](#); [Stannard 1993](#); [Farahani and Bausch 1995](#); [Huntingford et al. 1995](#); [Fisher et al. 2005](#); [Ortega-Farias et al. 2010](#); [Odhiambo and Irmak 2011](#)) showed some improvements in ET estimation (compared to the single-source structure formulation), but a decision on a suitable modeling structure cannot be resolved, due to differences in the parameterization and land surface conditions of those studies.

A challenge to be addressed in this thesis is to assess the relative significance of model structure and parameterization by examining various resistance methods for some typical model structures over a variety of land surfaces (see **Chapter 3**).

1.1.2 Scale Issues in Evapotranspiration Estimation

As briefly identified, satellite-based remote sensing data are a primary forcing for ET estimation at large spatial scales. However, satellite images and products are at various spatial and temporal resolutions; often those with fine (e.g. \leq daily) temporal resolution have coarser (e.g. ≥ 250 km for optical and ≥ 1 km for thermal bands) spatial resolutions and vice versa ([McCabe and Wood 2006](#)). Such spatio-temporal resolution mismatches can cause large errors in ET estimation. As described earlier, the combination, complementary and radiation-based type of ET models only use thermal data for estimation of the available energy (not directly for ET) and hence the errors in thermal data may only have minimal influence on the resulting ET. However, thermal data are critical for energy balance models, as they rely explicitly on the near surface temperature gradient ([Kalma et al. 2008](#)). The main difficulty in the use of thermal data is that temporal changes in thermal state of the land surface take place at short time scales ([Kustas and Anderson 2009](#)) and hence thermal images taken at one time cannot be used with meteorological data measured at another time, even when the time difference is in the order of a few tens of minutes ([Kustas et al. 2004](#)).

Such limitations reduce the application of satellites like Landsat (e.g. ≤ 120 m in thermal band) for continuous monitoring of ET, as those satellites have relatively coarse (i.e. 16 days) temporal resolutions. Although methods have been developed for disaggregation of coarse resolution thermal images ([Kustas et al. 2003](#); [Agam et al. 2007](#); [Karnieli et al. 2010](#)) or for deriving fine resolution fluxes using process-based data-fusion methods ([Norman et al. 2003](#); [Anderson et al. 2004b](#); [Anderson et al. 2011](#)), fine resolution thermal images are still critical for a variety of energy balance ET models ([Bastiaanssen et al. 1998a](#); [Su 2002](#); [Allen et al. 2007b](#)). In particular, at the time of writing this thesis, the non-commercial satellites with fine resolution multi-

spectral thermal bands are limited to ASTER⁵ sensor onboard Terra, ETM+⁶ onboard Landsat 7 and TIRS⁷ sensor onboard Landsat 8 (Irons et al. 2012), with the first one having problem with its SWIR⁸ sensor, the second one having significant (around 22%) gaps due to the SLC⁹-off problem (Markham et al. 2004; Chen et al. 2012) and the latter is only recently (February 2013) launched and needs to be thoroughly validated for ET estimation purposes.

Due to such issues in fine resolution thermal data, images and products from sensors like the Moderate Resolution Imaging Spectroradiometer (MODIS; twice daily, 1 km) or from geostationary satellites (e.g. GOES¹⁰-10 satellite; 30 minute, 4 km) are used for ET estimation using the energy balance models (Inamdar and French 2009; Anderson et al. 2011; Shu et al. 2011), but often without accounting for the errors that might result from the use of such coarse spatial resolution thermal data (Jia et al. 2003; Nagler et al. 2005a; Senay et al. 2007; Zwart and Bastiaanssen 2007; Immerzeel and Droogers 2008; El Tahir et al. 2011; Gibson et al. 2011; Gokmen et al. 2012).

The widespread use of coarse resolution thermal images motivated a number of studies to quantify the errors associated with spatial resolution (Moran et al. 1997; Su et al. 1999; Anderson et al. 2003; Brunsell and Gillies 2003; Kustas et al. 2003; Sridhar et al. 2003; Kustas et al. 2004; McCabe and Wood 2006; Anderson et al. 2007; Li et al. 2008; Hong et al. 2009; Anderson et al. 2011; Brunsell and Anderson 2011; Tian et al. 2012). To assess the usability of coarse scale satellite imagery, a common approach has been to study the effect of spatial aggregation (i.e. increase in pixel size) on the resulted sensible or latent heat flux products (McCabe and Wood 2006; Li et al. 2008). The rationale behind such studies is related to the theoretical limitations of the ET models in response to the pixel size. In particular, the majority of remote sensing ET methods and their associated parameterization are developed based on patch scale observations (i.e. in-situ sensors) or fine scale satellite images (e.g. 30 to 120 m), but they are often applied to coarse (kilometric) resolution images. Moreover, the coarse spatial resolution of remote sensing images used for estimation of variables and parameters of the ET models can have a mixed (positive and negative) influence on the validation process (Su et al. 1999; Brunsell and Gillies 2003; McCabe and Wood 2006), which increase the uncertainties in the evaluation of the modelling performance.

Spatial aggregation studies have generally examined either the influence of aggregating input data and variables (i.e. 'input aggregation') (Su et al. 1999; McCabe and Wood 2006; Brunsell and Anderson 2011), or the effects of aggregating the resulted heat fluxes (i.e. 'flux aggregation') (Sridhar et al. 2003) or both (Moran et al. 1997; Hong et al. 2009; Tian et al. 2012). Although the magnitude and spatial variability of the resulting coarse resolution heat fluxes have been examined in previous contributions, the main mechanisms of aggregation, in particular the

⁵ Advanced Spaceborne Thermal Emission and Reflection Radiometer

⁶ Enhanced Thematic Mapper Plus

⁷ Thermal Infrared Sensor

⁸ Shortwave Infrared

⁹ Scan Line Corrector

¹⁰ Geostationary Operational Environmental Satellite

influence of aggregating each model's input or parameter on the resulting flux (i.e. the pathology of aggregation errors) is not well investigated. For example, the errors in heat flux estimation (caused by aggregation of the fine resolution images) are generally assigned to the land surface heterogeneity (Moran et al. 1997; Hong et al. 2009; Gebremichael et al. 2010) or are loosely attributed to a vegetation index (Tian et al. 2012). However, it has not been identified if such errors are directly from the uncertainties in near-surface temperature gradient or due to the influence of aggregation on the model parameters (e.g. aerodynamic resistance). A more informative scaling assessment technique may be to track down the propagation of aggregation errors within the modeling algorithm to identify the relative contribution of different variables and parameters in error generation and to identify the most influential ones.

A challenge to be addressed in the current thesis is to assess the pathology of aggregation errors in a process-based energy balance model – an issue developed further in **Chapter 4**.

1.1.3 Uncertainty Issues in Evapotranspiration Estimation

Understanding the errors and uncertainties in ET estimation is necessary in evaluating model products, in particular when they are used in operational applications. The sources of uncertainty are partially known and can be generally attributed to the errors in different components of the estimation procedure, including: input data, model structure, model parameters and response variable(s) (measured heat fluxes). However, while the error culprits are qualified, the quantity and distribution of such errors is not well known, due mainly to the complexity and data demanding nature of the models and challenges in independent measurement. Therefore, evaluation of the integrated uncertainty, while accounting for the main sources of errors, has not been practically feasible (Richardson et al. 2012).

Part of the above mentioned infeasibility arises from the inadequacy of observations and a lack of knowledge of the evapotranspiration process itself (i.e. theoretical). In contrast to classical disciplines like chemistry or physics which often deal with closed or practically controllable systems, hydrological science deals with an open natural system comprised of complex interactive processes with uncertainties inherent in all components (Beven 1989; Beven and Freer 2001; Beven 2006). As a result, the uncertainties in ET models are often evaluated by sensitivity analysis, in which the rate of changes in one variable or parameter is evaluated, while other components of the system are fixed (Beven 1979; Su 2002).

The development from a standard sensitivity analysis to a more holistic probabilistic (stochastic) technique for error assessment has been seen in some limited hydrological applications, including rainfall-runoff modelling (Kuczera et al. 2006) and groundwater studies (Dagan 1985). Such probabilistic uncertainty analysis approaches allow an explicit examination of data and modelling uncertainties using probability distributions. The few cases of probabilistic uncertainty analysis in ET modelling have focused on evaluating the uncertainties in surface resistance parameterization of the Penman-Monteith type of models (Samanta et al. 2007; Samanta et al. 2008; van der

Tol et al. 2009; Li et al. 2010b; Mackay et al. 2012), without explicitly accounting for other sources of errors in input data and response variables. However, data uncertainty (e.g. for meteorological variables) has an important role in the integrated uncertainty of the process-based ET models (Raupach et al. 2005). In particular, the energy balance type of ET models greatly rely on meteorological data such as land surface and air temperatures along with wind speed for estimating heat fluxes, and a small change in each of those inputs can cause large errors in the resulting heat fluxes. However, the relative magnitude of the errors associated with each of these variables is not determined in a quantitative manner (van der Kwast et al. 2009; Gibson et al. 2011; Timmermans et al. 2011).

A challenge to be addressed in this thesis is to quantitatively evaluate the uncertainties of a process-based energy balance model by developing a tailor-made probabilistic uncertainty analysis approach (see **Chapter 5**).

1.2 Objectives of the Thesis

From the brief literature review, a number of outstanding issues and problems in estimating evapotranspiration were identified. This thesis aims to address the knowledge gaps identified in the previous sections by utilizing the state-of-the-art tools, data sources, algorithms and statistical methods. To do this, the investigation will employ a range of: i) high-quality meteorological and flux observations; ii) satellite based remote sensing data; iii) Bayesian stochastic and other statistical analysis techniques; and iv) sophisticated programming and data analysis.

Overall, the key objectives of this research can be summarized as following:

- 1- Characterise the behaviour of fundamental evapotranspiration approaches and their performance across widely varying biomes and land surface conditions;
- 2- Identify the importance and role of model structure and parameterization on flux estimation;
- 3- Quantify the effect of input and flux aggregation on the estimation of evapotranspiration;
- 4- Develop a Bayesian uncertainty analysis framework to understand the role of data uncertainty in flux estimation.

1.3 Thesis Outline

The following chapters are reproduced, with some minor modifications, from a series of manuscripts that are published, accepted or submitted to international peer reviewed journals. A more detailed literature review focusing on the specific subject of the chapter is presented in the introduction section of each chapter. While the chapters are independent in scope and research questions, they form an integral part of the whole thesis. Therefore, some common background and literature review in the chapters can be expected, which is due to the interdependence of the application, scaling and uncertainty issues in ET estimation.

In **Chapter 2** an assessment of the performance of a variety of models, each belonging to a fundamental evapotranspiration estimation approach, is explored. The particular models examined include:

- the Surface Energy Balance System (SEBS) model (Su 2002) (an energy balance approach)
- the single source Penman-Monteith model (Monteith 1965) (a combination approach)
- the advection-aridity model (Brutsaert 2005) (a complementary approach)
- a modified Priestley-Taylor model (Fisher et al. 2008) (a radiation-based approach)

Each of the above mentioned models was simulated using a high-quality multi-year database of tower based meteorological observations, accompanied with some remote sensing retrievals of vegetation indices required for resistance parameterization. The model results were compared against eddy-covariance measured latent heat fluxes derived from the same towers. These meteorological forcing and flux data were derived from twenty FLUXNET towers located across various biomes including: grasslands, croplands, shrublands, evergreen needleleaf forest and deciduous broadleaf forest. Results from **Chapter 2** provide insights into the strength and limitation of each model over the studied land surface conditions. In particular, the influence of environmental controls on ET estimation, including the effects of surface roughness, moisture and energy availability and vegetation phenology, is explored.

Chapter 3 examines the significance of model structure and parameterization in a variety of the Penman-Monteith type of ET models. To assess the effects of model structure, three forms of the Penman-Monteith models including a single-source (Monteith 1965) (PM), a two-layer (Shuttleworth and Wallace 1985) (SW) and a three-source (Mu et al. 2011) (Mu) type of models were used. Also, different parameterizations for aerodynamic and surface resistances are employed. The variety of models provides an opportunity to examine and intercompare fourteen different scenarios of model-parameter combination. The assessments in **Chapter 3** highlight the importance of both model structure and parameterization in ET estimation. In particular, it is shown that the best performing scenarios are from the simpler PM and SW models, but not from the most detailed model (Mu). Also, results showed that a simpler parameterization of surface resistance is more efficient than a more data-demanding one, perhaps due to the role of data uncertainty. However, a simpler aerodynamic resistance did not always produce the best results and a detailed model with accounting for the roughness of surface provided better performance. Moreover, all scenarios showed limitations in ET estimation in the colder months of the year. The results from **Chapter 2** and **Chapter 3** provide some necessary insights on the choice of modeling approach, model structure and resistance parameterization, in particular for large scale studies encompassing a range of land surface conditions.

Chapter 4 evaluates the consequences of spatial aggregation on the performance of a typical energy budget type modelling approach: in this case, the SEBS model (Su 2002). Two cases of input aggregation and flux aggregation are examined over a

heterogeneous agricultural area throughout the cropping season using Landsat 5 images. Results of this chapter indicate a greater sensitivity of the SEBS model to the aggregation of vegetation index products, than to the aggregation of thermal images. The analysis showed that the main cause for such sensitivity to the aggregation of vegetation index products is related to the errors in the estimation of roughness parameters at coarser resolutions. Results of this chapter provide insights into the uncertainties and errors of ET estimates, especially when such models are used with coarse resolution remote sensing data.

Having explored some of the issues related to uncertainty in terms of scale and application assumptions, a more detailed analysis of this theme is presented in **Chapter 5**. Here, a Bayesian inference technique is developed for uncertainty analysis of the process-based ET models, with a case study using the SEBS model. The study area encompasses a multi-tower setup in a heterogeneous agricultural area that provides the necessary observations for developing the needed prior distributions of the input data uncertainties. Results showed that the main source of uncertainty in sensible heat flux estimation was the observation of land surface temperature, as the footprint of the in-situ land surface temperature sensors are much smaller than the effective footprint of the sensible heat flux (sonic anemometer) sensor. Results of this chapter provide insights on the expected errors and uncertainties in the heat fluxes estimated by the SEBS model.

Chapter 6 provides a summary of the results of this thesis along with a general discussion on the contributions made and details of further work that is required to continue advances in our understanding of this important process.

Chapter 2

Multi-Site Evaluation of Terrestrial Evapotranspiration Models

The original research described in this Chapter has been published as:

Ershadi, A., McCabe, M.F., Evans, J.P., Chaney, N.W., Wood, E.F., '[Multi-site evaluation of terrestrial evapotranspiration models using globally distributed FLUXNET data](#)', *Agricultural and Forest Meteorology*, 187(0): 46-61

Reprinted with permission from Elsevier

Reprinted with altered style and minor modifications

2 Multi-Site evaluation of Terrestrial Evapotranspiration

Models

Abstract

The performance of four commonly applied land surface evapotranspiration models evaluated using a high-quality dataset of selected FLUXNET towers. The models that were examined include an energy balance approach (Surface Energy Balance System; SEBS), a combination-type technique (single source Penman-Monteith; PM), a complementary method (advection-aridity; AA) and a radiation based approach (modified Priestley-Taylor; PT-JPL). Twenty FLUXNET towers were selected based upon satisfying stringent forcing data requirements and representing a wide range of biomes. These towers encompassed a number of grassland, cropland, shrubland, evergreen needleleaf forest and deciduous broadleaf forest sites. Based on the mean value of the Nash-Sutcliffe Efficiency (*NSE*) and the root mean squared difference (*RMSD*), the order of overall performance of the models from best to worst were: ensemble mean of models (0.61, 64), PT-JPL (0.59, 66), SEBS (0.42, 84), PM (0.26, 105) and AA (0.18, 105) [statistics stated as (*NSE*, *RMSD*)]. Although PT-JPL uses a relatively simple and largely empirical formulation of the evaporative process, the technique showed improved performance compared to PM, possibly due to its partitioning of total evapotranspiration (canopy transpiration, soil evaporation, wet canopy evaporation) and lower uncertainties in the required forcing data. The SEBS model showed low performance over tall and heterogeneous canopies, which was likely a consequence of the effects of the roughness sub-layer parameterization employed in this scheme. However, SEBS performs well overall. Relative to PT-JPL and SEBS, the PM and AA showed low performance over the majority of sites, due to their sensitivity to the parameterization of resistances. Importantly, it should be noted that no single model was consistently best across all biomes. Indeed, this outcome highlights the need for further evaluation of each model's structure and parameterizations to identify sensitivities and their appropriate application to different surface types and conditions. It is expected that the results of this study can be used to inform decisions regarding model choice for water resources and agricultural management, as well as providing insight into model selection for global flux monitoring efforts.

Keywords: multi-model intercomparison; latent heat flux; energy balance; Penman-Monteith; advection-aridity; Priestley-Taylor

2.1 Introduction

Reliable estimates of evapotranspiration (ET) are required for the accurate representation of mass and energy exchanges at the land surface. In hydrological and water resource studies, an evapotranspiration model is required to characterize the exchange of moisture between the surface and the overlying atmosphere. Not surprisingly, the choice of model can have considerable impact on water resource planning and decision support across a range of temporal and spatial scales. Improved

understanding of the influence of model choice on flux estimation is required in order to better characterize the fidelity of these simulations, particularly in light of an increasing number of regional and global scale efforts to produce land surface heat flux data products (Jiménez et al. 2011a; Mueller et al. 2013).

A number of models have been developed for the estimation of either the reference, potential or actual values of evapotranspiration (see reviews of Kalma et al. 2008 and Wang and Dickinson, 2012). The reference evapotranspiration is defined as the evapotranspiration from a hypothetical, well-watered ‘reference’ crop (Allen 2000), while potential evapotranspiration is the maximum evapotranspiration for a given surface if moisture is not limiting (Penman 1948; Irmak and Haman 2003). Estimation of the reference and potential evapotranspiration is usually based on meteorological data using relatively straightforward techniques (Penman 1948; Doorenbos and Pruitt 1975; Allen et al. 1998). On the other hand, actual evapotranspiration is the evapotranspiration from the land surface, either wet or moisture “stressed”, which requires consideration of resistance schemes to describe the environmental constraints on evaporative water loss (Brutsaert 1982; Rana and Katerji 2000). As a result, scaling of the potential and reference evapotranspiration to actual values is often problematic due to the difficulties in parameterization of the soil-plant-atmosphere interactions and other bio-physiological constraints. These difficulties are especially pronounced in arid and semi-arid environments with limitations on water availability.

The majority of models used in the estimation of the actual evapotranspiration can be categorized broadly into energy balance approaches, combination type techniques, complementary methods or radiation-based schemes (Brutsaert 1982, 2005). The central concept behind the formulation of these models is the transfer of sensible heat and water vapour from the land surface to the overlying atmosphere: a process that is well described by the Monin-Obukhov similarity theory (Monin and Obukhov 1945; Brutsaert 1982). In energy balance approaches such as the Surface Energy Balance System (SEBS) (Su 2002), the focus is on the transfer of sensible heat flux (H), with the actual evapotranspiration (or the latent heat flux, λE) estimated as the residual term in the general energy balance equation ($\lambda E = R_n - G_0 - H$), where λE is actual evapotranspiration in $\text{W}\cdot\text{m}^{-2}$ (used also to refer to the related term ET in this chapter), λ is the latent heat of vaporization ($= 2.43 \times 10^6 \text{ J}\cdot\text{kg}^{-1}$), R_n is net radiation ($\text{W}\cdot\text{m}^{-2}$) and G_0 is ground heat flux ($\text{W}\cdot\text{m}^{-2}$). Combination type models of actual evapotranspiration, conceptualized well by the ubiquitous Penman-Monteith approach (Monteith 1965), are based on the similarity in heat and water vapour transfer, as defined by the Bowen ratio concept (Bowen 1926). The complementary approach to actual evapotranspiration, as described here by the advection-aridity method (Brutsaert and Stricker 1979), is based on the complementary feedback between actual and potential evapotranspiration. This complementary mechanism suggests that if actual evapotranspiration decreases below its true potential value, the amount of energy not used by evapotranspiration becomes available as sensible heat. Finally, radiation based approaches such as the Priestley-Taylor method (Priestley and Taylor 1972) describe a simplified form of the Penman-Monteith combination model,

allowing flux estimation with a minimum of meteorological and radiation information. More detailed descriptions and explanations of these model classes are provided in section 2.2.2.

All of the models described above vary in structural complexity, parameterization and the level of data required to run them. Hence, their performance in estimating actual evapotranspiration is expected to differ over various land surface types and conditions. Furthermore, models are expected to present different behaviour when dealing with the combined uncertainties of input data and parameterizations (Massman and Lee 2002; McCabe et al. 2005; Richardson et al. 2006; Williams et al. 2009; Ershadi et al. 2013a). Consequently, finding an appropriate model for a given land surface has motivated a number of model intercomparison studies. The majority of such studies have focused on an evaluation of the reference or potential evapotranspiration (Trambouze et al. 1998; Xu and Singh 2002; Lu et al. 2005; Bormann 2011; Fisher et al. 2011; Xystrakis and Matzarakis 2011), while others have examined actual evapotranspiration models. For instance, Crago and Brutsaert (1992) evaluated several evapotranspiration models, including the advection-aridity and Penman-Monteith schemes, over the First ISCLCP Field Experiment (FIFE) in Kansas and found that the advection-aridity model produced acceptable results under generally moist conditions. Sumner and Jacobs (2005) evaluated the Penman-Monteith and Priestley-Taylor methods against eddy covariance measurements of evapotranspiration over a natural pasture site in Florida and found that the Priestley-Taylor method, with a calibrated alpha coefficient (α_{PT}), provided the best estimates. Cleugh et al. (2007) compared energy balance and combination methods over forest and savannah sites in Australia. The authors found that while the Penman-Monteith combination technique provided an adequate estimate of the observed evapotranspiration ($R^2 = 0.74$, $RMSE = 27 \text{ W.m}^{-2}$), the energy balance approach did not, due to its sensitivity to uncertainties in the land surface temperature measurements. More recently, Vinukollu et al. (2011c) evaluated an energy balance, Penman-Monteith and Priestley-Taylor models over 16 METFLUX towers and concluded that the Priestley-Taylor performed the best out of these competing schemes. Liu et al. (2013) compared evaporation estimates from a number of models, including the Penman-Monteith model variant developed by Mu et al. (2011) (PM-Mu) and a Priestley-Taylor based model developed by (Miralles et al. 2011) (Global Land-surface Evaporation: the Amsterdam Methodology – GLEAM) over the Mongolian Plateau. They found that at the tower scale, the seasonal variability of the models matched well, except for the winter months, when PM-Mu overestimated ET.

Many of these evaluation and intercomparison studies have provided a solid assessment of a number of modeling schemes at particular locations. However, a basis from which to make an informed model choice remains missing. In particular, selection of the best candidate evapotranspiration model for global applications (Jiménez et al. 2011a; Mueller et al. 2011a) is not supported in any of the current model intercomparison contributions. This is due to a number of reasons, including:

- **Spatial and temporal extent:** most previous studies have compared models over single (or a few) locations and for relatively short time periods with limited

variability in the land surface type and condition. For example, the model evaluations by [Crago and Brutsaert \(1992\)](#), [Stannard \(1993\)](#), [Trambouze et al. \(1998\)](#) and [Sumner and Jacobs \(2005\)](#) were only performed over one location for 42 days, 55 days, 2 months and 10 months respectively;

- **Reduced range of models examined:** the most comprehensive studies were those undertaken by [Stannard \(1993\)](#) and [Vinukollu et al. \(2011c\)](#), where comparisons of energy balance, combination and radiation based methods were undertaken;
- **Low temporal resolution:** With the exception of [Sumner and Jacobs \(2005\)](#), [Pauwels and Samson \(2006\)](#) and [Shi et al. \(2008\)](#), the majority of previous studies have used daily ([Crago and Brutsaert 1992](#); [Xu and Chen 2005](#); [Schneider et al. 2007](#)) or monthly ([Vinukollu et al. 2011c](#)) temporal resolutions. Aggregation of input meteorological forcing to coarser temporal resolutions can greatly affect the simulation results, either positively by reducing the uncertainty in input data, or negatively by increasing the temporal mismatch between different input variables (and parameters). For example, one reason behind the poor performance of the energy balance approach in the [Cleugh et al. \(2007\)](#) study was the use of aggregated tower based meteorological data with 16 day aggregated Moderate Resolution Imaging Spectroradiometer (MODIS) land surface temperature;
- **Prior model calibration:** in a number of studies (e.g. [Sumner and Jacobs 2005](#); [Shi et al. 2008](#)), model parameters were calibrated locally, limiting the utility of the studied model to those specific locations or areas with similar meteorological and land surface conditions;
- **Model parameterization:** often, the vegetation parameters (e.g. leaf area index) required for parameterization of aerodynamic and surface resistances were assumed constant due to the limitations in the field or remote sensing observations. As a result, the dynamics of vegetation growth and its effects on evapotranspiration were overlooked. The incorporation of vegetation dynamics can significantly improve modeling performance, particularly in the models that are more sensitive to the parameterization of aerodynamic and surface resistances ([Cleugh et al. 2007](#); [Tang et al. 2011](#)).

In the present study, the objective is to understand and evaluate the performance of a number of the most commonly utilised models of actual evapotranspiration across a variety of land surface types and conditions. This effort is achieved by using a collection of high quality tower based data, collected over an extensive observation period that enables an adequate representation of meteorological variability.

The main research questions of this study include:

- What is the performance of the selected evapotranspiration models and their ensemble mean over different biomes and surface conditions?
- What is the performance of the selected evapotranspiration models over different seasons?
- Do more complex and data-intensive models perform better than simpler schemes?

- Do violations of a model underlying theoretical assumptions effect simulation performance? (e.g. impacts of footprint homogeneity, stability conditions)
- What are the main sources of uncertainty in evaporation estimation using the selected models?

2.2 Data and Methodology

2.2.1 Forcing Data

One of the principal limitations in the evaluation of evapotranspiration models is the availability of accurate and descriptive input forcing data. The FLUXNET project (Baldocchi et al. 2001; Agarwal et al. 2010) provides a high-quality, community based globally distributed dataset of surface heat fluxes and meteorological data, making them an appropriate source for model evaluation. In this study, 20 eddy covariance FLUXNET towers were selected across a range of representative biomes that included grassland (GRA), cropland (CRO), shrubland (SHR), evergreen needleleaf forest (ENF) and deciduous broadleaf forest (DBF).

2.2.1.1 Tower Based In-Situ Measurements

Four towers were selected for each biome type based on a number of criteria, including: a) variations in vegetation height; b) being spatially distributed; c) quality controlled; d) having extensive period of data with minimal gaps; and e) the availability of all required input data for simulation using the different models in this study. While there are approximately 545 towers within the FLUXNET database (http://fluxnet.ornl.gov/site_status), open access to the data and the range of input variables required for the comprehensive assessment of the evapotranspiration models used in this study significantly limits the choice of towers. In particular, soil moisture (required for surface resistance specification in the Penman-Monteith model) and longwave upward radiation data (used in the calculation of the land surface temperature for the SEBS model) were only available at a reduced number of sites. Likewise, the start of the selected tower records was limited to the year 2000, when remote sensing data required for the resistance parameterization was available (see section 2.2.1.2). The 20 selected towers provide sufficient data to capture a range of land surface conditions at each of the individual sites. The Santa Rita Creosote tower has the shortest data span used here (1.5 years), while the US Mead towers provided the longest (10 years) period of data. The average length of record across the towers is 5 years.

All tower data were filtered for daytime only measurements to avoid having to deal with negative net radiation and nighttime condensation, since these are conditions that are not well represented by any of the models. Daytime is defined to be when the shortwave downward radiation at the tower was greater than 20 W.m^{-2} . This criterion is rather strict, but selected to also filter out the times when early morning and late afternoon transitions in the atmospheric boundary layer occur. The physics of such conditions are not well captured by any of the models and would add uncertainties to

the estimated ET. Data were also filtered for a number of meteorological and quality control constraints to ensure the highest-quality forcing data set. These include rain events, frozen periods (when the air or land surface temperature are less than or equal to zero), negative observed turbulent fluxes, gap-filled records and low quality flagged FLUXNET data. Overall, more than 100 site-years of data, or approximately 500,000 filtered records, were selected for each of the four models. Characteristics of the selected eddy covariance towers are provided in Table 2-1. A map of the spatially distributed tower locations is presented in Figure 2-1.

The level of data pre-processing used in this study varies depending on the data source (refer to Column *L* of Table 2-1). Level 3 data are the quality controlled and gap-filled data obtained from fluxdata.org. Level 2 data are obtained from ameriflux.ornl.gov and no gap-filling or quality control is applied to those data. Although the AmeriFlux dataset provides level 3 data, only level 2 data are used here, since in Level 3 the longwave upward radiation is missing. Data from fluxdata.org are provided at half-hourly temporal resolution, while those from ameriflux.ornl.gov are at an hourly temporal resolution. Both temporal resolutions are used directly in the modeling intercomparison without any aggregation.

The data used from the towers include air temperature, wind speed, humidity, net radiation, ground heat flux and soil moisture. The land surface temperature was derived from tower observations of longwave upward radiation by inverting the Stefan-Boltzmann equation, with emissivity calculated from the Normalized Difference Vegetation Index (NDVI) using the methodology of [Sobrino et al. \(2004\)](#).

Chapter 2

Table 2-1: Selected flux towers and their attributes. z_g is the site elevation (above sea level) in m, z_m is tower height in m, h_c is the canopy height in m, Y is the number of years of data and L is the processing level of data.

	ID	Name	Country	Lat	Lon	z_g	z_m	h_c	Y	L	Reference
		Grasslands									
G1	PT-Mi2	Mitra IV Tojal	Portugal	38.5	-8.0	190	2.5	0.05	2	3	(Gilmanov et al. 2007)
G2	US-Aud	Audubon Research Ranch	USA	31.6	-110.5	1469	4	0.15	4	3	(Horn and Schulz 2011)
G3	US-Goo	Goodwin Creek	USA	34.3	-89.9	87	4	0.3	4	3	(Hollinger et al. 2010)
G4	US-Fpe	Fort Peck	USA	48.3	-105.1	634	3.5	0.3	4	3	(Horn and Schulz 2011)
		Croplands									
C1	US-ARM	ARM SGP – Lamont	USA	36.6	-97.5	314	60	0.5	4	3	(Lokupitiya et al. 2009)
C2	US-Ne3	Mead – rainfed	USA	41.2	-96.4	363	6	2.5	10	3	(Richardson et al. 2006)
C3	US-Ne1	Mead – irrigated	USA	41.2	-96.5	361	6	3	10	3	(Richardson et al. 2006)
C4	US-Bo1	Bondville	USA	40.0	-88.3	219	10	3	7	3	(Hollinger et al. 2010)
		Shrubland/Woody Savannahs									
S1	US-SRc	Santa Rita Creosote	USA	31.9	-110.8	991	4.25	1.7	1.5	2	(Cavanaugh et al. 2011)
S2	US-SRM	Santa Rita Mesquite	USA	31.8	-110.9	1116	6.4	2.5	7	2	(Cavanaugh et al. 2011)
S3	BW-Ma1	Maun- Mopane Woodland	Botswana	-19.9	23.6	950	13.5	8	2	3	(Veenendaal et al. 2004)
S4	AU-How	Howard Springs	Australia	-12.5	131.2	38	23	15	5	3	(Hutley et al. 2005)
		Evergreen Needleleaf Forest									
E1	NL-Loo	Loobos	Netherlands	52.2	5.7	25	52	15.9	5	3	(Sulkava et al. 2011)
E2	US-Fuf	Flagstaff - Unmanaged Forest	USA	35.1	-111.8	2180	23	18	6	2	(Román et al. 2009)
E3	DE-Tha	Anchor St. Tharandt - old spruce	Germany	51.0	13.6	380	42	30	2	3	(Delpierre et al. 2009)
E4	US-Wrc	Wind River Crane Site	USA	45.8	-122.0	371	85	56.3	9	2	(Wharton et al. 2009)
		Deciduous Broadleaf Forest									
D1	US-MOz	Missouri Ozark Site	USA	38.7	-92.2	219	30	24.2	5	2	(Hollinger et al. 2010)
D2	US-WCr	Willow Creek	USA	45.8	-90.1	520	30	24.3	5	3	(Curtis et al. 2002)
D3	US-MMS	Morgan Monroe State Forest	USA	39.3	-86.4	275	48	27	6	2	(Dragoni et al. 2011)
D4	DE-Hai	Hainich	Germany	51.1	10.5	430	43.5	33	3	3	(Rebmann et al. 2005)

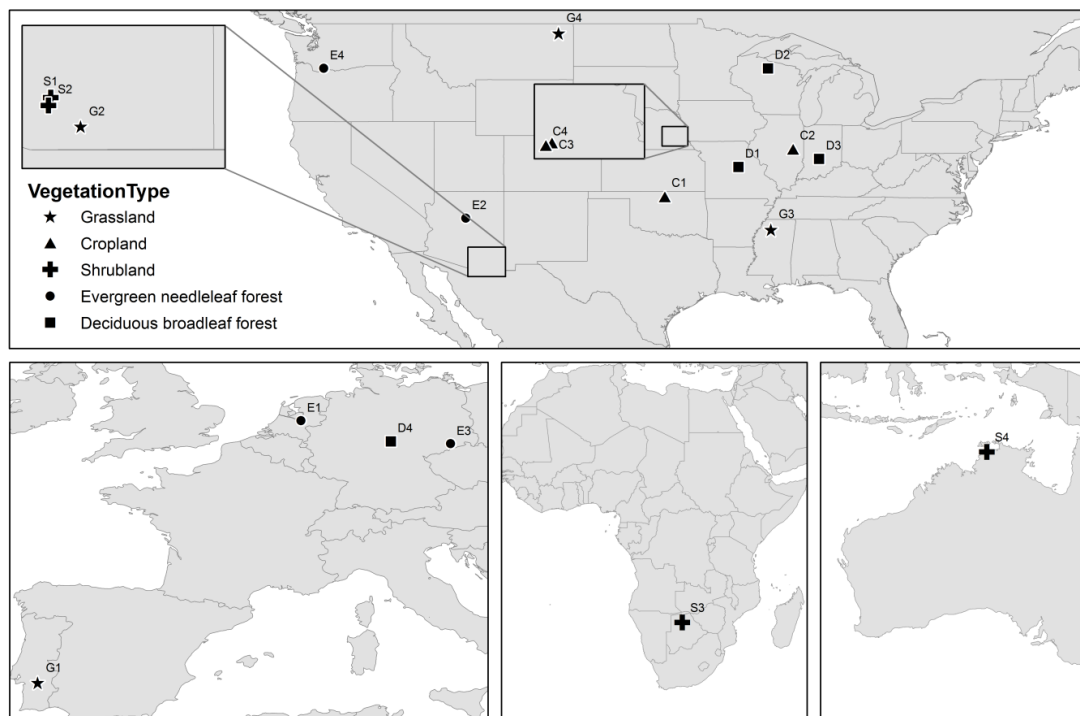


Figure 2-1: Location of the eddy-covariance towers used to provide forcing and validation data in this study.

2.2.1.2 Remote Sensing Based Measurements

Time series of NDVI was extracted from the MOD13Q1 product (Solano et al. 2010) at each tower location. The MOD13Q1 data are derived from the MODIS sensor onboard the Terra satellite and provide 250 m spatial and 16 days temporal resolution. Data were obtained from the Simple Object Access Protocol (SOAP) web services of the Oak Ridge National Laboratory (ORNL) MODIS Land Product Subsets (<http://daac.ornl.gov/MODIS/>). The 16-day gaps between successive NDVI records were filled using linear interpolation. The leaf area index and fractional vegetation cover (required for aerodynamic and surface resistance parameterizations) were calculated from the NDVI data using the methodology of Ross (1976a) and Jiménez-Muñoz et al. (2009) respectively. All evapotranspiration models use the same values of leaf area index and fractional vegetation cover for their parameterization.

2.2.2 Model Descriptions

2.2.2.1 The Surface Energy Balance System (SEBS): an Energy Budget Approach

The SEBS model of Su (2002) is a physically based model that uses a combination of remote sensing and in-situ observations to derive the land surface variables, radiative heat fluxes and roughness parameters required for calculating actual evapotranspiration. The main inputs to the SEBS model include land surface temperature, vegetation height and density, air temperature, humidity and wind speed, along with surface radiation components. When the measurement height of

meteorological variables is in the atmospheric surface layer, the SEBS model uses the Monin-Obukhov similarity theory (MOST) equations (Monin and Obukhov 1945). When the measurement height is within the mixed layer of the atmosphere, SEBS uses the Bulk Atmospheric Similarity Theory (BAST) (Brutsaert 1999). However, in the majority of cases, MOST equations are used unless the roughness of the surface is high or the height of the atmospheric surface layer is low. The MOST equations used in SEBS include stability-dependent flux-gradient functions for momentum and heat transfer, as described below:

$$u_a = \frac{u_*}{\kappa} \left[\ln \left(\frac{z-d_0}{z_{0m}} \right) - \Psi_m \left(\frac{z-d_0}{L} \right) + \Psi_m \left(\frac{z_{0m}}{L} \right) \right] \quad 2-1$$

$$\theta_s - \theta_a = \frac{H}{\kappa u_* \rho c_p} \left[\ln \left(\frac{z-d_0}{z_{0h}} \right) - \Psi_h \left(\frac{z-d_0}{L} \right) + \Psi_h \left(\frac{z_{0h}}{L} \right) \right] \quad 2-2$$

where z is the reference height above the land surface for measurement of the meteorological variables (m), u_a is wind speed (m.s^{-1}), u_* is the friction velocity (m.s^{-1}), ρ is the density of the air (kg.m^{-3}), c_p is specific heat capacity of air at constant pressure ($\text{J.kg}^{-1}.\text{K}^{-1}$), $\kappa=0.41$ is the von Karman's constant (-), θ_s is the potential land surface temperature (K), θ_a is the potential air temperature (K) at height z , H is the sensible heat flux (W.m^{-2}), d_0 is the zero-plane displacement height (m), z_{0m} is the roughness height for momentum transfer (m), z_{0h} is the roughness height for heat transfer (m) and Ψ_m and Ψ_h are the stability correction functions for momentum and heat transfer. L is the Obukhov length (m) defined as:

$$L = -\frac{\rho c_p u_*^3 \theta_v}{\kappa g H} \quad 2-3$$

with g the acceleration due to gravity (m.s^{-2}) and θ_v the atmospheric virtual potential temperature (K).

For atmospheric stability corrections in the atmospheric surface layer, the functions proposed by Beljaars and Holtslag (1991) are used for stable conditions and the functions proposed by Brutsaert (2005) are used for unstable conditions. The roughness length for momentum and heat transfer (z_{0m} and z_{0h}) are estimated in SEBS using the methodology developed by Su et al. (2001), which employs vegetation phenology, air temperature and wind speed.

SEBS uses a correcting method to scale the MOST derived sensible heat flux between hypothetical dry and wet limits based on the relative evapotranspiration concept. Finally, this scaled sensible heat flux can be used to calculate the latent heat flux (λE) as a residual term in the general energy balance equation as $\lambda E = R_n - G_0 - H$. Further details on the SEBS model description are provided by Su (2002) and Su et al. (2005).

2.2.2.2 Penman-Monteith (PM): a Combination Type Technique

The Penman-Monteith model (PM) incorporates heat and water vapour mass transfer principles and is therefore known as a combination equation. The Penman equation (Penman 1948) was developed originally for the estimation of potential evapotranspiration from open water and saturated land surfaces, but was later modified by Monteith (1965) with the introduction of a canopy resistance term to describe the influence of plants on the water vapour transfer through the roots, stems and leaves of the plants. The Penman-Monteith model of actual evapotranspiration can be formulated following Brutsaert (2005):

$$\lambda E = \frac{\Delta(R_n - G_0) + \rho c_p (e^* - e) / r_a}{\Delta + \gamma(1 + r_s / r_a)} \quad 2-4$$

where Δ (Pa.K⁻¹) is the slope of the saturation water vapour pressure curve $e^* = e^*(T_a)$ at the air temperature T_a , γ is the psychrometric constant defined as $\gamma = c_p p / (0.622 \lambda)$ in Pa.K⁻¹, $e^* - e$ is the vapour pressure deficit (Pa), e^* is saturation vapour pressure of the air (Pa), e is actual vapour pressure of the air (Pa) and r_a and r_s are aerodynamic and surface resistances (s.m⁻¹). The ratio r_s/r_a provides an indirect indication of the crop water status (Rana and Katerji 1998). Therefore, as water availability to a canopy decreases, the value of r_s increases and evapotranspiration decreases. Likewise, as a canopy approaches well-watered conditions, the surface resistance tends to zero and the PM equation converges to the original Penman formulation.

The aerodynamic resistance r_a was estimated using an equation suggested by Thom (1975) as following:

$$r_a = \frac{1}{\kappa^2 u_a} \left[\ln \left(\frac{z - d_0}{z_{0m}} \right) \ln \left(\frac{z - d_0}{z_{0v}} \right) \right] \quad 2-5$$

where z_{0v} is the roughness height for water vapour transfer (m). Following Brutsaert (2005) we assumed $z_{0v} = z_{0h}$ with z_{0h} and z_{0m} calculated using the Su et al. (2001) method, as employed in the SEBS model. For estimation of the surface resistance, the Jarvis scheme of Jacquemin and Noilhan (1990) is used as following:

$$r_s = \frac{r_s^{min}}{LAI \cdot F_1 \cdot F_2 \cdot F_3 \cdot F_4} \quad 2-6$$

where r_s^{min} is the minimum canopy resistance (s.m⁻¹) and LAI is the leaf area index (m².m⁻²). F_1 , F_2 , F_3 and F_4 are weighting functions (-) representing the effects of solar radiation, humidity, air temperature and soil moisture on plant stress. Following Chen and Dudhia (2001), the weighting functions can be expressed as:

$$F_1 = \frac{r_s^{min} / r_s^{max} + f}{1 + f} \quad \text{with } f = 0.55 \frac{R_g}{R_{gl}} \left(\frac{2}{LAI} \right) \quad 2-7$$

$$F_2 = \frac{1}{1 + h_s \times (q^* - q)}$$

$$F_3 = 1 - 0.0016(T_{ref} - T_a)^2$$

$$F_4 = \sum_{i=1}^{N_{root}} \frac{(\theta_i - \theta_{wilt})d_i}{(\theta_{ref} - \theta_{wilt})d_i}$$

where r_s^{max} is the maximum or cuticular canopy resistance ($s.m^{-1}$), R_{gl} is the minimum solar radiation necessary for transpiration ($W.m^{-2}$), R_g is the incident solar radiation ($W.m^{-2}$), h_s is a parameter associated with the water vapour deficit (-), $q^* - q$ represents the water vapour deficit ($kg.kg^{-1}$), T_{ref} is the optimal temperature for photosynthesis (K), T_a is the air temperature (K), d_i is the thickness of the i th soil layer (m), d_t is the total thickness of the soil layer (m) and N_{root} is the number of soil layers in the rooting zone.

In this study, the depth of the soil moisture sensor(s) is considered to be representative of the soil layer(s). Such an assumption is unlikely to be valid for the cases of vegetation with deep root system, since the change in surface soil moisture at the half-hourly or hourly time step will not be the same for the whole soil column. However, the limited availability of soil moisture data at tower locations reduces the capacity to improve the assumption further, so some compromise is unavoidable. The values of r_s^{max} , R_{gl} , h_s and T_{ref} are acquired based on the vegetation lookup tables used in the Noah land surface model.

Soil moisture content thresholds for field capacity (θ_{ref}) and wilting point (θ_{wilt}) provide characteristics of the soil type. As soil type information is not available for all sites from field investigations and the values in existing global soil databases are not reliable at the point scale, long-term surface layer soil moisture observations from each tower are used to determine the soil moisture thresholds (Calvet et al. 1998; Ladson et al. 2004; Zotarelli et al. 2010). To do this, the field capacity soil moisture threshold is determined as the 99th percentile of the after rain soil moisture records of the tower. As the short period of soil moisture data might cause lower values of the actual θ_{ref} using this technique, estimated θ_{ref} is truncated to the maximum θ_{ref} value suggested by the soil table used in the Noah land surface model. Similarly, the wilting point threshold is determined from the 1st percentile of the soil moisture records and is capped to the minimum value of the Noah soil table. Both vegetation and soil parameter tables of the Noah model can be obtained from <http://www.ral.ucar.edu/research/land/technology/lsm.php>.

2.2.2.3 Advection-Aridity (AA): a Complementary Method

The concept of complementary fluxes with advection-aridity was first developed by Bouchet (1963b) and further improved by Parlange and Katul (1992). The complementary relationship relies on the feedback between actual and potential evapotranspiration. When there is sufficient water available, evapotranspiration increases and approaches the potential value. In contrast, when water is limited, the

energy that would have been used for evapotranspiration is then used in the production of sensible heat flux. As a result, the vapour pressure deficit increases because of the lack of evapotranspiration, thus elevating the potential evapotranspiration (Huntington et al. 2011). As shown by Brutsaert (2005), the advection-aridity equation for estimation of evapotranspiration (λE) is:

$$E = (2\alpha_{PT} - 1) \frac{\Delta}{\Delta + \gamma} Q_{ne} - \frac{\gamma}{\Delta + \gamma} \frac{\rho(q^* - q)}{r_a} \quad 2-8$$

where α_{PT} is the Priestley-Taylor coefficient, considered here as 1.26 (Priestley and Taylor 1972; Eichinger et al. 1996), q is the specific humidity of the atmosphere (kg.kg^{-1}) and q^* is the specific humidity of the saturated air (kg.kg^{-1}) at temperature T_a . Also, $Q_{ne} = Q_n / \lambda$ with Q_n being available energy, defined as $Q_n = R_n - G_0$. Parameterization of the aerodynamic resistance r_a in this study is similar to that used for the Penman-Monteith model (Brutsaert and Stricker 1979; Brutsaert 2005). The main advantage of the advection-aridity complementary approach is that it does not require any information related to soil moisture, canopy resistance or other measures of aridity, as it relies solely on meteorological variables.

2.2.2.4 Modified Priestley-Taylor (PT-JPL): a Radiation Based Scheme

The Priestley-Taylor model (Priestley and Taylor 1972) is a simplified form of the Penman-Monteith model, developed for estimating potential evapotranspiration from an extensive wet surface under conditions of minimum advection (Pereira and Villa Nova 1992; Eichinger et al. 1996; Sumner and Jacobs 2005). This model is expressed by the following equation:

$$\lambda E = \alpha_{PT} \frac{\Delta}{\Delta + \gamma} (R_n - G_0) \quad 2-9$$

Scaling of the Priestley-Taylor potential evapotranspiration to actual evapotranspiration has been performed by modification or calibration of α_{PT} (Flint and Childs 1991) as a function of the environmental variables. However, in this study we use the modified form of the Priestley-Taylor model developed by Fisher et al. (2008) (hereafter PT-JPL), in which the α_{PT} is kept constant at 1.26 and the potential evapotranspiration is scaled to actual evapotranspiration based on bio-physiological constraints. In this model, total evapotranspiration is partitioned into canopy transpiration (λE_c), soil evaporation (λE_s) and wet canopy evaporation (λE_{wc}) defined as follows:

$$\begin{aligned} \lambda E_c &= k_c \times \alpha_{PT} \frac{\Delta}{\Delta + \gamma} R_n^c \\ \lambda E_s &= k_s \times \alpha_{PT} \frac{\Delta}{\Delta + \gamma} (R_n^s - G_0) \\ \lambda E_{wc} &= k_{wc} \times \alpha_{PT} \frac{\Delta}{\Delta + \gamma} R_n^c \end{aligned} \quad 2-10$$

where R_n^c is the net radiation for canopy, $R_n^c = R_n - R_n^s$ and R_n^s is the net radiation for soil given by $R_n^s = R_n \exp(-0.6LAI)$. Total evapotranspiration is then $\lambda E = \lambda E_c + \lambda E_s + \lambda E_{wc}$.

k_c , k_s and k_{wc} are reduction functions for scaling of potential evapotranspiration in each of canopy, soil and wet canopy components to their actual values and are defined as:

$$\begin{aligned} k_c &= (1 - f_{wet}) f_g f_T f_M \\ k_s &= f_{wet} + f_{SM} (1 - f_{wet}) \\ k_{wc} &= f_{wet} \end{aligned} \quad 2-11$$

where f_g is green canopy fraction, f_{wet} is relative surface wetness and f_T is air temperature constraint. f_M and f_{SM} are empirical factors used as a proxy for plant and soil water stress, respectively. The functions are defined as:

$$\begin{aligned} f_{wet} &= RH^4 \\ f_g &= f_{APAR} / f_{IPAR} \\ f_T &= \exp \left[- \left(\frac{T_a - T_{opt}}{T_{opt}} \right)^2 \right] \\ f_M &= f_{APAR} / f_{APAR_{max}} \\ f_{SM} &= RH^{VPD} \end{aligned} \quad 2-12$$

where f_{APAR} and f_{IPAR} are fractions of the photosynthesis active radiation (PAR) that is absorbed (APAR) and intercepted (IPAR) by green vegetation cover, defined as $f_{APAR} = 1.3632 \times SAVI - 0.048$ and $f_{IPAR} = NDVI - 0.05$. RH represents the relative humidity (fraction), VPD is vapour pressure deficit in kPa and the leaf area index, LAI , is calculated as $LAI = -\ln(1 - f_c) / k_{PAR}$ with $k_{PAR} = 0.5$ and $f_c = f_{IPAR}$. The optimum plant growth temperature (T_{opt}) is the air temperature at the time of peak canopy activity when the highest f_{APAR} and radiation and minimum VPD occur. Finally, $SAVI$ is the soil adjusted vegetation index, calculated as $SAVI = 0.45 \times NDVI + 0.132$.

While Fisher et al. (2008) estimated evapotranspiration using monthly means of tower based meteorological measurements of R_n , maximum T_a and average vapour pressure (e), this study uses half-hourly or hourly values of those variables for flux prediction.

2.2.2.5 Data Requirement of the Evapotranspiration Models

The four evapotranspiration models of this study differ in their required input data and the types of parameterizations employed. The Penman-Monteith model is the most complex and one of the most data demanding models as a result of aerodynamic and surface resistances requiring the explicit description of a number of variables and parameters. While there is no necessity for surface resistance parameterizations in the SEBS model, it still requires land surface temperature observations and is sensitive to

the temperature gradient near the surface. The advection-aridity model demands even less prescribed information, as it does not need soil moisture or land surface temperature. Overall, the modified Priestley-Taylor model is the least data-demanding model used in this study, requiring only air temperature, humidity, available energy and a vegetation index.

Table 2-2: List of required data and parameters for evapotranspiration models as used within this study.

Variable/Parameter	SEBS	AA	PM	PT-JPL
Land surface temperature	×			
Air temperature	×	×	×	×
Wind speed	×	×	×	
Humidity	×	×	×	×
Roughness parameters	×	×	×	
Soil moisture			×	
Net radiation	×	×	×	×
Ground heat flux	×	×	×	×
Soil/Vegetation parameters			×	
Vegetation Index (e.g. NDVI)	×	×	×	×

2.2.3 Statistical Evaluations

The statistical measures used to evaluate model performance include the coefficient of determination (R^2), slope, y-intercept, root-mean-squared difference ($RMSD$), relative error (RE) and the Nash-Sutcliffe efficiency coefficient (NSE). The coefficient of determination describes the degree of co-linearity between simulated and observed values and ranges between 0 and 1, with higher values indicating less error variance. In general, an $R^2 > 0.5$ is considered as acceptable performance (Moriasi et al. 2007). The relative error is defined as the $RMSD$ normalized by the mean values of observed data, with $RE = RMSD / \text{mean}(\lambda E_{obs})$. The Nash-Sutcliffe efficiency represents a normalized statistic that determines the relative magnitude of the residual variance (noise) compared to the measured data variance (Nash and Sutcliffe 1970) and is computed as:

$$NSE = 1 - \left[\frac{\sum_{i=1}^n (\lambda E_i^{obs} - \lambda E_i^{sim})^2}{\sum_{i=1}^n (\lambda E_i^{obs} - \lambda E_{mean})^2} \right] \quad 2-13$$

where λE_i^{obs} is the i th observed λE , λE_i^{sim} is the i th simulated λE , λE_{mean} is the mean of the observed λE and n is the total number of observations. NSE indicates how well the scatterplot of observed versus simulated data fits the 1:1 line. NSE values range between $-\infty$ and 1.0, with a $NSE = 1$ being the optimal value (Moriasi et al. 2007). In addition to the use of single statistics for evaluation of each tower, average values of NSE , R^2 or RE values for all towers of a biome (or of all 20 towers) are used as NSE_{avg} , R^2_{avg} and RE_{avg} for the cases in which an overall assessment of the models is required.

A general assumption in interpretation of the slope, y-intercept, R^2 , RE and NSE is that all of the errors are contained within the simulated values, such that the observed values are error free. This assumption is rarely the case, as λE observations are

uncertain due to a number of factors including representativeness of the source area, instrument sampling errors, land surface heterogeneity and random observation error. Recent work examining the impacts of forcing data error on model simulations of heat fluxes highlights the importance of characterizing the inherent observation error (Ershadi et al. 2013a; Chapter 5).

2.2.4 Energy Budget Closure at Flux Tower Sites

In evaluation of the heat flux models at short time intervals (e.g. hourly), the so-called non-closure issue has been observed by many researchers (e.g. Twine et al. 2000; Massman and Lee 2002; Barr et al. 2006; Haverd et al. 2007; Franssen et al. 2010). The lack of closure in energy balance at eddy covariance towers remains largely unexplained. Likewise, the best way to handle it in terms of data correction remains an open question (Foken et al. 2012). Many studies have shown that this non-closure problem is not due to the uncertainty and errors in observations alone. For example, Mauder and Foken (2006) showed that even at a well maintained site, careful application of all corrections to the raw high-frequency data can slightly reduce the residuals, but cannot completely remove them. One reason for the lack of closure in eddy covariance sites is attributed to unaccounted for advection fluxes. In addition, large eddies (with low frequency) associated with stationary secondary circulations (Foken 2008; Mahrt 2010) that generate over tall canopies and heterogeneous landscape are not usually measured at eddy covariance towers due to instrument limitations (Mauder et al. 2008; Foken et al. 2011; Foken et al. 2012). Kracher et al. (2009) attributed the lack of closure in energy balance to the ground heat flux or storage of the energy in the plant canopy. However, correction for this might result in a large ground heat flux or storage term that cannot be explained by the storage capacity of the soil or canopy (Foken et al. 2011).

One relatively simple way to account for the residual errors in turbulent heat flux measurements is to distribute them according to the Bowen ratio (i.e. $\beta = H / \lambda E$). This method is referred to as the “Bowen ratio” closure correction technique (Twine et al. 2000). Alternatively, the lack of closure can also be corrected by calculating the latent heat flux as a residual term in the energy balance equation (i.e. $\lambda E_{ER} = R_n - G_0 - H$) using the observed fluxes. This method is referred to as the “energy residual” closure correction technique. Either way, both techniques have a major and potentially adverse effect on the actual energy and water balance within the system being examined (Foken 2008).

In this study, both the “Bowen ratio” (BR) and “energy residual” (ER) closure correction techniques were evaluated against modelled evapotranspiration. Following Sumner and Jacobs (2005), the Bowen ratio correction is applied as:

$$\lambda E_{BR} = \frac{R_n - G_0}{1 + \beta} \quad 2-14$$

The corrected latent heat flux values that were less than half or more than double the uncorrected values were considered as missing data (less than 10% amongst all towers). The *NSE* coefficient of the simulated latent heat fluxes calculated against the

original, energy residual (ER) corrected and Bowen ratio (BR) corrected data are shown in Figure 2-2. A similar figure showing R^2 values is added to Appendix A.

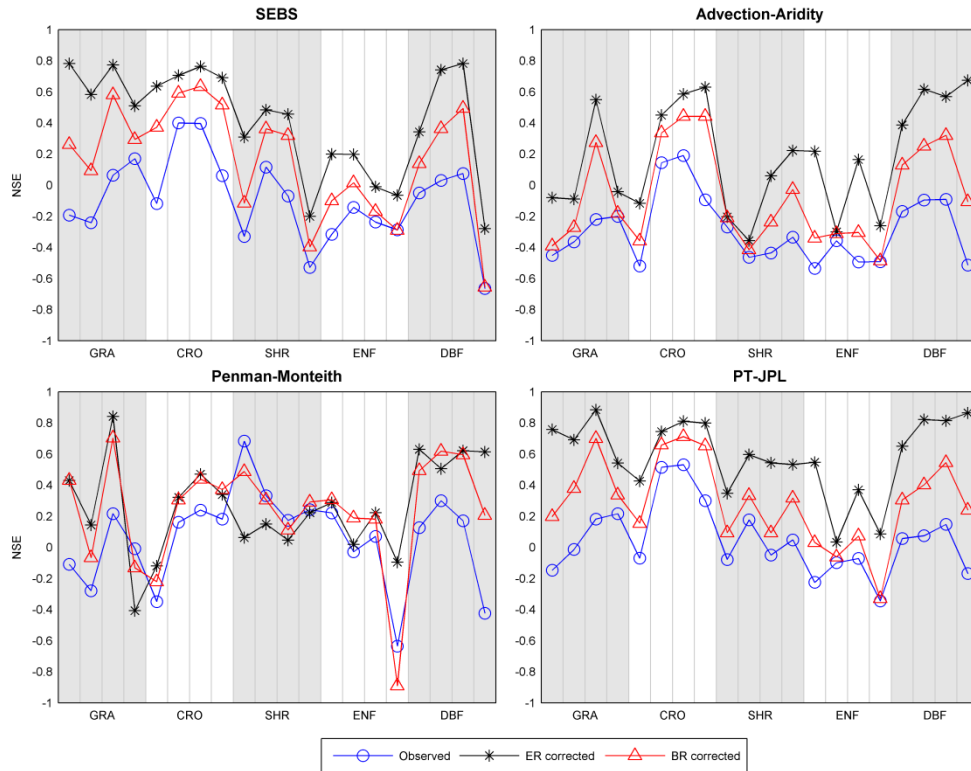


Figure 2-2: Comparison of Nash-Sutcliffe efficiency coefficient calculated for simulated latent heat flux versus observed, energy residual (ER) corrected and Bowen ratio (BR) corrected ones. GRA=Grassland, CRO=Cropland, SHR=Shrubland, ENF=Evergreen Needleleaf Forest, DBF=Deciduous Broadleaf Forest.

Figure 2-2 illustrates that for the majority of model types and land surface conditions, the simulated latent heat fluxes show improved agreement when employing the energy residual corrected latent heat fluxes. This agreement is perhaps because the ER corrected latent heat fluxes are based on the observed sensible heat fluxes rather than the observed latent heat fluxes. In other words, there may be a potential error source in the observed latent heat fluxes that influences their agreement with the modelled values.

Foken et al. (2011) attributed the reasons for lack of performance in Bowen ratio corrected latent heat fluxes to two concepts. The first is the lack of scalar similarity in sensible and latent heat fluxes (Finnigan et al. 2003; Ruppert et al. 2006; Mauder et al. 2008), which requires that these scalar quantities are transported with similar proportion in eddies of different size and shape. In particular, there are differences in turbulent exchanges for temperature and water vapour in tall and dense canopies, which result from dissimilarity of the sources for sensible and latent heat fluxes. This means that while the canopy top is the main source for heating of air during the day,

the source of water vapour is predominantly from within the canopy (Katul et al. 1995; Simpson et al. 1998; Katul et al. 1999; Ruppert et al. 2006). Subsequently, if there is no similarity between sensible and latent heat fluxes, the correction based on the Bowen ratio fails. A possible reason for the improved agreement in the BR corrected latent heat fluxes with the Penman-Monteith based simulations (see Figure 2-2) relative to the other model approaches, might be due to the explicit assumption of the Bowen ratio concept (i.e. similarity between sensible and latent heat fluxes) in the derivation of the Penman-Monteith equation. The second concept stated by Foken et al. (2011), relates to the difference in reliability of the eddy covariance system sensors. Maintaining the calibration of the infrared gas analyser (IRGA) sensor, which monitors the humidity fluctuations, is challenging. The IRGA sensor also has higher sensitivity in capturing the large eddies. In contrast, the sonic anemometer sensor can measure the fluctuation of the sonic temperature with greater reliability. Hence, more errors can be expected in the latent heat flux measurement than those of the sensible heat flux.

Accordingly, the energy residual (ER) corrected latent heat fluxes are used as the basis for evaluation of the evapotranspiration models of this study. It is important to note that the latent heat fluxes estimated using the different evapotranspiration models have a direct fractional (for PM, PT-JPL and AA) or residual (for SEBS) link with the observed available energy. Hence, the modelled latent heat fluxes are not completely independent from the Bowen ratio and/or energy residual closure corrected latent heat fluxes. Such dependencies and correlations might also contribute to the improved agreement that is observed in the energy residual closure correction technique.

2.3 Results

2.3.1 Performance of Models over the Entire Data Period

In this section, the performance of the evapotranspiration models is studied over the entirety of the available period of data collected for each tower. To do this, the statistical measures introduced in section 0 are calculated for all filtered data (see section 2.2.1), with the reference for model simulations being the energy residual (ER) closure corrected latent heat fluxes from measurements at each tower. In addition to the individual model results, an ensemble mean (EM) of the model estimates (with equal weights) is calculated and included in the analyses to develop an overall evaluation of performance. Results are summarized in plots of R^2 , RE and NSE for all towers, as is shown in Figure 2-3. Further statistical details on the performance of the models are provided as scatterplots and summary tables in Appendix A.

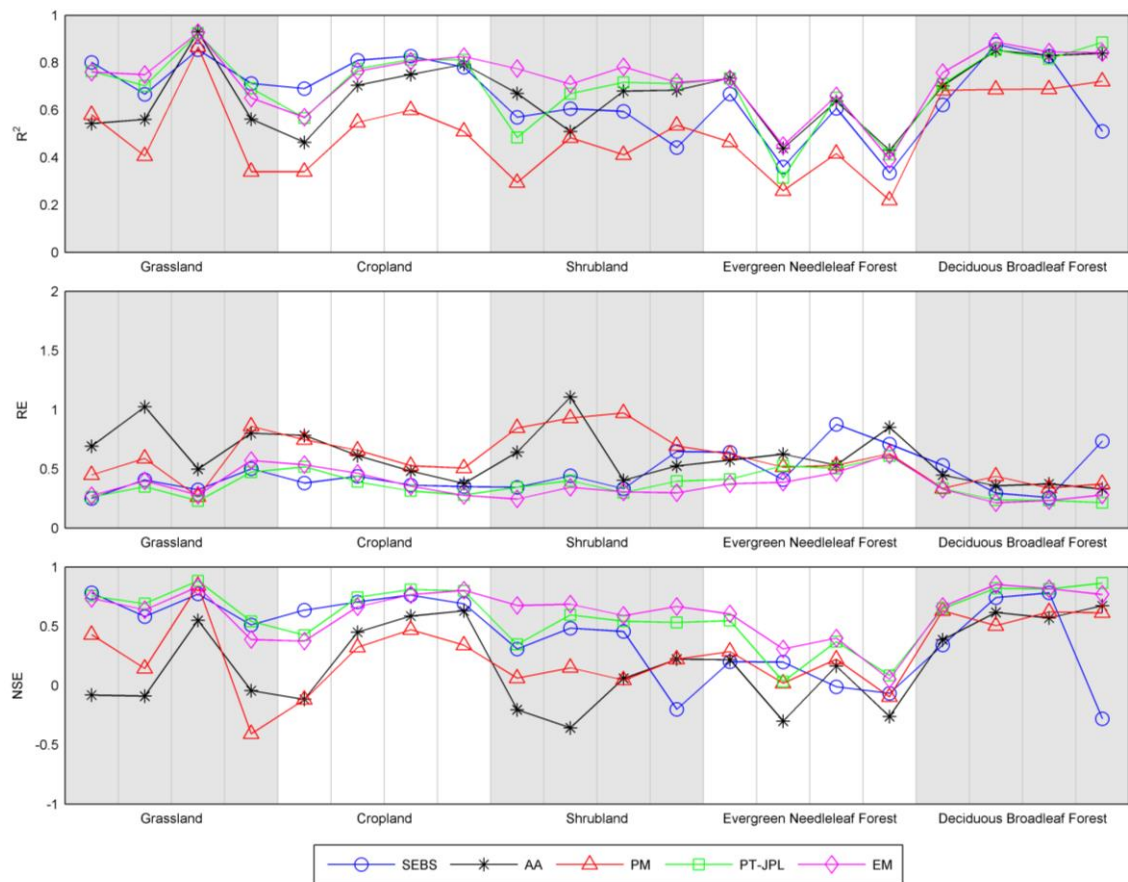


Figure 2-3: Comparison of the efficiency of the evapotranspiration models. RE is relative error (lower is better) and NSE is the Nash-Sutcliffe Efficiency coefficient (higher is better). Towers in each biome type are arranged from left to right (e.g. G1 to G4 for Grassland). EM is for ensemble mean of the models.

In Figure 2-3, the biomes are ordered based on the vegetation height, from grasslands on the left to the forest sites on the right. Likewise, within each biome, towers are ordered based on the vegetation height (lowest to highest from left to right) at each site. A similar figure (Figure A7) is also shown in the supplementary materials with towers arranged from left to right based on total rainfall.

The three selected statistical measures (R^2 , RE , NSE) are relatively consistent in representing the performance of each model over each tower. Generally, PT-JPL and SEBS have higher values of R^2 and NSE and lower values of RE . AA model showed high values of R^2 (comparable to those of PT-JPL and SEBS) over shrublands and forest biomes, but lower values of NSE and $RMSD$, meaning the ET estimation errors in the AA model are considerable. Accordingly, the performance of the AA and PM models is lower than both SEBS and PT-JPL. The performance of the AA and PM models is lower than both SEBS and PT-JPL, but the lower performance of those models show variations in the statistical measures within the different biomes. The performance of the ensemble mean is comparable to PT-JPL and SEBS over grasslands, croplands and deciduous broadleaf forest, but is higher than any other model across shrublands and

evergreen needleleaf forest sites (except for E4). If the mean values of NSE and $RMSD$ (i.e. the mean of the values shown in Figure 2-3 for all towers; represented as NSE_{avg} and $RMSD_{avg}$) are considered as a measure for the overall performance of the models, the ensemble mean (EM) presents the best overall performance with $NSE_{avg} = 0.61$ and $RMSD_{avg} = 64$. Amongst the individual models, PT-JPL model has a good overall performance, with $NSE_{avg} = 0.59$ and $RMSD_{avg} = 66 \text{ W.m}^{-2}$. The second good model is the SEBS with $NSE_{avg} = 0.42$ and $RMSD_{avg} = 84 \text{ W.m}^{-2}$. Amongst the models, the performance of the PM model is ranked third with $NSE_{avg} = 0.26$ and $RMSD_{avg} = 105 \text{ W.m}^{-2}$, while the AA model presents a $NSE_{avg} = 0.18$ and $RMSD_{avg} = 105 \text{ W.m}^{-2}$.

As expected, a models performance varies over the different biomes. In particular, almost all models have lower performance over evergreen needleleaf forest sites, but higher performance over deciduous broadleaf forest sites and cropland sites. Specifically, the SEBS model has good performance for grasslands and croplands with relatively high R^2 (> 0.67), moderate relative error (≤ 0.5), relatively high NSE (≥ 0.5) and slope values close to 1. However, for shrubland and forest sites with taller ($> 3 \text{ m}$) and heterogeneous canopies, the performance of the SEBS model decreases. As is explained in section 2.4.1, the reduced performance of the SEBS model may relate to the presence of the roughness sub-layer of those canopies. The PT-JPL model has R^2 values similar to the SEBS model in grassland and cropland sites, but its slopes are marginally lower (see scatterplots in Appendix A), suggesting an underestimation of evapotranspiration. Over tall canopies ($> 3 \text{ m}$), the PT-JPL model has better performance than the SEBS and other models in terms of NSE , slope, y-intercept and $RMSD$. The PM model underestimates evapotranspiration in the majority of towers across each biome type, with low values of slope (e.g. less than 0.75). The model also displays low values of R^2 (e.g. less than 0.5) for some towers in grassland, shrubland and evergreen needleleaf forest biomes. In contrast to the PM model, the AA model shows strong overestimation of evapotranspiration: in particular over grassland (slope ≥ 1.10) and deciduous broadleaf forest sites (slope ≥ 1.17). A more comprehensive summary of the performance of the models in each biome type is provided in Table 2-3.

Table 2-3: A summary of the performance of the evapotranspiration models. Biome types are defined as: GRA=Grassland, CRO=Cropland, SHR=Shrubland, ENF=Evergreen Needleleaf Forest, DBF=Deciduous Broadleaf Forest. The numbers in the parenthesis in each grid are biome averaged R^2_{avg} , RE_{avg} and NSE_{avg} (from left to right), and the numbers with bold font indicate the best performance. The numbers underneath the biome abbreviations in the first column denote the ranked order of models (SEBS, AA, PM, PT-JPL from left to right) based on their statistical performance (see Appendix A) over that particular land cover type

	SEBS	AA	PM	PT-JPL
GRA 4,1,3,2	(0.76; 0.37; 0.66) - Good performance with $NSE_{avg} = 0.66$ and slope close to 1 - $RMSD \leq 59 \text{ W.m}^{-2}$ and $NSE \geq 0.51$	(0.71; 0.73; 0.21) - Overestimation with slope ≥ 1.1 - highest $RMSD$ values	(0.55; 0.54; 0.25) - Underestimation in all sites except in G3	(0.77; 0.33; 0.72) - Best performance with $NSE_{avg} = 0.77$ and slope close to 1 - underestimation at G1 and G2, with slope ≤ 0.83 - lowest values of $RMSD$ (44-55 W.m^{-2})
CRO 1,4,2,3	(0.78; 0.38; 0.7) - good performance with tower based $R^2 \geq 0.69$ and $RMSD \leq 68 \text{ W.m}^{-2}$, slope ≥ 0.90 and y-intercept $\leq 51 \text{ W.m}^{-2}$	(0.68; 0.56; 0.39) - overestimation at C1 and C2 with y-intercept ≥ 40 - higher y-intercept in C2 (rainfed crop) than C3 (irrigated crop)	(0.5; 0.61; 0.25) - lower R^2 than other models - underestimation in C1 and C4 - more scatterness for $\lambda E < 300 \text{ W.m}^{-2}$	(0.74; 0.38; 0.69) - Except in C1, its performance is comparable to the SEBS model
SHR 4,1,3,2	(0.55; 0.44; 0.26) - good performance for S1, S2 and S4 compared to other models - underestimation in S3 with slope = 0.8	(0.64; 0.67; -0.07) - overestimation in S1, S2 and S3 with slope > 1.3	(0.43; 0.86; 0.12) - underestimation in all sites with slope ≤ 0.3	(0.65; 0.36; 0.5) - best performance compared to other models - underestimation in S1 with slope = 0.7
ENF 4,3,1,2	(0.49; 0.66; 0.08) - overestimation in E1 and E3 with slope = 1.2 - underestimation in E2 and E4 with slope < 0.6	(0.56; 0.64; -0.05) - overestimation in E1 and E3 with slope ≥ 1.2 - overestimation in E2 and E4 with y-intercept $\geq 54 \text{ W.m}^{-2}$	(0.34; 0.57; 0.11) - underestimation in all sites with slope ≤ 0.7	(0.53; 0.51; 0.26) - good performance in E1 and E3 ($R^2 \geq 0.65$, slope $\cong 1$, $RMSD \leq 79 \text{ W.m}^{-2}$) - underestimation in E2 and E4 with slope ≤ 0.8
DBF 4,3,2,1	(0.71; 0.45; 0.4) - overestimation in all towers except in D3	(0.81; 0.38; 0.56) - overestimation with slope ≥ 1.1 - negative y-intercept at D2, D3 and D4	(0.7; 0.37; 0.59) - underestimation except at D4 - $R^2 > 0.68$ and $NSE \geq 0.5$ in all sites	(0.82; 0.25; 0.79) - best performance with highest NSE compared to other models

2.3.2 Performance of Models at Monthly Timescales

Given the temporal changes in water and energy availability that occur throughout the year, it is of interest to examine the impact of such variations on these different evapotranspiration models. To study possible seasonal influences on the performance of the models (and the ensemble mean), we examined the temporal changes in monthly *NSE* for half-hourly and hourly ET. For each tower, we first calculated the *NSE* for all half-hourly or hourly data in each month of the multi-year tower records. Then, a single average of those per-month *NSE* values was calculated for each model across each tower, with the results plotted in Figure 2-4. A similar figure showing monthly-based R^2 values is also presented in Appendix A. To support identifying the temporal trend of ET at each site, the monthly average of observed ET for each tower is calculated as μ_E , which is used to calculate the normalized fraction of monthly evapotranspiration (f_E) via equation 2-15. Time series of f_E are shown in thick grey lines in each panel of Figure 2-4.

$$f_E = \frac{\mu_E - \min(\mu_E)}{\max(\mu_E) - \min(\mu_E)} \quad 2-15$$

Although the lack of data for some towers will influence the statistical significance of the calculated per-month average values (e.g. there are 4 towers with less than 2 years of data records), the results are expected to reflect the dominant trends in model performance, since most biomes contain a sufficiently long record.

To evaluate the performance of the models in different seasons, we use the term “seasonality” i.e. a model with high seasonality is a model that only performs well for a few months of the year. Figure 2-4 shows that each model has a different behaviour in seasonality at different towers and even at towers that belong to the same biome type. For example, the SEBS model shows better performance in summer months at E3 (DE-Tha), but the opposite (i.e. lower performance in summer) at E4 (US-Wrc). As another example, SEBS shows no seasonality in G1 (PT-Mi2) tower, but some seasonality in G2 (US-Aud) and G3 (US-Goo).

Not discounting the cases mentioned above, some general trends can be observed in the seasonality of the models in Figure 2-4. For example, all models (and the ensemble mean) indicate a degree of seasonality in the cropland and deciduous broadleaf forest sites. However, the number of months with higher *NSE* values is lower for PM and the AA models. Moreover, these two models show stronger seasonality than do the SEBS and PT-JPL models. One other important observation is the poor performance of PM, AA and SEBS models over the shrubland sites, showing a number of near-zero or negative values of monthly-based *NSE* during the year. Similar to the observations made for Figure 2-3, monthly-based *NSE* values of the ensemble mean are higher than the models in majority of the cases, but they have seasonality trends (mostly similar to PT-JPL seasonality trends).

Figure 2-4 also shows the significance of growing and non-growing seasons on ET modeling at cropland sites. Here, growing season is referred to the periods when crops

can be grown – considered around May to October in the northern regions of US, which is the case for C1 to C4 towers. The results show higher values of *NSE* (e.g. 0.7 to 0.9) during the growing season for all models and the ensemble mean at C2 to C4 sites. However, the results for C1 are different, with no distinct peak in the monthly-based *NSE*. From the data, the reason for different response of the models at C1 tower is not clear, but it might be due to the strong change in the cropping pattern of the site, which for the four years of simulations was wheat-corn-wheat-soybean.

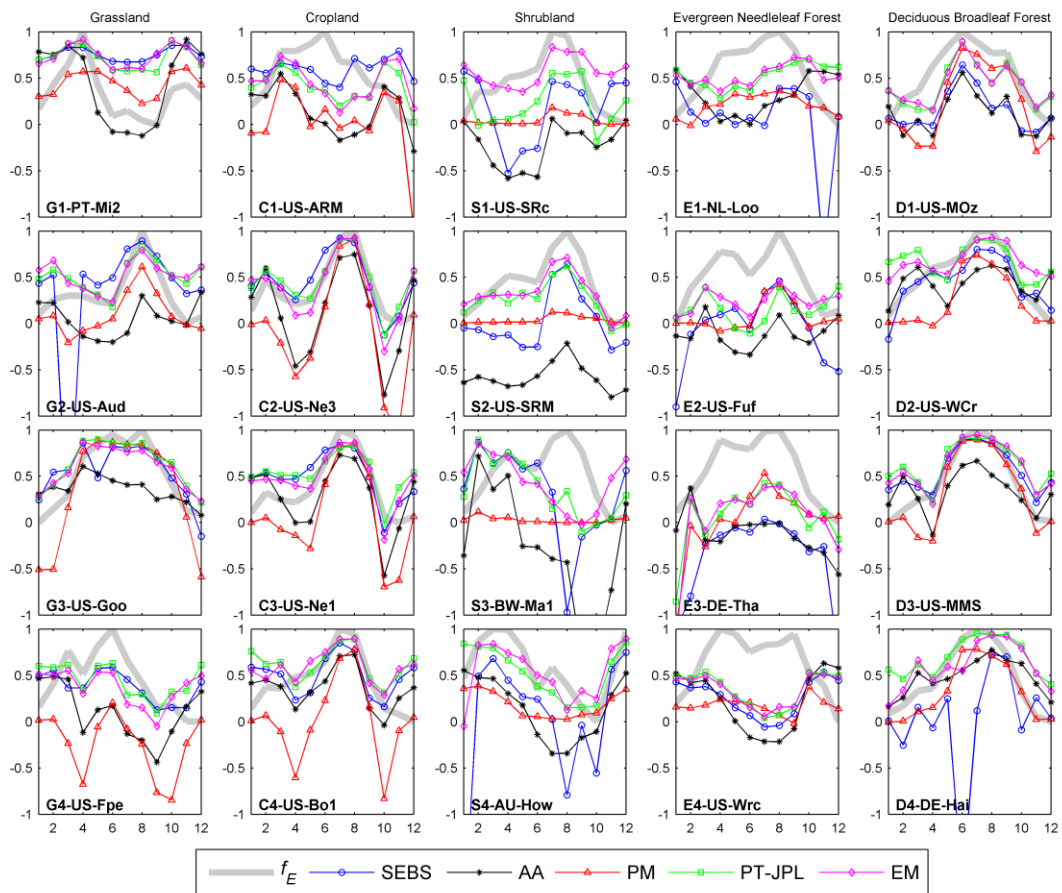


Figure 2-4: Mean per-month value of the Nash-Sutcliffe Efficiency calculated for each of the four studied models at each of the 20 tower locations. The x-axis represents month of the year, while each point on the graph represents the temporally averaged per-month NSE calculated for all available tower record years (see Table 2-1 for details on individual tower data length). Note that the per-month NSE values are for half-hourly or hourly scale ET data, not in monthly scale. f_E is normalized fraction of monthly observed ET . EM is for ensemble mean of the models.

2.4 Discussion

The results presented in the sections above are of interest in studying the performance of the evapotranspiration models across different biome types. However, comparison of the results against findings from relevant previous studies can be useful in understanding and diagnosing the main causes for the lack of performance for some models relative to others.

2.4.1 SEBS Model Performance

The SEBS model performed well in grassland and cropland sites having short canopies (e.g. less than 3 m) and displayed limited seasonality in its performance over the majority of the examined towers. However, SEBS also showed reduced performance over (tall) forest and (heterogeneous) shrubland landscapes. This limitation of SEBS can be attributed to an uncertainty that exists in the structure of the SEBS model: the form of the MOST equations used in SEBS do not have correction terms to adjust for

the so called roughness sub-layer effects (Harman and Finnigan 2007; Harman 2012). This limitation was addressed in a recent contribution by Weligepolage et al. (2012) for a forest site.

Other reasons for the reduced performance of the SEBS model in certain instances might relate to errors in the input data and model parameterizations. For example, SEBS showed reduced performance over shrubland ($NSE_{avg} = 0.26$) and evergreen needleleaf forest sites ($NSE_{avg} = 0.08$), where the heterogeneity in the landscape is likely to be strong and the representative source area for various input variables or parameters might be different. In particular, SEBS is sensitive to the terms that control the transfer of heat from the land surface to the atmosphere, including the temperature difference between the land surface and the atmosphere and the parameterization of the aerodynamic resistance. Therefore, any errors and uncertainties in the observations of the land surface temperature, air temperature, wind speed and roughness parameters will directly influence the performance of the SEBS model. Due to the complexity of the heat transfer and energy balance mechanisms and deficiencies in the spatially representative in-situ observations, it is not clear which variable or parameter has a greater role in the final sensible or latent heat product. Consequently, there is no agreement in previous research regarding the main cause of uncertainties in the SEBS model performance. These uncertainties have been attributed to the roughness parameters (Timmermans et al. 2013), land surface temperature errors (van der Kwast et al. 2009) or total errors in the temperature gradient and wet limit criteria (Gibson et al. 2011).

In a recent contribution, Ershadi et al. (2013a) used a Bayesian inference technique to quantitatively estimate the errors and uncertainties of input data in estimation of the sensible heat flux over soybean and corn towers in the SMEX02 (Soil Moisture Experiment 2002) study area (see **Chapter 5**). They showed that amongst air temperature, wind speed and land surface temperature, the latter had the strongest effect on the mismatch between observed and estimated sensible heat flux, with Bayesian inferred values of the land surface temperature differing by up to ± 5 °C from the in-situ observed data. They attributed such difference to the divergence between the footprint of the in-situ land surface temperature sensor and the footprint of the eddy covariance tower. As the heterogeneity of the land surface in the majority of the towers in this study is much stronger than those of the SMEX02 study area, it might be relevant to assume larger differences in the source area (footprint) of meteorological variables than those of the flux variables, which contribute to explaining a large degree of errors observed in the SEBS results.

2.4.2 AA Model Performance

The AA model showed relatively high values of R^2_{avg} (comparable to those of PT-JPL and SEBS), but overall its performance ($NSE_{avg} = 0.18$ and $RMSD_{avg} = 105 \text{ W.m}^{-2}$) was associated with relatively large overestimations of evapotranspiration (e.g. slope ≥ 1.05) across all biomes. Comparison of the results of this study with previous research is not completely feasible, due to different forms of wind functions being used for aerodynamic resistance (Crago et al. 2005) and in some cases, model parameters being

calibrated (Liu et al. 2012). However, the seasonality (underestimation in winter or dry condition) and significant biases, in particular over grassland and deciduous broadleaf forest sites, have been observed and documented in previous studies (Ali and Mawdsley 1987; Crago and Brutsaert 1992; Qualls and Gultekin 1997; Hobbins et al. 2001; Crago and Crowley 2005). For example, Han et al. (2011) observed significant bias in evapotranspiration estimations of the advection-aridity model over different grassland and cropland sites of China. Also, Huntington et al. (2011) evaluated a modified advection-aridity model over arid shrublands in eastern Nevada and found monthly evapotranspiration overestimated, but the annual averages (for two years) were within the uncertainty of the measurement accuracy (~10%).

A possible explanation for the errors found in the current evaluation of the AA model might be associated with the assumption of a constant α_{PT} for all towers. While the original advection-aridity model does not require calibration of its α_{PT} parameter, some studies have shown that the Priestley-Taylor coefficient (α_{PT}) varies for different regions and with vegetation type. For example, Pauwels and Samson (2006) observed an annual cycle in the calculated values of α_{PT} with mean annual average value of 1.21 ± 0.79 over grass, which they found is related to the annual cycle of the humidity of the soil. In addition, Yang et al. (2012) found that α_{PT} in the advection-aridity model has significant seasonality in the Asian monsoon region, with larger α_{PT} value in winter than in summer.

The poor performance of the AA model over shrubland and forest sites ($NSE_{avg} = 0.15$ and $RMSD_{avg} = 108 \text{ W.m}^{-2}$) might be associated with the assumption of a neutral atmosphere that is intrinsic in the formulation of this model (Brutsaert 1982). This assumption is invalid over tall and heterogeneous land surfaces where the instability in the turbulence is significant and the roughness sub-layer might influence eddy-covariance measurements. In addition, as noted for the SEBS model, errors and uncertainties in input data and roughness parameterization and mismatch between the sources areas for input and response variables, all contribute to the low performance of the AA model.

2.4.3 PM Model Performance

Although widely used across a range of land cover and climate conditions, the results of this study identified some limitations in the application of the form of the Penman-Monteith approach used in this study ($NSE_{avg} = 0.26$ and $RMSD_{avg} = 105 \text{ W.m}^{-2}$). In many instances, there was a significant underestimation of evapotranspiration (slope ≤ 0.9) and considerable seasonality over a number of towers: in particular, those situated in croplands or in deciduous forests. The seasonality results indicated that in the colder months the performance of the model is limited, with large errors resulting in an underestimation of evapotranspiration.

Similar challenges in the performance of the PM model have been identified in a number of previous studies, where errors were attributed to the land surface conditions and uncertainties in input data. For example, Burba and Verma (2005) identified that the difference in Penman-Monteith estimations of evapotranspiration

in native tallgrass prairie and cultivated wheat, is strongly related to the effects of soil moisture stress and variations in green foliage area, with meteorological variables having a smaller impact. Conversely, [Ferguson et al. \(2010\)](#) found that the choice of vegetation parameterization, followed by surface temperature, has the greatest impact on PM derived evapotranspiration.

Given the multi-model scheme of this study, comparison with the PT-JPL model would provide a practical means to identify some of the limitations of the PM model. In particular, it might be expected that if high-quality input data were used, this model should outperform the PT-JPL model given the theoretical advances of the Penman-Monteith approach over the Priestley-Taylor model (see sections 2.2.2.2 and 2.2.2.4). However, an evaluation of a single-source PM model (similar to that of the current study), the two-layer [Shuttleworth and Wallace \(1985\)](#) and the three-source [Mu et al. \(2011\)](#) model with a range of r_a and r_s parameterization techniques (for the same towers of this study) ([Ershadi et al. In Review-b; Chapter 3](#)) has shown that resistance parameterization, in particular the surface resistance, has an important role in PM type models: indeed, more important than the actual structure of the model. As such, better performance of the PT-JPL model (compared to the PM model) is related to an effective use of biological and environmental constraints in reducing the potential Priestley-Taylor ET to its actual values, not necessarily to just the ET partitioning structure of the PT-JPL method.

In summary, the possible sources of uncertainty in the PM model might be related to: a) uncertainties inherent in the structure of the Jarvis scheme for surface resistance estimation ([Alves et al. 1998; Kumar et al. 2011](#)); b) errors associated with the soil moisture data that influence the estimation of surface resistance; and c) uncertainties in the estimation of aerodynamic resistance (e.g. assumption of neutral stability) ([Brutsaert 1982; Mahrt and Ek 1984](#)). As the PM model shows reduced performance with the high-quality tower scale dataset of this study, some caution is prudent for application of this model at increased spatial scales in which data might be expected to contain larger uncertainties: at least with the model structure and parameterizations used within the current study.

2.4.4 PT-JPL Model Performance

Overall and amongst individual models, the PT-JPL model displayed the most consistent performance ($NSE_{avg} = 0.59$ and $RMSD_{avg} = 66 \text{ W.m}^{-2}$) suggesting that it can be considered as a reliable model for evapotranspiration estimation over a range of land surface conditions. However, in the majority of cases (e.g. G1, C3, S1, E3, D3) the performance of PT-JPL and SEBS were close. The PT-JPL approach showed limited seasonality in model performance (see section 2.3.2) relative to other models and provided the highest statistical measures of agreement to the observations. Similar performance has been reported by [Fisher et al. \(2008\)](#), with an average R^2 of 0.9 and 7% bias for monthly data for a three year period over 16 FLUXNET sites (some of which are included in the current study). More recently, [Vinukollu et al. \(2011c\)](#) identified superior performance of the PT-JPL model in 12 eddy covariance towers, located in grasslands, croplands and woody savannahs, for a three year period using monthly

averages of hourly data. However, they found significant bias in summer months, which corresponds to the growing season.

Results from the current study show that the PT-JPL is relatively insensitive to the vegetation height and consequently to the roughness sub-layer effects, in contrast to the SEBS model – the next best performing model. The PT-JPL approach does not require the specification of aerodynamic and surface resistances. As such, uncertainties in the estimation of the roughness length parameters have no influence on evapotranspiration estimates in the PT-JPL model. The PT-JPL model requires a minimum of input variables, including NDVI, air temperature, available energy and humidity (see Table 2-2). Therefore, propagation of uncertainties from other variables such as land surface temperature, wind speed and soil moisture provide no adverse influences on this model. Moreover, the PT-JPL model relies on plant functions and bio-physiological parameterization of the land surface that provide a simple yet seemingly robust representation of the interactions between vegetation and the atmosphere. The net radiation and air temperature are the main driving forces for the PT-JPL model and they generally have lower uncertainty in observations (hence resulting in better model performance).

The PT-JPL model did exhibit reduced performance over the evergreen needleleaf forest towers, which might be attributed to the limitation of NDVI in capturing the vegetation dynamics of this biome (Xiao et al. 2004). Consequently, such uncertainties in NDVI estimation are translated to errors in the estimation of the constraint function parameters (f_{wet} , f_g , f_T , f_M , f_{SM}) of the PT-JPL model over the evergreen needleleaf forests. Although the PT-JPL model performed well compared to other models of this study, the sensitivity of this model to its constraint function parameters and to the α_{PT} parameter for different land surface conditions are issues worth further investigation. One recent contribution (García et al. 2013) examined a sensitivity analysis of the PT-JPL model at the daily scale over an open woody savannah (Sahel) and Mediterranean grassland (Spain) site. The authors found that f_{SM} and f_T are the most sensitive parameters, contributing to the uncertainty of the estimated evapotranspiration by 22% and 18% respectively. Such figures are useful in determining the main causes of uncertainty in evapotranspiration estimation by the PT-JPL model, in particular in the global applications of this model.

2.4.5 Performance of the Ensemble Mean Method

The ensemble mean of the models produced the best overall estimates of ET across the towers, with $NSE_{avg} = 0.61$ and $RMSD_{avg} = 64 \text{ W.m}^{-2}$. The method also showed limited seasonality trends (similar to PT-JPL) in monthly-based ET prediction. The overall NSE values of the ensemble mean method (Figure 2-3) were comparable to those of the PT-JPL method over individual towers for grasslands, croplands and deciduous broadleaf forest biomes in majority of the cases. However, over shrublands and evergreen needleleaf forest sites, where all the models performed relatively poorly, the ensemble mean method produced higher NSE values (except for E3 and E4). Such results may be helpful for large scale applications, where selecting a single

candidate ET model is challenging (Jiménez et al. 2011a; Vinukollu et al. 2011a; Ferguson et al. 2012; Mueller et al. 2013).

Multimodel ensemble approaches are used in hydrological assessment of climate change scenarios (Christensen and Lettenmaier 2006; Graham et al. 2007; Sheffield and Wood 2008), climate change projections (Tebaldi and Knutti 2007), groundwater assessment (Neuman 2003), hydrological modeling for streamflow prediction (Wood and Rodríguez-Iturbe 1975; Duan et al. 2007) and remote sensing soil moisture estimation (Guo et al. 2007). However, applications of multimodel ensemble approaches for ET estimations are limited to relatively few cases exploring the spatial variability of ET at global scales (Jung et al. 2010; Vinukollu et al. 2011a). Further research is needed to develop and evaluate an effective multimodel ensemble approach for large scale ET estimation, perhaps by using probabilistic (e.g. Bayesian) approaches for weighting the models based on their skills for various biomes and climates.

2.4.6 Limitations of the current study

One of the limitations of the current study is the exclusion of evaporation and sublimation of snow in the model evaluations (data records for such conditions were filtered from the analysis). While the topic is important and significant in ET modeling, the models used here were originally developed for, and routinely applied in, non-frozen conditions (see literature review in section 2.1). In particular, the roughness parameterization used for SEBS, PM and AA approaches is based on the Su et al. (2001) model, which uses vegetation indices for non-snowy surfaces. Extending such parameterization to snow-covered surfaces is an active and ongoing research topic in its own right (Helgason and Pomeroy 2011; Reba et al. 2012), but is not within the scope of the current study.

Another aspect of this chapter that has the potential for further research relates to the use of *in situ* data forcing and accounting for the inherent uncertainties in that data (e.g. meteorologic variables and available energy) as well as uncertainties in the model parameters (e.g. roughness and resistances) (McCabe et al. 2013). One of the key constraints in incorporating uncertainty evaluations in model intercomparisons is the limited capacity and availability of datasets for evaluating such uncertainty. That is, flux towers are sparse (e.g. ~ 500 globally), their global and temporal coverage is incomplete and they do not account for spatial heterogeneity at a site.

Although uncertainty evaluations are not included in the current chapter, the uncertainties related to parameterizations, land surface temperature and meteorological data forcing are partially explored in the subsequent chapters. For example, the influence of model structure and resistance parameterization on the PM type of models is evaluated in Chapter 3, the influence of spatial resolution of thermal images on ET modeling using the SEBS model is explored in Chapter 4 and the issue of data uncertainty in sensible heat flux estimation using the SEBS model is evaluated in Chapter 5.

Uncertainties from estimation of available energy are also important in ET modeling, but have often been neglected in ET model evaluations (Vinukollu et al. 2011a;

Vinukollu et al. 2011c). These have not been explicitly examined in this thesis for a number of reasons, but primarily because of data limitations. In addition to the previously identified deficiencies of the existing flux tower network, tower data usually only provide the total net radiation, not its individual components, complicating the task of uncertainty assessment. At tower scale evaluations (i.e. the focus of the current chapter), remote sensing retrievals of available energy components have been shown to be within 5-10% of daytime values (Kustas and Norman 1996; Wang et al. 2012a; Wang and Dickinson 2013) – a much higher degree of accuracy than comparable meteorological retrievals from remote platforms or model simulations (Avissar and Pielke 1989; Buizza et al. 1999; Thorne et al. 2005). Although, such uncertainty figures are around three times lower than the expected uncertainties in ET estimation (e.g. 15-30%; Kalma et al. 2008), integration of the errors when calculating the available energy product might be significant at larger scales and may reduce the reliability of regional to global scale ET estimates. Evaluation of available energy uncertainty in this thesis is limited to evaluating the influence of T_s pixel size on available energy errors in Chapter 4, but further work is required to investigate the issue of error propagation in available energy, especially with the recent development of a number of global scale product and related activities (Jiménez et al. 2011a; Mueller et al. 2013).

2.5 Conclusion

In this study, four evapotranspiration models were evaluated over a multi-tower database at hourly or half-hourly temporal resolutions. Models differed in their assumptions, data requirements and parameterization, ranging from comprehensive and complex approaches such as the Penman-Monteith and energy balance schemes, to more simple and semi-empirical approaches, such as the Priestley-Taylor and advection-aridity techniques. Results showed that the PT-JPL model, followed closely by the SEBS model, provided improved performance relative to the PM, as parameterised in section 2.2.2.2, and the AA models.

Results of this model intercomparison offer guidance on areas of research that are needed to address some outstanding issues in the application of these models. One such area is in the quantification of the total (integrated) uncertainties for model simulations. Such “integrated” uncertainty would comprise the uncertainties in model structure (e.g. formulation, partitioning), parameterization (e.g. roughness, resistances), input data (e.g. meteorological data) and response variables (e.g. latent heat flux). Differences between the spatial resolution of point scale input data and model parameters derived from satellite data as well as footprint difference between input data (e.g. land surface temperature) and observed fluxes, also contribute to these elements of uncertainty (McCabe and Wood 2006; Ershadi et al. 2013b). Discriminating these various sources of error within model simulations would allow for the diagnosis and identification of the main sources of errors in evaporation estimation. A Bayesian type approach might be useful in handling such uncertainties, while conserving the model context (Kavetski et al. 2006a; Samanta et al. 2007; Mackay et al. 2012; Ershadi et al. 2013a). In such a Bayesian uncertainty framework, the non-closure of energy sources can be included as an error source in the response variables.

A further issue in the evaluation of ET models is the role of temporal resolution. In the current study, the focus was on hourly and half-hourly resolutions, principally because ET models are strictly valid only in steady state conditions (i.e. captured at periods of ≤ 1 hour) (Brutsaert 1982; Katerji et al. 2010). At coarser temporal resolutions (e.g. daily, monthly), the modeling performance might be expected to increase due to an elimination of closure issues (Finnigan et al. 2003) or the noise-reduction mechanism of temporal averaging on input data and measured ET. An assessment of temporal aggregation effects on both input data and the flux products is recommended, as many studies use aggregation to daily and monthly scales, without first assessing the impact of uncertainties on model results (Crago and Brutsaert 1992; Xu and Chen 2005; Schneider et al. 2007; Vinukollu et al. 2011c).

The sensitivity of some of the models examined here to variations in the underlying land surface conditions implies a need for caution in efforts towards routine global application. Perhaps the key message of this analysis is that one single model is not able to outperform all others when considered across a range of landscapes. That is, there might not be one scheme appropriate for all land cover types. Yet, this remains the predominant approach when developing global flux data sets: a single solution, single model product. For global products to provide useful insight across the diverse terrestrial landscapes encountered in global application, an alternative approach is required. The improved results obtained from the ensemble mean method of this study suggests constructing an ensemble evaporation product, whereby individual products are weighted according to their performance over particular land cover types, might be a reliable candidate approach. To do this requires an expansion on the type of evaluation effort undertaken here, extrapolating across more towers, different land cover types (bare soil, snow, water bodies) and over longer time periods. With the expanding array of available flux towers, computational resources and data sets with which to drive these different modeling schemes, such an approach is certainly achievable for future product development. Recent activities within the GEWEX LandFlux initiative (Mueller et al. 2013) and also within the WACMOS ET project (<http://wacmoset.estellus.eu>), may provide a potential framework for implementation of such multi-model ensemble ET products.

Acknowledgement

Funding for this research was provided via an Australian Research Council (ARC) Linkage (LP0989441) and Discovery (DP120104718) project, together with a top-up scholarship to support Ali Ershadi from the National Centre for Groundwater Research and Training (NCGRT) in Australia. We thank the METFLUX site investigators for allowing us to use their meteorological data. This work used eddy covariance data acquired by the FLUXNET community and in particular by the AmeriFlux (U.S. Department of Energy, Biological and Environmental Research, Terrestrial Carbon Program: DE-FG02-04ER63917 and DE-FG02-04ER63911) and OzFlux. We acknowledge the financial support to the eddy covariance data harmonization provided by CarboEuropeIP, FAO-GTOS-TCO, iLEAPS, Max Planck Institute for Biogeochemistry, National Science Foundation, University of Tuscia, Université Laval and Environment Canada and US Department of Energy and the database development and technical

support from Berkeley Water Center, Lawrence Berkeley National Laboratory, Microsoft Research eScience, Oak Ridge National Laboratory, University of California - Berkeley, University of Virginia. Data supplied by T. Kolb, School of Forestry, Northern Arizona University, for the US-Fuf site was supported by grants from the North American Carbon Program/USDA NRI (2004-35111-15057; 2008-35101-19076), Science Foundation Arizona (CAA 0-203-08) and the Arizona Water Institute. Matlab scripts for automatic downloading of MOD13Q1 data were provided by Dr Tristan Quaife, University College London via the web portal at http://daac.ornl.gov/MODIS/MODIS-menu/modis_webservice.html. We acknowledge the contributions provided via the LandFlux-EVAL initiative and the WACMOS ET project.

Chapter 3

Impact of Model Structure and Parameterization on Penman-Monteith Type Evapotranspiration Models

The original research described in this Chapter has been submitted for publication as:

Ershadi, A., McCabe, M.F., Evans, J.P., Wood, E.F., '[Impact of model structure and parameterization on Penman-Monteith type evaporation models](#)', *Journal of Hydrology*, In Review

Copyright in this work may be transferred to the Elsevier without further notice, and this version may no longer be the latest version.

3 Impact of Model Structure and Parameterization on Penman-Monteith Type Evapotranspiration Models

Abstract

The impact of model structure and parameterization on the estimation of evapotranspiration (ET) is investigated across a range of Penman-Monteith type models. To examine the role of model structure on flux retrievals, three different retrieval schemes are compared. These model structures include a traditional single-source Penman-Monteith model (PM) (Monteith 1965), a two-layer model based on Shuttleworth and Wallace (1985) (SW) and a three-source model based on the Mu et al. (2011) scheme (Mu). To evaluate the impact of parameterization choice on model performance, a number of commonly used formulations for aerodynamic and surface resistances were substituted into the different model schemes. The subsequent response of the three model types to variation in their parameterization schemes was evaluated against data from twenty globally distributed FLUXNET towers, representing a cross-section of biomes that include grassland (GRA), cropland (CRO), shrubland (SHR), evergreen needleleaf forest (ENF) and deciduous broadleaf forest (DBF).

Scenarios based on 14 different model structure and parameterization combinations identified a range of responses over the studied biomes. The scenarios were ranked based on their mean value of Nash-Sutcliffe Efficiency (i.e. NSE_{avg}) for the towers within each biome type. Results indicated that the best performing model/parameter combinations were scenarios based on the PM model (over GRA, CRO, SHR) and the SW model (over ENF and DBF). Interestingly, these highly ranked scenarios all shared the simple lookup table based surface resistance parameterization of the Mu model, while a more complex Jarvis multiplicative method for r_s produced lower values of NSE_{avg} . Likewise, the top-ranked scenarios all employed a version of the Thom (1975) equation for aerodynamic resistance that incorporated dynamic values of the roughness parameters: except over DBF sites, where the simpler aerodynamic resistance approach of the Mu model showed enhanced performance. While the Mu surface resistance method relaxes the need for soil moisture data, the Thom aerodynamic resistance approach requires wind speed and vegetation height data, potentially limiting the application of the model over GRA, CRO, SHR and ENF.

A number of limitations of PM type models were observed, particularly in estimating evapotranspiration during colder months of the year. All model and parameter combinations showed higher NSE values for warmer months of the year, with lower values during the colder months. These and other issues indicate the sensitivity of the PM type models to structure, parameterization and time of simulation and highlight the need for their further development and assessment. Given the widespread application of PM type approaches, the importance of correctly specifying a robust and appropriate parameterization is critical in obtaining reliable retrievals. Indeed, the variability of model response as a function of parameterization requires special attention when the method forms the basis of agricultural management, drought forecasting and climate change projection applications.

Keywords: evapotranspiration; latent heat flux; eddy covariance; FLUXNET; grassland; cropland; shrubland; evergreen needleleaf forest; deciduous broadleaf forest

3.1 Introduction

Accurate estimates of evapotranspiration (ET) are required in water resources management, irrigation management and hydrologic studies. For this reason, a range of models have been developed to provide evapotranspiration products across different spatial and temporal scales (Rana and Katerji 2000; Kalma et al. 2008; Wang and Dickinson 2012). The Penman-Monteith (PM) model (Monteith 1965) is one of the most widely used models for the estimation of evapotranspiration, as it has a process-based formulation that requires commonly available meteorological variables, including air temperature, wind speed, humidity and radiation. The PM model forms the theoretical basis of a number of continental and global scale evapotranspiration models (Cleugh et al. 2007; Ferguson et al. 2010; Mu et al. 2011; Yan et al. 2012) and land surface schemes (Chen and Dudhia 2001; Kumar et al. 2011): albeit with some variation in formulation and parameterization. In addition, PM is advocated as an operational approach through the Food and Agriculture Organization (FAO) (Doorenbos and Pruitt 1975; Allen et al. 1998) and is widely employed in irrigation planning, operation and management (Allen 2000; Allen et al. 2005; Er-Raki et al. 2007; Jabloun and Sahli 2008).

Underlying the performance of this common approach are important issues of model structure and parameterization that influence the utility of the technique for general application. In its simplest form, the Penman-Monteith model is a one source ‘big-leaf’ model that lumps the heterogeneity of the land surface into a single evaporative element. In this configuration, no distinction is made between evaporation from bare soil, evaporation from canopy intercepted water or transpiration via the canopy. However, other versions of the PM model have been developed that consider the land surface as a layered system (e.g. Shuttleworth and Wallace 1985) or discriminate components of the land surface into different evaporative sources (e.g. soil and canopy), with a PM model formulated in each layer or component (e.g. Cleugh et al. 2007).

Inherent in the choice of model structure is the development and choice of appropriate parameterizations to describe the physical processes occurring within the system. In PM type models, the aerodynamic and surface resistance schemes (r_a and r_s) represent critical controls on heat and vapor flux transfer through the soil, plant and atmospheric continuum. Theoretically, the transfer of heat from the land surface to the atmosphere is opposed by the aerodynamic resistance, which is formulated as a function of the roughness of the surface, wind speed and the stability of the atmosphere (Thom et al. 1975). Although there are aerodynamic resistances for both heat and water vapour transfer (they are also conceptually different), these are often assumed equivalent for hydrological applications (Brutsaert 1982). While the aerodynamic resistance characterizes the degree of “atmospheric connection” of the surface layer to the surrounding atmosphere, the surface resistance describes the

biophysical controls of the canopy system on the transfer of water vapour from soil pores or plant stomata to the air just above the surface.

Given the importance of the resistance parameterization in flux estimation, a number of investigations have examined their application in PM type models. The underlying assumption in many of these studies has been that if the resistance parameters are estimated accurately, then the (single-source) PM type model should be able to provide an accurate estimate of evapotranspiration (Raupach and Finnigan 1988). This perception motivated efforts to develop new algorithms and to expand upon existing representations of both the aerodynamic resistance (e.g. Thom et al. 1975; Bailey and Davies 1981; Verma 1989) and the surface resistance (e.g. Ball 1987; Noilhan and Planton 1989; Rana and Katerji 1998; Todorovic 1999). Several subsequent papers have examined the effects of improved parameterizations on PM model simulations (Beven 1979; Alves and Santos Pereira 2000; Pauwels and Samson 2006; Furon et al. 2007; Irmak and Mutiibwa 2010; Katerji et al. 2010). For example, in studies of soybean and maize crops, Bailey and Davies (1981) and Irmak and Mutiibwa (2010) found that the PM model was insensitive to aerodynamic resistance. In contrast, Alves and Santos Pereira (2000) studied a drip-irrigated lettuce field and found that the reduced performance of the PM model was related to not accounting for the wind speed or aerodynamic resistance. Other contributions have related the pitfall of the single-source PM model to the lack of performance in r_s parameterization. In particular, locally calibrated r_s models are shown to have an improved performance compared to uncalibrated r_s models, due possibly to aggregating all uncertainties of ET modeling in the calibration of r_s (Rana and Katerji 2000; Katerji et al. 2010; Liu et al. 2012). For example, Katerji et al. (2010) found that a semi-empirical calibrated surface resistance method (Rana and Katerji 1998) performed well over irrigated crops (R^2 between 0.8 and 0.93), while a process-based surface resistance model (Todorovic 1999) underestimated ET over grasslands and overestimated in taller crops (soybean, sorghum and vineyard).

In addition to uncertainties that originate from inadequate surface resistance and aerodynamic resistance formulations, the single-source structure of the PM model can also cause errors in the estimation of evapotranspiration. In terms of model structure, the single-source PM model was originally developed for the special case of a dense, well-watered canopy that absorbs most of the available energy. However, in sparse canopies evaporation from the soil can be as important as the canopy transpiration (Shuttleworth and Wallace 1985). In these scenarios, the partitioning of total evapotranspiration to different sources or layers is important (Allen et al. 2011b). Furthermore, the 'big leaf' assumption requires that the sources of heat and water vapour occur at the same level within the canopy (Finnigan et al. 2003; Foken et al. 2012). This requirement might be met in a short and dense canopy or a bare soil surface, but is unlikely to be true for a tall or sparse canopy (Wallace 1995).

As a consequence of these limitations and a desire to develop approaches with more general or universal application, a number of efforts have been directed towards improving the structure of the "single source" PM model to multi-layer or multi-source schemes. In a multi-layer scheme, the representation of the soil-canopy-atmosphere

system is improved by vertically dividing the canopy structure into separate layers, with each utilizing the PM model, but linked via a network of resistances. Such a multi-layer configuration means that the aerodynamic resistances are coupled in series and have interactions (Shuttleworth and Wallace 1985; Choudhury and Monteith 1988; Dolman 1993). In multi-source schemes, the total ET from the land surface is generally partitioned into evaporation from the soil, transpiration from the canopy and evaporation from the intercepted water in the canopy (with the latter absent in two-source schemes). In contrast to multi-layer schemes, multi-source schemes have resistances that are often in parallel and hence have no interaction (Kustas 1990; Brenner and Incoll 1997; Mu et al. 2011; Wang and Yamanaka 2012).

A combined form of multi-source schemes with both parallel and series resistance coupling is also possible (Daamen 1997; Mo and Beven 2004; Hu et al. 2009; Villagarcía et al. 2010). While the combined multi-layer and multi-source schemes might provide a more comprehensive realization of the physics of the heat and vapour transfer (Allen et al. 2011b), difficulties in providing the required data and parameters for such schemes limit their general application. For example, in evaluation of a three source clumped model in a dryland area, Villagarcía et al. (2010) found that the depth of soil moisture measurement was a major controller of the estimated surface resistances: it should be close to the surface for the soil component, but for the vegetation component the soil moisture sensor should be positioned at a deeper depth, where the effects of extremely low values of the superficial layer of soil is excluded or attenuated. Moreover, uncertainties in input data and parameters might affect the accuracy of such models (Mo and Beven 2004) and therefore calibration is often used for their parameterization (Dolman 1993).

Few studies have focused on an intercomparison of the PM based models to evaluate the significance and effectiveness of both the model structure and the choice of parameterization. Stannard (1993) compared a one source PM model with the two-layer model of Shuttleworth and Wallace (1985) in a semi-arid environment and found that the two-layer model ($R^2=0.78$) had an improved performance relative to the one-source description ($R^2=0.56$), as it was more representative of the heterogeneity of the land surface. In another PM based model study, Huntingford et al. (1995) compared the single-source PM model with a two-source model (sources representative of bushes and herbs) and the two-layered model of Shuttleworth and Wallace (1985) across a Sahelian savannah. Their two-source model was a simple extension of the one-source PM model with different surface resistances for bushes and herbs. They found that the one-source model performed adequately in dry conditions, but that the two-layered model improved the evapotranspiration estimations in post-rainfall conditions when the soil surface is wet. Moreover, they identified that the two-source model was suitable for those cases when each source extracts water from a separate layer within the soil. In a completely different biome, Fisher et al. (2005) found similarity in the magnitude and trends of the single-source PM model ($R^2=0.46$) and the two-layered Shuttleworth and Wallace (1985) model ($R^2=0.43$) when evaluated over a pine forest.

In reviewing the literature, it is readily apparent that there are few definitive outcomes with which to guide the selection of the most appropriate model configuration for a particular land surface. A missing element of many previous efforts was a comprehensive examination of model and data characteristics, such as the role of model structure (e.g. one-source, multi-layer, multi-source), impact of model parameterizations (e.g. resistances and roughness) and variability in climate zone and biome type (e.g. grasslands, cropland, forest). Furthermore, due to data limitations, most studies were performed over relatively short periods of weeks to months (e.g. [Stannard 1993](#); [Huntingford et al. 1995](#)), with few cases extending into yearly time periods (e.g. [Fisher et al. 2005](#); [Ortega-Farias et al. 2010](#)). Clearly, multi-year datasets are better able to represent the dynamics in the bio-physiological and hydro-meteorological variability of the land surface: issues that are central in evapotranspiration estimation and comprehensive model evaluation.

These issues provide the motivation to evaluate the role of model structure and parameterization across a range of PM type models. For this purpose, we selected three model structures: the original single-source [Monteith \(1965\)](#) model, the two-layer [Shuttleworth and Wallace \(1985\)](#) model and the three-source [Mu et al. \(2011\)](#) model. Each of these schemes was then integrated with various aerodynamic and surface resistance parameterizations. To maintain a realistic range of land surface dynamics, we utilize a globally distributed set of eddy covariance towers comprised of (relatively) long periods of data. These in-situ measurements provide both the needed meteorological forcing to drive the different schemes and also to evaluate the model simulations. Our model intercomparison exercise is used to address the following research questions: What is the significance of model structure in the performance of Penman-Monteith type models? What is the relative significance of aerodynamic and surface resistances? Which of the model structures and parameterizations are most appropriate for the accurate simulation of evapotranspiration over different landscapes?

3.2 Data and Methodology

3.2.1 Input Forcing and Evaluation Data

The same forcing data of **Chapter 2** are used for the development and evaluation of the models in this study.

3.2.2 Description of Penman-Monteith Model Structures

Following is a detailed description of each of the models examined in this analysis, along with the default resistance schemes that comprise the implemented version of the model. While the model formulations are well described herein, the reader is referred to the principal model reference for further details.

3.2.2.1 Single-Source Penman-Monteith (PM) Model

The single-source model used in this chapter is the one introduced in section 2.2.2.2. In the Penman-Monteith (PM) model, it is assumed that water first needs to diffuse through leaves against a surface resistance, before diffusing into the atmosphere

against an aerodynamic resistance (Pauwels and Samson 2006). The PM model conceptualizes the land surface as a so-called “big leaf”, describing the land surface-atmosphere exchange via a single bulk stomatal resistance and a single aerodynamic resistance to heat and vapour. The aerodynamic resistance formulations used in the standard PM model of this study is that of Thom (1975) (equation 2-5; hereafter Thom’s equation). Following Brutsaert (2005), we assume $z_{0v} = z_{0h}$. It is common practice to use roughness parameters (d_0, z_{0m}, z_{0h}) with fixed values calculated as a fraction of the canopy height. The equations suggested by Brutsaert (2005) are therefore used for roughness parameterization:

$$\begin{aligned} d_0 &= 0.66h_c \\ z_{0m} &= 0.1h_c \\ z_{0h} &= 0.01h_c \end{aligned} \quad 3-1$$

For the estimation of the bulk surface resistance, the Jarvis scheme of Jacquemin and Noilhan (1990) (equation 2-7; hereafter Jarvis method) with the parameterization of Chapter 2 is used.

3.2.2.2 Two-Layer Shuttleworth-Wallace (SW) Model

The simple ‘big-leaf’ Penman-Monteith model was extended to a two-layer version by Shuttleworth and Wallace (1985) (SW) that included separate canopy and soil layers. The total evapotranspiration in the SW model is $\lambda E = C_c PM_c + C_s PM_s$, where PM_c and PM_s are terms that represent the PM equation applied to full canopy and to bare soil:

$$PM_c = \frac{\Delta A + \frac{\rho c_p D - \Delta r_a^c A_s}{r_a^a + r_a^c}}{\Delta + \gamma [1 + r_s^c / (r_a^a + r_a^c)]} \quad 3-2$$

$$PM_s = \frac{\Delta A + \frac{\rho c_p D - \Delta r_a^s (A - A_s)}{r_a^a + r_a^s}}{\Delta + \gamma [1 + r_s^c / (r_a^a + r_a^c)]} \quad 3-3$$

and A is the available energy for the complete canopy ($A = R_n - G_0$) and A_s is the available energy at the soil surface ($A_s = R_n^s - G_0$). R_n^s is net radiation at the soil surface, which can be calculated using Beer’s law as $R_n^s = R_n \exp(-C LAI)$, with $C = 0.7$ representing the extinction coefficient of the crop for net radiation. C_c and C_s are resistance functions for canopy and soil (respectively) and given by the following equations:

$$C_c = \left[1 + \frac{R_c R_a}{R_s (R_c + R_a)} \right]^{-1} \quad 3-4$$

$$C_s = \left[1 + \frac{R_s R_a}{R_c (R_s + R_a)} \right]^{-1} \quad 3-5$$

where

$$\begin{aligned} R_a &= (\Delta + \gamma)r_a^a \\ R_s &= (\Delta + \gamma)r_a^s + \gamma r_s^s \\ R_c &= (\Delta + \gamma)r_a^c + \gamma r_s^c \end{aligned} \quad 3-6$$

The bulk stomatal resistance of the canopy (r_s^c) is a ‘surface’ resistance, which is influenced by the surface area of the vegetation. In the original derivation of the SW model, the bulk stomatal resistance was calculated by upscaling the leaf scale stomatal resistance r_{ST} based on the leaf area index (LAI) as $r_s^c = r_{ST}/2 \cdot LAI$, with r_{ST} assumed as a constant value or calibrated based on evapotranspiration observations. However, we derive the bulk canopy resistance using the Jarvis scheme of [Noilhan and Planton \(1989\)](#), as is used in a number of previous studies of the Shuttleworth-Wallace model (e.g. [Zhou et al. 2006](#); [Zhang et al. 2008](#); [Irmak 2011](#); [Odhiambo and Irmak 2011](#)). The soil surface resistance (r_s^s) is derived from the above mentioned Jarvis scheme, using the ‘Barren and Sparsely Vegetated’ category of the Noah vegetation table for the bare soil.

Three aerodynamic resistances appear in the SW model: an aerodynamic resistance between the soil/substrate surface and the canopy source height (r_a^s); a bulk boundary layer resistance of vegetative elements in the canopy (r_a^c); and an aerodynamic resistance between the canopy source height and a reference level above the canopy (r_a^a). The bulk boundary layer resistance (r_a^c) is calculated by scaling the leaf scale mean boundary layer resistance r_b to the canopy scale using LAI , as $r_a^c = r_b/2 \cdot LAI$, with r_b considered constant at $25 \text{ s} \cdot \text{m}^{-1}$ ([Shuttleworth and Wallace 1985](#)). However, r_a^a and r_a^s are calculated using the following equations ([Shuttleworth and Gurney 1990](#)) (hereafter SG90):

$$r_a^a = \frac{1}{\kappa u_*} \ln \left(\frac{z - d_0}{h_c - d_0} \right) + \frac{h_c}{nK_h} \left\{ \exp \left[n \left(1 - \frac{z_{0m} + d_0}{h_c} \right) \right] - 1 \right\} \quad 3-7$$

$$r_a^s = \frac{h_c \exp(n)}{nK_h} \left\{ \exp \left(-\frac{nz'_{0m}}{h_c} \right) - \exp \left[-n \left(\frac{z_{0m} + d_0}{h_c} \right) \right] \right\} \quad 3-8$$

where z'_{0m} is the roughness length of bare soil surface (=0.01 m) ([van Bavel and Hillel 1976](#)) and n is the eddy diffusivity decay constant (dimensionless), which is assumed fixed at 2.5 for agricultural crops by [Shuttleworth and Wallace \(1985\)](#). However, following [Zhang et al. \(2008\)](#) and based on the values given by [Brutsaert \(1982\)](#), we assume $n = 2.5$ when $h_c < 1$ m and $n = 4.25$ when $h_c > 10$ m. For the cases where $1 \geq h_c \geq 10$, a linear interpolation is applied as $n = 0.1944h_c + 2.3056$. The eddy diffusion coefficient at the top of canopy (K_h in $\text{m}^2 \cdot \text{s}^{-1}$) is calculated as $K_h = \kappa u_* (h_c - d_0)$, with u_* calculated as $u_* = \kappa u_a / \ln[(z - d_0)/z_{0m}]$. As is common in general applications of the SW model, the roughness variables d_0 and z_{0m} are

assumed as a fraction of the vegetation height (Brutsaert 2005), with $d_0 = 0.6\dot{h}_c$ and $z_{0m} = 0.1h_c$.

The original SW model has been further developed to improve its model structure (Choudhury and Monteith 1988; Brenner and Incoll 1997; Lhomme et al. 2012) and parameterization (Shuttleworth and Gurney 1990; Farahani and Ahuja 1996). The model has been used across a range of land cover types, including: salt marsh grass (Moffett and Gorelick 2012), rangelands (Stannard 1993), wheat (Raupach and Finnigan 1988), millet (Wallace et al. 1990), barely (Tourula and Heikinheimo 1998), soybean (Odhiambo and Irmak 2011), maize (Lagos et al. 2009), vineyards (Zhang et al. 2008; Ortega-Farias et al. 2010), cherry orchard (Li et al. 2010a), desert shrubs (Li et al. 2011), pine forest (Fisher et al. 2005), Douglas fir forest (Kelliher et al. 1986) and boreal forest (Iritz et al. 1999). The SW model has also been adopted for application in general circulation models (Dolman 1993).

3.2.2.3 Three-Source Mu et al. (2011) (Mu) Model

The three source PM model used in this investigation is based on that developed by Mu et al. (2011). The Mu model was first introduced by Cleugh et al. (2007) as a single source model, but was further developed as a two-source model (for soil and canopy) by Mu et al. (2007) and used for global estimation of evapotranspiration. The model was further improved by Mu et al. (2011) and introduced as a three-source model in which total evapotranspiration is partitioned into evaporation from a wet canopy (λE_{wc}), transpiration from the canopy (λE_t) and evaporation from the soil (λE_s), defined as $\lambda E = \lambda E_s + \lambda E_t + \lambda E_{wc}$.

Evaporation from wet canopy

Evaporation from a wet canopy (intercepted water) is calculated using the following equation:

$$\lambda E_{wc} = f_c f_w \frac{\Delta A_c + \rho c_p (e^* - e) / r_a^{wc}}{\Delta + \gamma \frac{r_s^{wc}}{r_a^{wc}}} \quad 3-9$$

where f_w is the relative surface wetness and calculated as $f_w = RH^4$, which is based on the concept originally developed by Fisher et al. (2008). In the original Mu model daily average values of RH were used and f_w was assumed zero when daily average $RH < 0.7$. However, here we used hourly (or half-hourly) data and did not filter f_w based on low RH values.

The aerodynamic resistance r_a^{wc} and surface resistance r_s^{wc} for wet canopy are defined as:

$$r_a^{wc} = \frac{r_h^{wc} r_r^{wc}}{r_h^{wc} + r_r^{wc}} \quad 3-10$$

$$r_s^{wc} = \frac{1}{f_w g_e LAI} \quad 3-11$$

where r_h^{wc} is wet canopy resistance to sensible heat flux and r_r^{wc} is the wet canopy resistance to radiative heat transfer, which are formulated as following:

$$r_h^{wc} = \frac{1}{f_w g_h LAI}$$

$$r_r^{wc} = \frac{\rho c_p}{4\sigma T_a^3}$$
3-12

where g_e and g_h are leaf conductance to evaporated water vapor and sensible heat (respectively) per unit LAI and σ is the Stefan-Boltzmann constant. Based on [Mu et al. \(2011\)](#), g_h and g_e are assumed similar and constant for each biome as listed in Table 3-1.

The parameterization of the available energy in the Mu model is somewhat different from the SW model. In the Mu model, the available energy for crop and soil is partitioned based on the fractional vegetation cover (f_c) as $A_c = f_c R_n$ and $A_s = (1 - f_c)R_n - G_0$.

Canopy transpiration

The canopy transpiration λE_t is calculated as:

$$\lambda E_t = f_c (1 - f_w) \frac{\Delta A_c + \rho c_p (e^* - e) / r_a^t}{\Delta + \gamma (1 + r_s^t / r_a^t)}$$
3-13

where r_a^t and r_s^t are aerodynamic and surface resistances for transpiration, respectively. The bulk canopy resistance (r_s^t) is the inverse of the bulk canopy conductance (C_c) and calculated as:

$$r_s^t = 1 / C_c$$
3-14

The assumption here is that the stomatal conductance (G_s^{st}) and cuticular conductance (G_s^{cu}) are in parallel, but both are in series with the canopy boundary-layer conductance G_s^b . Therefore, the canopy conductance to transpiration is calculated as:

$$C_c = \begin{cases} (1 - f_w) \frac{(G_s^{st} + G_s^{cu}) G_s^b}{G_s^{st} + G_s^{cu} + G_s^b} LAI, & LAI > 0, (1 - f_w) > 0 \\ 0 & , LAI = 0, (1 - f_w) = 0 \end{cases}$$
3-15

where $G_s^b = g_h$, $G_s^{cu} = r_{corr} g_{cu}$ and $G_s^{st} = C_L m(T_{min}) m(VPD) r_{corr}$ with VPD being the vapour pressure deficit (Pa). The leaf cuticular conductance (g_{cu}) is per unit LAI and assumed equal to 0.00001 m.s^{-1} for all biomes. Also, the mean potential stomatal conductance (c_L) is per unit leaf area and is assumed constant for each biome (Table 3-1). The r_{corr} is the correction factor for G_s^{st} to adjust it based on the standard air temperature and pressure (20 °C and 101,300 Pa) using the following equation:

$$r_{corr} = \frac{1}{\frac{101300}{P_a} \left(\frac{T_a + 273.15}{293.15} \right)^{1.75}} \quad 3-16$$

$m(T_{min})$ is a multiplier that limits potential stomatal conductance by minimum air temperature (T_{min}) and $m(VPD)$ is a multiplier used to reduce the potential stomatal conductance when $VPD = e^* - e$ is high enough to reduce canopy conductance. Following [Mu et al. \(2007\)](#), $m(T_{min})$ and $m(VPD)$ are calculated as following:

$$m(T_{min}) = \begin{cases} 1 & T_{min} \geq T_{min}^{open} \\ \frac{T_{min} - T_{min}^{close}}{T_{min}^{open} - T_{min}^{close}} & T_{min}^{close} < T_{min} < T_{min}^{open} \\ 0 & T_{min} \leq T_{min}^{close} \end{cases} \quad 3-17$$

$$m(VPD) = \begin{cases} 1 & VPD \leq VPD_{open} \\ \frac{VPD_{close} - VPD}{VPD_{close} - VPD_{open}} & VPD_{open} < VPD < VPD_{close} \\ 0 & VPD \geq VPD_{close} \end{cases} \quad 3-18$$

Values of T_{min}^{open} , T_{min}^{close} , VPD_{open} and VPD_{close} are listed in Table 3-1 for each biome type. Also, the aerodynamic resistance to canopy transpiration, r_a^t , is calculated based on the convective heat transfer resistance r_h and radiative heat transfer resistance r_r , assuming they are in parallel using the following equation ([Thornton 1998](#)):

$$r_a^t = \frac{r_h^t r_r^t}{r_h^t + r_r^t} \quad 3-19$$

where $r_h^t = 1/g_{bl}$ and $r_r^t = r_r^{wc}$ with g_{bl} being the leaf-scale boundary layer conductance per unit LAI and assumed equal to that of the sensible heat (i.e. $g_{bl} = g_h$).

Soil evaporation

Evaporation from the soil surface is calculated as the sum of evaporation from wet soil (λE_{ws}) and evaporation from saturated soil (λE_{ss}), such that:

$$\lambda E_s = \lambda E_{ws} + \lambda E_{ss} \quad 3-20$$

Partitioning of the soil surface to wet and saturated components is based on the relative surface wetness f_w , with the evaporation from the wet soil calculated as:

$$\lambda E_{ws} = f_w \frac{\Delta A_s + (1 - f_c) \rho c_p (e^* - e) / r_a^s}{\Delta + \gamma \frac{r_s^s}{r_a^s}} \quad 3-21$$

Similarly, evaporation from the saturated soil is calculated as:

$$\lambda E_{ss} = RH^{VPD/\beta} (1 - f_w) \frac{\Delta A_s + (1 - f_c) \rho c_p (e^* - e) / r_a^s}{\Delta + \gamma \frac{r_s^s}{r_a^s}} \quad 3-22$$

where r_a^s and r_s^s are aerodynamic and surface resistances for the soil surface. $RH^{VPD/\beta}$ is a soil moisture constraint that is used following Fisher et al. (2008). This function is based on the complementary hypothesis and describes land-atmosphere interactions via the air vapour pressure deficit VPD and relative humidity RH , with β assigned a constant value of 200. The soil surface resistance r_s^s is calculated as:

$$r_s^s = r_{corr} r_{totc} \quad 3-23$$

where r_{totc} is a function of VPD and biological parameters r_{bl}^{min} and r_{bl}^{max} as follows:

$$r_{totc} = \begin{cases} r_{bl}^{max} & VPD \leq VPD_{open} \\ r_{bl}^{max} - \frac{(r_{bl}^{max} - r_{bl}^{min}) \times (VPD_{close} - VPD)}{VPD_{close} - VPD_{open}} & VPD_{open} < VPD < VPD_{close} \\ r_{bl}^{min} & VPD \geq VPD_{close} \end{cases} \quad 3-24$$

VPD_{open} is the VPD when there is no water stress on transpiration and VPD_{close} is the VPD when water stress causes stomata to close almost completely, halting plant transpiration. Values for r_{bl}^{max} , r_{bl}^{min} , VPD_{open} and VPD_{close} are listed in Table 3-1.

The aerodynamic resistance at the soil surface (r_a^s) is parallel to both the resistance to convective heat transfer (r_h^s) and the resistance to radiative heat transfer r_r^s , with its components calculated as:

$$r_a^s = \frac{r_h^s r_r^s}{r_h^s + r_r^s} \quad 3-25$$

where $r_r^s = r_r^{wc}$ and $r_h^s = r_s^s$.

Table 3-1 shows the Biome-Property-Lookup-Table (BPLT) used in the Mu model. As explained by Mu et al. (2011), VPD and T_{min} parameters derive from calibrations performed by Zhao et al. (2005), but other parameters are calibrated based on biome aggregated observed ET and Gross Primary Production (GPP) values at 46 Ameriflux tower sites, some of which are included in the current study.

Table 3-1: The Biome-Property-Lookup-Table (BPLT) adopted from Mu et al. (2011). Land covers are defined as evergreen needleleaf forest (ENF); evergreen broadleaf forest (EBF); deciduous needleleaf forest (DNF); deciduous broadleaf forest (DBF); mixed forest (MF); woody savannahs (WL); savannahs (SV); closed shrubland (CSH); open shrubland; grassland, urban and built-up, barren or sparsely vegetated (GRA); cropland (CRO)

Crop	ENF	EBF	DNF	DBF	MF	CSH	OSH	WL	SV	GRA	CRO
T_{min}^{open} (°C)	8.31	9.09	10.44	9.94	9.5	8.61	8.8	11.39	11.39	12.02	12.02
T_{min}^{close} (°C)	-8	-8	-8	-6	-7	-8	-8	-8	-8	-8	-8
VDP_{close} (Pa)	3000	4000	3500	2900	2900	4300	4400	3500	3600	4200	4500
VPD_{open} (Pa)	650	1000	650	650	650	650	650	650	650	650	650
g_h (m.s ⁻¹)	0.04	0.01	0.04	0.01	0.04	0.04	0.04	0.08	0.08	0.02	0.02
g_e (m.s ⁻¹)	0.04	0.01	0.04	0.01	0.04	0.04	0.04	0.08	0.08	0.02	0.02
c_L (m.s ⁻¹)	0.0032	0.0025	0.0032	0.0028	0.0025	0.0065	0.0065	0.0065	0.0065	0.007	0.007
r_{bl}^{min} (m.s ⁻¹)	65	70	65	65	65	20	20	25	25	20	20
r_{bl}^{max} (m.s ⁻¹)	95	100	95	100	95	55	55	45	45	50	50

3.2.3 Including Dynamic Roughness Parameterization

In addition to assuming roughness parameters as a constant fraction of the vegetation height as detailed above, these variables can also be estimated via a physically-based method. [Su et al. \(2001\)](#) used vegetation phenology, air temperature and wind speed to provide dynamic values of roughness parameters based on the land surface condition. In the [Su et al. \(2001\)](#) method, the roughness height for momentum transfer is calculated as:

$$z_{0m} = h_c \left(1 - \frac{d_0}{h_c}\right) \exp\left(-\frac{\kappa}{\beta}\right) \quad 3-26$$

where h_c is the vegetation height and β is the ratio of friction velocity to the wind speed at the canopy top, calculated as $\beta = c_1 - c_2 \exp(-c_3 C_d LAI)$ with $c_1 = 0.32$, $c_2 = 0.264$, $c_3 = 15.1$ and the drag coefficient $C_d = 0.2$. The roughness length for heat transfer (z_{0h}) can be derived by assuming an exponential relationship between z_{0m} and z_{0h} as $z_{0h} = z_{0m} / \exp(\kappa B^{-1})$, where B^{-1} is the inverse Stanton number. To estimate the κB^{-1} parameter, the method of [Su et al. \(2001\)](#) suggests:

$$\kappa B^{-1} = \frac{\kappa C_d}{4C_t \beta \left(1 - \exp\left(-\frac{n_{ec}}{2}\right)\right)} f_c^2 + 2f_c f_s \frac{\kappa \beta z_{0m} / h_c}{C_t^*} + \kappa B_s^{-1} f_s^2 \quad 3-27$$

where f_c is the fractional canopy coverage and f_s is its complement (for soil coverage). C_t is the heat transfer coefficient of the leaf and C_t^* is the heat transfer coefficient of the soil. As stated by [Su \(2002\)](#), the first term of equation 3-27 follows the full canopy only model of [Choudhury and Monteith \(1988\)](#), the third term is that of [Brutsaert \(1982\)](#) for a bare soil surface and the second term describes the interaction between vegetation and a bare soil surface. Following [Brutsaert \(1999\)](#), for a bare soil surface the κB_s^{-1} is calculated as $\kappa B_s^{-1} = 2.46 Re_*^{1/4} - \ln(7.4)$ with Re_* being the Reynolds number.

3.2.4 Developing Model Parameterization Scenarios

To examine the influence of resistance schemes and model structure, we developed fourteen unique scenarios to guide model evaluation, details of which are provided in Table 3-2. For the default model implementations described above (denoted here as PM^0 , SW^0 and Mu^0), parameterizations of the aerodynamic and surface resistances are not modified. For each model type, alternative scenarios are developed to examine the influence of aerodynamic and surface resistance parameterization and are denoted by superscripts 1, 2, 3, 4 (e.g. PM^1 , PM^2). For example, a comparison of PM^0 and PM^1 (see Table 3-2) illustrates the effect of changing the surface resistance parameterization only, while comparison of PM^0 and PM^2 show the effect of changing the aerodynamic resistance parameterization only (via a change in roughness parameterization). Also, PM^3 and PM^4 show the combined effect of both aerodynamic and surface resistances. For the SW model, comparison of SW^0 and SW^1 isolates the effect of changing the surface resistance parameterization only, while comparison of SW^0 and SW^2 shows the effect of changing the aerodynamic resistance parameterization only. Also, the purpose of SW^3 and SW^4 are similar to those of PM^3 and PM^4 . For the Mu model, three alternative scenarios are considered to examine the effects of changing aerodynamic resistance (with static and dynamic roughness) and surface resistance.

Table 3-2: Features of the 14 model/parameterisation combinations for estimating evapotranspiration.

Scenario	ET model	Surface resistance	Aerodynamic resistance	Roughness
PM^0	PM	Jarvis	Thom	Fixed
PM^1	PM	Mu	Thom	Fixed
PM^2	PM	Jarvis	Thom	Dynamic
PM^3	PM	Mu	Thom	Dynamic
PM^4	PM	Mu	Mu	N/A
SW^0	SW	Jarvis	SG90	Fixed
SW^1	SW	Mu	SG90	Fixed
SW^2	SW	Jarvis	Thom	Dynamic
SW^3	SW	Mu	Thom	Dynamic
SW^4	SW	Mu	Mu	N/A
Mu^0	Mu	Mu	Mu	N/A
Mu^1	Mu	Mu	Thom	Dynamic
Mu^2	Mu	Mu	Thom	Fixed
Mu^3	Mu	Jarvis	Mu	N/A

3.2.5 Energy Budget Closure at Flux Tower Sites

The issue of non-closure in the measurements of eddy covariance towers has been discussed in a number of previous studies (Twine et al. 2000; Wilson et al. 2002). The issue was also examined in a recent study covering a range of ET schemes and using the same tower sites as employed here (Ershadi et al. In review-a; Chapter 2). Two

methods for correction of closure have been used: i) the energy residual method (i.e. $\lambda E_{corr} = R_n - G_0 - H$), and ii) the Bowen-ratio method. Both closure correction methods have been used in evaluating a range of evapotranspiration models (Anderson et al. 2005; Nagler et al. 2005b; Su et al. 2005; Sumner and Jacobs 2005; Li et al. 2008). In **Chapter 2** we found that both the energy residual and Bowen ratio closure correction techniques presented similar performance. However, it was determined that the energy residual closure correction technique presented performance better overall flux response, so that approach has been maintained here to address the issue of non-closure in in-situ flux observations.

3.3 Results

In this section the performances of the fourteen developed scenarios are compared in order to evaluate both model structure and model parameterization. First, the different scenarios for each model are compared to identify the influences and implications of resistance parameterization on model choice. Next, the best performing scenario for each biome is identified.

3.3.1 Penman-Monteith Model

To evaluate the single-source PM model, four scenarios were defined with various resistance formulations: PM¹ for surface resistance only, PM² for aerodynamic resistance only and PM³ and PM⁴ for the combined effect of adjusting both aerodynamic and surface resistances. The impact of changing the surface resistance scheme from the standard Jarvis implementation (Equation 2-6) (PM⁰) to that used in the Mu model (Equation 3-14) (PM¹) is shown in Figure 3-1. A key assumption in the surface resistance parameterization of the Mu model (based on Fisher et al. 2008) is that the near-surface humidity reflects variations in the soil moisture and hence a humidity-index can be substituted for soil-water stress. The improved performance observed in the PM¹ scenario may indicate some validity of this assumption, if not actual causality. If this approach can be shown to provide a good representation of the surface resistance, it would remove the reliance on the use of error-prone soil moisture data in calculating this variable. Results indicate that based on the *NSE*, an improved modeling performance is observed for all towers, except for G1, S2, D1 and D2 sites. This improvement in *NSE* is more evident for cropland sites, where the range in *NSE* is increased from 0.1-0.4 to 0.5-0.7 and the range in *RMSD* is reduced from 106-124 W.m⁻² to 71-99 W.m⁻² (see Appendix B for statistics). In this case, Mu's surface resistance parameterization seems to provide higher performance in ET estimation when using the single-source PM model at cropland sites. The change in *NSE_{avg}* is also positive for shrublands (0.1→0.3) and evergreen needleleaf forest (0.1→0.2), but *NSE_{avg}* is 0.4 for both cases in the deciduous broadleaf forest sites due to various responses of towers across this biome (change in *NSE* is positive for D4, negative for D1 and D2 and similar for D3).

In the PM² scenario, adjusting the aerodynamic resistance parameterization via the use of dynamic roughness values (from the Su et al. 2001 model) only slightly improved modeling performance. This improvement is more significant for croplands

(NSE_{avg} changed from 0.2 to 0.4), evergreen needleleaf forest (NSE_{avg} changed from 0.1 to 0.2) and for deciduous broadleaf forest sites (NSE_{avg} changed from 0.4 to 0.6). The changes in NSE_{avg} from PM^0 to PM^2 were lower for grasslands (0.3→0.4) and shrublands (0.1→0.2), as perhaps the effects of parameterising the aerodynamic roughness are less important in these biomes.

PM^3 presents the combined effect of both aerodynamic resistance (Thom's r_a with dynamic roughness) and surface resistance (Mu's r_s). Therefore, comparing PM^3 with PM^1 (Thom's r_a with fixed roughness, Mu's r_s) should isolate the effect of adding dynamic roughness to the calculations of ET. Such a comparison shows that the NSE is increased (from 0.01 to 0.17) for all towers except in S4. These results are in accord with the comparison of PM^2 and PM^0 and show the positive effect of adding dynamic roughness to formulations of the single-source PM.

Comparison of PM^3 and PM^2 isolates the influence of changing surface resistance parameterization from Jarvis to Mu, with aerodynamic resistance calculated using Thom's equation with dynamic roughness. Results of this comparison confirm the finding of the case examining PM^0 and PM^1 : that in terms of NSE , use of Mu's surface resistance can increase the model performance in most sites except G1, S2 and the deciduous broadleaf forest sites.

The PM^4 scenario is designed to investigate if the simple lookup-table based aerodynamic parameterization of the Mu model (equation 3-19) can be used in the one-source PM model. The benefit of this approach is that the method does not require either roughness parameters or wind speed. Comparison of NSE values of the PM^4 with those of the PM^3 scenario shows that overall, NSE for towers decreased in PM^4 , except in the deciduous broadleaf forest sites. Therefore, use of the lookup table based approach of Mu for r_a parameterization is not recommended if wind and vegetation height data are available.

However, comparison of PM^4 and PM^0 shows that in the cases that wind, vegetation height and soil moisture data are not available, use of the Mu based r_a and r_s parameterizations can increase NSE in the sites, except in G1 and in shrubland sites. This is an important result, as these data are most commonly unavailable in data scarce regions.

Overall, the PM^3 configuration provides the best performance across most biomes, except over deciduous broadleaf forest sites where PM^2 is the best performing scenario. Both PM^3 and PM^4 utilise Thom's equation with dynamic roughness, which requires reliable wind speed and vegetation height data. The results also suggest that the Jarvis scheme (used in PM^2) scenario is useful for deciduous broadleaf forest sites, but for over other biomes, the simpler Mu model resistance is sufficient.

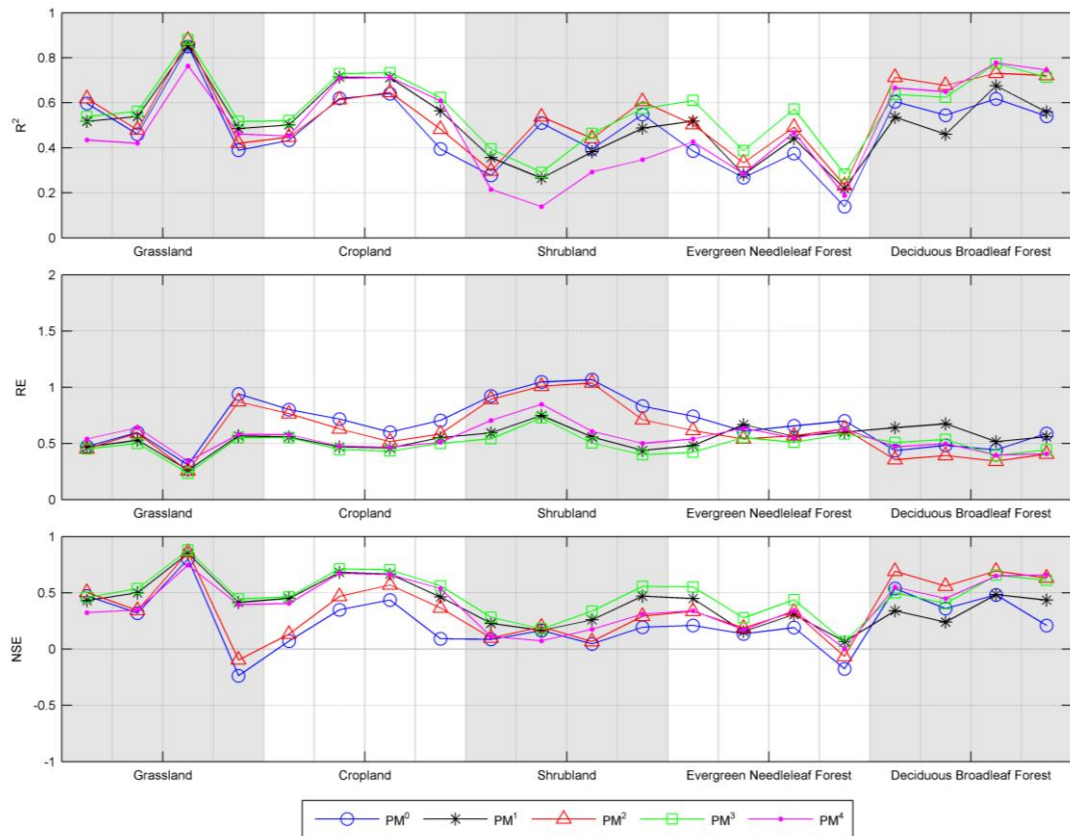


Figure 3-1: Performance of the PM model in adjusting the resistance parameterization. RE is relative error ($RE = RMSD / \text{mean}(\lambda E_{obs})$) and NSE is the Nash-Sutcliffe efficiency. The x-axis displays the various landcover types used in the simulations, with vegetation height increasing from left-to-right (both within and between biomes).

In addition to the whole period results shown in Figure 3-1, the seasonal cycle of evapotranspiration can have a major effect on the performance of the models (see **Chapter 2**). To study the effects of tower based seasonality, we calculated monthly based NSE values for each year from their hourly or half-hourly records using the method developed in section 2.3.2. The average of each monthly NSE within different years was then calculated and plotted for each of the PM scenarios (see Figure 3-2). Time series of f_E (see equation 2-15) are shown in each panel of Figure 3-2 (thick grey lines) to identify the temporal trend of evapotranspiration at each site.

It is important to note that the number of years of available tower data differs between towers, with four towers having less than two years of data (see Table 2-1). As a result, particularly wet or dry years may influence inter-annual model performance and hence the seasonal variability of NSE . However, the similarity in the trends of monthly NSE (e.g. higher NSE in warmer months and vice versa) for the towers of each biome indicates that the trends shown in Figure 3-2 are relatively representative of the sensitivity of the PM type of models to the seasonal variation of energy and water availability.

The effects of seasonal variation are evident for all biomes, especially over croplands and deciduous broadleaf forest sites and to a lesser extent over grasslands, with lower

values of NSE in the colder months and higher values in the warmer months. Temporal changes in NSE are less evident across evergreen needleleaf forest sites (except for E3), as the PM scenarios do not seem to perform well over this biome type. Over shrublands, PM^0 and PM^2 (which have the Jarvis r_s parameterization in common) show no seasonality in NSE . However, for the PM^1 , PM^3 and PM^4 scenarios (which use the Mu r_s parameterization), the seasonality in NSE is more evident, in particular over S3 and S4. Strong seasonality in NSE values across all biomes implies that PM model estimates are mostly valid in the warmer (e.g. summer) months and application of this model in colder months involves large uncertainties in ET estimation.

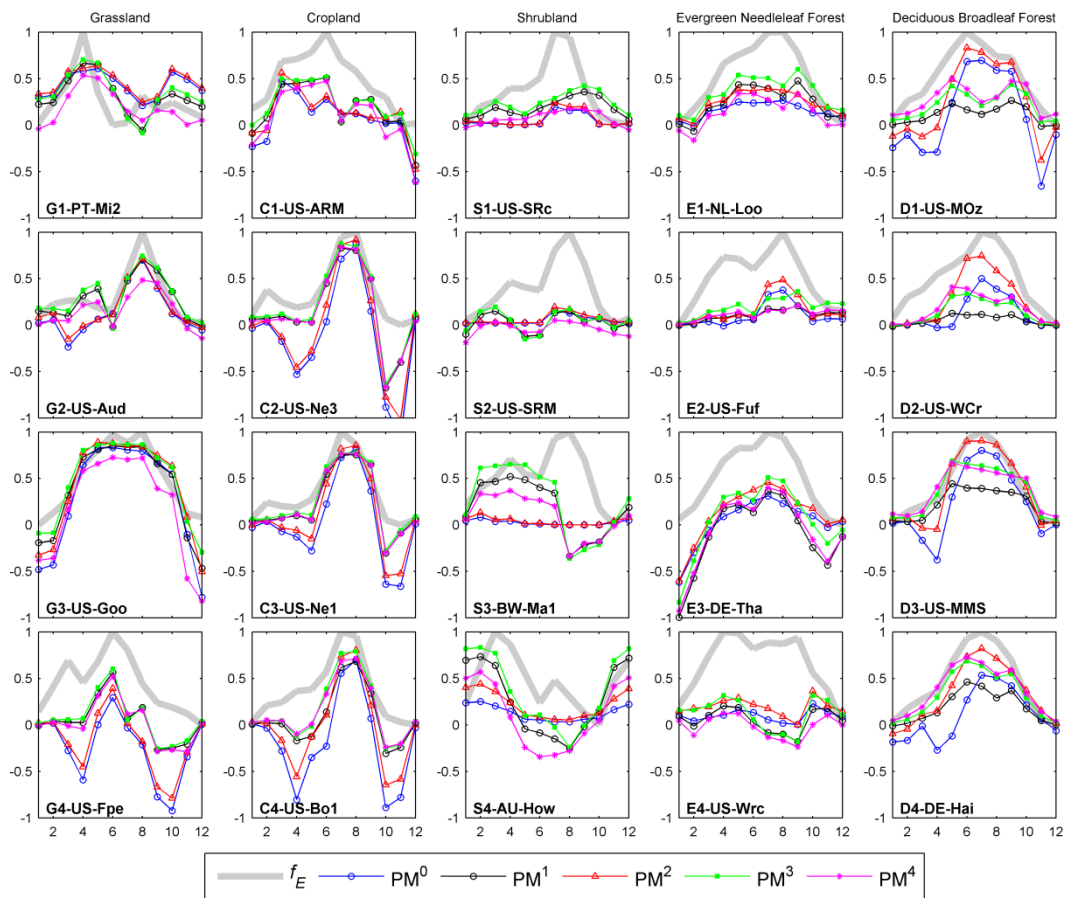


Figure 3-2: Mean monthly values of the Nash-Sutcliffe Efficiency (NSE) calculated for the PM model's scenarios at each of the 20 tower locations. The x-axis represents month of the year, while each point on the graphs of PM^0 to PM^4 represents the temporally averaged monthly NSE calculated for all available tower record years (see Table 2-1 for details on individual tower data length). f_E is normalized fraction of monthly observed evapotranspiration.

3.3.2 Shuttleworth-Wallace Model

Four alternative scenarios are developed for the SW model. These include changes from the standard Jarvis scheme (Equation 2-6) (SW^0) to the method used in the Mu model (Equation 3-14) (SW^1). The SW^2 scenario refers to a change in the aerodynamic resistance parameterization from the standard SG90 approach (Equations 3-7 and 3-8) to Thom's equation with dynamic roughness (from the [Su et al. 2001](#) model). SW^3

refers to a change in both aerodynamic resistance (dynamic roughness, Thom's equation) and surface resistance (Mu model), while the SW⁴ scenario incorporates both the aerodynamic and surface resistances of the Mu model (see Table 3-2 for full description of these combinations).

Figure 3-3 describes the variations of R^2 , RE and NSE coefficients for these different scenarios. A change in surface resistance from Jarvis to Mu (SW⁰ to SW¹) had limited influence on evapotranspiration estimation over grassland sites (NSE_{avg} increased from 0.4 to 0.5), but improves the NSE in evapotranspiration estimation for three towers in croplands (0.1→0.4). A possible reason for the limited change at C1 might be related to the phenological difference of this site, given its short canopy height ($h_c = 0.5$ m) compared to the other cropland towers ($h_c > 2.5$ m). Changes from SW⁰ to SW¹ shows decreased NSE_{avg} across the shrubland sites (0.1→0.0), but increases across the evergreen needleleaf forest (0.0→0.1) and deciduous broadleaf forest sites (-0.3→0.2). Overall, a change in surface resistance had less impact in comparison to that observed for the single-source PM model (see Figure 3-1).

The influence of change in aerodynamic resistance from SG90 in SW⁰ to Thom's equation with dynamic roughness in the SW² scenario is variable. The change increased NSE across most sites, except in G3, G4 and C1. It also increased R^2 , except in G3, G4, C1, C2 and C3. As such, employing Thom's equation with dynamic roughness can positively influence SW model performance across the majority of biome types. In particular, results for the deciduous broadleaf forest sites were considerably improved, with NSE_{avg} changing from -0.4 in SW⁰ to 0.7 in SW². A change in NSE_{avg} was also evident for croplands (0.1→0.4), shrublands (0.1→0.2) and evergreen needleleaf forest (0→0.2). The larger positive response to the changes in r_a parameterization in the cropland and deciduous broadleaf forests can be related to the structure of those canopies: Thom's r_a equation with dynamic roughness is better able to represent the aerodynamic transfer processes when full canopy and soil/understory layers are in series.

In evaluation of the SW³ scenario (Mu's r_s , Thom's r_a), a comparison was first made with SW² (Jarvis's r_s , Thom's r_a) to examine the influence of change in r_s parameterization. SW³ showed an increase in NSE_{avg} (0.2→0.4) for evergreen needleleaf forest sites, a smaller increase (0.4→0.5) in croplands and variable (decrease and increase) in other biomes. A comparison of SW³ and SW⁰ should identify the influence of changing both r_s and r_a . In previous scenarios, the (positive) response of the models to the use of Mu's r_s parameterization (in comparison of SW¹ and SW⁰) and Thom's r_a parameterization (in comparison of SW² and SW⁰) were shown. It might be expected then, that using both of those resistance parameterization would positively influence model performance. Results show that from SW³ to SW⁰, NSE values were increased except for grassland sites and C1, S1 and S2. In particular, NSE_{avg} is considerably increased in croplands (0.1→0.5), evergreen needleleaf forest sites (0→0.4) and deciduous broadleaf forest sites (-0.4→0.7). Overall, if wind and vegetation height data are available, use of the SW³ configuration results in improved model performance everywhere except in grasslands.

If wind, vegetation height and soil moisture data are not available, a configuration similar to SW⁴ can be set up to estimate both r_s and r_a using the Mu parameterization. Comparison of SW⁴ and SW⁰ can identify whether a simpler and less data demanding resistance parameterization can be usefully employed in flux estimation. Results show that such parameterization is effective in deciduous broadleaf forest sites, with NSE_{avg} changing from -0.4 to 0.7, evergreen needleleaf forest sites (0→0.2) and croplands (0.1→0.3). However, grasslands (0.4→0) and shrublands (0.1→-0.1) are not improved.

Comparison of the SW⁴ model with SW³ allows the effects of aerodynamic resistance parameterization to be examined. A reduction in NSE values from SW³ to SW⁴ was observed in all biomes except in deciduous broadleaf forest sites, where SW⁴ showed slightly higher NSE_{avg} (0.73) than SW³ (0.67). As such, the use of the SW⁴ configuration is not advised for biomes except deciduous broadleaf forest sites. Comparison of SW¹ and SW⁴ allows examination of the influence of change in r_a (from the SG90 to the Mu method). Results for this evaluation show a mixed response, with a reduction in NSE across sites except for C4, S2 and all forest sites, where positive changes were observed. As such, if wind and vegetation height data are available, the Thom's equation with dynamic roughness can provide the best results, except in deciduous broadleaf forest sites.

Amongst the studied biomes, the SW¹ scenario has the best performance over grasslands, SW⁴ has the best performance over deciduous broadleaf forest sites, while for the other biomes the SW³ is the best option. The use of the Mu surface resistance in SW¹, SW³ and SW⁴ relaxes the need for soil moisture data, but accurate wind speed and canopy height data are required in the use of SG90 and Thom's aerodynamic resistance parameterizations, which are elements of the SW¹ and SW³ scenarios. Likewise, application of Mu model's r_a parameterization in deciduous broadleaf forest sites can relax the need for such wind and canopy height data.

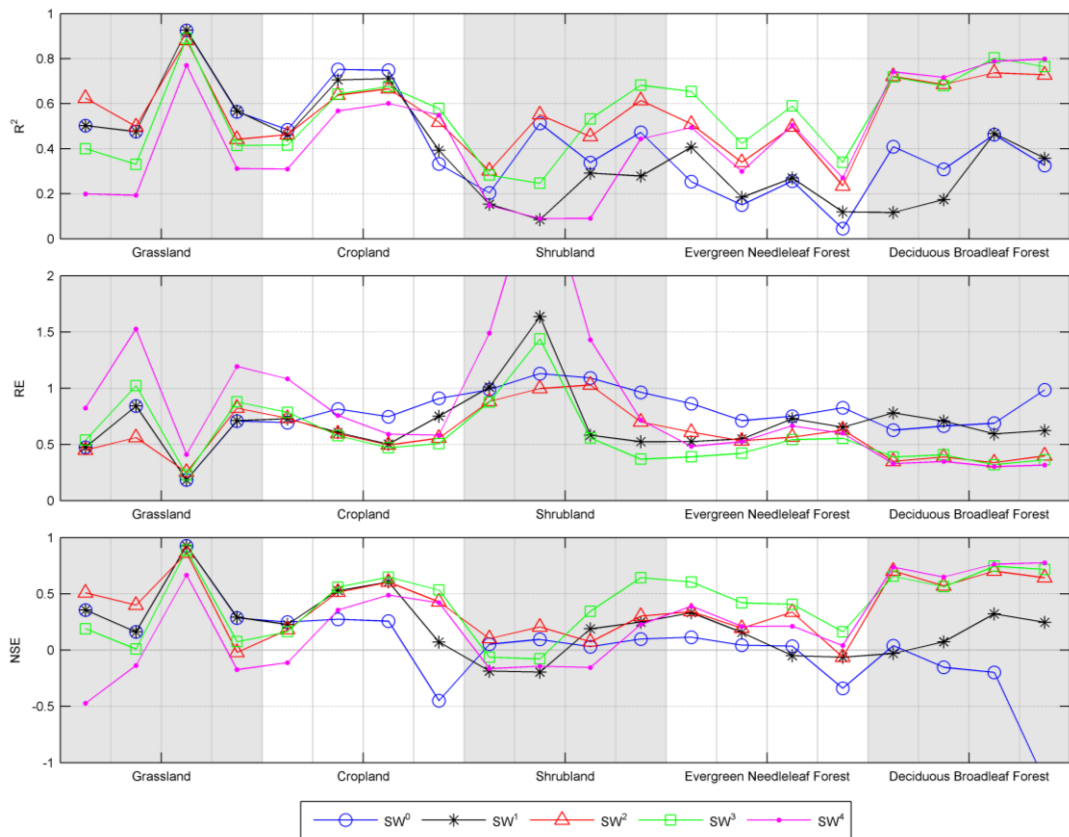


Figure 3-3: Performance of the SW model in adjusting the resistance parameterization. RE is relative error ($RE = RMSD / \text{mean}(\lambda E_{obs})$) and NSE is the Nash-Sutcliffe efficiency. The x-axis displays the various landcover types used in the simulations, with vegetation height increasing from left-to-right (both within and between biomes). The (not shown) RE value for SW^4 scenario is 3.

Figure 3-4 shows monthly NSE values for the various SW scenarios. The seasonality trends of NSE for the SW scenarios are similar to those of PM scenarios (see Figure 3-2). All scenarios display seasonality over croplands and deciduous broadleaf forest sites (except SW^1), but this is less evident for evergreen needleleaf forest sites due to environmental and biological conditions. Seasonality in shrubland sites is also apparent for all scenarios, except for SW^0 . Similar to the PM scenarios, seasonality in SW model scenarios limits application of this model in colder months.

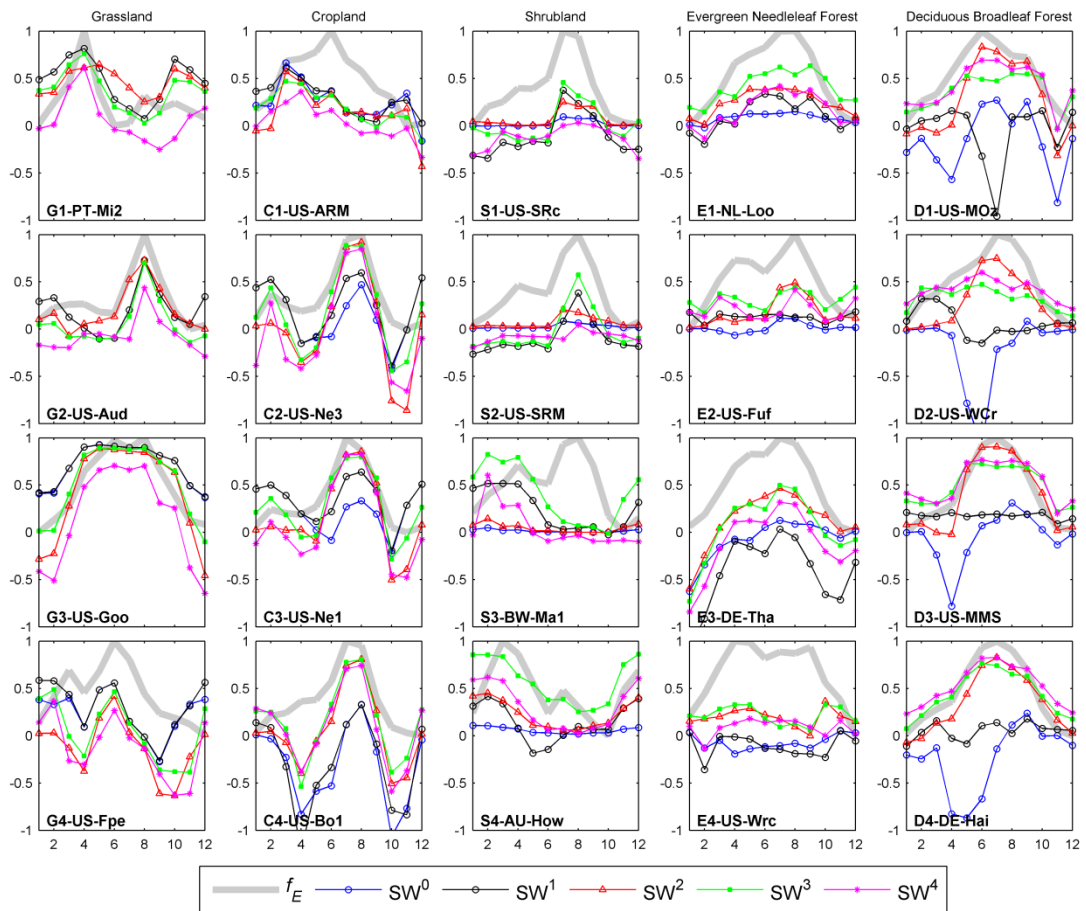


Figure 3-4: Mean monthly values of the Nash-Sutcliffe Efficiency (NSE) calculated for the SW model's scenarios at each of the 20 tower locations. The x-axis represents month of the year, while each point on the graph of SW^0 to SW^4 represents the temporally averaged monthly NSE calculated for all available tower record years (see Table 2-1 for details on individual tower data length). f_E is normalized fraction of monthly observed evapotranspiration.

3.3.3 Mu Model

For the Mu model, three additional scenarios to the default representation were examined. In the first two scenarios (Mu^1 and Mu^2), only the influence of aerodynamic resistance parameterization is considered. The default aerodynamic resistance parameterization of the Mu model uses constant values of r_a , which can be evaluated by using Thom's equation with dynamic roughness values (Mu^1) or using fixed values of roughness as fractions of canopy height (Mu^2). A similar change in parameterization was applied by [Ferguson et al. \(2010\)](#) to the [Mu et al. \(2007\)](#) version of this model, although they did not evaluate its influences on evapotranspiration. In the Mu^3 scenario, the Jarvis surface resistance scheme is used in combination with the default aerodynamic resistance of the Mu model.

Figure 3-5 illustrates the variations of R^2 , RE and NSE coefficients calculated for the standard implementation (Mu^0) together with the adjusted aerodynamic resistance scenarios of Mu^1 , Mu^2 and Mu^3 scenarios. It is evident that both Mu^1 and Mu^2 exhibit similar performances, with R^2 , RE and NSE values close to those of the Mu^0 scenario.

This suggests that the change in aerodynamic resistance in the Mu model, even with the use of dynamic roughness parameters (in Mu^1), has limited influence on the models performance – perhaps due to calibration of r_a parameters for this model (see section 3.2.2.3 and Table 3-1). One exception is a slight reduction of NSE in the deciduous broadleaf forest sites (NSE_{avg} reduced from 0.7 to 0.5) when fixed roughness values are used. Use of the Jarvis surface resistance in the Mu^3 scenario reduced the performance of flux estimation with lower values of NSE , in particular over croplands (NSE_{avg} changed from 0.7 to 0.5) and evergreen needleleaf forest sites (NSE_{avg} changed from 0.3 to 0.1). As such, the Mu model's surface resistance can produce more reliable results than use of the Jarvis method; perhaps because soil moisture uncertainties reduce the reliability of the Jarvis method. Such findings are important in the use of the Mu model in data sparse regions where accurate wind speed and soil moisture data are not available.

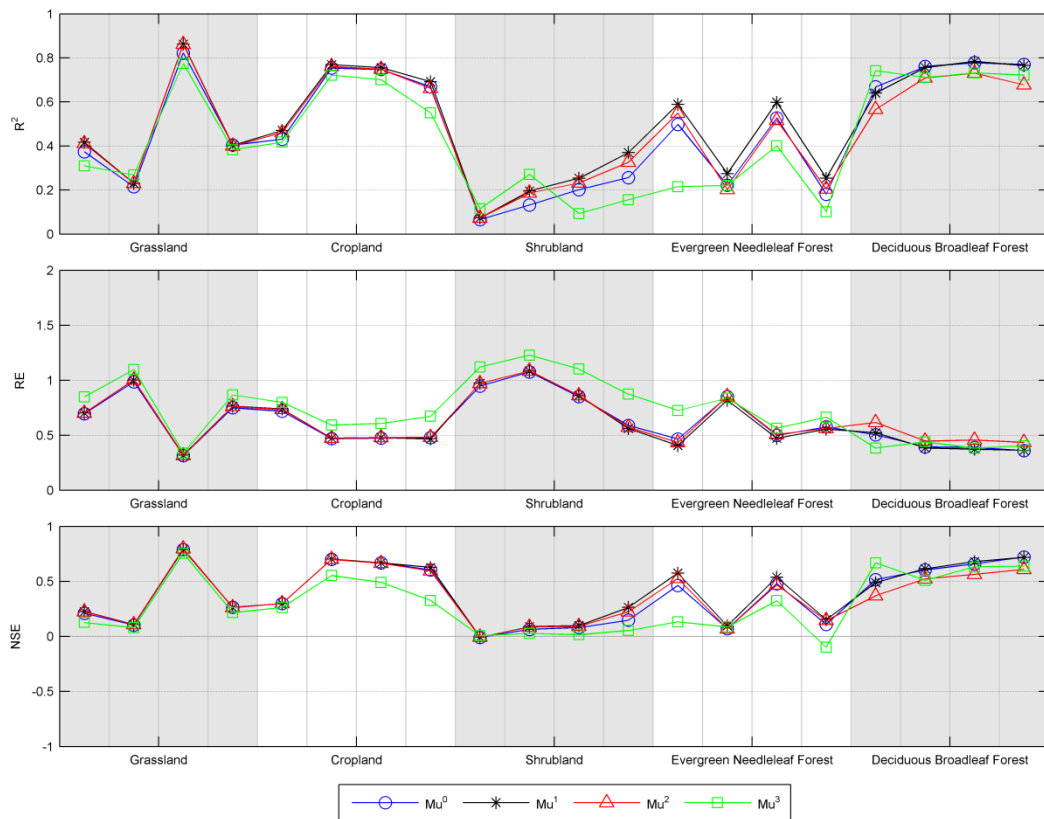


Figure 3-5: Performance of the Mu model in adjusting the resistance parameterization. RE is relative error ($RE = RMSD / \text{mean}(\lambda E_{obs})$) and NSE is the Nash-Sutcliff efficiency. The x-axis displays the various landcover types used in the simulations, with vegetation height increasing from left-to-right (both within and between biomes).

Figure 3-6 shows monthly NSE variations for the Mu model scenarios. Most scenarios of the Mu model shows seasonality, especially over croplands (except C1) and deciduous broadleaf forest sites. In the cases where NSE values are close to zero and have no temporal changes (e.g. S2, E2, G2), this is indicative of low performance of that particular scenario. From Figure 3-5, the differences between monthly averaged NSE values of the Mu^0 , Mu^1 and Mu^2 scenarios are small for grasslands, croplands and

shrublands. However, *NSE* differences are larger for the forest sites. Similar to the PM and SW examples, lower efficiency of Mu scenarios in colder months limits their applications in these periods.

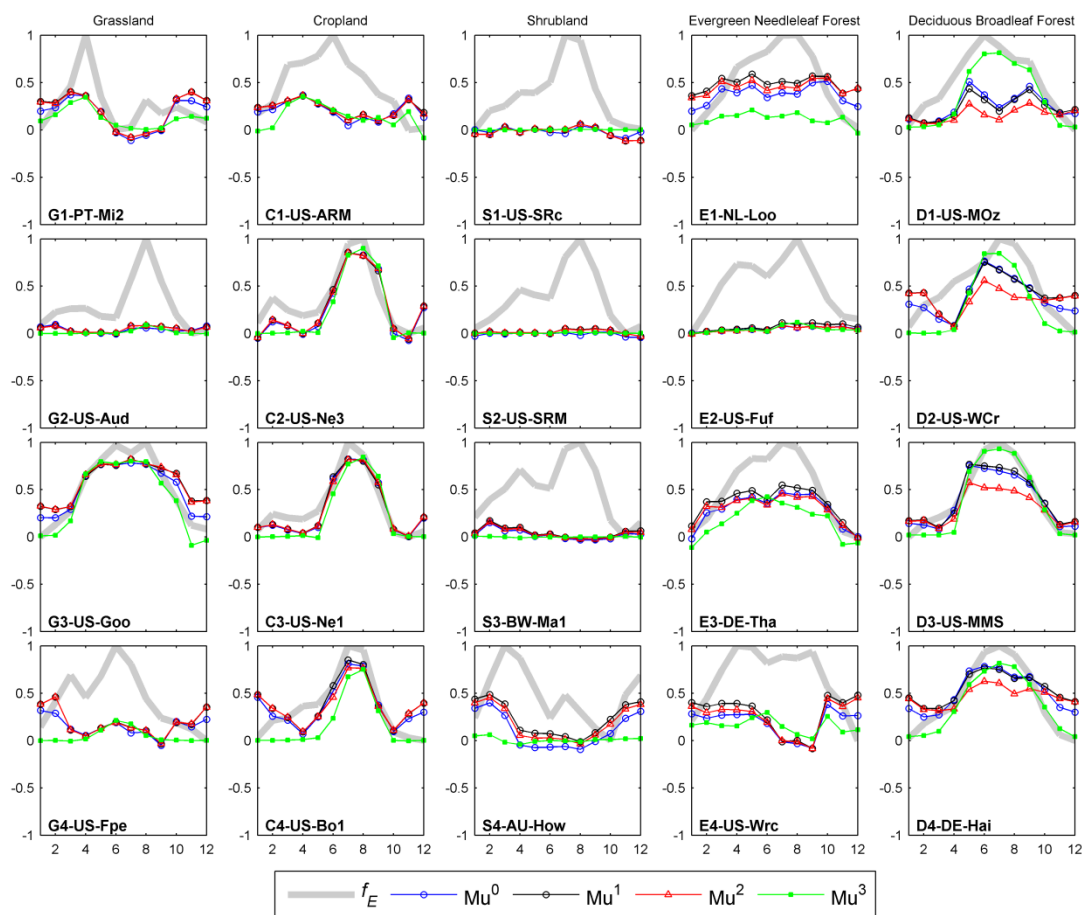


Figure 3-6: Mean monthly values of the Nash-Sutcliffe Efficiency (*NSE*) calculated for the Mu model's scenarios at each of the 20 tower locations. The x-axis represents month of the year, while each point on the graphs of Mu^0 to Mu^3 represents the temporally averaged monthly *NSE* calculated for all available tower record years (see Table 2-1 for details on individual tower data length). f_E is normalized fraction of monthly observed evapotranspiration.

3.3.4 Identification of the Best Performing Scenarios

To develop an overall understanding on the performance of the reviewed scenarios, the NSE_{avg} of each scenario for each biome is calculated and shown in Table 3-3. From this table, the PM^3 scenario is identified as the highest NSE_{avg} over grasslands, croplands and shrublands. The best scenario for evergreen needleleaf forest sites is SW^3 and for deciduous broadleaf forest sites is SW^4 . In all of these scenarios (PM^3 , SW^3 , SW^4) the surface resistance is calculated using the Mu method (requires no soil moisture data).

The Mu model's aerodynamic resistance method is only used in the SW^4 scenario. However, in the PM^3 and SW^3 scenarios, the aerodynamic resistance is calculated using Thom's equation with dynamic roughness, which demands reliable wind and canopy

height data. As those data are not always available for large scale applications, the alternative is to determine whether the scenarios that use $\text{Mu } r_a$ over grasslands, croplands, shrublands and evergreen needleleaf forest sites can produce similar efficiencies in modeling. Inspection of the NSE_{avg} values in Table 3-3 shows that for grasslands the alternative scenario is PM^4 ($NSE_{avg} = 0.42$), for croplands there are two alternative scenarios (Mu^0 and PM^4 ; both have $NSE_{avg} = 0.57$) and for evergreen needleleaf forest sites the alternative scenario is Mu^0 ($NSE_{avg} = 0.29$). However, no alternative scenario for SW^3 that uses the $\text{Mu } r_a$ can be found for the shrubland sites. Hence, an estimate of canopy height and wind speed over shrubland sites is required to use SW^3 scenario simulations.

Table 3-3: NSE_{avg} values of all scenarios over various biomes. Values with bold font show the top-ranked scenarios for each biome and the underlined values show the runner-up(s). Biomes shown in the first column and are grasslands (GRA), croplands (CRO), shrublands (SHR), evergreen needleleaf forest (ENF) and deciduous broadleaf forest (DBF).

Biome	Model	Scenario				
		0	1	2	3	4
GRA	PM	0.34	0.53	0.40	0.56	<u>0.42</u>
	SW	0.43	0.45	0.44	0.30	-0.01
	Mu	0.33	0.33	0.34	0.30	N/A
CRO	PM	0.24	0.57	0.39	0.61	<u>0.57</u>
	SW	0.09	0.36	0.44	0.48	0.29
	Mu	<u>0.57</u>	0.57	0.56	0.43	N/A
SHR	PM	0.13	0.26	0.17	0.31	0.15
	SW	0.07	0.00	0.17	0.21	-0.05
	Mu	0.07	0.11	0.10	0.03	N/A
ENF	PM	0.10	0.25	0.20	0.34	0.22
	SW	-0.03	0.10	0.21	0.40	0.22
	Mu	<u>0.29</u>	0.35	0.31	0.12	N/A
DBF	PM	0.41	0.37	0.65	0.54	0.58
	SW	-0.35	0.15	0.66	<u>0.67</u>	0.73
	Mu	0.63	0.63	0.52	0.63	N/A

3.4 Discussion

The influence of model structure and resistance parameterization is important in the performance of the Penman-Monteith type of evapotranspiration models (Allen et al. 2011a). However, understanding the effects of such model structure and parameterization configurations is non-trivial due to the mixed influence of data uncertainty, hydrometeorological variability and the complexity of the modeling system (Raupach and Finnigan 1988). As such, a range of data and models are required to formulate and evaluate some representative and diagnostic modeling scenarios.

In the present study, fourteen different scenarios were developed to examine how changes in default resistance parameterization of a single-source, a two-layer and a

three-source PM type model might influence their performances in the reproduction of actual ET. Intercomparison of these scenarios provided insights into the influence of both model structure and parameterizations. In the following sections, an examination of the scenarios is provided, followed by a discussion on some possible reasons for discrepancies in model performances between this and previous studies.

3.4.1 Influence of Model Structure and Parameterization

Comparison of the alternative scenarios within each model type (e.g. PM¹ to PM⁴) and the scenarios across models (i.e. PM, SW, Mu) is useful to evaluate the influence of model resistance parameterization on ET simulation. For the scenarios of the PM and Mu models, the aerodynamic resistance alone has a relatively minor role in the performance of ET simulation: in accord with the findings of [Bailey and Davies \(1981\)](#) and [Irmak and Mutiibwa \(2010\)](#). Change in the aerodynamic parameterization in the Mu model scenarios was not significant and showed only minor improvement on model performance. Comparison of PM³ and PM⁴ scenarios (from Thom to Mu r_a) indicates that the simple lookup-table approach of the Mu model reduced the performance of the PM model (except over deciduous broadleaf forest). As such, where the required wind and canopy height data are available, Thom's equation with dynamic roughness is recommended.

Analysis of the PM model scenarios illustrate that the surface resistance parameterization can significantly affect the performance. The resistance method of the Mu model increased the overall performance in croplands and to a lesser extent in evergreen needleleaf forest sites (also in some grassland and shrubland sites). However, that parameterization did not improve the results in the deciduous broadleaf forest sites, a grassland (G1) and a shrubland (S2) site. The response of the Mu model scenarios to a change in surface resistance parameterization was somewhat different. In all Mu scenarios, the default r_s parameterization performed better than that of the Jarvis equation.

The SW model showed more variability to the resistance parameterization with mixed responses to each of the scenarios. As such, there is no single scenario (amongst the SW model scenarios) that performs the best across all biomes. Analysis of the SW scenarios showed that over grasslands, application of the SG90 aerodynamic resistance and the Mu model surface resistance (SW¹) provided the best overall NSE_{avg} . Over other biomes, the use of Thom's aerodynamic resistance with dynamic roughness together with the Mu r_s parameterization is an appropriate setup (SW³). Results also show that application of both Mu r_a and Mu r_s in the SW⁴ scenario provided reliable estimates only for the deciduous broadleaf forest sites.

Overall, the top-ranked scenarios (see section 3.3.4) for each biome (based on NSE_{avg}) were shown to be: PM³ for grasslands (0.56), croplands (0.61) and shrublands (0.31), SW³ for evergreen needleleaf forest (0.40) and SW⁴ for deciduous broadleaf forest sites (0.73) (NSE_{avg} shown in the parenthesis). The common element of these scenarios is the use of the Mu surface resistance. PM³ and SW³ use Thom's aerodynamic resistance with dynamic roughness, whereas SW⁴ uses the Mu r_a . The Mu model itself showed low sensitivity to r_a parameterization and its r_s parameterization improved

other models. Interestingly, none of the top-ranked scenarios were from this model. This may have some implications for the suitability of this model for global scale ET estimation in the MODIS MOD16 products (<http://www.ntsg.umd.edu/project/mod16>) (Polhamus et al. 2013): keeping in mind the inherent data limitations of global flux estimation approaches (Jiménez et al. 2011a; Mueller et al. 2013).

An important consideration on the choice of model parameterization is the availability of reliable data. Application of the surface resistance method of the Mu model is important in relaxing the needs for soil moisture data and is likely to facilitate its application in field to larger scale estimation. These findings reflect results from an experiment using a modified Priestley-Taylor model (PT-JPL model; Fisher et al. 2008). Like the Mu model, the PT-JPL approach does not use wind speed and soil moisture and comparisons against more complex models illustrated improved flux reproduction (Vinukollu et al. 2011c; Ershadi et al. In review-a). However, the aerodynamic resistance method of the top-ranked scenarios examined here (except for deciduous broadleaf forest sites) all used Thom's equation with dynamic roughness, which requires reliable wind speed and vegetation height data. Accurate wind speed data are not available for the majority of areas and the only source for vegetation height at the global scale is a static product developed by NASA-JPL (Simard et al. 2011). This 1 km spatial resolution product has limited capability over short vegetation (e.g. grasslands and croplands) and at the moment, is not a dynamic product. Although the Mu model is designed for large scale applications with coarse spatial (1 km) and temporal (8 day to yearly) resolutions, this study showed that its resistance parameterizations can be used at the tower scale.

Part of deficiencies in the performance of the models, especially over shrubland sites (with NSE < 0.3) is likely related to the coarse spatio-temporal resolution (i.e. 250 m, 16 days) of the MODIS data used for estimation of vegetation indices (which are subsequently used for parameterization of aerodynamic and surface resistances). Shrubland sites display considerable land surface heterogeneity and the contrasting bare soil and vegetation elements may not be well captured at the coarser remote sensing scale (Stott et al. 1998; Lu et al. 2003; Montandon and Small 2008). A difference between the results of this and previous studies that have reported higher performance of the PM type of models, may reflect the inherent uncertainties introduced via the input data, since the majority of prior investigations were performed with detailed field observations of vegetation characteristics (Huntingford et al. 1995; Brenner and Incoll 1997; Domingo et al. 1999; Li et al. 2011). For example, Li et al. (2011) used the SW model over desert shrubs and found satisfactory agreements with observed evapotranspiration ($R^2 = 0.78$, $RMSD = 0.25 \text{ mm}\cdot\text{d}^{-1}$) when using detailed observations of the vegetation parameters and a calibrated Ball-Berry type (Ball 1987) model of the canopy resistance. There is a clear need for high quality in-situ phenological descriptions to undertake the types of globally distributed analysis performed here, but unfortunately they are often lacking.

A deficiency identified in the PM type of models relates to the effects of seasons on the performance (see Figure 3-2, Figure 3-4 and Figure 3-6). Croplands, deciduous broadleaf forest and (to a lesser extent) grasslands and shrublands have higher values

of *NSE* in the warmer months of summer, but their *NSE* values decrease considerably in colder months. In particular, all PM and Mu scenarios show higher values of *NSE* at cropland towers (C2 to C4) during the growing season (May to October), which is in accord with the findings in Section 2.3.2. Likewise, SW scenarios show similar temporal patterns, but the magnitude of *NSE* for SW⁰ and SW¹ is lower, perhaps due to the sensitivity of the SW model to aerodynamic parameterization in those scenarios (SG90 r_a with fixed roughness).

Reduced temporal variation in monthly *NSE* values at the evergreen needleleaf forest sites can be explained by lower variations in the biological controls (i.e. steady transpiration) during the year. These results indicate that environmental (e.g. available energy) and biological (e.g. presence of transpiring leaves) mechanisms have a major role on model performance (Granier et al. 1996; Wever et al. 2002; Wang and Dickinson 2012). The seasonality issue was persistent across all of model scenarios. As such, it seems that changes in model structure and resistance parameterizations cannot recover such issues, and applications of the Penman-Monteith type of models may result in uncertainties during colder months, regardless of the biome type.

3.4.2 Review of Differences between Current and Previous Studies

In contrast to a number of previous studies that indicated moderate to satisfactory performance of the PM type evapotranspiration models over a range of landcover types (e.g. Stannard 1993; Huntingford et al. 1995; Domingo et al. 1999; Li et al. 2011), the results of this intercomparison and evaluation study suggest somewhat reduced performance. Possible reasons for the observed variability in model performance can be attributed to a number of factors discussed below.

3.4.2.1 Differences in Temporal Resolution

In the current study, the analysis is based on direct use of half-hourly or hourly data from eddy covariance towers, whereas in the majority of previous studies (e.g. Stannard 1993; Huntingford et al. 1995; Fisher et al. 2005), simulations were performed at either a daily time step or first performed at hourly resolution and subsequently aggregated to daily (or monthly) time steps (Vinukollu et al. 2011c). These differences in temporal resolution inevitably contribute to variations observed between this and previous studies. Likewise, the impact of temporal aggregation of input (e.g. air temperature) (Fisher et al. 2008; Mu et al. 2011) and response (e.g. heat fluxes) (Fisher et al. 2005) data from (sub)-hourly to daily resolution on the performance of the evapotranspiration models is not well understood.

It is expected that model evaluations undertaken at coarser temporal resolutions will provide somewhat better agreement due to: a) an elimination of closure issues (Finnigan et al. 2003); b) a reduction of temporal mismatches in data records; or c) the smoothing effects of aggregation on input and response variables. However, it is potentially misleading to report such statistics given that the application of these models is usually desired at the finer temporal resolution. In particular, PM type models are strictly valid only in steady state conditions: that is, for time scales from a few minutes to 1 hour (Brutsaert 1982; Katerji et al. 2010). The theory is often in stark

contrast to the general application and assumption of scale (both temporal and spatial) invariance in the application of PM and related models.

3.4.2.2 Differences in the Duration of Analysis

Generally, the duration of model evaluations in previous studies was shorter than those of the present study, due possibly to the challenges of obtaining long term data sets and other limitations. Further, the period of data in some studies coincided with the growing season (e.g. [Tourula and Heikinheimo 1998](#)), when energy/water availability and vegetation biological and phenological mechanisms have a better match with the inherent assumptions of the combination theory ([Monteith 1965](#); [Brutsaert 1982](#)) and hence can influence the performance of the models ([Odhiambo and Irmak 2011](#)). Monthly *NSE* analysis of the base scenarios shown in Figure 3-2, Figure 3-4 and Figure 3-6 clearly show that for almost all biomes, in particular for croplands and deciduous broadleaf forest sites, the peak of *NSE* values (i.e. the time of higher performance) coincides with summer months: the season that coincides with a number of PM model evaluations ([Tourula and Heikinheimo 1998](#); [Odhiambo and Irmak 2011](#)). With longer periods of data, the temporal frequency of energy and moisture deficit conditions increases. In such deficit conditions, the chance of violating the theoretical assumptions of the PM model and the uncertainties in parameterization of the resistances increase. Such uncertainties would ultimately be expected to cause a reduction in modeling performance.

3.4.2.3 Differences in Measurement Technique

In this study, the eddy covariance is the only instrumental technique providing flux observations. A number of previous studies have used other measurement approaches, including the Bowen ratio energy balance (BREB), scintillometers, (micro-) lysimeters and sap flow devices. Uncertainty associated with advection effects and closure issues remain unaccounted for in all instrument based approaches ([Allen et al. 2011a](#)) and may result in improved (or degraded) model performance depending on the site physical details, quality of collections and myriad other factors.

3.4.2.4 Calibration of the Resistance Parameters

Local calibration of surface resistances using in-situ observed data is avoided in this study to make the results extendable to similar locations. However, a number of previous studies have divided the period of data to calibration and validation periods and have used calibrated surface resistances ([Stannard 1993](#); [Hu et al. 2009](#); [Li et al. 2011](#)) to evaluate the ET modeling performance in the validation period. Such applications of the models can improve the modeling performance, but reduce the generalization of the results. A similar explanation might be made for the improved performance of the scenarios that use μr_s (see section 3.2.2.3), as its parameters (see Table 3-1) are derived by calibration (using 41 Ameriflux towers, aggregated for each biome) ([Zhao et al. 2005](#); [Mu et al. 2011](#)). However, such biome scale calibration produces more generic parameterization, compared to local calibrations which produce site specific parameterization.

3.4.2.5 Uncertainties in Input Data

The values of LAI and f_c used in this study for parameterization of the aerodynamic and surface resistances are derived from NDVI data with 250 m spatial and 16 days temporal resolutions. As noted previously, such coarse resolution data may result in uncertainties in the estimation of the resistances, and consequently in evapotranspiration modeling. In particular, the coarse spatial resolution might not be sufficient to produce representative vegetation indices for the canopy structure in highly heterogeneous landscapes such as shrublands. The low performance of the SW model in these landscapes ($NSE_{avg} = -0.05$ to 0.21) might be associated with such input uncertainties. Although the effects of spatial pixel resolution in heat flux generation have been explored in some models (McCabe and Wood 2006; Long et al. 2011; Ershadi et al. 2013b), such evaluations have not been extensively studied for Penman-Monteith type approaches. Forcing data uncertainties can also influence the performance of the models due to a mismatch between the footprint of meteorological sensors and the footprint of eddy-covariance system (Ershadi et al. 2013a; Chapter 5).

3.5 Conclusion

In this study, the effects of model structure and parameterization on a suite of Penman-Monteith type models were investigated. The structure of the models varied from single-source, two-layer and three-source models. To examine the influence of choice of model parameterization, a number of commonly employed resistance schemes were substituted into the default model structure, with subsequent simulations evaluated against locally measured ET for a number of distributed flux tower sites.

Results clearly illustrated the variability in model performance over the different biomes, with no single model structure or scenario providing the best results over all selected sites. Changes in resistance parameterizations, in particular the surface resistance, were seen to strongly influence the performance of the models. However, this response was not consistent across all studied biomes. In a comparison of the Jarvis multiplicative scheme against the Mu lookup table approach for r_s , the latter scheme showed improved results when applied to the single-source PM model (except in the deciduous broadleaf forest sites) and across all biomes when using the Mu evapotranspiration model. The same change in resistance showed variable behaviour in the SW model over the biomes. Importantly, no single model structure consistently provides the best results and the combined effect of both model structure and parameterization is critically important for PM type models.

When the “best” scenarios were identified for each biome (based on NSE_{avg}), the Mu model’s surface resistance parameterization proved to be a common element. For the aerodynamic resistance, the top-ranked scenarios shared the Mu r_a method for deciduous broadleaf forest sites only, and shared the Thom’s r_a equation with dynamic roughness for all other biomes. The limitation of the Thom scheme is the requirement for reliable wind speed and canopy height data, which are not always available. In addition to the direct influence of resistance parameterizations, all of the PM type

scenarios displayed higher values of *NSE* during the warmer (summer) months regardless of biome type, which indicates the influence of environmental and biological conditions of the land surface on these schemes. As such, application of PM models at times of limited available energy is with high uncertainties.

A key consideration from the findings of this work relates to the application of PM type models across a range of hydrological and related disciplines. Penman-Monteith type of approaches have been used (with modifications in structure and parameterizations) in a number of global scale ET datasets (Sheffield et al. 2009; Zhang et al. 2010b), global circulation models (Dolman 1993) and Land Surface Models (Chen et al. 1997; Sheffield and Wood 2007). Hence, the uncertainties and errors originated from non-optimum structure or parameterization of the models can greatly influence the accuracy of estimated ET results, evaluations of the global ET trends (Jiménez et al. 2011a; Mueller et al. 2013) and the decisions made based on such results: including, but not limited to drought (Sheffield and Wood 2008), land-atmosphere interactions (Seneviratne et al. 2006) and climate change projections (Droogers et al. 2012).

As the identified top-ranked scenarios of this study were different for different biomes, an ensemble approach in global ET estimation (comprised of optimum resistance parameterization methods for each biome) might be an appropriate approach for global flux estimation (Jiménez et al. 2011a; Mueller et al. 2011a; Mueller et al. 2013). Alternatively, a biome-specific tiled ET product could be developed by using the best model/parameterization configuration for each biome type. In either case, further understanding the role of parameterization on model performance is critical in assessing the impact of choice on derived products. This is especially true for applications such as drought monitoring, water resources and agricultural management and climate change assessment, which all integrate the modelling of ET as a variable in their process investigations.

Acknowledgement

Funding for this research was provided via an Australian Research Council (ARC) Linkage (LP0989441) and Discovery (DP120104718) project, together with scholarship to support Ali Ershadi from the National Centre for Groundwater Research and Training (NCGRT) in Australia. We thank the METFLUX site investigators for allowing the use of their meteorological data. This work used eddy covariance data acquired by the FLUXNET community and in particular by the AmeriFlux (U.S. Department of Energy, Biological and Environmental Research, Terrestrial Carbon Program: DE-FG02-04ER63917 and DE-FG02-04ER63911) and OzFlux programs. We acknowledge the financial support to the eddy covariance data harmonization provided by CarboEuropeIP, FAO-GTOS-TCO, iLEAPS, Max Planck Institute for Biogeochemistry, National Science Foundation, University of Tuscia, Université Laval and Environment Canada and US Department of Energy and the database development and technical support from Berkeley Water Center, Lawrence Berkeley National Laboratory, Microsoft Research eScience, Oak Ridge National Laboratory, University of California - Berkeley, University of Virginia. Data supplied by T. Kolb, School of Forestry, Northern Arizona University, for the US-Fuf site was supported by grants from the North

American Carbon Program/USDA NRI (2004-35111-15057; 2008-35101-19076), Science Foundation Arizona (CAA 0-203-08), and the Arizona Water Institute. Matlab scripts for automatic extraction of NDVI time series at towers were provided by Dr Tristan Quaife, University College London via the web portal at http://daac.ornl.gov/MODIS/MODIS-menu/modis_webservice.html

Chapter 4

Effects of Spatial Aggregation on the Multi-Scale Estimation of Evapotranspiration

The original research described in this Chapter has been published as:

Ershadi, A., McCabe, M.F., Evans, J.P., J.P. Walker, (2013) '[Effects of spatial aggregation on the multi-scale estimation of evapotranspiration](http://dx.doi.org/10.1016/j.rse.2012.12.007)', Remote Sensing of Environment, 131, 51-62, <http://dx.doi.org/10.1016/j.rse.2012.12.007>

Reprinted with permission from Elsevier

Reprinted with altered style and minor modifications

4 Effects of Spatial Aggregation on the Multi-Scale Estimation of Evapotranspiration

Abstract

The influence of spatial resolution on the estimation of land surface heat fluxes from remote sensing is poorly understood. In this study, the effects of aggregation from fine (< 100m) to medium (approx. 1 km) scales are investigated using high resolution Landsat 5 overpasses. A temporal sequence of satellite imagery and needed meteorological data were collected over an agricultural region, capturing distinct variations in crop stage and phenology. Here, we investigate both the impact of aggregating the input forcing and of aggregating the derived latent heat flux. In the input aggregation scenario, the resolution of the Landsat based radiance data was increased incrementally from 120 m to 960 m, with the land surface temperature calculated at each specific resolution. Reflectance based land surface parameters such as vegetation height and leaf area index were first calculated at the native 30 m Landsat resolution and then aggregated to multiple spatial scales. Using these data and associated meteorological forcing, surface heat fluxes were calculated at each distinct resolution using the Surface Energy Balance System (SEBS) model. Results indicate that aggregation of input forcing using a simple averaging method has limited effect on the land surface temperature and available energy, but can reduce evapotranspiration estimates at the image scale by up to 15%, and at the pixel scale by up to 50%. It was determined that the predominant reason for the latent heat flux reduction in SEBS was a decrease in the aerodynamic resistance at coarser resolutions, which originates from a change in the roughness length parameters of the land surface due to the aggregation. In addition, the magnitude of errors in surface heat flux estimation due to input aggregation was observed to be a function of the heterogeneity of the land surface and evaporative elements. In examining the response of flux aggregation, fine resolution (120 m) heat fluxes were aggregated to coarser resolutions using a range of common spatial interpolation algorithms. Results illustrate that a simple averaging scheme provides the best choice for flux aggregation compared to other approaches such as nearest neighbour, bilinear interpolation or bicubic interpolation, as it not only preserves the spatial distribution of evapotranspiration, but most importantly conserves the mass balance of evaporated water across pixel and image scales.

Keywords: Landsat; MODIS; Surface Energy Balance System (SEBS); flux aggregation; input aggregation; upscaling; land surface temperature; uncertainty; roughness; aerodynamic resistance

4.1 Introduction

Evapotranspiration (ET) is a complex process that incorporates interactions across a range of terrestrial and atmospheric variables, including the land surface temperature, air temperature, wind speed and humidity, as well as vegetation height and density (Brutsaert 1982). As a consequence, evapotranspiration can be highly variable in space and time, particularly over heterogeneous surfaces. Given the importance of evapotranspiration in characterizing aspects of the hydrological cycle, understanding

the nature and degree of this variability has been an ongoing effort in the hydrological and related sciences (Entekhabi and Eagleson 1989; Settle and Drake 1993; Anderson et al. 2003; McCabe and Wood 2006; Brunsell and Anderson 2011). While there are established methods to estimate surface heat fluxes between the point and patch scales (e.g. eddy covariance and scintillometry approaches), such local, such local scale estimates cannot easily be extrapolated beyond the field to basin scales: although there are some approaches that attempt to do this (Jung et al. 2009). Given the spatial and temporal variability of the evapotranspiration process (McCabe et al. 2005), a practical method for the routine estimation of spatially distributed heat fluxes at both the field and basin scales is through the use of remote sensing techniques (Norman et al. 1995; Bastiaanssen et al. 1998a; Su 2002; Anderson et al. 2003; Allen et al. 2007a).

A number of remote sensing evapotranspiration models like SEBS (Su 2002), SEBAL (Bastiaanssen et al. 1998a) and METRIC (Allen et al. 2007b) have been developed and validated at the patch scale using fine resolution satellite imagery (e.g. Landsat and ASTER) (Bastiaanssen et al. 1998b; Allen et al. 2007a; Tasumi and Allen 2007; Timmermans et al. 2007; Choi et al. 2009; van der Kwast et al. 2009). However, there are cases when these methods are used with much coarser resolution data from sensors like AATSR (Advanced Along Track Scanning Radiometer), MODIS (Moderate Resolution Imaging Spectroradiometer) and AVHRR (Advanced Very High Resolution Radiometer) (Jia et al. 2003; Zwart and Bastiaanssen 2007; Elhag et al. 2011; Gibson et al. 2011; Gokmen et al. 2012) in order to broaden the scope of their application. Unfortunately, the effects of subsequent changes in the spatial resolution on modeling performance and the implicit scaling influences that occur as a result of these are addressed in relatively few studies (McCabe and Wood 2006; Hong et al. 2009; Gebremichael et al. 2010; Long et al. 2011; Tian et al. 2012).

Validation of turbulent heat fluxes using remote sensing algorithms can be significantly influenced by the spatial resolution of the data (Su et al. 1999). In particular, aggregation of the input forcing can have mixed influences on the evaluation of the resultant heat flux (Su et al. 1999; Brunsell and Gillies 2003; McCabe and Wood 2006). Likewise, validating coarse resolution measurements is generally more difficult due to the additional uncertainty introduced by the scale discrepancy between ground measurements and the coarse spatial resolution imagery (Hong et al. 2009; Gebremichael et al. 2010; Long et al. 2011). Furthermore, the mismatch between the variable being represented and the resolution at which it can be retrieved provides another level of uncertainty in the estimation process. For instance, the effects of spatial resolution of land surface temperature and roughness parameters on heat and vapor transfer are not well understood, particularly as the satellite resolution increases (Becker and Li 1995; Brunsell and Anderson 2011).

To address such issues, a number of studies have evaluated the aggregation (or up-scaling) effects on heat flux estimation (Entekhabi and Eagleson 1989; Famiglietti and Wood 1994; Su et al. 1999; Kustas and Norman 2000; Nakaegawa et al. 2001; Brunsell and Gillies 2003; Kustas et al. 2004; McCabe and Wood 2006; Hong et al. 2009; Wang and Currit 2011). In general, aggregation can be applied either on the input forcing of

the evapotranspiration models, or it can be applied to the fluxes derived from fine resolution input fields (i.e. aggregate then calculate versus calculate then aggregate). To examine these different approaches further, the concepts of ‘input aggregation’ and ‘flux aggregation’ are explored.

Aggregation of the input forcing has an immediate influence on the representative heterogeneity of the surface and affects the land surface control on heat flux generation (Brunsell and Gillies 2003). One of the underlying assumptions for most physically based evapotranspiration models is the requirement for homogeneous conditions across a pixel, including homogeneity in both land surface (vegetation type, roughness, temperature) and meteorological conditions. To date, the effect of spatio-temporal variability of surface and atmospheric fields on heat flux generation remain poorly explained and quantified (Brunsell et al. 2008).

In addition to the aggregation of input forcing, resultant surface heat fluxes may require subsequent aggregation for a range of purposes e.g. to allow spatially consistent comparison and evaluation of General Circulation Model (GCM) and Regional Climate Model (RCM) outputs (Jiménez et al. 2011b; Mueller et al. 2011b). Likewise, GCM and RCM models require input forcing with a coarse spatial resolution that is generally much larger than the spatial resolution of remote sensing sensors. Therefore, an aggregation procedure is used to bridge the scale gap between remote sensing derived fluxes and the input requirements for large scale models (Hong et al. 2009). Further, flux aggregation is useful (and sometimes necessary) in comparisons of heat fluxes derived from geostationary images and those from polar-orbiting satellites (Brunsell and Anderson 2011).

Moran et al. (1997) evaluated the effect of radiance aggregation on temperature and consequently on the sensible heat flux over a semi-arid rangeland in Arizona, finding negligible change in the land surface temperature, but large errors (more than 50%) in the sensible heat flux across heterogeneous areas having small vegetation elements within the pixels. The authors indicated that the uncertainty in flux estimation by input aggregation was due mainly to the non-linearity of the relations between the sensor signals, estimated variables and fluxes, and the inherent heterogeneity of the landscape. Hong et al. (2009) examined the aggregation of radiance from Landsat ETM+ resolution (30 m) to MODIS resolution (250 m) using the SEBAL model (Bastiaanssen et al. 1998a) and found that the peak of the histogram of latent heat flux increased 10-25% due to input aggregation. In a related study, Gebremichael et al. (2010) found that both input and flux aggregation procedures produced similar spatial patterns in SEBAL. Recently, Long et al. (2011) found that input aggregation of Landsat data to MODIS resolutions resulted in similar spatial mean values of sensible heat flux but with smaller spatial standard deviations.

For studies examining flux aggregation, Moran et al. (1997) found that errors in the aggregation of turbulent fluxes were highly influenced by the heterogeneity of the site and due mainly to variations in atmospheric stability, aerodynamic roughness and patchy vegetation structures. Separate to the underlying surface heterogeneity, Sridhar et al. (2003) evaluated the performance of the nearest neighbour, bilinear and bicubic interpolation methods for aggregation of evapotranspiration, finding that

nearest neighbour and bilinear methods provided better performance than bicubic interpolation. [Hong et al. \(2009\)](#) found that flux aggregation using simple averaging and nearest neighbour methods can preserve the mean value of the original image and that the nearest neighbour method performed better than simple averaging by preserving the spatial variability of the fluxes.

While the majority of previous aggregation studies have employed semi-empirical evapotranspiration methods (e.g. SEBAL), a physically-based approach is used here for simulation of the land surface interactions and heat flux estimation. Doing this provides an opportunity to directly quantify the effect of input aggregation on each of the contributing components of heat flux estimation, including the land surface temperature, roughness parameters, aerodynamic resistance and available energy. Also, while flux aggregation techniques have been examined previously (see above), an evaluation of these approaches based on conservation of the evaporative mass balance ([Raupach 1995](#); [Raupach and Finnigan 1995](#)) has not been examined. Preservation of the evaporated water volume across scales provides a superior measure of performance of the flux aggregation than considering spatial statistical aspects of the aggregation alone.

In this research effort, we examine the following hypotheses: a) that the effect of aggregation on input variables and parameters is not equal and that the roughness parameters are more significantly influenced by aggregation than other input variables; b) that errors due to the input aggregation are a function of the land surface heterogeneity and the size of the evaporative elements; and c) that a simple averaging approach is the best candidate for flux aggregation based on preservation of the hydrological mass balance.

4.2 Description of Study Area and Data Sources

The focus of these investigations is a heterogeneous agricultural region located in a semi-arid environment in the south-east of Australia. The 10.8×10.8 km region is situated in the agriculturally rich and economically important Murrumbidgee catchment (a sub-catchment of the Murray Darling Basin), comprising natural drylands in the northern and eastern directions and active irrigation areas elsewhere. An irrigation canal passes through the study area from the south to northeast (see Figure 4-1).

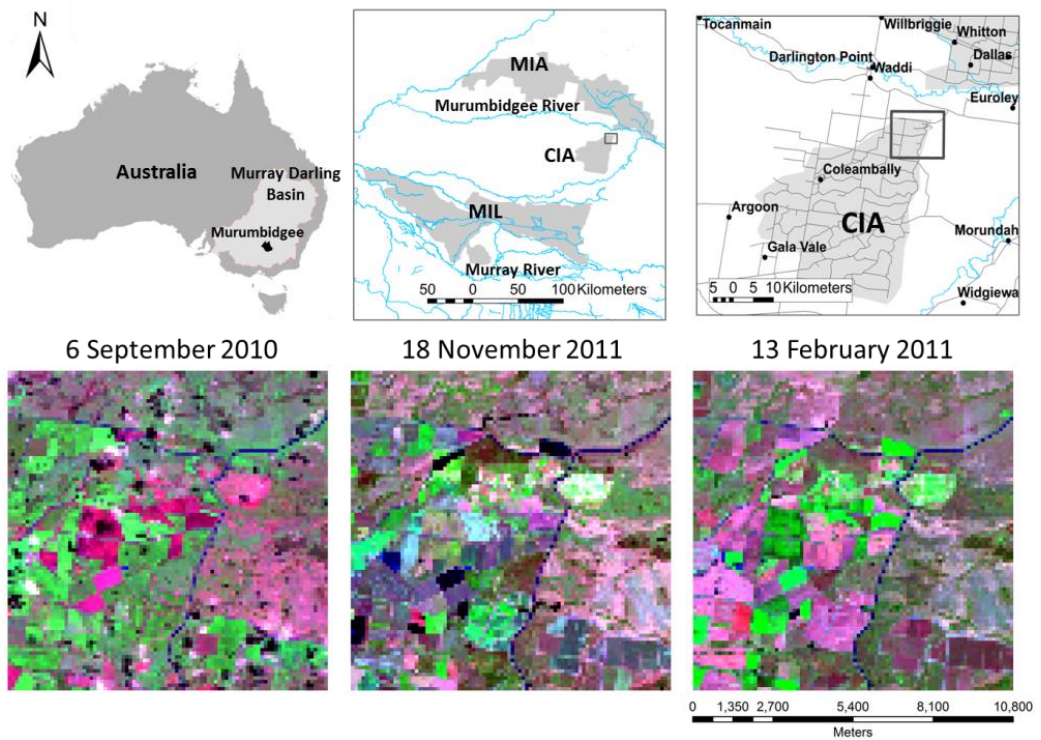


Figure 4-1: Location of the study area in Australia's Murray-Darling Basin (top-left), with the Murrumbidgee sub-catchment (top-middle) and the Coleambally irrigation area (top-right) also identified. Bottom panels show the Landsat band combination (7-4-2) colour composites for selected days at 120 m resolution. Green indicates vegetation and pink to magenta indicates bare soil. MIA represents the Murrumbidgee Irrigation Area, CIA the Coleambally Irrigation Area and MIL the Murrumbidgee Irrigation Limited regions.

4.2.1 Meteorological Data

A meteorological station located in the centre of the study site provided the necessary meteorological forcing data. Observed variables included half-hourly air temperature, humidity, wind speed and atmospheric pressure, along with a Kipp and Zonen CNR1 four way net radiometer that provided detailed radiation budget components. Figure 4-2 presents the daily variations of net radiation, air temperature and wind speed for the selected days.

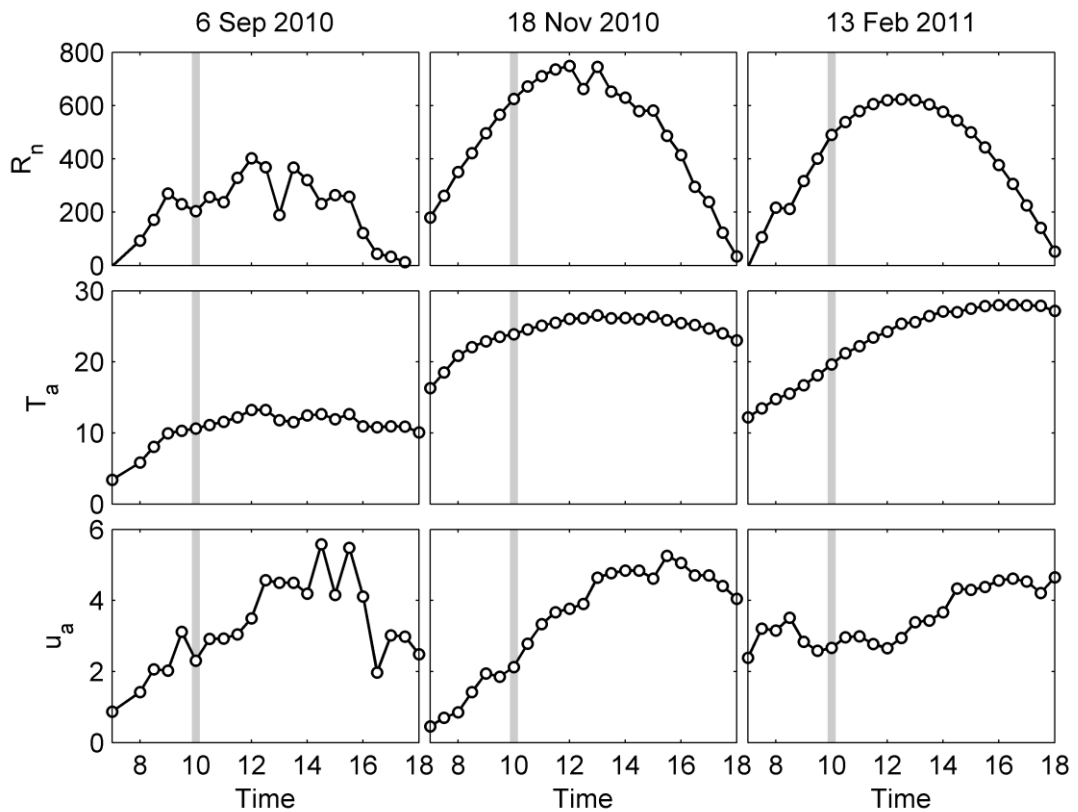


Figure 4-2: Variations of net radiation (R_n in $\text{W}\cdot\text{m}^{-2}$), air temperature (T_a in $^{\circ}\text{C}$) and wind speed (u_a in $\text{m}\cdot\text{s}^{-1}$) for selected days. The thick grey line shows the time of the Landsat satellite overpass.

4.2.2 Satellite Data

Landsat 5 TM overpasses (Path 93, Row 84) were evaluated during the cropping calendar, with three satellite images representing different crop-growth stages selected on 6 September 2010, 18 November 2010 and 13 February 2011 (see Figure 4-1). As shown in Figure 4-2, 6 September 2010 is not a clear sky day, although no clouds are apparent in the acquired Landsat image. However, other times within the 30 minute period of tower observations (corresponding to the Landsat overpass) might have been affected by clouds. Therefore, meteorological variables are possibly uncoupled from the land surface conditions seen in the Landsat image of 6 September 2010, which results in uncertainties for evapotranspiration estimations based on this image. Images and tower records for 18 November and 13 February present clear-sky conditions.

The raw Landsat radiance data were aggregated across spatial increments of 120 m, from 120 m (the native resolution) up to the MODIS equivalent 960 m scale. Land surface temperature was calculated at each resolution from the aggregated radiance data. This last step is particularly important in estimating the T_s , as the relationship between radiance and T_s is non-linear. Aggregating the temperature directly (as opposed to averaging the radiances and then calculating the temperature), would subsequently increase the uncertainty in retrievals (McCabe et al. 2008). Vegetation

structural parameters including vegetation height (h_c) (Su 2001a), leaf area index (LAI) (Ross 1976b) and fractional vegetation cover (f_c) (Campbell and Norman 1998) are calculated from fine resolution NDVI (Normalized Difference Vegetation Index) and then aggregated to coarser resolution by simple averaging.

4.2.2.1 Land Surface Temperature, Radiative Fluxes and Vegetation Indices

Digital numbers in all bands of the Landsat images were converted to top of atmosphere radiance and reflectance values, and subsequently to land surface temperature following the methodology of Chander and Markham (2003) and Chander et al. (2007), after atmospheric correction using MODTRAN 5 software (Berk et al. 2008). For the atmospheric correction, temperature and water vapour profiles were determined from the MOD7L2 products of the MODIS sensor. For each of the aggregation scenarios, the upward longwave (LW_u) radiation was calculated using the spatially equivalent land surface temperature. In all cases, the emissivity and albedo were obtained from aggregated Landsat products. The downward longwave and shortwave radiation components were assumed uniform over the study area, with values obtained from the meteorological tower observations. The ground heat flux (G_0) at each scale of aggregation was calculated as a fraction of the net radiation (R_n), based on the fractional vegetation cover (f_c) following Su (2002):

$$G_0 = R_n(\Gamma_c + (1 - f_c)(\Gamma_s - \Gamma_c)) \quad 4-1$$

in which it is assumed that the ratio of soil heat flux to net radiation $\Gamma_c = 0.05$ for full vegetation canopy (Monteith 1973) and $\Gamma_c = 0.315$ for bare soil (Kustas and Daughtry 1990). An interpolation is then performed between these limiting cases using the fractional canopy coverage, f_c .

For estimation of the NDVI, Landsat band 3 and band 4 were used, following the relationship of Sobrino et al. (2004). Subsequently, the leaf area index (LAI) was derived from the NDVI data (Fisher et al. 2008), and emissivity calculated using the methodology of Sobrino et al. (2004).

4.2.3 Surface Energy Balance System (SEBS) Model

SEBS (Su 2002) is a physically based approach for the estimation of actual evapotranspiration using combined inputs from remote sensing and in-situ observations. The main forcing data to the SEBS model include the land surface temperature, vegetation height and density, air temperature, humidity and wind speed. The principal element of the SEBS model is its robust formulation for estimation of the sensible heat flux using either Monin-Obukhov Similarity Theory (MOST) (Monin and Obukhov 1945) for the atmospheric surface layer (ASL) domain or the Bulk Atmospheric Similarity Theory (BAST) (Brutsaert 1999) for the mixed layer domain of the atmospheric boundary layer. In the majority of cases (and as employed here), MOST equations are used unless the roughness of the surface is high and/or the ASL is low. The MOST equations used in SEBS include stability-dependent flux-gradient functions for momentum and heat transfer (equations 2-1 to 2-3) to estimate sensible heat flux (H).

The roughness length for momentum and heat transfer (z_{0m} and z_{0h}) used in the MOST equations are functions of the bio-meteorological conditions of the land surface. These two key parameters are estimated in SEBS using the methodology developed by [Su et al. \(2001\)](#), which employs vegetation phenology, air temperature and wind speed (equations 3-26 and 3-27).

After estimation of the sensible heat flux, SEBS uses a scaling method to adjust the derived sensible heat flux between hypothetical dry and wet limits based on the relative evaporation concept. This scaled H is then used to derive the latent heat flux (λE) as a residual term in the general energy balance equation. Further details on the formulation and implementation of the SEBS method are available from [Su \(2002\)](#), [Su et al. \(2005\)](#) and [McCabe and Wood \(2006\)](#). The flowchart of the key calculation steps in the SEBS model is presented in Figure 4-3.

4.3 Methodology

In order to study the effects of aggregation on the distribution and magnitude of surface heat fluxes, SEBS model simulations were performed for two scenarios, comprising 1) input aggregation and 2) flux aggregation. Here, input aggregation first scales the remote sensing forcing data required by SEBS to the relevant resolution at which the heat flux calculations were performed (i.e. aggregate then calculate). To examine flux aggregation, SEBS latent heat flux retrievals were determined using the fine resolution Landsat derived data (in 120 m) and then aggregated to the subsequent resolutions (calculate then aggregate). The aggregation resolutions of this study were 120, 240, 480, 600, 720, 840 and 960 m, and the simple averaging method used for input aggregation. The 120 m resolution is the nominal resolution of the thermal channel (band 6) of the Landsat 5 TM, while the 960 m resolution is the closest integer multiplier to the nominal 1 km resolution of the MODIS daily land surface temperature products (including MOD11A1). The 240 m and 480 m resolutions provide an evaluation of the aggregation transfer effects between 120 m to 960 m and also approach the daily 250 m and 500 m MODIS visible band products which have been used in other approaches for disaggregation of T_s and flux data ([Anderson et al. 2011](#)). A flowchart of the simulation scenarios including the resolutions, interpolation methods and the source of input data is presented in Figure 4-3.

For the input aggregation scenario, the aim is to evaluate the suitability of MODIS resolution land surface temperature for field scale evapotranspiration estimation. With the suspension of Landsat 5 (from November 2011), the only sources of fine resolution land surface temperature data are from the ETM+ sensor on-board Landsat 7, the ASTER sensor on-board Terra, and TIRS sensor on-board Landsat 8 which all have limited capability in providing the required temporal resolution for many water resource applications. However, daily land surface temperature products can be obtained from MODIS and AVHRR sensors at coarse spatial resolutions, which can be integrated with vegetation parameters derived from optical sensors on-board a number of operational satellites (e.g. Landsat, SPOT, IRS) that provide fine spatial (25m) but coarse temporal resolutions (16 to 22 days). In contrast to the land surface temperature which changes rapidly, the vegetation condition can be assumed

relatively constant at weekly time scales. Hence, for the input aggregation of Landsat data in this study, radiance data (band 6) are directly aggregated to provide the required resolutions of T_s , while reflectance data are used to first calculate the high resolution land surface parameters (e.g. vegetation height, LAI) and are then aggregated separately. Roughness parameters (d_0, z_{0m}, z_{0h}) are calculated at each distinct resolution using the aggregated vegetation parameters (h_c, LAI, f_c).

As noted for the case of input aggregation described above, a simple averaging method was used in up-scaling the higher resolution flux values to the MODIS scale. However, to examine the influence of the choice of interpolation routine on flux aggregation, nearest neighbour, bilinear and bicubic interpolation approaches were also examined.

For nearest neighbour, the value of the aggregated pixel is the value from the fine resolution pixel that lies at the centroid of the coarse pixel. For bilinear interpolation, the aggregated pixel value is a weighted average of pixels in the nearest 2-by-2 neighbourhood. In the bicubic interpolation, the aggregated pixel value is a weighted average of pixels in the nearest 4-by-4 neighbourhood. The 1.8×1.8 km study area includes 90×90 pixels at 120 m resolution. To prevent edge effects in aggregation from 120 m to 480 m and 960 m resolutions, the last two rows and columns were ignored for these scales. As such, aggregation is performed for an 88×88 pixel region. Similarly, an 84×84 region is used for 840 m resolution aggregation. All 90×90 pixels are used for the other aggregated resolutions.

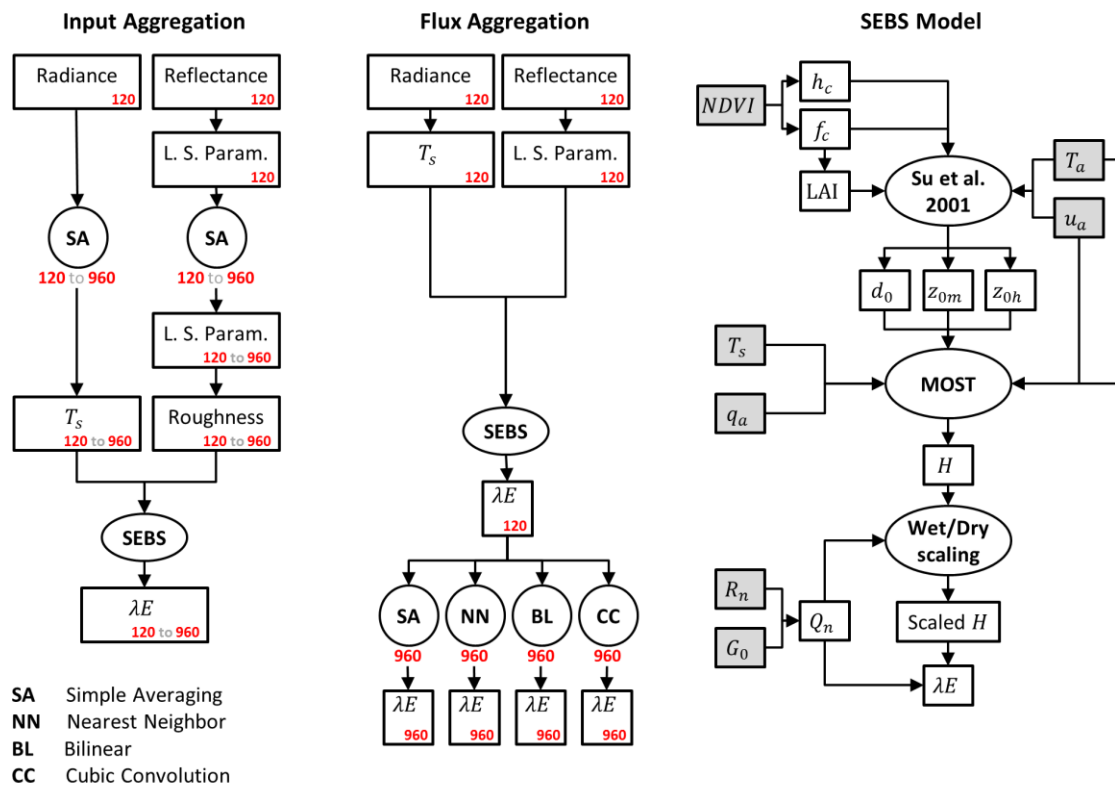


Figure 4-3: Flowchart of input aggregation (left) and flux aggregation (middle) scenarios. SEBS model flowchart is also shown in the right side. L. S. Param. refers to land surface parameters,

including vegetation height, LAI , fractional vegetation cover, emissivity and albedo derived from reflectance bands. Numbers in each box are spatial resolution in meters. For the SEBS flowchart, Q_n is available energy as $Q_n = R_n - G_0$.

To allow for an evaluation of the aggregation effects in the input aggregation scenario, each aggregated product or variable (e.g. radiative and turbulent fluxes) is compared with its corresponding value at the native 120 m resolution. In some previous aggregation studies (e.g. [Li et al. 2008](#)), the relationship between increased pixel size and improved agreement with measured heat fluxes (i.e. perhaps as a response to “matching” the larger pixel with the footprint of the eddy covariance instrument) has been evaluated. The aim in this current study is to evaluate the errors and uncertainties in evapotranspiration estimation when the spatial resolution of the input variables and parameters increase, not to compare against in-situ measurements.

4.4 Results and Discussion

For each of the selected days in September, November and February, the SEBS model was used to calculate latent and sensible heat fluxes for the aggregation scenarios identified in Figure 4-3. Results for each scenario are presented and discussed in the following sections.

4.4.1 Input Aggregation: Effect of Surface Temperature and Vegetation

Spatial maps, density plots and statistical measures were used to assess the influence of input aggregation on flux retrievals. In the spatial maps and density plots, λE is presented at 120, 240, 480 and 960 m resolutions. However, for statistical evaluation of the aggregation effects, additional resolutions of 360, 600, 720 and 840 m were also calculated. The statistical measures used for analysis of input aggregation include the spatial mean, relative error, root mean square difference (*RMSD*) and the coefficient of determination, R^2 ([Willmott 1982](#); [Timmermans et al. 2007](#); [Kalma et al. 2008](#); [Moore et al. 2009](#)).

Maps of land surface temperature and latent heat flux for each aggregated resolution are shown in Figure 4-4. As the magnitude of both T_s and λE in September is almost half that of the November and February images, a single consistent colour scheme is not used. Figure 4-4 illustrates that there is significant spatial variability across all three days at the 120 m resolution retrievals. The spatial standard deviation of λE is increased from 28 $\text{W}\cdot\text{m}^{-2}$ in September to 41 and 54 $\text{W}\cdot\text{m}^{-2}$ respectively in November and February. This variability is due in part to the agricultural practices and different phenological stages of crops in the study region. In particular, in the central west of the study area there are well defined agricultural fields that have low evapotranspiration rates in November, but which exhibit high values in the February image as a response to irrigation. Although the land surface temperatures in the majority of the November and February images are relatively similar, air temperature in November (24 °C) is higher than air temperature in the February image (20 °C). Therefore, for the same land surface temperature, the temperature gradient between the land surface and the atmosphere in November is 4 °C lower than February. This results in lower sensible heat fluxes in the November image. Moreover, net radiation in November (625 $\text{W}\cdot\text{m}^{-2}$)

is higher than February ($490 \text{ W}\cdot\text{m}^{-2}$) at the location of the meteorological tower. Consequently, the latent heat flux in the November image is higher than that of the February image.

In Figure 4-4b, degradation in the spatial pattern, range and magnitude of λE is evident in the aggregated fluxes from 240 m to 960 m. While loss of some spatial detail is evident in the 240 m retrievals of T_s and λE , the range, magnitude and spatial patterns of λE are maintained. However, loss in spatial information is not spatially uniform at the 480 m resolution, and is a function of the size of the more strongly evaporating elements of the scene. At the 960 m pixel resolution, the range, magnitude and spatial variability in both T_s and λE images are noticeably reduced. Similar trends were observed by Li et al. (2008) in an aggregation study ranging across 30 m to 960 m over a semi-arid region.

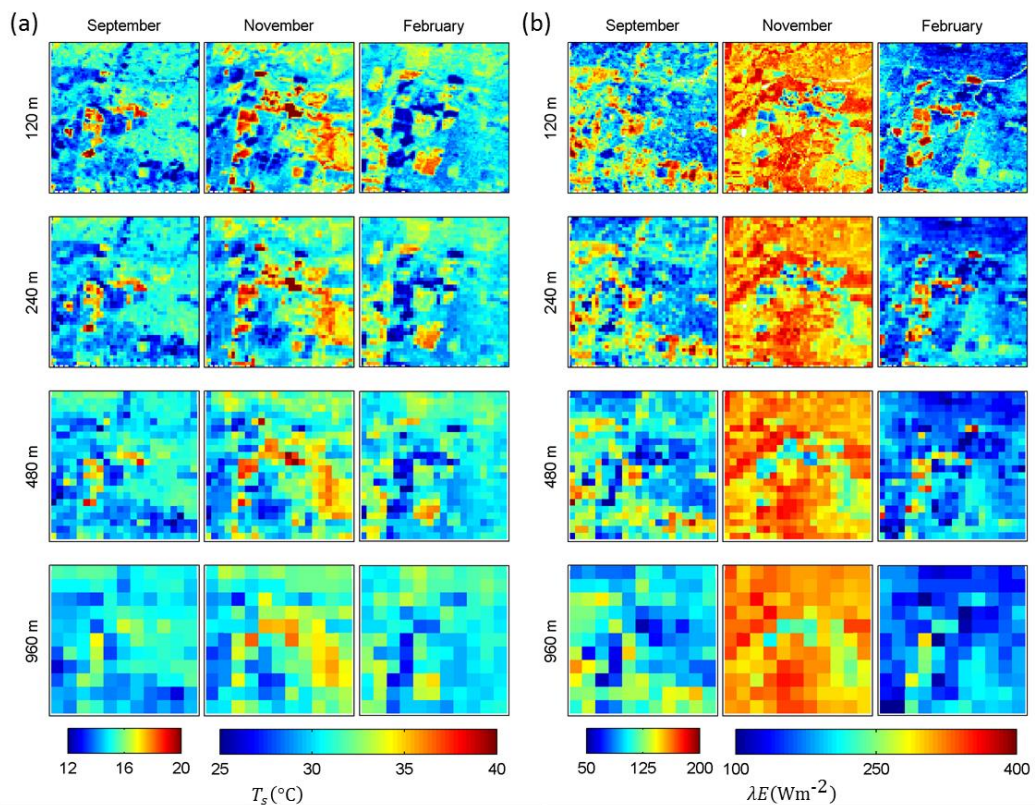


Figure 4-4: Spatial maps of a) the land surface temperature and b) the resulting evapotranspiration from the SEBS model using a simple averaging approach.

4.4.1.1 Image Scale Errors due to the Input Aggregation

To provide a quantitative evaluation of the effect of input aggregation on evapotranspiration estimation, density and cumulative density plots of λE maps for 120, 240, 480 and 960 m resolutions are presented in Figure 4-5. For the density plots, the frequency of each interval is normalized by the area under the frequency curve.

As can be seen from Figure 4-5, the range of λE values varies with each aggregation resolution. Likewise, increases in the peak of the density plots with aggregation do not persist across all days. This is in contrast to observations in Hong et al. (2009), who

found that the peak of the histogram of latent heat flux increased 10-25% as a response to aggregation. However, this difference might be attributed to the model structure difference between SEBS and SEBAL: in particular, SEBALs sensitivity to the choice of hot and cold pixel locations. Aggregation of input forcing shifts the peak of the density plot of the February image towards lower values of λE , which is apparent in the cumulative density plots, indicating that aggregation increased the frequency of lower λE values. However, it is not generic and depends on the underlying land surface condition, the spatial interpolation method and the heat flux model. For example, [Gebremichael et al. \(2010\)](#) found contrary results to the present study (i.e. a lower frequency of low λE values), using a simple averaging aggregation of ASTER thermal images (90 m) to MODIS resolution, due possibly to: a) their methodology (SEBAL); b) differences in study area and eco-hydrological conditions of the surface; or c) different parameterization of the roughness parameters and aerodynamic resistance.

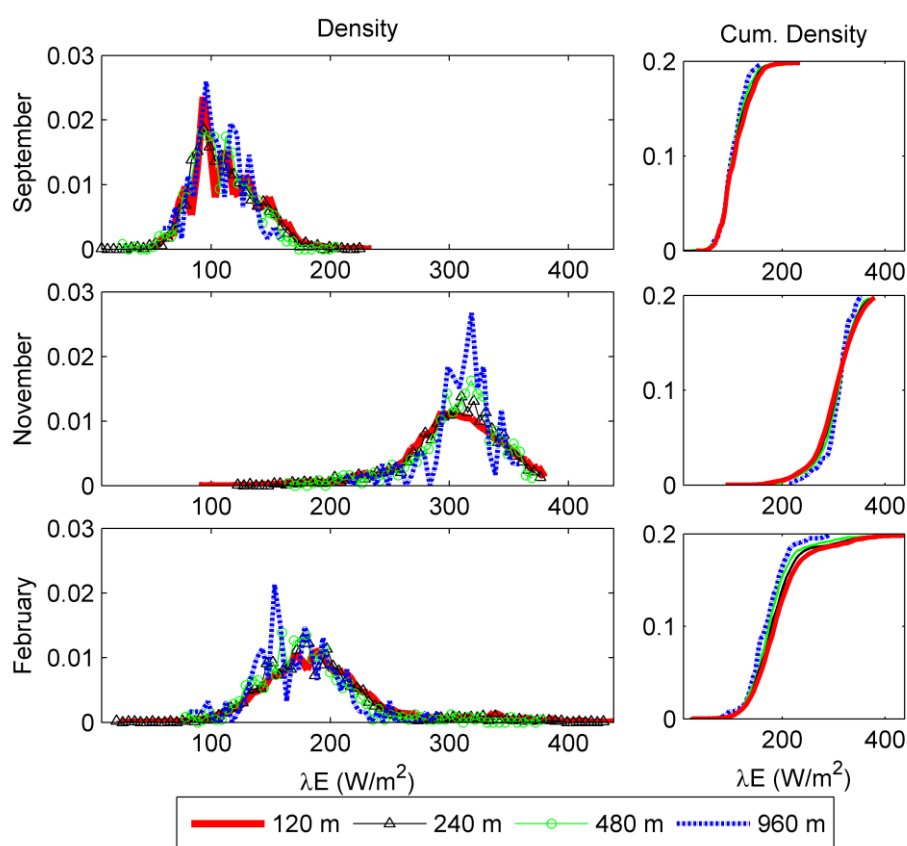


Figure 4-5: Density (left) and cumulative density (right) plots of λE for three selected days from original 120 m data and aggregation of input forcing to coarser resolutions.

For an evaluation of the effect of input aggregation on the magnitude and spatial variability of the latent heat flux and related parameters at the satellite image scale, the mean (μ) and standard deviation (σ) of simulated flux values were examined. In Figure 4-6a, the relative spatial mean (μ_r) and relative spatial standard deviation (σ_r) values for key variables across the aggregated maps are shown. The relative spatial mean for each variable in each aggregated resolution is derived by dividing the spatial

mean of the aggregated coarse resolution image by the spatial mean of the original fine resolution image. For example, for λE at 960 m resolution, the expression is $\mu_{r_{\lambda E}} = \mu_{\lambda E(960)}/\mu_{\lambda E(120)}$, where $\mu_{\lambda E}$ is the spatial average of λE . Similarly, $\sigma_{r_{\lambda E}} = \sigma_{\lambda E(960)}/\sigma_{\lambda E(120)}$, with σ being the spatial standard deviation.

The relative spatial mean and relative spatial standard deviation are derived for key input and flux variables of SEBS across all aggregated resolutions and plotted in Figure 4-6. Variables analysed include the land surface temperature (T_s), friction velocity (u_*), aerodynamic resistance (r_a), sensible heat flux (H), latent heat flux (λE) and available energy ($Q_n = R_n - G_0$). Here, the aerodynamic resistance (r_a) is calculated as

$$r_a = \frac{1}{\kappa u_*} \left[\ln \left(\frac{z - d_0}{z_{0h}} \right) - \Psi_h \left(\frac{z - d_0}{L} \right) + \Psi_h \left(\frac{z_{0h}}{L} \right) \right] \quad 4-2$$

The aerodynamic resistance (r_a) aids in characterising the roughness of the surface for momentum and heat transfer, and is thus useful in representing the combined effects of vegetation structure and the aerodynamic stability of the atmosphere (Brutsaert 1982, 2005).

The plots in Figure 4-6a illustrate that the relative spatial mean (μ_r) in the land surface temperature is constant, due to the simple averaging scheme used for aggregation. Relative spatial mean values for Q_n are also constant and indicate that the aggregation of emissivity and albedo products does not affect the image scale spatial average of the available energy. However, relative spatial mean values for u_* are increased while they are decreased for r_a across aggregated resolutions. These responses are due to the combined effects of aggregation on the roughness properties of the surface. Consequently, decreases in the aerodynamic resistance cause an increase in the sensible heat flux in the September and February images. However, in the November image, H is decreased by a decrease in the aerodynamic resistance due to the SEBS algorithm, as it scales H between hypothetical dry and wet limits (Su 2002). As a response to the change in the sensible heat flux variation, a decrease is evident for λE in the September and February images with an increase in the November image λE . However, the magnitude of change in H and λE is not the same for all selected days, and is related to the change in the roughness properties (z_{0m} , z_{0h}) of the land surface. For example, the February image shows greater sensitivity to the aggregation, resulting in a larger decrease in the relative mean of λE through aggregation.

In contrast to the relative spatial mean (μ_r), the relative spatial standard deviation (σ_r) for all selected variables and parameters is decreased through aggregation. While T_s and Q_n have relatively similar σ_r for all days, the rate of decrease in σ_r for u_* and r_a are different in the September image than those of the November and February images. This response is related to the change in the spatial variability of roughness length parameters, which can be best evaluated at the pixel scale.

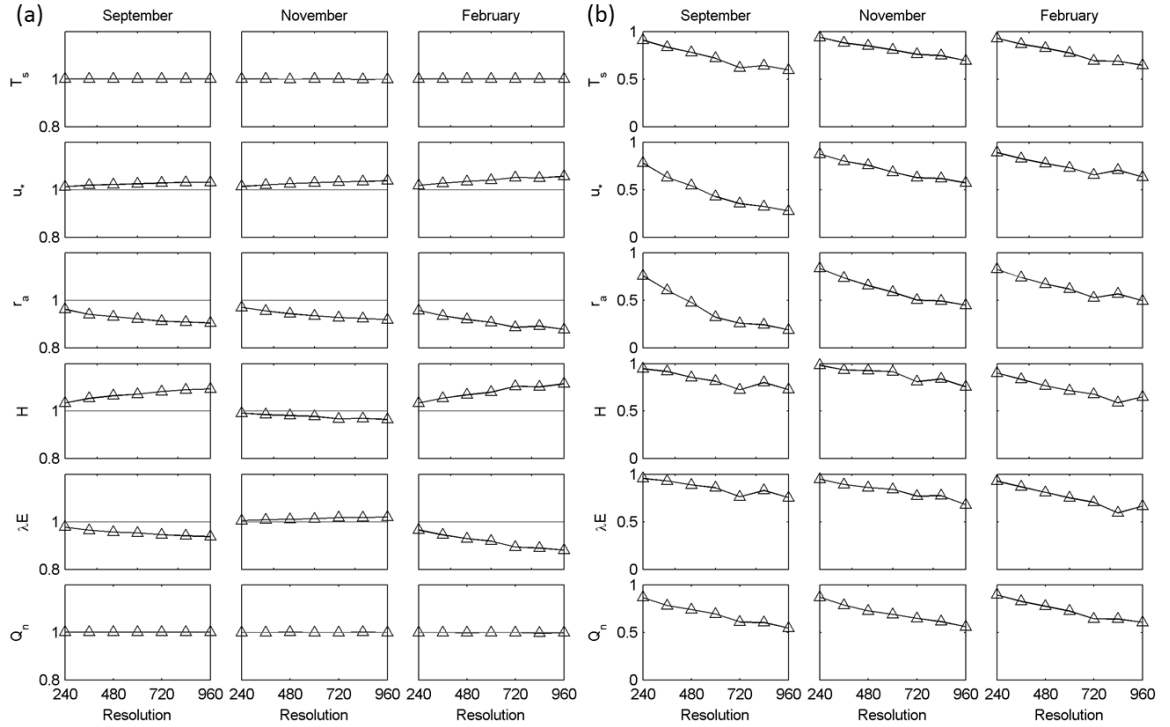


Figure 4-6: (a) variations of the relative spatial mean (μ_r) and (b) relative spatial standard deviation (σ_r) for T_s ($^{\circ}\text{C}$), u_* ($\text{m}\cdot\text{s}^{-1}$), r_a ($\text{s}\cdot\text{m}^{-1}$), H ($\text{W}\cdot\text{m}^{-2}$), λE ($\text{W}\cdot\text{m}^{-2}$) and Q_n ($\text{W}\cdot\text{m}^{-2}$) across aggregated resolutions from 240 to 960 m, increasing by 120 m increments.

4.4.1.2 Pixel Scale Errors due to the Input Aggregation

To understand the effect of input aggregation at the pixel scale, each coarse resolution pixel is compared against the unaltered 120 m pixels located within it. For example, the land surface temperature value from a 960 m pixel is compared to the 8×8 set of 120 m pixels from which it is comprised. To be able to make such comparison, a coarse 960 m resolution pixel can be considered as a set of 8×8 pixels all having the same value. The statistical measure for this comparison is the ‘relative error’ (or ‘estimation error’) defined as $E_r = \text{RMSD} / \mu$ (Kalma et al. 2008), where RMSD is the root-mean-square difference between the coarse resolution pixel and its constituent 120 m resolution pixels, and μ is the spatial mean value of those 120 m pixels. The relative error (E_r) is calculated for each coarse resolution pixel of the aggregated images for the key input and flux variables of the SEBS model across all aggregated resolutions, with the mean and percentiles (25th and 75th) of relative error (E_r) maps plotted in Figure 4-7.

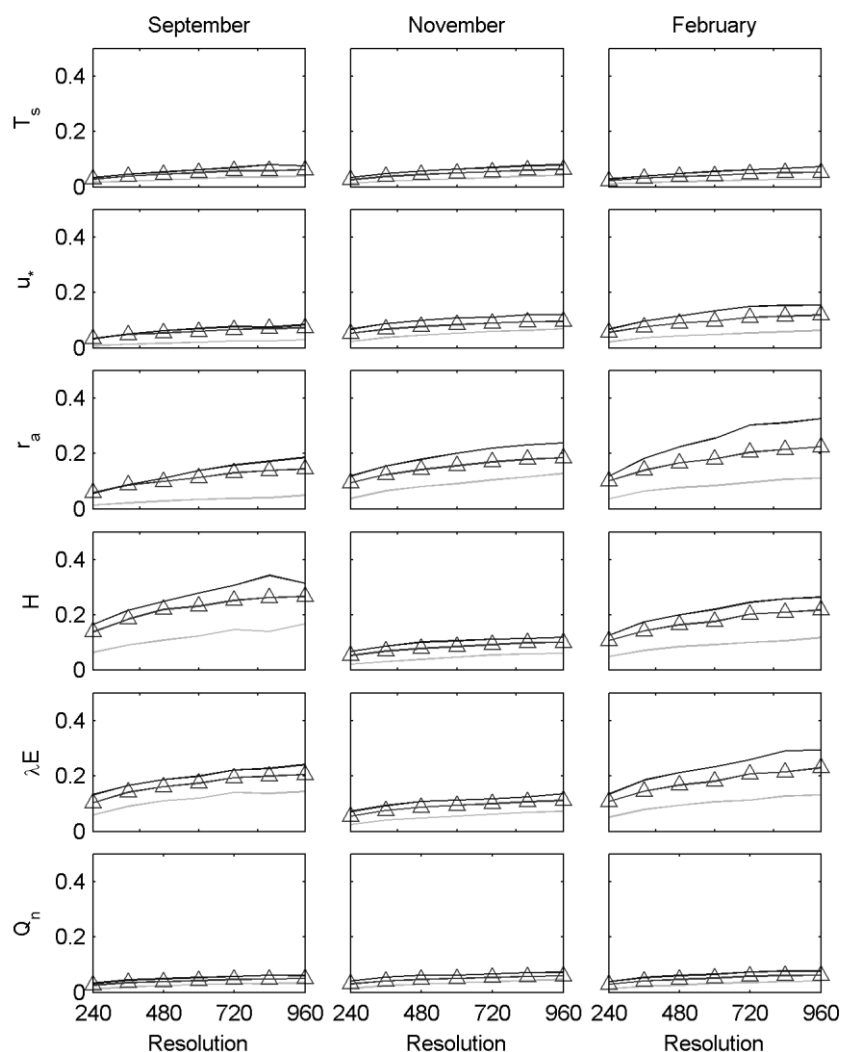


Figure 4-7: The relative error (E_r) at the pixel scale for T_s ($^{\circ}\text{C}$), u_* ($\text{m}\cdot\text{s}^{-1}$), r_a ($\text{s}\cdot\text{m}^{-1}$), H ($\text{W}\cdot\text{m}^{-2}$), λE ($\text{W}\cdot\text{m}^{-2}$) and Q_n ($\text{W}\cdot\text{m}^{-2}$) across aggregated resolutions from 240 to 960 m, increasing by 120 m increments. Triangles represent the mean relative errors and lines above and below identify the 75th and 25th percentiles respectively for each aggregated resolution.

The plots in Figure 4-7 illustrate that the pixel scale relative errors in the land surface temperature (T_s) and available energy (Q_n) are low (less than 5%). However, similar to the satellite image scale results, relative errors in u_* and r_a are higher (with wider percentile ranges) due to a response to the combined effects of aggregation errors on the roughness properties of the surface. Such a finding is in agreement with Moran et al. (1997) who identified negligible change in the land surface temperature aggregation, but large errors (greater than 50%) in the sensible heat flux over a heterogeneous study area.

As meteorological variables such as wind speed and air temperature are assumed constant for the study area (and hence for all pixels at all resolutions), only the land surface parameters derived from the Landsat image impact on the pixel scale spatial variability of u_* and r_a . The friction velocity (u_*) is related to the roughness height for

momentum transfer (z_{0m}) and the instability of the atmosphere caused by such roughness. However, r_a is related to both z_{0m} (via u_*) and z_{0h} (roughness height for heat transfer) and hence has more variability than u_* across all resolutions in all three days. This influence is clearly apparent in the wider bounds of the 25th and 75th percentiles of r_a compared to those of u_* .

To evaluate the effect of input aggregation on the spatial variability of relative errors, pixel scale E_r maps of aerodynamic resistance (r_a) and latent heat flux (λE) are presented in Figure 4-8. It is clear that the spatial distribution of errors in both r_a and λE are related to the variation of the land surface and may be associated with changes in the roughness height parameters. For example, in the 240 m error maps of Figure 4-8a, pixels with high relative errors are linked with the location of the irrigation canals and the borders of agricultural fields where the land surface type (especially the roughness of the surface) changes at the pixel scale. However, by increasing pixel size, such scale effects reduce and the land surface type at the landscape scale influences the magnitude and distribution of the relative errors instead (e.g. for the border of drylands and irrigation areas).

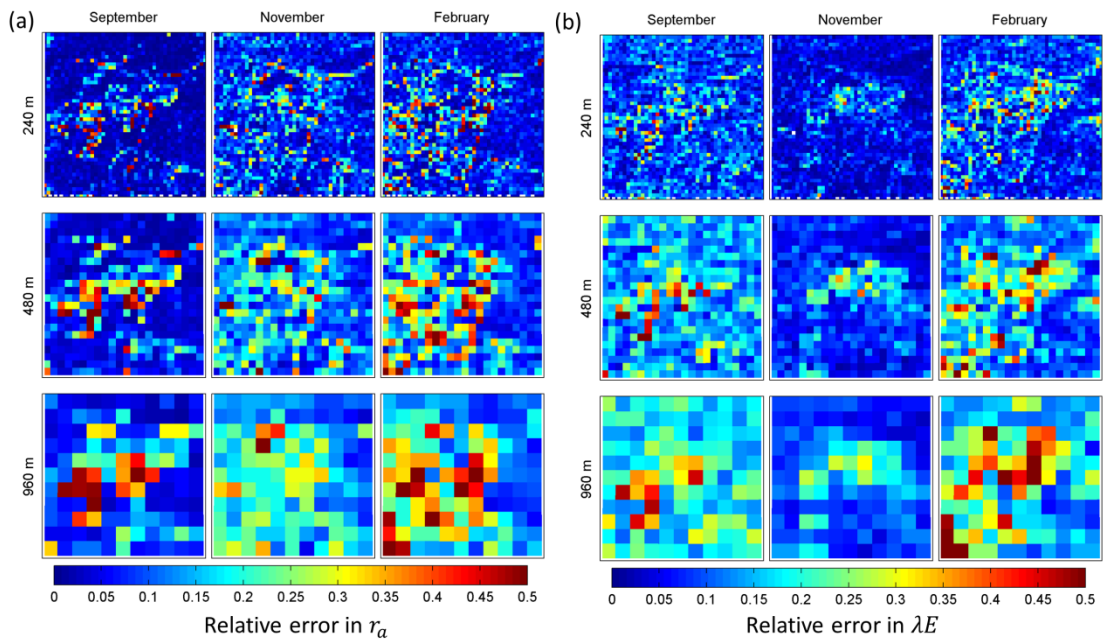


Figure 4-8: Pixel scale relative errors in (a) the aerodynamic resistance and (b) the latent heat flux due to input aggregation.

Figure 4-8b illustrates the presence of large pixel scale errors (greater than 40%) in λE estimation at the 960 m resolution for February and September. The November images have relative errors of approximately 20% in agricultural areas at this same resolution. Differences in the relative errors of available energy (Q_n) and heat fluxes (H and λE) at pixel scale highlight the important role of aerodynamic resistance parameterization in flux estimation, which is directly related to the estimation of roughness height parameters (z_{0m} , z_{0h} , d_0). Further research on the uncertainty analysis of roughness estimation at coarse scale resolutions is required to better characterise the degree of this influence.

It should be emphasized that the effect of aggregation of input forcing on the roughness height parameters (and subsequently to the evapotranspiration estimation) described here, will be general to those methods based upon the form of Monin-Obukhov Similarity theory equations as employed in SEBS. While they may also be pertinent to other flux estimation techniques involving these parameters, research by [Allen et al. \(2007b\)](#) and [Long et al. \(2011\)](#) has shown that roughness parameters play an insignificant role in METRIC and SEBAL (both are a form of energy balance approach). The main reason for this lies in the structure (formulation and parameterization) of METRIC and SEBAL, as these models use modified forms of flux-gradient functions (with simplifications and empiricism), resulting in their different response to the scaling of roughness parameters.

4.4.2 Effects of Flux Aggregation Approach

Aggregation of fluxes from fine to coarse resolutions is a common practice in regional to global climate model evaluation ([Jiménez et al. 2011b](#); [Mueller et al. 2011b](#)) and in the assessment of coarser scale flux products such as those derived from geostationary satellites ([Brunsell and Anderson 2011](#)). As such, it is important to understand how aggregated fluxes differ from the fluxes at the native resolution in terms of their statistical structure, magnitude and spatial distribution. There are a number of commonly used spatial interpolation methods that can be employed for such aggregation and it is likewise important to identify their effects on preserving the spatial characteristics of the original fine resolution fluxes. To better understand whether the choice of aggregation technique has an effect on evapotranspiration estimates, ET (or the latent heat flux, λE) was calculated using the original Landsat data at 120 m resolution and then aggregated to 960 m resolution using the simple averaging, nearest neighbour, bilinear and bicubic interpolation methods, all of which are common approaches in spatial interpolation.

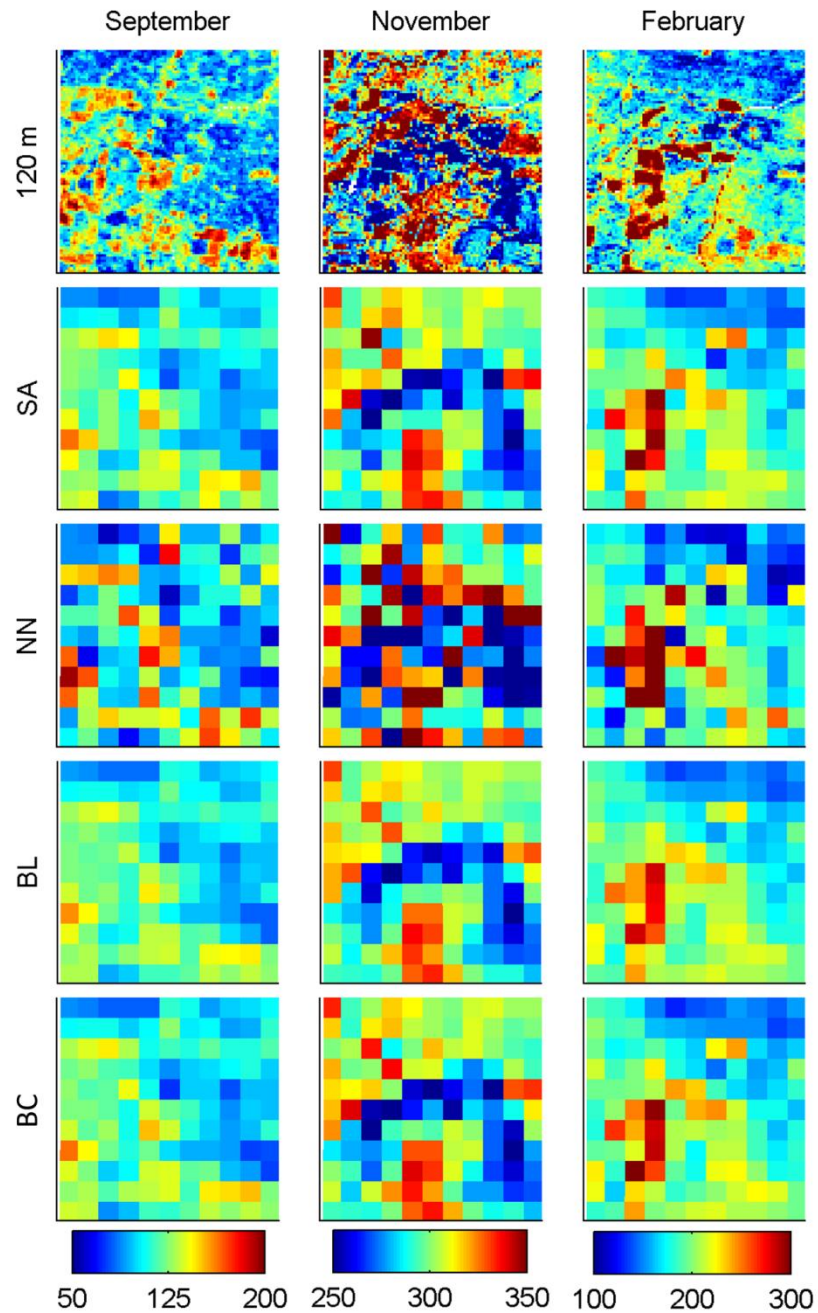


Figure 4-9: Native resolution (top) and aggregated latent heat flux (λE) from Landsat using simple averaging (SA), nearest neighbour (NN), bilinear (BL) and bicubic interpolation (BC) aggregation methods to the equivalent 960 m resolution of the MODIS sensor.

Figure 4-9 presents the response of evapotranspiration aggregation using these different techniques, showing that the spatial details present in the fine resolution evapotranspiration maps decrease dramatically by the 960 m resolution. The nearest neighbour (NN) approach causes sharp discrepancies in the flux values, while the SA, BL and BC produce a smoother transition between pixel responses. In contrast to the NN aggregation, the visual difference between SA, BL and BC is not significant, with all exhibiting similar spatial patterns. In terms of statistical metrics, all aggregation methods yield a similar image scale mean (mean of all pixels of the image) compared

to the fine resolution evapotranspiration images. However, for image scale standard deviation (as a measure of spatial variability), NN aggregated images show an improved match against their corresponding fine resolution image, which is statistically significant and in agreement with previous research results (e.g. [Sridhar et al. 2003](#); [Hong et al. 2009](#)), but is not significant from a hydrological perspective (as shown below).

In order to evaluate the uncertainties associated with flux aggregation using these different approaches, values of evapotranspiration in $\text{W}\cdot\text{m}^{-2}$ are converted to volumetric evapotranspiration, and errors due to the aggregation are calculated for each coarse resolution pixel as $ET_{960} - ET_{120}$. As can be seen in Figure 4-10, the SA approach produces no errors, but underestimation and overestimation errors in volumetric evapotranspiration are evident in NN method maps for all days. In contrast to NN, volumetric evapotranspiration errors for BL and BC are lower.

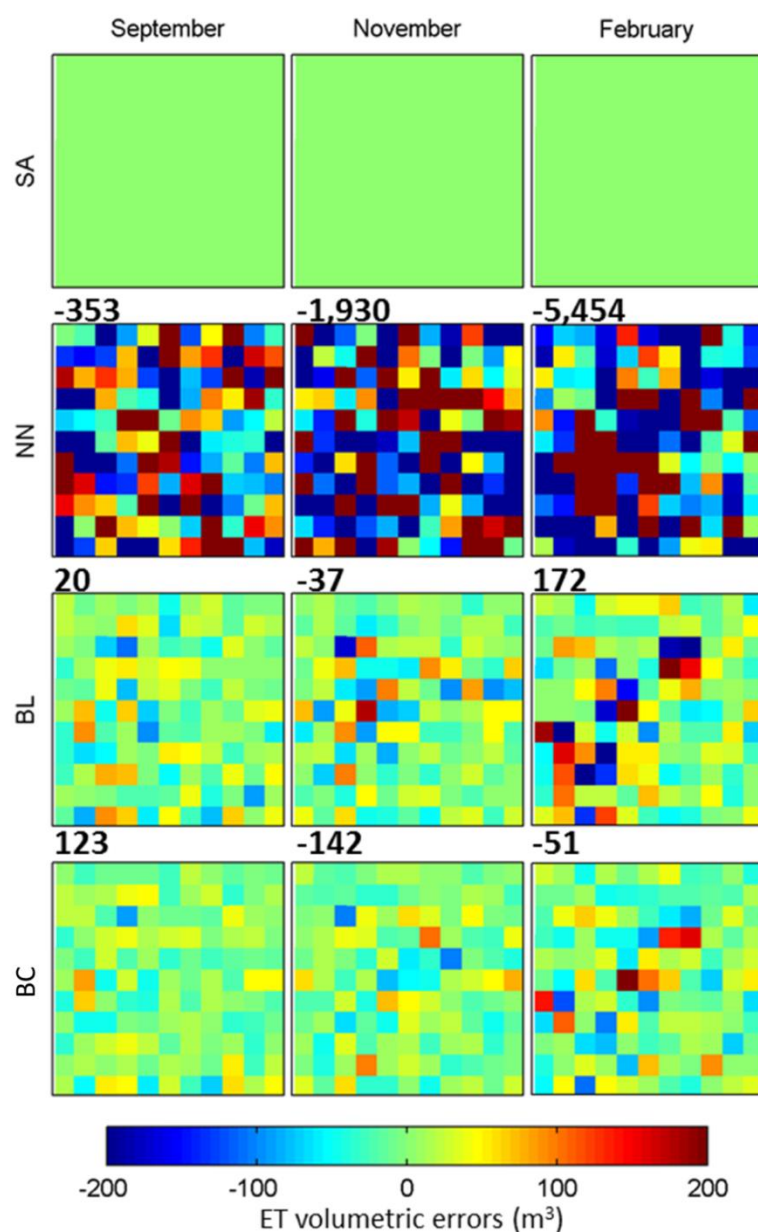


Figure 4-10: Errors in estimation of the total mass of evapotranspiration (in m^3) due to the aggregation of the latent heat flux for different spatial interpolation methods. Negative values mean aggregated pixels are less than the original fine resolution values. Numbers above the images for NN, BL and BC are spatial sum.

When undertaking regional scale analysis or water balance estimation, the pixel scale volumetric evapotranspiration errors can accumulate and potentially cause large mass imbalances in hydrologic studies. To evaluate this, total volumetric evapotranspiration errors have been calculated for the study area as shown on each image of Figure 4-10. It is clear that the SA method has the best performance in preserving the mass balance, which is in accordance with the flux conservation principles discussed by [Raupach \(1995\)](#) and [Raupach and Finnigan \(1995\)](#). According to flux conservation principle, the net scalar fluxes average linearly over the land surface. The NN method results in a significant underestimation of evapotranspiration at the image scale for all Landsat images. Although BL and BC produced lower errors than the NN approach,

they still result in an imbalance and hence are not suitable for flux aggregation. From a hydrological perspective, the simple averaging approach is the preferred technique for flux aggregation.

4.5 Summary and Conclusion

Understanding the effects of aggregation on the estimation of hydrological variables is of considerable importance, especially in relation to the accurate retrieval of land surface fluxes from remote sensing observations. The availability of remote sensing images from fortnightly to sub-daily temporal resolutions and from meters to kilometre spatial resolutions provides a great opportunity for operational assessment and management of water resources. As fine resolution imagery has shorter temporal resolutions (e.g. fortnightly) and often limited availability due to atmospheric influences, coarser resolution images from MODIS type sensors provide greater utility to the water resources community. Therefore, it is crucial to understand the implications of coarse resolution retrieval of heat fluxes relative to higher resolution responses.

To examine the influences of spatial scale on remotely sensed land surface heat flux estimation, an evaluation of the aggregation effects on a temporal sequence of high resolution Landsat 5 TM images was performed. The scaling effect on simulations was examined by a) aggregating the key input forcing of surface temperature and vegetation, and b) assessing the influence of the flux aggregation approach on flux retrieval. It was determined that the influence of input forcing aggregation resulted in the underestimation of evapotranspiration at the satellite image scale, with up to 15% lower retrievals than occurred at the original high resolution Landsat image. It was reasoned that the most likely explanation for this response was an increase in the aerodynamic resistance, originating from a change in the roughness height estimation across aggregated resolutions. However, comparison with similar studies suggested that the significance of input aggregation on roughness parameterization (and subsequently on evapotranspiration estimation) may be specific to the SEBS model. Further work examining other model structures and types is clearly required, given the influence of these parameterizations shown here. Results also show that in aggregating fine resolution fluxes to coarser scales, a simple averaging scheme outperforms other common approaches by preserving both the spatial distribution of evapotranspiration and the magnitude of volumetric evapotranspiration at the pixel and image scales. In contrast, a nearest neighbour method for flux aggregation can cause large errors.

While this study was limited to the spatial resolution of MODIS thermal data, coarser resolution (but high temporal response) geostationary satellite data could also be investigated, and the study area expanded to include basin and regional scale responses. Such an analysis would provide a more comprehensive spatio-temporal scaling scheme for heat flux simulations than that undertaken here (although it should be noted that this study is one of a few that attempts to examine the temporal scaling response by including multiple Landsat images across a changing land surface condition). Another issue that requires further consideration, relate to the effects of

aggregation on the estimation of vegetation structure parameters (e.g. leaf area index) and subsequently on roughness parameterization (e.g. z_{0m} , z_{0h}). Aggregation of such data could have considerable impact on the so-called $T_s - VI$ family of evapotranspiration models (Carlson 2007; Petropoulos et al. 2009; Long et al. 2011). Spatial scaling has the capacity to alter the geometry of the scatterplot space between the land surface temperature and vegetation indices, which would affect the geometry of dry and wet edges and consequently the resulting evapotranspiration. Likewise, by expanding this analysis to encompass a greater range of surface types, conditions and resolutions, a generalization of the results from this study to other hydrometeorological conditions and ecosystems may be made.

Acknowledgement

Funding of this research is provided jointly by an Australian Research Council (ARC) Linkage project (LP0989441) and scholarship support for Ali Ershadi from the National Centre for Groundwater Research and Training (NCGRT) in Australia. Authors appreciate free access to Landsat and MODIS images used in this research from the USGS (through EarthExplorer – earthexplorer.usgs.gov) and NASA (through LAADS-Web – ladsweb.nascom.nasa.gov). Mr Robert Pipunic from the University of Melbourne is thanked for providing the required meteorological data used in this study.

Chapter 5

A Bayesian Uncertainty Analysis of Heat Flux Estimation

The original research described in this Chapter has been published as:

Ershadi, A., McCabe, M. F., Evans, J.P., Mariethoz, G., Kavetski, D. (2013) '[A Bayesian analysis of sensible heat flux estimation: quantifying uncertainty in meteorological forcing to improve model prediction](http://dx.doi.org/10.1002/wrcr.20231)', *Water Resources Research*, 49(5), 2343-2358, <http://dx.doi.org/10.1002/wrcr.20231>

Reprinted with permission from American Geophysical Union

Reprinted with altered style and minor modifications

5 A Bayesian Uncertainty Analysis of Heat Flux Estimation

Abstract

The influence of uncertainty in land surface temperature, air temperature and wind speed on the estimation of sensible heat flux is analysed using a Bayesian inference technique applied to the Surface Energy Balance System (SEBS) model. The Bayesian approach allows for an explicit quantification of the uncertainties in input variables: a source of error generally ignored in surface heat flux estimation. An application using field measurements from the Soil Moisture Experiment 2002 (SMEX02) is presented. The spatial variability of selected input meteorological variables in a multi-tower site is used to formulate the prior estimates for the sampling uncertainties and the likelihood function is formulated assuming Gaussian errors in the SEBS model. Land surface temperature, air temperature and wind speed were estimated by sampling their posterior distribution using a Markov chain Monte Carlo (MCMC) algorithm. Results verify that Bayesian inferred air temperature and wind speed were generally consistent with those observed at the towers, suggesting that local observations of these variables were spatially representative. Uncertainties in the land surface temperature appear to have the strongest effect on the estimated sensible heat flux, with Bayesian inferred values differing by up to ± 5 °C from the observed data. These differences suggest that the footprint of the in-situ measured land surface temperature is not representative of the larger scale variability. As such, these measurements should be used with caution in the calculation of surface heat fluxes and highlight the importance of capturing the spatial variability in the land surface temperature: particularly for remote sensing retrieval algorithms that use this variable for flux estimation.

Keywords: evapotranspiration; Surface Energy Balance System; Bayesian inference; SMEX02; land surface temperature; surface heat flux

5.1 Introduction

Evapotranspiration (ET) is a major component of the hydrological cycle (Brutsaert 2005) and can account for more than 90% of the precipitation in semi-arid and arid regions (Wang et al. 2012b). Accurate estimation of evapotranspiration is required to better constrain and understand hydrometeorological behaviour across a range of systems and scales: locally, regionally and globally. ET is usually represented as the latent heat flux (λE) from the land surface to some level in the overlaying atmosphere. Although there are a number of techniques available to estimate the land surface fluxes of heat and water (Kalma et al. 2008; Wang and Dickinson 2012), a common approach is via evaluation of the energy balance at the surface. In models using this approach, ET (or latent heat flux, λE) is usually derived as the residual term of the energy budget, i.e. $\lambda E = R_n - G_0 - H$, where R_n is the net radiation, G_0 is the ground heat flux and H is the sensible heat flux. In such instances, it is the calculation of H that is of key importance in the estimation of ET. One example from this family of models is the Surface Energy Balance System (SEBS) model (Su 2002), an energy balance method

that is widely used to estimate actual ET via a combination of remote sensing and in-situ meteorological observations (Su et al. 2005; McCabe and Wood 2006).

Model simplifications, natural variability in system response, and issues of measurement or sampling errors in the input forcing cause mismatches between the modelled and observed responses, both in physically-based (e.g. SEBS) and empirical models (Samanta et al. 2007; Kalma et al. 2008). Probabilistic (stochastic) modelling methodologies are hence of particular interest, because they allow an explicit examination of data and modeling uncertainties using probability distributions (Kavetski et al. 2006a; Luo et al. 2007) or empirical ensembles (Pan et al. 2008; Peters-Lidard et al. 2011). Probabilistic approaches have been used previously in groundwater models (Dagan 1985), conceptual rainfall-runoff models (Kuczera et al. 2006) and integrated water resources systems (Castelletti and Soncini-Sessa 2007). However, there are limited cases detailing the use of probabilistic frameworks in heat flux modeling. In a recent contribution, van der Tol et al. (2009) developed a Bayesian approach for the estimation of heat fluxes over vegetated land surfaces and showed that the integration of different prior information within a land surface modeling scheme improved the estimation of model parameters. Samanta et al. (2007) and Li et al. (2010b) used a Bayesian approach to fit the Penman-Monteith model to half-hourly transpiration rates for a sugar maple stand in different regions, finding considerable uncertainties in predicted transpiration. In general, the non-linearity of the model equations, process complexity and the difficulties in specifying realistic uncertainty models represent challenging research problems for developing and applying probabilistic techniques in heat flux models.

In energy balance methods (including SEBS), the estimation of the sensible heat flux presents greater difficulties than the estimation of the available energy flux (i.e. $R_n - G_0$). The sensible heat flux H is the transfer of heat from the land surface to the atmosphere, represented conceptually as a temperature gradient, $H \approx (T_s - T_a)/r_a$, where T_s is the land surface temperature, T_a is the air temperature and r_a is the aerodynamic resistance to heat transfer. Note that r_a is itself a function of the wind speed u_a and of the aerodynamic roughness of the land surface. Given this expression, the main uncertainties in the estimation of the sensible heat flux in SEBS arise due to uncertainties in the input meteorological variables (T_s , T_a , u_a) and in the aerodynamic roughness parameterization.

Timmermans et al. (2011) found that uncertainties in the estimation of H via SEBS were likely due to the incorrect parameterization of the roughness height for heat. On the other hand, van der Kwast et al. (2009) found that SEBS is more sensitive to the surface temperature errors than to the surface aerodynamic parameters. In another study, Gibson et al. (2011) found that SEBS is sensitive to T_s and T_a , depending on the land cover and wet limit criteria. As can be seen, identifying the true nature of the uncertainties resulting from these input variables remains a challenging and unresolved task.

The aim of this chapter is to provide insights into the spatial representativeness of the key input meteorological variables by quantifying the uncertainties in their actual measurements. More specifically, our research questions are: a) which meteorological

forcing set (land surface temperature, air temperature or wind speed) has the greatest influence on the uncertainty in sensible heat flux values estimated using the SEBS model? and b) what are the likely reasons for such uncertainties?

These questions are investigated using a Bayesian inference technique, where uncertainties in the observed input and response data are represented using probability distribution functions (PDFs) and the SEBS model is used to describe the physics of the sensible heat flux process. Inferred values of the input variables are then used to quantitatively estimate the errors in their measurements. The likely causes of these uncertainties are then discussed. One of the major differences between the current study and previous investigations is the use of Bayesian uncertainty analysis instead of a sensitivity analysis to quantify the errors in sensible heat flux estimation. Moreover, instead of associating all uncertainties to the parameterization of the models (Samanta et al. 2007; Samanta et al. 2008; van der Tol et al. 2009), this chapter examines the uncertainties inherent within the input variables used in heat flux estimation.

5.2 Field Measurements and Site Description

This investigation is based on data from the Walnut Creek (WC) watershed, centred at 41.96° N, 93.6° W and located near Ames, Iowa in the USA. Meteorological and flux data for the study area were measured across 12 eddy covariance towers, collected as part of the Soil Moisture-Atmospheric Coupling Experiment (SMACEX) and the Soil Moisture Experiment 2002 (SMEX02) campaigns (Kustas et al. 2005; Prueger et al. 2009) during June and July 2002. The locations of the towers within and around the study area are shown in Figure 5-1.

The land cover of the region is comprised primarily of either corn (*Zea Mays L.*) or soybean (*Glycine Max L. Merr.*). Nearly 95% of the region and watershed is used for row crop agriculture, with 80% of that being corn and soybean in equal proportions. The climate is humid, with an average annual rainfall of 835 mm/year. The topography is characterized by low relief and poor surface drainage. Dominant soil types of the study area are clay and silty clay loams, with generally low permeability (Hatfield et al. 1999).

Meteorological data along with surface heat flux and vegetation measurements are available for 20 days from June 20 to July 9, 2002 (day-of-year 171-190). During this time period, the vegetation grew rapidly and surface soil moisture changed from dry to wet due to rainfall events in early July. The eddy covariance flux towers provided measurements of the friction velocity (u_*), sensible heat flux (H) and latent heat flux (λE). Air temperature and humidity were measured using Vaisala HMP-45C instruments and sonic temperature and wind speed fluctuations were measured using Campbell Scientific CSAT3 sonic anemometers. Radiometric temperatures were measured using Apogee thermal-infrared radiometers (model IRTS-P) with a nominal 60° field of view. The Apogee sensor height is kept at 2.5 m above soybean and 5 m above corn canopies in all corresponding towers. The effective canopy level footprint area for the land surface temperature sensor was approximately 7 m² for soybean towers and 26 m² for corn towers. All data for rain periods are removed from the

analysis, as the CSAT sonic instrument does not provide reliable results during such conditions. In addition, sporadic spikes and values with invalid range are removed. During the field campaign, the vegetation height (h_c), leaf area index (LAI) and fractional vegetation cover (f_c) varied with crop growth stage (Anderson et al. 2004a), with ranges shown in Table 5-1.

Table 5-1: Range of vegetation height (h_c), leaf area index (LAI) and fractional vegetation cover (f_c) during the study period.

Crop	h_c (m)	LAI ($m^2 \cdot m^{-2}$)	f_c
Soybean	0.2-0.6	0.4-3.7	0.2-0.9
Corn	0.7-2.2	1.1-5.6	0.5-1.0

Meteorological and heat flux data are averaged to 30 minutes. The measured sensible heat flux data are used without any closure correction. All records are filtered for rain events and limited to the daytime period from 07:30 AM to 18:00 PM local time. More detailed site information and a description of the experiments can be found in Kustas et al. (2005) and Prueger et al. (2005).

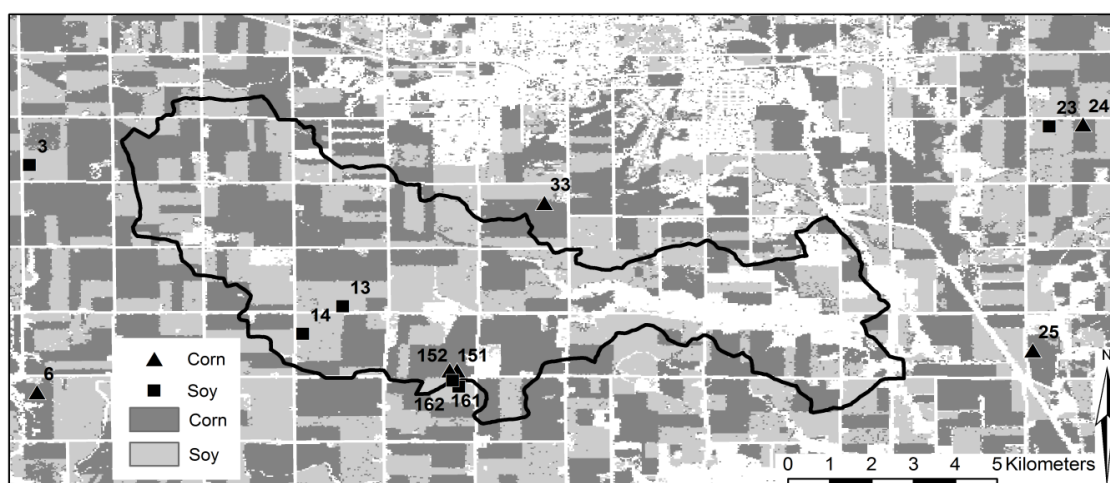


Figure 5-1: Walnut Creek Basin (thick black line) and location of soybean and corn towers. The land use map of the region is shown in the background.

5.3 Modeling Approach

5.3.1 Surface Energy Balance System (SEBS)

SEBS (Su 2002) is a physically based modeling approach that uses a combination of remote sensing and in-situ observations to derive the land surface variables, radiative heat fluxes and roughness parameters required for the calculation of turbulent heat fluxes at the land surface (see section 2.2.2.1). The main inputs to the SEBS model

include land surface temperature, vegetation height and density, air temperature, humidity and wind speed, along with surface radiation components. The key aspect of SEBS is its robust formulation for the estimation of the sensible heat flux using either the Monin-Obukhov Similarity Theory (MOST) equations (Monin and Obukhov 1945) for the atmospheric surface layer, or the Bulk Atmospheric Similarity Theory (BAST) (Brutsaert 1999) for the mixed layer of the atmospheric boundary layer. In the majority of cases, the MOST equations are used unless the roughness of the surface is high or the atmospheric surface layer height is low. The MOST equations used in SEBS include stability-dependent flux-gradient functions for momentum and heat transfer (equations 2-1 to 2-3) to estimate the sensible heat flux (H).

After the estimation of H , SEBS uses a scaling method to scale the derived H between hypothetical dry and wet limits based on the relative evaporation concept. Finally, this scaled H can be used to calculate the latent heat flux λE as a residual term in the general energy balance equation, i.e. as $\lambda E = R_n - G_0 - H$. Figure 4-3 provides a schematic representation of the model as employed in this application (see Su (2002) for further details on the model description and formulation).

5.3.2 The Bayesian Inference Technique

In standard deterministic applications of the SEBS model, all input variables are fixed and constant at each simulation time step. In contrast, in a stochastic application, inputs and response variables can be considered as probability distributions or empirical ensembles of values, the envelope of which represents the range of plausible values. This allows for an accounting of uncertainties such as input variations across a heterogeneous site.

For stochastic application of the SEBS model in this study, a Bayesian inference technique (BIT) is developed and linked with the SEBS model. The approach is partially analogous to the Bayesian total error analysis (BATEA) model (Kavetski et al. 2003; Kavetski et al. 2006a) and focuses on the uncertainty in the SEBS input forcings. In the terminology and notation adopted here, observed variables are indicated with a tilde (\sim), while their posterior estimates are indicated with a hat ($\hat{}$).

Let us assume a deterministic model $h(x)$ that maps the forcing x into the response y ,

$$y \leftarrow h(x, \beta) \tag{5-1}$$

where β is the vector of model parameters which, in this study, is kept fixed at pre-estimated values, including the roughness height parameters (d_0, z_{0m}, z_{0h}). In this study, these parameters are pre-estimated deterministically using the Su et al. (2001) model for each half-hourly time step at each tower.

Following Kavetski et al. (2003), the observed input data \tilde{x} is assumed to be corrupted by errors (e.g. due to measurement and sampling). A prior distribution of the true inputs, denoted by x , is constructed as follows,

$$x \leftarrow p(x|\tilde{x}, \omega_x) \tag{5-2}$$

where ω_x are parameters of the input error model x .

The observed response data \tilde{y} is also assumed to be corrupted by errors,

$$\tilde{y} \leftarrow p(\tilde{y}|y, \omega_y) \quad 5-3$$

where \tilde{y} is the observed response (e.g. sensible heat flux) and $p(\tilde{y}|y, \omega_y)$ describes the response errors given the true response y and response error parameters ω_y .

In the hierarchical Bayesian framework detailed above, x are “latent variables” and correspond to estimates of the true inputs; they are not directly observed but are rather inferred as part of the BIT-SEBS procedure. The error model parameters ω_x and ω_y describe the statistical properties (e.g. mean and variance) of input and response variables, respectively (Renard et al. 2011). In this application, the values of ω_x and ω_y are estimated and fixed prior to the BIT-SEBS inference using a separate data analysis procedure detailed later in this section.

In this study, the key objective of the BIT-SEBS scheme is to estimate x given the observed meteorological forcing \tilde{x} and the observed response \tilde{y} using prior information on the magnitude and distribution of the data errors (specified using ω_x and ω_y). The Bayesian posterior for this quantity, conditioned on the observed data, is as follows:

$$p(x|\tilde{x}, \tilde{y}, \beta, \omega_x, \omega_y) = \frac{p(\tilde{y}|x, \beta, \omega_y) p(x|\tilde{x}, \omega_x)}{p(\tilde{x}, \tilde{y}, \beta, \omega_x, \omega_y)} \quad 5-4$$

where the likelihood function $p(\tilde{y}|x, \beta, \omega_y)$ represents the probability of observing the data \tilde{y} given the “estimated” true inputs x , the model parameters β , the response error parameter ω_y and the deterministic model hypothesis (SEBS).

Since the denominator $p(\tilde{x}, \tilde{y}, \beta, \omega_x, \omega_y)$ is a normalization factor independent of x , the following expression of proportionality can be used:

$$p(x|\tilde{x}, \tilde{y}, \beta, \omega_x, \omega_y) \propto p(\tilde{y}|x, \beta, \omega_y) p(x|\tilde{x}, \omega_x) \quad 5-5$$

The input error model $p(x|\tilde{x}, \omega_x)$ reflects any independent estimates of x , e.g. based on observed input data \tilde{x} , available prior to the analysis of the observed response data \tilde{y} (hence it is also independent from the model parameters β). In physically based models such as SEBS, input variables are often measurable and have physical meaning and valid ranges that can be used to formulate informative priors based on independent data analysis. In this study, we represent our prior knowledge of x as follows,

$$p(x|\tilde{x}, \omega_x) = N(x|\tilde{x}, \sigma_x^2) \quad 5-6$$

where $N(z|\mu, \sigma^2)$ denotes the Gaussian PDF of a random variable z with mean μ and standard deviation σ .

In equation 5-6, we set the prior mean of x to \tilde{x} , which is equivalent to ignoring systematic errors in the observations. The prior standard deviation σ_x is specified by analyzing the spatial variability of the observed forcing field, thus corresponding to sampling uncertainty. This variability can be expressed as an absolute quantity, or as a fraction of \tilde{x} , or as a range based on expert knowledge of the input uncertainty.

In the context of the inference equation 5-4, which is conditioned on the observed response data \tilde{y} , the error model in equation 5-6 plays the role of a prior on x before \tilde{y} is analyzed. Note that formulating the input error model as $p(x|\tilde{x}, \omega_x)$, rather than $p(\tilde{x}|x, \omega_x)$, corresponds to using Bayes identity $p(x|\tilde{x}, \omega_x) = p(\tilde{x}|x, \omega_x) p(x)$ in combination with a non-informative prior $p(x) \propto \text{const}$. It is also possible to use additional information, such as the average climatology, to define an informative prior $p(x)$ (Huard and Mailhot 2006).

The likelihood function is formulated by assuming that the differences between the observed responses and the SEBS predictions (i.e. the residual errors) are approximately Gaussian,

$$p(\tilde{y}|x, \beta, \omega_y) = N(h(x, \beta)|\tilde{y}, \sigma_y^2) \quad 5-7$$

where $h(x, \beta)$ is the SEBS response produced using the input x and the SEBS parameters β , \tilde{y} is the observed response variable and σ_y is the standard deviation of the errors in the response variable (which may include errors in the response data and in the model structure).

5.3.3 MCMC Sampling of the BIT-SEBS Posterior Distribution

The posterior distribution $p(x|\tilde{x}, \tilde{y}, \omega_x, \omega_y)$ can be approximated using a Monte Carlo or Markov Chain Monte Carlo (MCMC) sampling scheme. Due to the high dimensionality of the posterior PDF in this work, the Slice Sampling MCMC method of Neal (2003) is used. This method uses the prior as a proposal distribution and avoids requiring the user to specify a high-dimensional proposal distribution (Noh et al. 2010).

A flowchart of the computational algorithm is shown in Figure 5-2. At each step of the MCMC simulation, the slice sampling algorithm draws a candidate value x from the prior distribution (equation 5-6), runs the SEBS model with the candidate inputs x , and evaluates the likelihood function (equation 5-7). This procedure is then repeated until the MCMC iterations converge. Other Monte Carlo methods for sampling from the posterior include standard Metropolis methods (Kavetski et al. 2006b, a), which in some cases can be adapted to exploit the time dependence of the model (Kuczera et al. 2010). To ensure that the MCMC algorithm explored all parts of the prior distributions, convergence diagnostics are applied as detailed in section 5.4.1.

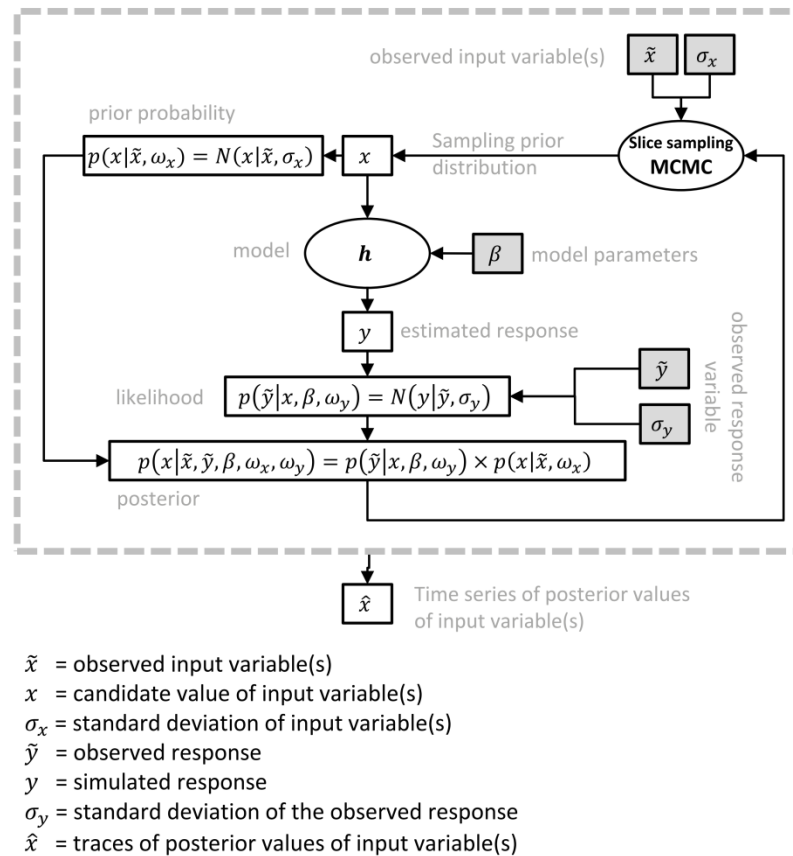


Figure 5-2: Computational flowchart of the Bayesian inference procedure in BIT-SEBS using the slice sampling MCMC. Input data and parameters are highlighted in grey squares.

5.3.4 BIT-SEBS Methodology for Analysing SMEX02 Tower Data

5.3.4.1 Prior Uncertainty Analysis of Input Variables

The “uncertain” input meteorological variables of the SEBS model used in this study include the air temperature (T_a), land surface temperature (T_s) and wind speed (u_a). For each of the uncertain input meteorological variables, a Gaussian prior PDF is specified, with a mean equal to the measured value and a standard deviation σ_x proportional to the spatial variability of the observed values. Hence, for each time step, the standard deviations of T_s , T_a and u_a are calculated as the standard deviation of observations across all 12 towers within the study area. In the case of wind speed, the Gaussian prior distribution was truncated at zero to avoid negative wind speeds being sampled when the observed values are small relative to their potential variability.

Other input variables (e.g. humidity) are assumed constant and equal to the observed value in the tower. SEBS model parameters (d_0 , z_{0m} , z_{0h}) are also calculated deterministically for each time step at each tower using the corresponding measured vegetation height and density and meteorological variables. Due to careful in-situ observations of the vegetation parameters at each tower (Anderson 2003; Kustas et al.

2005), the dynamics in aerodynamic roughness of the surface are preserved, and uncertainties in parameterization of the roughness height are expected to be reduced.

Figure 5-3 presents measured values of precipitation, land surface temperature, air temperature and wind speed during the study period across all towers. A rain event on day-of-year 172 was followed by a 12-day dry period, causing the soil moisture to decrease from field capacity to relatively dry conditions. Subsequently, some rain events during day-of-year 185 to 188 increased the soil moisture. Figure 5-3 shows that relative to the corn towers, soybean towers measure higher land surface temperature, air temperature and wind speeds.

As described in section 5.3.2, the Bayesian inference for each of the meteorological variables (T_s , T_a , u_a) requires the construction of a prior for each variable, at each time step and for each tower. Here, each meteorological variable at each simulation time step at each of the 12 towers is given its own Gaussian prior PDF, with mean given by the observed value at tower x , at time t , and a standard deviation estimated from the range of observed values within each of the 12 towers at time t . As the eddy covariance towers within the SMEX02 domain provide a reasonable coverage of the study area (see Figure 5-1), the range of the observed meteorological values across these towers is assumed to be indicative of the spatial variability.

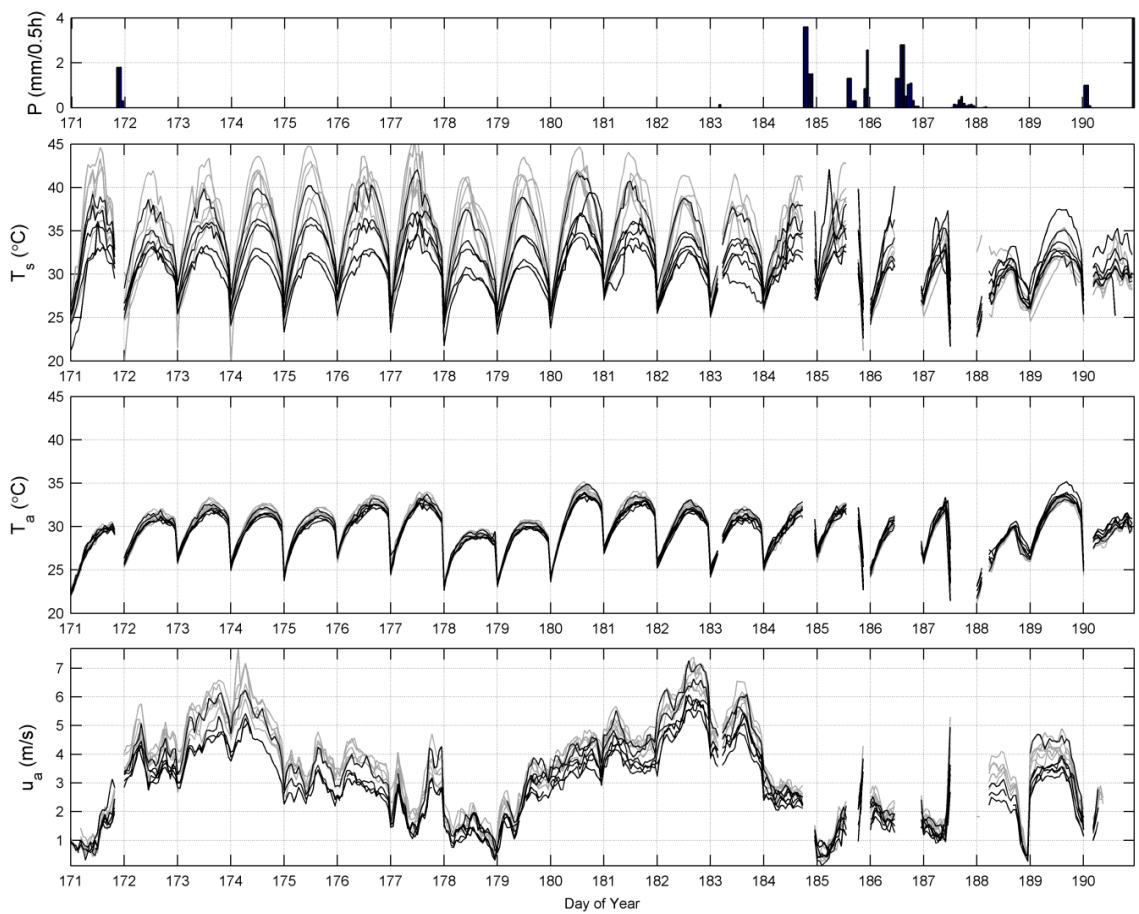


Figure 5-3: Time series of the land surface temperature T_s , air temperature T_a and wind speed u_a for all 12 towers (6 over soybean and 6 over corn) of the SMEX02 campaign during the daytime. Grey lines represent soybean towers and black lines the corn towers. The tower averaged precipitation is shown in the upper panel. Gaps in the data record reflect the removal of rain periods from the analysis, given the influence that these have on flux observations.

Based on the values of all towers, the standard deviations σ for each time step are calculated for T_s , T_a and u_a and shown in Figure 5-4. As σ_{T_s} have larger values than σ_{T_a} and σ_{u_a} , its priors are wider. The width of the prior controls the uncertainty bound of each input variable and hence directly affects the inference (see section 5.4.2).

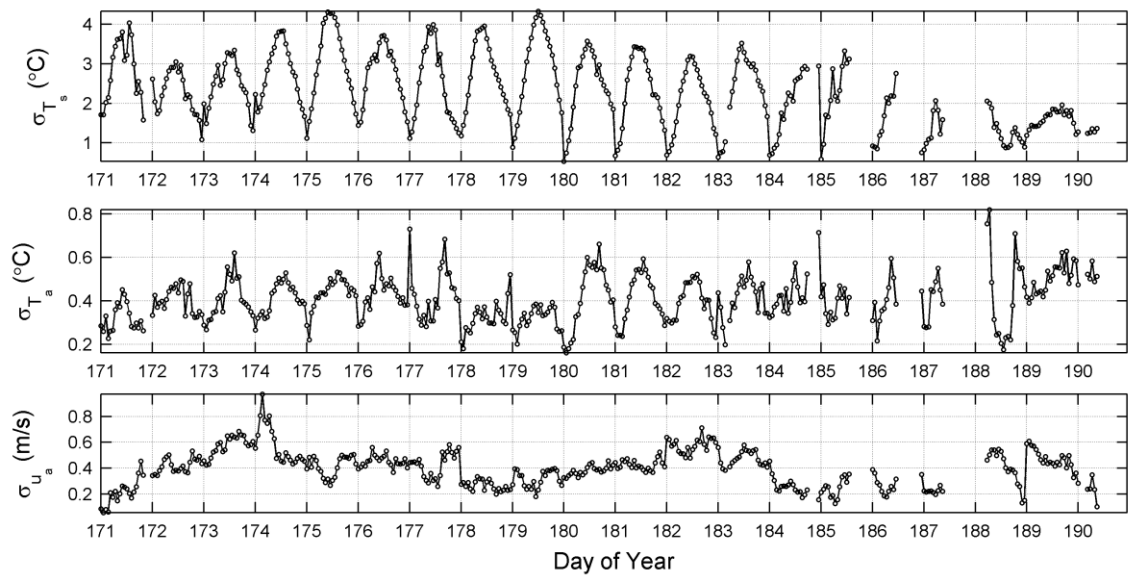


Figure 5-4: Time series of the standard deviation (σ) for T_s (°C), T_a (°C) and u_a ($\text{m}\cdot\text{s}^{-1}$) derived from all of the SMEX02 towers at each time step during daytime.

To appraise the assumption of Gaussian priors, Figure 5-5 shows quantile-quantile (QQ) plots of the tower data used to construct the priors (results for two representative time steps are shown). Land surface and air temperatures appear reasonably Gaussian, while the wind speed distributions exhibit heavier tails, representing a limitation of the Gaussian assumption.

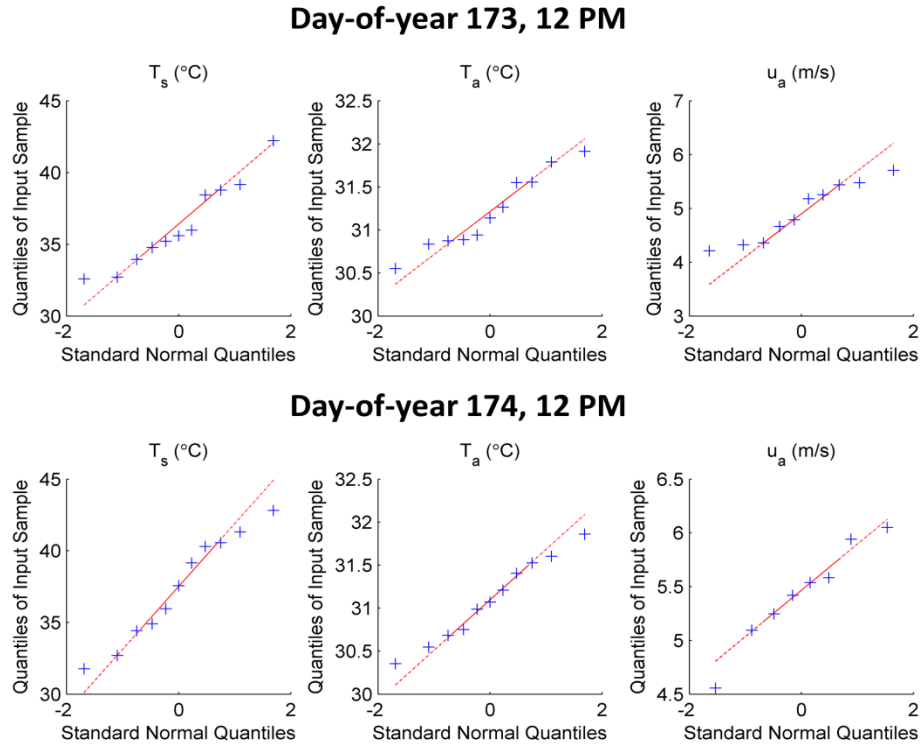


Figure 5-5: Quantile-Quantile (QQ) plots of the land surface temperature T_s , air temperature T_a and wind speed u_a for all towers at 12:00 PM (local time) on day-of-year 173 and 174.

5.3.4.2 Prior Uncertainty Analysis of Response Variable

The response variable in this Bayesian investigation is the sensible heat flux observed at each of the eddy covariance towers. A number of recent studies (e.g. [Hollinger and Richardson 2005](#); [Meyers and Baldocchi 2005](#); [Foken 2008](#); [Mauder et al. 2008](#); [Foken et al. 2012](#); [Richardson et al. 2012](#)) have highlighted the uncertainties in eddy covariance estimations of turbulent heat fluxes. In addition to standard data quality controls (e.g. coordinate rotation, density correction) that need to be performed on the high-frequency eddy covariance measurements, there are issues related to inadequacy of fetch, heterogeneity of the footprint, improper averaging times and non-capture of large eddies that add to the uncertainties in the eddy covariance estimates ([Allen et al. 2011a](#)).

To include the uncertainties of sensible heat flux observations in the Bayesian inference of the input variables, prior PDFs of H are developed, with the observed sensible heat flux H_o considered as the mean of the prior PDF. The standard deviation of the PDF, σ_H , is expressed as a fraction r of the observed sensible heat flux, $\sigma_H = r \times H_o$. The choice of σ_H has a direct influence on the inference of the input variables. Smaller values of σ_H (e.g. with $r = 0.05$) correspond to a lower uncertainty in the observations of the sensible heat flux, which causes larger deviations of the inferred values of input forcing from their observed values. In contrast, larger values of

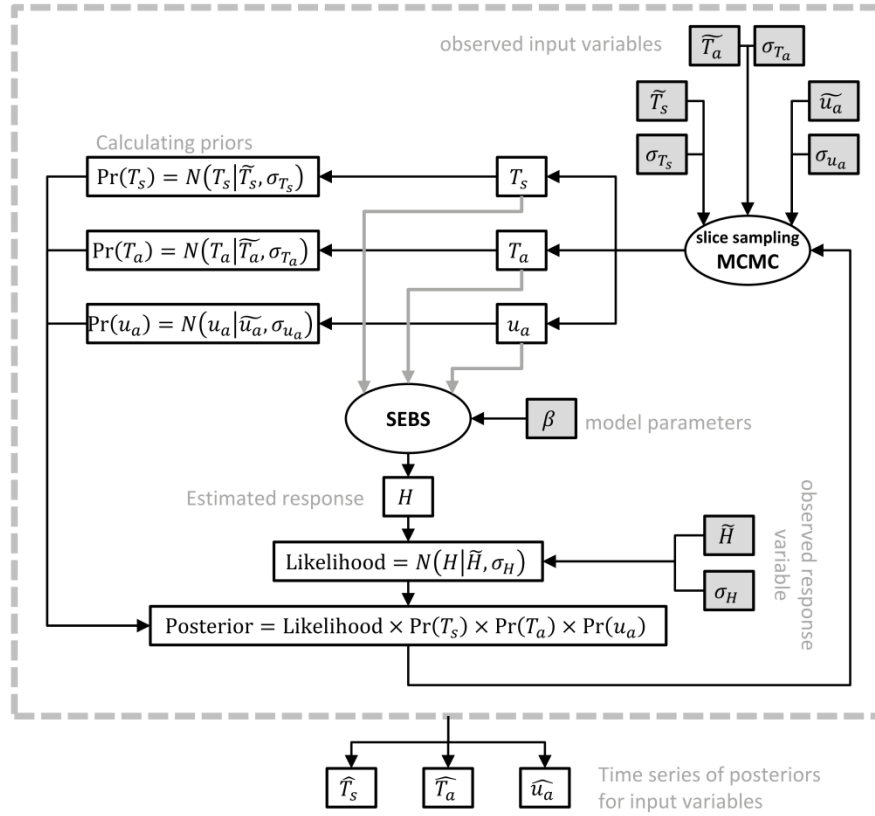
σ_H (e.g. with $r = 0.15$) correspond to higher uncertainty in the observations of the sensible heat flux and cause smaller deviations of the inferred input values.

Determination of the best (or optimum) value of r is not possible, as the uncertainty in sensible heat flux observations is poorly described. Also, the spatial variability of H cannot be used to develop PDFs of H due to the difference in the extent and heterogeneity of the footprints amongst towers. [Allen et al. \(2011a\)](#) identified that the errors in the estimation of the latent heat flux using eddy covariance systems for a well maintained site, in terms of standard deviation from the mean, are in the range of 10-15%. Based on these measures, we estimate that the standard deviation for sensible heat flux is around 10% of the measured value (i.e. $r = 0.1$), as sensible heat flux estimations are often more reliable than latent heat flux estimations in eddy covariance towers ([Foken 2008](#); [Mauder et al. 2008](#); [Richardson et al. 2012](#)).

To evaluate the sensitivity of the inference to the value of r , we examined three cases: $r = 0.05$, $r = 0.10$ and $r = 0.15$. The sensitivity analysis was based on the residuals Δ of the inferred and observed values, computed as $\Delta_x = X_i - X_o$, where X can be T_s , T_a , or u_a and subscripts i and o refer to inferred and observed values respectively. Results showed that in all three cases of r , the relative variation in the range and magnitude of ΔT_s , ΔT_a and Δu_a were similar (i.e. ΔT_s is an order of magnitude higher than ΔT_a and Δu_a - see Appendix C). Consequently, variation of r amongst selected values has no significant influence in identifying the most uncertain variable. Therefore, $r = 0.1$ is adopted in the computation of results in the following sections.

5.3.4.3 Posteriors Estimation and Inference using BIT-SEBS

Figure 5-6 shows the overall procedure in estimation of the posterior values of the input variables. For each time step and at each tower, prior analysis of data uncertainty was carried out as described above. MCMC simulations were then performed using the Slice Sampling method (section 5.3.2). The results of the Bayesian simulations can then be represented as time series of the posterior values for T_s , T_a and u_a for each tower record. Following an MCMC convergence assessment, the time series of posterior estimates of input variables were then used as estimates of the meteorological input variables (section 5.4.2) and also to provide insights into their uncertainties (section 5.4.3).



- \tilde{x} = observed input variable ($\tilde{T}_s, \tilde{T}_a, \tilde{u}_a$)
- x = candidate value of input variable (T_s, T_a, u_a)
- σ_x = standard deviation of input variable ($\sigma_{T_s}, \sigma_{T_a}, \sigma_{u_a}$)
- \tilde{H} = observed response
- H = simulated response in the BIT-SEBS
- σ_H = standard deviation of the observed response
- \hat{x} = traces of posterior values of input variable ($\hat{T}_s, \hat{T}_a, \hat{u}_a$)

Figure 5-6: The overall procedure used in BIT-SEBS to estimate input meteorological variables. Input data and parameters are shown in grey squares. The procedure is applied at each time step of each tower.

5.4 Results

5.4.1 Convergence Analysis of the MCMC Iterations

A convergence study of the MCMC samples was undertaken as follows. The number of iterations necessary for MCMC chain convergence was estimated visually by plotting traces of the MCMC samples against the number of iterations for all chains (Kass et al. 1998). Figure 5-7 shows the MCMC chain traces and their cumulative mean for 3,000 samples (iterations), with a thinning factor of 10 and a burn-in period of 1,000 samples for the 12:00 PM time stamp of tower WC162 (soybean) for day-of-year 173. Here, a thinning factor of 10 means that a total of 30,000 samples were generated, but only every 10th sample was retained (this reduces the effects of serial correlation of the MCMC samples). A burn-in period of 1,000 samples means that the first 1,000 samples were discarded. From Figure 5-7 it can be seen that the cumulative means of the

posterior traces are stationary after approximately 1,000 iterations, suggesting adequate convergence of the MCMC samples.

For quantitative evaluation of the MCMC convergence and assessment of the adequacy of the chain numbers, the potential scale reduction factor $\sqrt{\hat{R}}$ of Gelman and Rubin (1992) is used. As recommended by Brooks and Gelman (1998), the criterion for acceptance of the Bayesian modeling is that $\sqrt{\hat{R}} < 1.2$. Any MCMC chain that did not meet this criterion was rejected and was not considered in the inference.

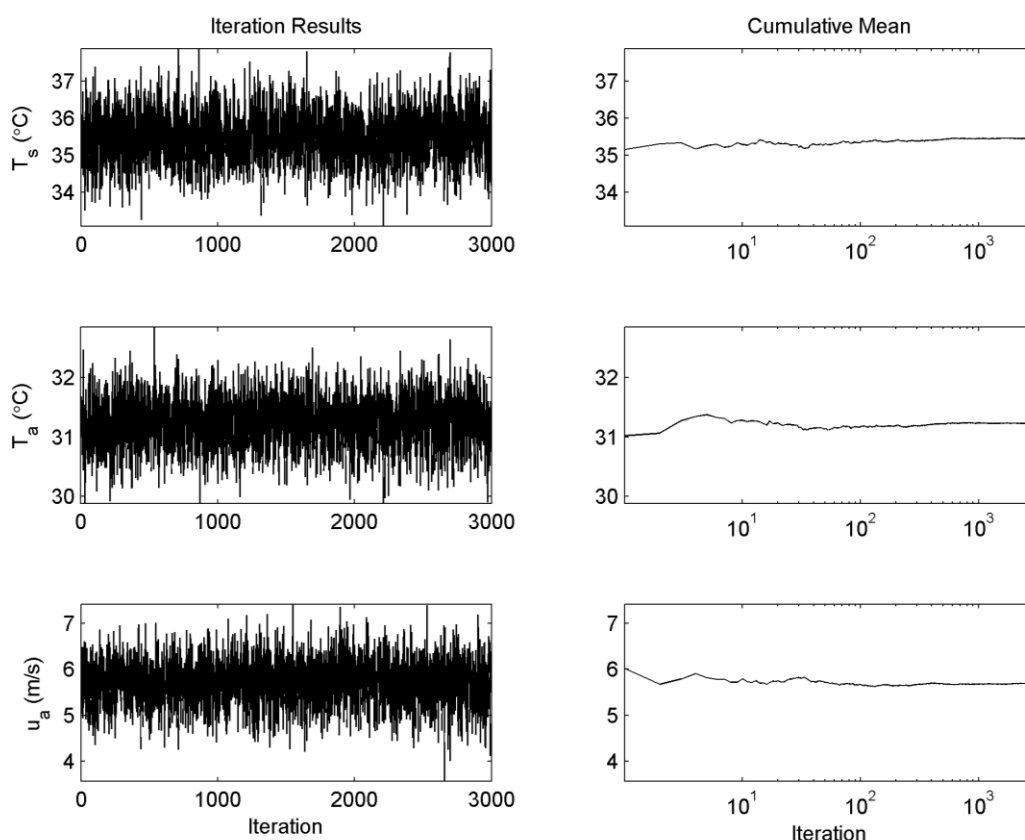


Figure 5-7: Traces of the posterior input meteorological variables in the Markov chain traces (left) and their corresponding cumulative mean (right; with x-axis in logarithmic scale). Results represent a single 12:00 PM time stamp for day-of-year 173 at tower WC162 (soybean). The means of all variables appear stationary after about 1,000 iterations.

Histograms of the MCMC samples from the posterior are shown in Figure 5-8. The histograms have symmetric shapes and are well approximated by Gaussian distributions. In addition, Figure 5-8 shows that BIT-SEBS has refined the estimates of T_s compared to their prior estimates, whereas for T_a and u_a the data was non-informative and BIT-SEBS did not result in any refinement of the prior estimates.

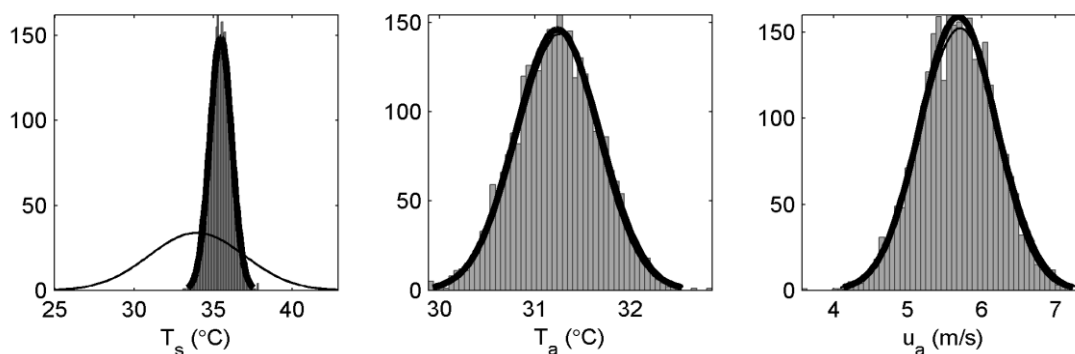


Figure 5-8: Prior and posterior distributions of input meteorological variables for the 12:00 PM time stamp of tower WC162 (soybean) for day-of-year 173. The thin line is the prior distribution (Gaussian PDF), the histogram represents the MCMC samples from the posterior distribution, and the thick line is a Gaussian PDF fitted to the histogram of posteriors.

As the posterior distributions of each input variable are approximately Gaussian, their mean values (which also correspond to the most-likely values) are taken as the point estimates of that variable. These inferred values are then used in evaluation of the performance of the Bayesian inference (section 5.4.2) and quantification of the uncertainties (section 5.4.3).

5.4.2 Bayesian Uncertainty Analysis of SEBS Inputs

The SEBS model is used to estimate the sensible heat flux in both “deterministic” and Bayesian “stochastic” estimation schemes, with Figure 5-9 presenting a schematic of the overall procedure. In deterministic estimation, the observed values of the meteorological variables were used for direct estimation of the sensible heat flux (the traditional flux estimation approach). However, in stochastic estimation, the inferred values of T_s , T_a and u_a are used.

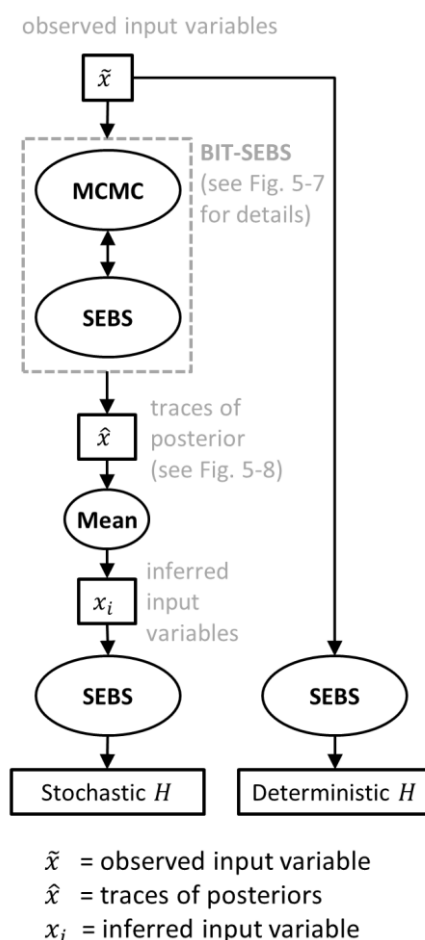


Figure 5-9: The overall procedure to simulate sensible heat fluxes in SEBS using both stochastic and deterministic forms. x denotes the input forcing (T_{sr} , T_{ar} , U_a). The procedure is applied at each time step of each tower.

Figure 5-10 presents a scatterplot of both the deterministic and stochastic estimates of sensible heat flux values against measured eddy covariance data for day-time half-hourly records for all soybean (top panel) and all corn towers (bottom panel). Linear regression statistics for each scatter plot are also shown in this figure. The E_{rel} term refers to a relative error measure defined as $E_{rel} = RMSD / [\max(H_{obs}) - \min(H_{obs})]$, where $RMSD$ is the root mean squared error between observed and simulated sensible heat flux and H_{obs} is the observed sensible heat flux. As is apparent from Figure 5-10, stochastic simulation of sensible heat flux using Bayesian inferred values of T_s , T_a and u_a improves the correlations for both corn and soybean towers, with an R^2 increase from 0.68 to 0.99 for soybean and from 0.62 to 0.98 for corn. In addition, the relative error decreases from around 10% to 1% for both soybean and corn towers.

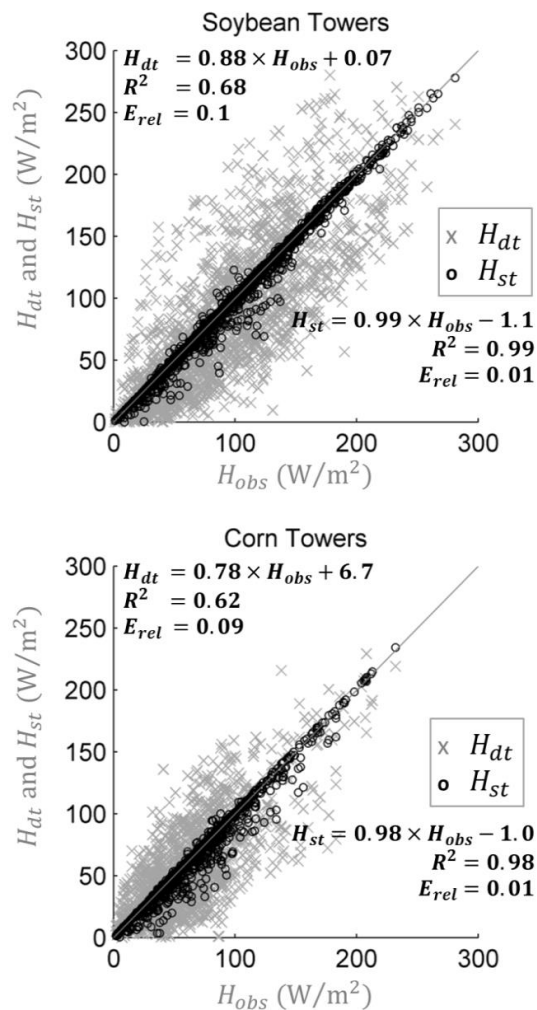


Figure 5-10: Scatterplots of observed sensible heat flux (H_{obs} ; x-axis) versus deterministic simulated (H_{dt}) and stochastic simulated (H_{st}) for all day-time soybean (top) and corn (bottom) half-hourly tower values. Linear regression statistics of both H_{dt} and H_{st} are also shown. The quantity E_{rel} represents the relative error, defined as the *RMSD* divided by the range of observations. The 1:1 line is also shown.

Time series of the observed, deterministic simulated and stochastic simulated sensible heat flux for 6 selected towers (with fewest data gaps) are presented in Figure 5-11, with R^2 and E_{rel} values shown for both deterministic and stochastic simulations. The deterministic simulated sensible heat flux is in agreement with the observed values for the majority of towers, with R^2 values between 0.4 (tower WC162) and 0.8 (tower WC13). However, a clear underestimation of sensible heat flux in deterministic results is evident for WC13 and WC161. Also, deterministic simulated sensible heat fluxes of WC162 have clear forward diurnal shifts. In contrast, the stochastic simulated values are in better agreement with the observed values, showing improved R^2 values of 0.96-0.99.

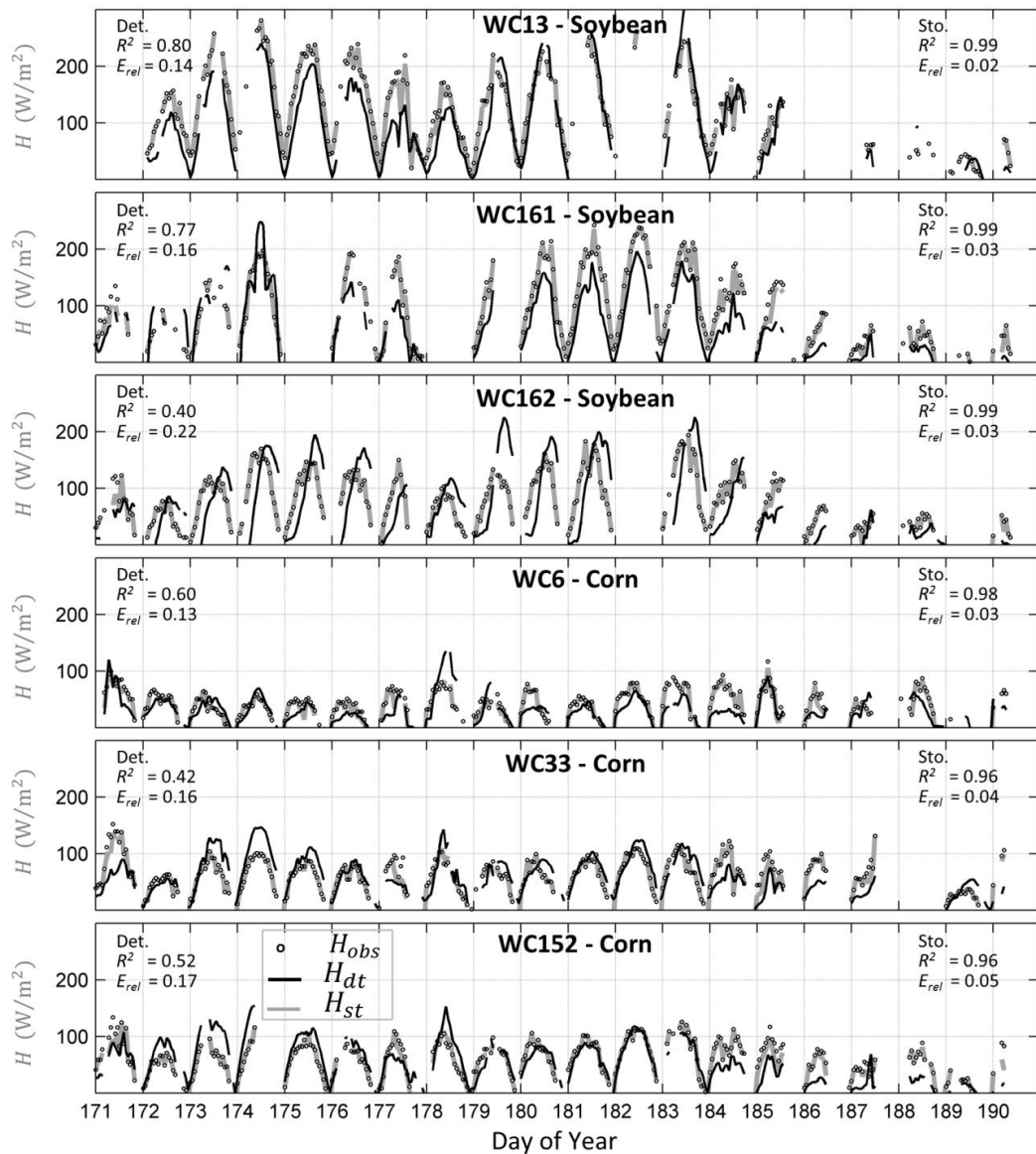


Figure 5-11: Time series of observed sensible heat flux H_{obs} , stochastic simulated H_{st} and deterministic simulated sensible heat flux H_{dt} for 6 selected towers. For each panel, R^2 and E_{rel} are given for deterministic (Det.) and stochastic (Sto.) linear regressions.

It is apparent that by using the inferred values of T_s , T_a and u_a , the performance of linear regressions of half-hourly results improves significantly, with R^2 and slope values close to 1 and a considerable decrease in relative errors. The improved model performance in the stochastic simulations is due to the inference of the input variables from the observed responses (section 5.3.2) and should not be viewed as indicative of the performance in predictive applications. Instead, our aim here is to use the inferred values of the input variables to gain further insights into the errors and uncertainties associated with them, and to gain insights into which input variables are likely to be contributing to the predictive uncertainty. In particular, the next sections examine and discuss which inferred inputs differ most from their observed values.

It should be emphasized that the specification of the priors (in particular, their standard deviations) has a significant influence on the performance of the inference in BIT-SEBS. The importance of the choice of priors is illustrated in the example presented in Appendix C. In this case, BIT-SEBS simulations are performed for tower WC13 (soybean) assuming that each variable shares the same larger standard deviation of T_s . Results show that when using such a set of non-informative priors, the efficiency in the stochastic estimation of the sensible heat flux is greatly reduced and the time series of the differences between inferred and observed values for all three variables are in the same approximate range. Assigning a realistic and representative range of uncertainty to the input variables is known to be of key importance to the fidelity of such hierarchical Bayesian approaches (e.g. as discussed by [Renard et al. 2010](#); [Renard et al. 2011](#)). In this study, this is pursued by considering the spatial variability of the inputs as a proxy for the sampling errors in these quantities.

In summary, although the true values of the selected input meteorological variables are unknown, the inferred values using BIT-SEBS can be considered as an accurate estimate of such true values due to the following reasons:

1. The prior distribution of input variables are based on the spatial variability of the measurements within a relatively dense network of towers;
2. The likelihood function contains a physically-based model with established relations between input data and estimated sensible heat flux;
3. Errors in the parameterization of the SEBS model are likely to be relatively small (due to the quality of the field observations of the vegetation characteristics);
4. The MCMC analysis of the posterior distributions appears to have converged, according to the diagnostics employed;
5. The posterior distributions are well-behaved and approximately Gaussian and there is no evidence of incompatibility with the corresponding prior distributions;
6. Stochastic simulations of the SEBS model using the inferred input variables resulted in consistent estimates of the response variable (sensible heat flux).

Therefore, differences between the inferred and observed values of the input variables are likely to be primarily comprised of observational errors. Further examination of the inferred input observations is undertaken in the following section.

5.4.3 Inferred Values of Meteorological Variables

To evaluate the performance of the Bayesian inference, results are first examined for a sample day for both a soybean and a corn tower. To evaluate the approach more closely, the differences between inferred and observed meteorological values for all towers are also presented. Figure 5-12 plots the inferred values of T_s , T_a and u_a for day-of-year 173 from a representative soybean (WC162) and corn tower (WC152). Grey lines in each panel indicate the observed values from amongst the additional 11 soybean and corn towers, which can be used to establish whether the range and trend in observed and inferred values are in accord with the other measurements across the study domain.

As can be seen from Figure 5-12a, the observed T_s has a different diurnal cycle than is present in the other towers, due perhaps to sensor time delay, alignment or geometric configuration. If the observed values of T_s , T_a and u_a from this tower were to be used in SEBS in deterministic simulations, the resulting sensible heat flux would be very different from the observed H (R^2 of 0.22 and $RMSD$ of 52 W.m^{-2} ; see Figure 5-12g). On the other hand, the Bayesian estimated values of H match well with the observed sensible heat flux and improve R^2 to 0.99 and $RMSD$ to 0.86 W.m^{-2} . To achieve this, the Bayesian inference approach identifies alternative values of T_s that provide a better match to the diurnal variations represented across the other towers. Given that the inferred values of T_a and u_a are close to the observed values (see Figure 5-12c and Figure 5-12e) it seems that, for this tower at least, the main uncertainty in flux estimation results from the T_s observations, with absolute differences between observed and inferred values of up to $3 \text{ }^\circ\text{C}$. This difference is well within the expected spatial variability observed within in-situ surface temperature measurements over agricultural fields (McCabe et al. 2008).

For the corn tower, the inferred values of the land surface temperature are up to $2 \text{ }^\circ\text{C}$ lower than the observed values (see Figure 5-12b). Similar to the soybean tower example above, the Bayesian inferred values of air temperature and wind speed remain quite close to the observed values, indicating that these seem to be spatially representative. Figure 5-12h shows that the deterministic estimate of H via standard application of SEBS is considerably higher than the observed flux estimate. Through use of the inferred land surface temperature values, a significantly improved simulation of the observed sensible heat flux is achieved, with R^2 increased from 0.86 to 0.99 and $RMSD$ reduced from 41 W.m^{-2} to 1.3 W.m^{-2} .

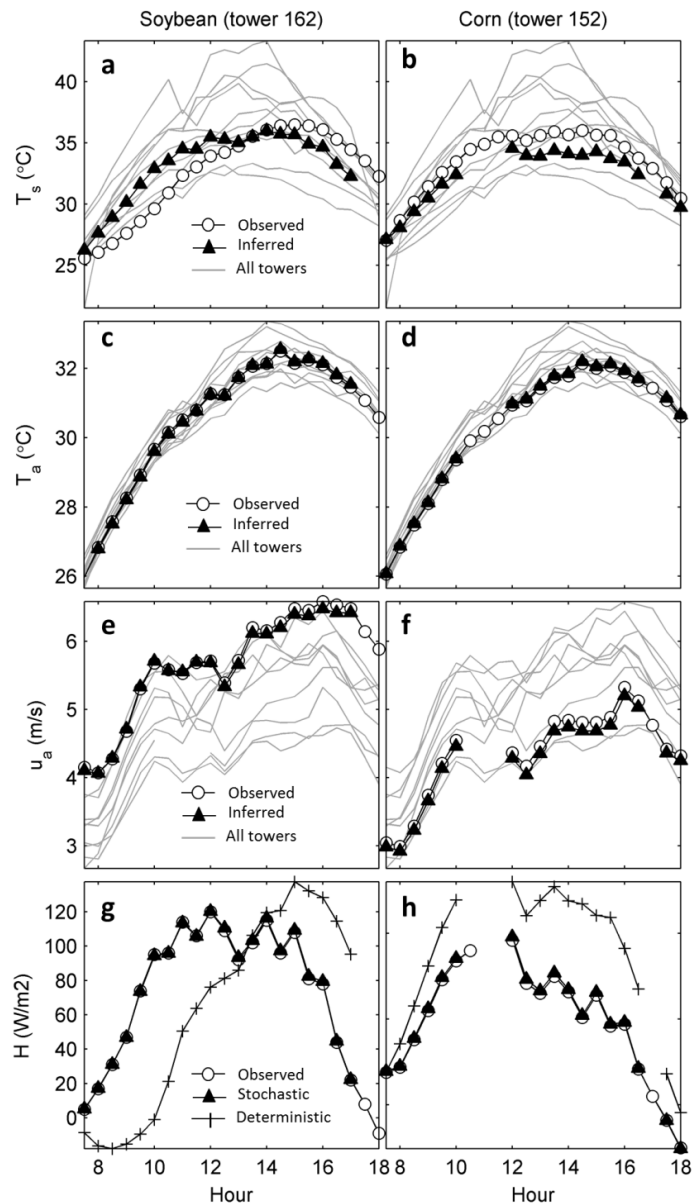


Figure 5-12: Observed and Bayesian inferred values of meteorological variables for a soybean tower (left, WC162) and corn tower (right, WC152). The grey lines in the top three rows represent the observed values for the other 11 flux towers. In the bottom panels, the observed, deterministic calculated and stochastic generated sensible heat fluxes are shown. The x-axis for all panels indicate hour of the day (local time) for day-of-year 173.

To evaluate the performance of the Bayesian inference for all towers, the difference between observed and inferred values of T_s , T_a and u_a are calculated as $\Delta X = X_o - X_i$, where X is the variable of interest (T_s , T_a or u_a) and subscript o represents the observed and subscript i the inferred value of the variable. Time series of ΔT_s , ΔT_a and Δu_a are shown in Figure 5-13. A bar plot of the all-tower averaged precipitation is also shown to support interpretation of the results. For all panels (except precipitation), grey lines represent the time series of soybean and black lines the corn towers.

For all towers, differences between Bayesian inferred and observed values are larger for the land surface temperature (ΔT_s values of up to ± 5 °C) than for either the air temperature or wind speed. One possible reason for this difference is the disparity between the footprint of the in-situ Apogee land surface temperature sensors and the CSAT sonic anemometer that is used to derive the sensible heat flux at the eddy covariance tower. The effective footprint of the Apogee sensors used in this study are on the order of a few square meters (approximated as circles with areas of 26.2 m^2 over corn and 6.5 m^2 over soybean), while the sonic anemometer measures eddies that originate from a non-local (relative to the in-situ sensor) distance upwind of the tower (Schmid 2002), representing a source area of several hundreds of square meters.

Figure 5-13 indicates that the differences between the Bayesian inferred and observed T_s at the soybean towers is more significant (and frequent) than those at the corn towers, due possibly to the lower fractional vegetation cover and the effect of bare soil on the locally observed T_s (McCabe et al. 2008). For the corn towers, the fractional vegetation cover is higher than for soybean towers, and hence the footprint of surface temperature is more likely to be spatially stable and spatially representative. In contrast to ΔT_s , values of ΔT_a have lower variability and their magnitude is within the range of the sensor accuracy (± 0.3 °C). The lower values of ΔT_a suggest that due to atmospheric mixing and turbulence in the air, the footprint of the in-situ air temperature sensor (HMP-45C) is more representative of the footprint of the sonic instrument. However, this reasoning cannot be extended to Δu_a , as the wind speed in this study derives directly from the CSAT sonic anemometer rather than from independent measurements. Nevertheless, for the majority of cases, the range of Δu_a is less than $0.5 \text{ m}\cdot\text{s}^{-1}$, which indicates that observations of the wind speed in each individual tower are likely to be representative of the domain average (apart from a number of clearly identifiable periods). The few days with higher Δu_a values (e.g. day-of-year 178) are days with lower values of wind speed in the area (see Figure 5-3), which indicates that when wind speed is lower, the spatial variability in its value is larger.

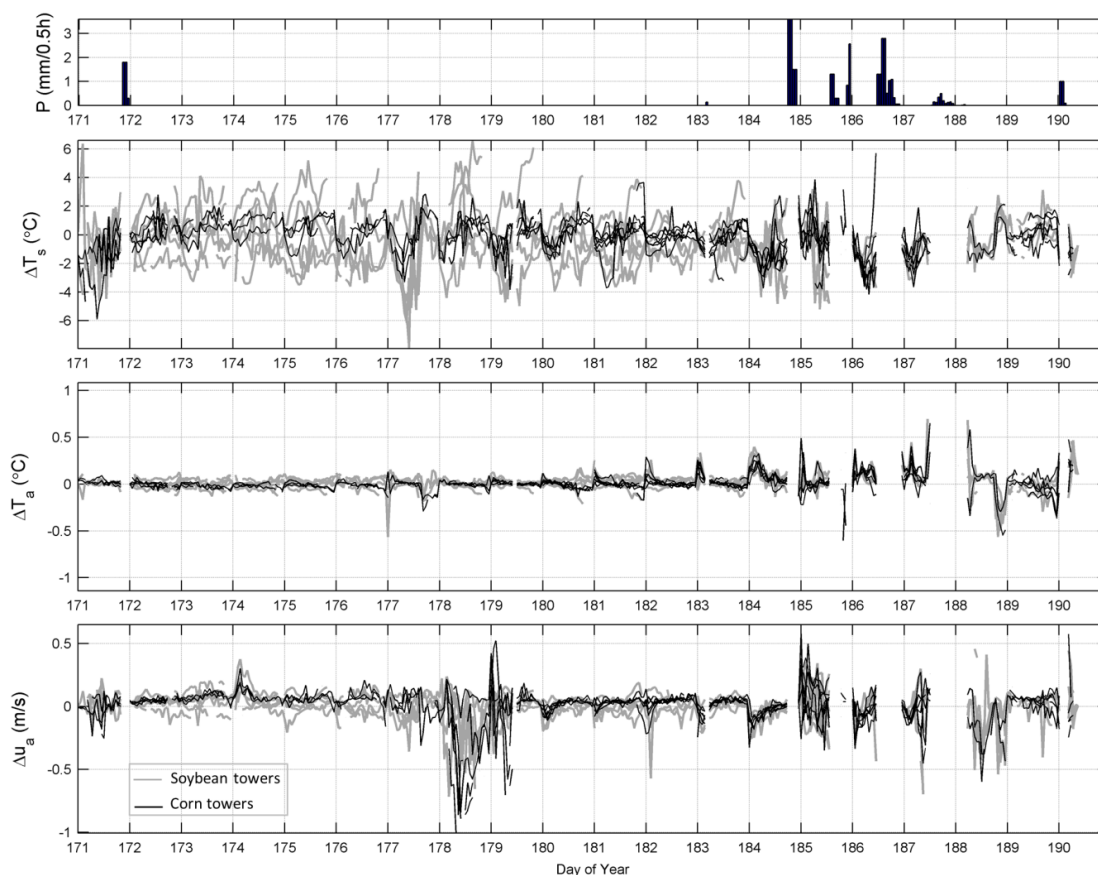


Figure 5-13: Differences between Bayesian inferred and observed values for land surface temperature, air temperature and wind speed. Soybean towers are shown in grey and corn towers in black. Top panel shows average precipitation occurring during the field campaign.

5.5 Discussion

Sources of uncertainty in Earth system models are varied and can include errors due to simplifications in the model structure, errors in the observations of the input forcing, uncertainties in parameterization of the model, or errors in the observations of the response variables (sensible heat flux in this study). In general, understanding and quantifying the uncertainty in such modeling schemes is nontrivial, due to the complexity of the interactions between the land surface and the atmosphere and the combined effects of all sources of error (Kalma et al. 2008).

In the present study, errors associated with the measurements of meteorological input forcing were estimated based on their application in determining sensible heat flux using the Surface Energy Balance System (SEBS) model over a number of eddy covariance towers. Input forcing included air temperature, land surface temperature and wind speed. Results indicate that the main uncertainty contributing to flux prediction arises due to uncertainties in the local observations of the land surface temperature, with differences between inferred and observed values of up to ± 5 °C. A number of previous studies have identified that errors in the land surface temperature can have a direct and significant effect on the estimation of the sensible heat flux. For

example, [van der Kwast et al. \(2009\)](#) found that in well irrigated fields, H estimated by SEBS can deviate up to 70% with only a 0.5 °C difference in surface temperature. It is worth noting that this behaviour is not distinct to SEBS alone: similar sensitivities appear in other energy balance models, and represent a considerable problem for energy balance based approaches that require the use of an infrared surface temperature ([Kalma et al. 2008](#)). For instance, [Timmermans et al. \(2007\)](#) identified that a 3 °C deviation in surface temperature can cause errors in the sensible heat flux estimation of up to 75% in the TSM model ([Norman et al. 2000](#)) and 45% in the SEBAL model ([Bastiaanssen et al. 1998a](#)).

Looking beyond sensitivity analysis of modeling schemes to surface temperature, we suggest that the main reason for the differences between observed and Bayesian inferred values of the land surface temperature is the disparity in the spatial representativeness (or footprint) of the sensors. In particular, the local scale footprint of in-situ measurements of the land surface temperature (using Apogee sensors) are unlikely to correspond with the footprint scale of flux observations made with eddy covariance systems ([Kljun et al. 2004](#); [Su et al. 2005](#); [Kustas et al. 2006](#); [Vickers et al. 2010](#)). Due to atmospheric turbulence and mixing, air temperatures and wind speeds will have lower spatial variability than the land surface temperature. Likewise, the footprint of the locally measured T_a and u_a will more closely match the footprint of the observed eddy covariance based fluxes.

Use of the locally observed land surface temperature without spatial scaling and footprint correction has significant implications for the validation of heat flux models. For example, [Su et al. \(2005\)](#) showed that errors in the land surface temperature are the main reason for discrepancies between modelled and simulated heat fluxes in the SMEX02 towers. However, they partially corrected such errors by modification and adjustment of the emissivity. In image scale applications, footprint models ([Leclerc and Thurtell 1990](#); [Schuepp et al. 1990](#); [Schmid 2002](#)) have been used for correction of in-situ observed land surface temperature using remote sensing images ([Kustas et al. 2006](#); [Li et al. 2008](#); [Timmermans et al. 2009](#)). In a footprint model, the observed sensible heat flux is related to the orientation and length of the footprint of a source area located in the upwind direction of the eddy covariance tower. Footprint models can characterize this source area (as a distance or region) based on the measurement height, aerodynamic surface roughness (z_{0m} and z_{0h}) and atmospheric stability ([Bastiaanssen et al. 1998b](#)). However, length and orientation of the source area cannot be quantitatively used in adjustment of the local land surface temperature observations, unless a remote sensing image is available. Hence, with suitable refinement, the methodology developed in this chapter could serve as a practical tool for quality control and evaluation of the tower based land surface temperature observations and their spatial scaling.

Although this study focused on the uncertainties of the meteorological variables, other uncertainties in the model structure and parameterization may exist. As such, the Bayesian inferred values of the land surface temperature might be partly contaminated by the effect of such uncertainties. The importance of model structure and parameterization uncertainties is highlighted in a number of recent studies. [Zhang](#)

et al. (2010a) observed that the choice of z_{0m} formula and the MOST function for temperature (f_T) significantly influenced the agreement between sensible heat flux calculated for a scintillometer and an eddy covariance system. Also, van der Kwast et al. (2009) observed that the roughness parameters (h_c , z_{0m} , d_0) can cause large deviations in the modeling of sensible heat flux. In addition, Verstraeten et al. (2008) found that the estimation error due to the uncertainty of roughness length for heat transfer is important: even more so than the uncertainty on temperature, wind speed and stability correction. The Bayesian model of this study is sensitive to the number of priors and their inter-dependencies, and as such it is not practical to include uncertainty of the model roughness parameters. In particular, the Su et al. (2001) method employed in SEBS for estimation of the roughness parameters (z_{0m} and z_{0h}) uses wind speed and air temperature as input variables. Hence, introducing roughness parameters as priors is likely to be problematic. However, careful measurement of the vegetation height and density during the SMEX02 field campaign suggest that uncertainties in the roughness parameterization are not likely to be significant in this study. Another important consideration is the scale of uncertainty evaluations: this study was at tower scale and the results cannot be extended to larger (e.g. regional) spatial scales. In particular, errors due to the spatial variability in input meteorological forcing might be significant in large scale applications, or in the cases with large land cover variations (e.g. extensive bare soil in vicinity of irrigation fields), resulting in large errors in heat flux estimation (Kustas and Albertson 2003; Bertoldi et al. 2008).

Preliminary evaluations indicate that BIT-SEBS is sensitive to the parameters of the prior PDFs. In the case of the Gaussian prior PDFs, the definition of the standard deviation of the input variables has a direct influence on the inference performance and convergence of the MCMC simulations. Likewise, the performance of the Bayesian technique in the estimation of the input variables depends upon the accuracy and validity of the prior information. This is especially important in hierarchical Bayesian inference, where the use of non-representative priors can result in poor or meaningless posterior estimates. Therefore, in order to provide a quantitative measure of the spatial variability within these variables, we recommend that new installations of field based eddy covariance measurements provide a few additional spatially distributed instruments that measure the key meteorological variables such as land surface temperature, air temperature and wind speed. Such instrumentation might include traditional point-based infrared and air temperature sensors located within the footprint of the eddy-covariance tower, or more spatially representative devices such as the recently developed fibre-optic Distributed Temperature Sensing networks (Selker et al. 2006). For existing datasets with single tower observations, it is important to quantify the bound of uncertainty (i.e. standard deviation of the prior PDF) for each time stamp of observation. A first approximation might be to assume that the footprint of air temperature and wind speed are similar to the sonic instrument, while the footprint of land surface temperature is different (i.e. smaller) to the sonic instrument footprint (i.e. low values for σ_{T_a} and σ_{u_a} and high values for σ_{T_s}).

5.6 Conclusions

In this study, the uncertainties associated with input meteorological variables over a multi-tower site were quantitatively evaluated using a Bayesian inference scheme coupled with the Surface Energy Balance System (SEBS) model. Results confirm that the performance of physically based energy balance methods in heat flux estimation strongly depends upon the representativeness of the input meteorological variables. In particular, uncertainties in local observations of the land surface temperature have considerable effect on the mismatch between the observed and modelled sensible heat flux over both soybean and corn fields. As such, the land surface temperature cannot be assumed to provide spatially representative values in the computation of the sensible heat flux observed at the tower scale: at least not without some prior spatial scaling. Characterizing this spatial variability of surface temperature using high resolution remote sensing retrievals or exploiting stand-alone tower data to inform the prior distributions of forcing uncertainty, provide a number of directions for further investigation, development and application of the approach developed here.

Acknowledgements

Funding for this research is provided jointly by an Australian Research Council (ARC) Linkage project (LP0989441), Discovery Project (DP120104718) and top-up scholarship support for Ali Ershadi from the National Centre for Groundwater Research and Training (NCGRT) in Australia. The work was also supported by the NCI National Facility at the ANU via the provision of computing resources to the ARC Centre of Excellence for Climate System Science.

Chapter 6

Synthesis and Thesis Recommendations

6 Synthesis and Thesis Recommendations

Evapotranspiration (ET) is an important but challenging hydrological variable, constituting a key component of almost all hydrological and water resources studies (Stull 1988; Maidment 1992; Brutsaert 2005). Despite the long history of ET science, rooting back to the early works of Dalton (1802) and extending to the modern techniques developed in the twentieth century (Monin and Obukhov 1945; Penman 1948; Monteith 1965; Brutsaert 1982), there remain a number of unknowns in efforts towards developing a comprehensive understanding of the ET process. Some of the principal knowledge gaps can be attributed to the choice of an appropriate model and its parameterization (i.e. application challenges; **Chapters 2 and 3**), consequences of using coarse resolution data in ET models (i.e. scaling challenges; **Chapter 4**) and understanding and quantifying the sources of error in ET modeling (i.e. uncertainty challenges; **Chapter 5**). These outstanding challenges have been identified through literature review briefly in **Chapter 1** and in more detail in the introduction section of the respective chapters. Accordingly, the key research objectives of this thesis have been identified as follows:

1. Characterise the behaviour of fundamental evapotranspiration approaches and their performance across widely varying biomes and land surface conditions;
2. Identify the importance and role of model structure and parameterization on flux estimation;
3. Quantify the effect of input and flux aggregation on the estimation of evapotranspiration;
4. Develop a Bayesian uncertainty analysis framework to understand the role of data uncertainty in flux estimation.

The focus in each of **Chapters 2 to 5** has been to address one of the research objectives. The current chapter aims to provide an integrated review and synthesis by providing a brief and summarized, but rather broad and interlinked discussion, on all aspects of the thesis. Afterwards, a discussion is provided on the main implications of the results and to shed light on potential future research contributions.

6.1 Thesis Overview and Conclusions

The current section is a review and synthesis of the thesis outcomes, highlighting the main contribution of the research. In the following, an overall picture of the main findings is depicted by providing a brief description of the materials and methods, a short summary of the main findings and some notes on the limitation of the analyses. The interlinked summaries provide an opportunity to highlight some important facts and figures additional to the details presented in the preceding chapters.

6.1.1 Model Intercomparison and Assessment

A key objective of the thesis has been to provide insights into some application challenges of evapotranspiration estimation, including: the performance of different ET approaches, issues of model structure and importance of model parameterization. To add generality to evaluations, a high-quality multi-annual database of half-hourly

and hourly meteorological and flux observations is used across twenty towers distributed geographically over a range of distinctive biomes. From a global scale perspective, the studied biomes are important and represent a range of land surfaces, which included: grasslands (GRA), croplands (CRO), shrublands (SHR), evergreen needleleaf forests (ENF) and deciduous broadleaf forests (DBF). The representativeness in the range of models, type of biomes, range of crop heights, geographical distribution of towers and the length of data records used in **Chapters 2** and **3** allowed examination of the distinctive knowledge gaps in the application aspects of ET modelling and provided guidance towards optimum model selection in large scale studies.

Results obtained in **Chapter 2** clearly identified the range of responses and relative performance of some fundamental ET models over the selected towers. The models included the Surface Energy Balance System (SEBS) model (Su 2002), the Penman-Monteith (PM) model (Monteith 1965), the advection-aridity (AA) model (Brutsaert 2005) and the modified Priestley-Taylor (PT-JPL) model (Fisher et al. 2008), representing energy balance, combination, complementary and radiation-based type of models, respectively. The models are different in describing the details of ET process and data/parameterization requirements, with PM and SEBS being more complex and data demanding than simpler AA and PT-JPL.

Based on the mean values of the examined statistical metrics (e.g. Nash-Sutcliff Efficiency – *NSE*), the ensemble mean of the models provided the best results. Amongst the individual models, the overall performance rank from best to worst was in the order: PT-JPL, SEBS, PM and AA, with PT-JPL and SEBS presenting relatively similar performances. However, no single model was consistently the best across all biomes. The following is a brief review on the main characteristics, advantages and limitations of the studied ET models:

The PT-JPL model

The model scales the potential ET of the original Priestley and Taylor (1972) model to actual values, utilizing reduction functions parameterized via bio-physiological characteristics of the land surface (Fisher et al. 2008). The model showed relatively good performance (based on *NSE*) over almost all biomes, compared to PM and AA. In the majority of the towers the performance of PT-JPL and SEBS were similar; but in contrast to the SEBS, the PT-JPL showed insensitivity to vegetation height (and consequently to the roughness sub-layer effects). Monthly-based *NSE* analysis of (half-) hourly estimates showed the PT-JPL provided less variations in its performance in different seasons, compared to the PM and AA.

The PT-JPL can be considered a reliable model for ET estimation across a range of land surface conditions, in terms of both performance and data requirements. The model needs the least data forcing, demanding only the net radiation, vegetation indices, air temperature and humidity. As a result, the need for some often erroneous and scarce data like soil moisture, wind speed, vegetation height and land surface temperature is relaxed. A limitation of the model is requiring at least a year of data to determine the

optimum air temperature, which constrains its application when data are temporally scarce. Also, the model showed reduced performance over ENF towers, possibly due to non-representativeness of the vegetation indices in demonstrating the phenological dynamics.

The SEBS model

The model is directly developed from the Monin-Obukhov Similarity Theory (Monin and Obukhov 1945) and the energy balance principle (Brutsaert 1982), detailing the physical processes of heat transfer and ET. Results in **Chapter 2** showed the model provided good results (often comparable to the PT-JPL), in particular over short canopies (i.e. grasslands and croplands). The model's performance showed less sensitivity to the season, compared to PM and AA.

The model relaxes the need for surface resistance parameterization, but is sensitive to the parameterization of aerodynamic resistance. In particular, it performed inadequately (compared to the PT-JPL) over tall and heterogeneous canopies, due to its limitations in the reproduction of heat transfer in the roughness sub-layer. The model also performed poorly at some shrubland and evergreen needleleaf forest sites (compared to other biomes), where the land surface heterogeneity caused strong sub-pixel variability of the heat flux sources. A cause of uncertainty at those sites was the non-representativeness of the coarse (250 m) remote sensing data for aerodynamic resistance parameterization.

Based on the results obtained in **Chapter 5**, a source of uncertainty in the SEBS model simulations is the mismatch between local longwave upward radiation (or land surface temperature) sensor's footprint and that of the sonic anemometer. Such uncertainties are less important for other models which use longwave upward radiation (or land surface temperature) only for estimation of available energy.

The Penman-Monteith model

The model is relatively complex and detailed in description of the ET process, is data demanding and requires identification of the surface and aerodynamic resistance parameters. Overall, results from **Chapter 2** showed significant underestimation of ET across many towers when using this approach. Further examination in **Chapter 3** identified that resistance parameterization, in particular the surface resistance, has an important role in PM type models, while the structure of the model in partitioning of the evaporative sources is not a key factor. The model also showed lower modeling efficiency (i.e. low *NSE*) for the times when the land surface had lower values of ET, i.e. in the colder seasons, especially over croplands and deciduous broadleaf forest sites.

The advection-aridity model

The model relaxes the need for land surface temperature data and parameterization of the surface resistance, and directly estimates ET using air temperature, humidity, available energy, wind speed and surface roughness. The performance of the model

was lower than SEBS and PT-JPL, and showed relatively large overestimations across all biomes. Similar to the PM model, AA performed worst over grassland and deciduous broadleaf forest sites. Possible causes for these results were attributed to the use of a constant α_{PT} and errors in the parameterization of aerodynamic resistance. In particular, the model assumes neutral atmospheric conditions, which is invalid over tall and heterogeneous land surfaces where the instability in the turbulence is significant and the roughness sub-layer might influence eddy-covariance measurements.

Although the analyses of **Chapter 2** is one of the most comprehensive performed for this range of data and models, it was still not inclusive in covering all type of biomes (e.g. wetlands) and climates (e.g. dry, arctic). Also, the length (i.e. period) of data was not equal for all towers, and caused (statistically) non-representative estimates. For the time being, it is reasonable to assume that the overall performance rank of the models, and the seasonal dependence of performances, will remain unchanged - even if a perfect dataset is used. However, the need for updating the results (hopefully with improved FLUXNET data) remains a recommendation for continued investigation: especially where improvements in model parameterizations are provided (see below).

6.1.2 Influence of Model Parameterisation on Performance

The analyses performed in **Chapter 3** complemented the results obtained in **Chapter 2** in providing insights into the important role of both model structure and parameterization. Below is a summary of the materials and methods used for the study, followed by a list of important findings supported with brief expansion on the discussions.

The structural details of the models in inclusion of evaporative sources (i.e. soil evaporation, canopy transpiration, canopy evaporation) increased from the traditional single-source Penman-Monteith model (PM) (Monteith 1965), to a two-layer model based on Shuttleworth and Wallace (1985) (SW) and a three-source model based on the Mu et al. (2011) scheme (Mu). A range of different resistance parameterizations were used to examine the models response and included a simple lookup table based surface and aerodynamic resistance parameterizations of the Mu model, a Jarvis type surface resistance method developed by Noilhan and Planton (1989) and the aerodynamic resistance estimation methods developed by Thom et al. (1975) and Shuttleworth and Gurney (1990). The aerodynamic resistances were used with both fixed (Brutsaert 2005) and dynamic (Su et al. 2001) values of roughness parameters. The combination of model/parameters resulted in 14 different scenarios, which were analysed using the same FLUXNET database of **Chapter 2**.

Assessment of the scenarios showed that no single model/parameterization combination provided the best results across all biomes, indicating the importance and effectiveness of both model structure and parameterization for the PM type ET models. In terms of the best scenarios for each individual biome (based on the overall *NSE*), results indicated that the single source PM model structure performed better over grasslands, croplands and shrublands, and the two-layer SW model had better performance over forest biomes. Source partitioning of total ET (i.e. model structure)

was not a key factor for improving the performance, as none of the best scenarios were from the Mu model's structure. The top-ranked scenarios all shared the simpler surface resistance parameterization of the Mu model, while the more detailed method of [Noilhan and Planton \(1989\)](#) produced lower values of *NSE*. Likewise, the top-ranked scenarios employed the [Thom et al. \(1975\)](#) aerodynamic resistance method (with dynamic roughness), except over the deciduous broadleaf forest sites where the simpler aerodynamic resistance approach of the Mu model showed enhanced performance. While the Mu surface resistance method relaxed the need for soil moisture data, the [Thom et al. \(1975\)](#) aerodynamic resistance approach required wind speed and vegetation height data, potentially limiting the application of the model over the biomes other than deciduous broadleaf forest.

Similar to the evapotranspiration models studied in **Chapter 2**, the scenarios of **Chapter 3** showed limitations in estimating lower ET values, usually associated with colder seasons. The results suggest that the performance seasonality is not specifically due to either structure or parameterizations of the models – at least for those evaluated in **Chapter 3**. However, understanding the cause of such season-specific sensitivities is nontrivial due to the integrated impact of model and data uncertainty.

6.1.3 Scaling Issues in Evapotranspiration

Chapter 4 focused on the impact of resolution-induced data uncertainties on heat flux estimation. The issue of spatial resolution has been central in remote sensing ET estimation methods. In particular, the energy balance methods like SEBS directly use thermal images to quantify near-surface temperature gradient and optical images for parameterization of aerodynamic resistance. In **Chapter 4**, the effects of both input and flux aggregation (i.e. upscaling) on the SEBS derived ET were examined. For the input aggregation assessment, land surface temperature and vegetation parameters were aggregated from 120 m to 960 m and then used to estimate heat fluxes at each resolution. For flux aggregation, the estimated fluxes at 120 m resolution were directly aggregated to 960 m. The data used in this study included three Landsat 5 scenes captured during the cropping period of a heterogeneous semi-dry agricultural area.

The results identified the consequences of input aggregation, with the main source of uncertainty in the estimation of roughness parameters, not directly in the land surface temperature aggregation. Such roughness parameterization uncertainties caused around 20% ET errors at the image scale, but increased to 40% when the errors were examined at the pixel scale (i.e. for the area within each coarse pixel individually). The direct implication of the finding is that if the effects of pixel resolution are not considered in the SEBS model, model application with coarse resolution data cannot provide sufficient accuracy for field scale estimation.

Results from the flux aggregation analysis showed the suitability of the simple averaging technique in hydrological applications, as it conserves the total flux. Although other spatial interpolation methods like nearest neighbour, bilinear and bicubic are accessible from software platforms (e.g. NCL, IDL) and show widespread use in the literature, the application of such approaches can result in large errors in the evaporated mass of water: an often overlooked consequence of aggregation.

The findings of **Chapter 4** are important for selecting a suitable model for coarse resolution data. While coarse data produce large errors (at pixel scale) in the SEBS derived ET, they would cause lower errors for the PT-JPL or the Mu model, as the use of thermal data is only for longwave upward radiation component of the available energy. A further aspect of scaling issues in heat flux estimation is related to the spatial representativeness of the thermal data and the errors that may result from the small footprint of the thermal sensor. These were examined in **Chapter 5** and summarized in the following section.

6.1.4 Uncertainty in Evapotranspiration

Uncertainty is an inherent component in ET estimation, but is often “hidden” in the formulation and parameterization of the model and in the spatio-temporal resolution of data forcing. **Chapter 5** focused on understanding and quantifying the data uncertainty through application of the SEBS heat flux model using a tailor-made Bayesian inference technique. Data from a multi-tower site located in a heterogeneous agricultural area were used for evaluations. Carefully measured vegetation data limited the uncertainties in estimation of roughness parameters, and provided opportunities to focus on data uncertainties.

The uncertainty analysis illustrated that the land surface temperature is the most uncertain input variable in sensible heat flux estimation (compared to air temperature and wind speed). The main reason for greater uncertainty in the land surface temperature was attributed to the smaller footprint of the land surface temperature sensor, compared to the footprint of the sonic anemometer. Uncertainty assessments performed in **Chapter 5** showed the potential application of the developed probabilistic Bayesian technique in resolving the complexity of mixed errors in process-based ET models. Further expansion on the application of the Bayesian technique is provided in the subsequent section.

6.2 Recommendations and Future Work

The review and synthesis of the findings provided insights into the science of evapotranspiration, but also disclosed and highlighted some important aspects of its process that are required to be addressed in future research, detailed in the following sections.

6.2.1 Application of ET models

Results of **Chapter 2** and **Chapter 3** provided guidance on areas of research that are needed to address some outstanding issues in the application of the models, detailed in the following:

Implications for model applications

One important observation in the chapters was the performance variability in models and scenarios across biomes. The variability highlighted a key consideration in large

scale application of the models: there is no best model everywhere. That is, no one model or its parameterization variant can perform the best over all land surfaces. The implication is in stark contrast to common practice in today's hydrological applications.

An alternative recommendation is developing an ensemble ET product using a range of models and parameterizations, and weighting each product based on its relative performance, obtained from assessments over a comprehensive FLUXNET dataset. The ensemble product would not only provide more confidence on the validity of the estimations, but also result in a range of values to develop probabilistic flux estimates, which are necessary for climate change applications (Räsänen and Palmer 2001). To obtain robust model rankings, it is necessary to evaluate the models over a range of biomes using a multi-annual dataset and the assessments should be expanded beyond the constrained number of sites and biomes used in this thesis.

Impact of grid-based data uncertainties on ET estimates

In large scale applications (Miralles et al. 2011; Vinukollu et al. 2011b) the data forcing are in grid form, developed by spatio-temporal interpolation of in-situ or remote sensing retrievals, or from model reanalysis (Sheffield et al. 2006; Rienecker et al. 2011). Uncertainties of such grid-based data are different (often higher) than those supplied by towers, and can greatly influence ET estimates. An assessment of the models with both tower-based and grid-based data forcing will be useful to examine the sensitivity of the models to such uncertainties. This is the focus of ongoing research.

Development of the SEBS model to account for roughness sub-layer

Assessments in **Chapter 2** showed a reduction in the SEBS model's performance over tall and heterogeneous vegetation, where the towers are often located within the roughness sub-layer. The structural deficiencies in the SEBS model for addressing the roughness sub-layer effects can be fixed by extending the MOST equations (Weligepolage et al. 2012). A global assessment of an extended SEBS model can be seen as a valuable future contribution.

Sensitivity analysis of the PT-JPL model parameterization

Assessing the sensitivity of the PT-JPL model to its constraint function parameters and to the α_{PT} parameter for different land surface conditions is an ongoing research topic (García et al. 2013), but would be worth further investigating using the Bayesian inference technique developed in **Chapter 5**, as well as with the scaling assessment method used in **Chapter 4**.

Field scale application of the PT-JPL and Mu models

The models originally developed for large scale (regional to global) ET estimation were shown to be less data demanding and more reliable, in particular over grasslands and croplands. The models can be potentially used in patch and field scale applications, perhaps with modified parameterizations. Further development and testing of the models for such scales, and intercomparison with widely used field scale remote sensing ET models like SEBS, TSEB (Norman et al. 1995), SEBAL (Bastiaanssen et al. 1998a) and METRIC (Allen et al. 2007b) is recommend for future studies.

6.2.2 Scale

Analysis of the scaling issues in heat flux estimation in **Chapter 4** provided important insights into the key influences of spatial resolution on the SEBS model's performance. Some future guidelines regarding the scaling issues are as following:

Extending scaling assessments to more sites and models

The energy balance, combination, complementary and radiation-based ET approaches use optical and thermal data in different ways, and have various sensitivities to input aggregation. A future contribution can be on extending the aggregation assessments of **Chapter 4** to data and models used in **Chapter 2** through examining spatial aggregation in a number of Landsat images (or images from similar satellites) for a multi-year period at each tower. The study will provide a solid background to further develop remote sensing compatible ET models.

Extending scaling assessment to a broader range of resolutions

The spatial resolution range in the analysis of **Chapter 4** was from 120 to 960 m, matching the thermal band resolutions of Landsat 5 and MODIS images. The resolution range can be extended to geostationary type satellites, which have fine temporal (e.g. half-hourly), but coarse spatial (e.g. 5 km) resolutions. Such broad ranges have already been examined by Anderson et al. (2007) and Brunsell and Anderson (2011) for the ALEXI model (Norman et al. 2003), but the error tracking method of **Chapter 4** will be useful to assess error propagations and to determine the relative contribution of data and parameters in the integrated aggregation error.

Parameterization development for vegetation phenological metrics

Analyses in **Chapter 4** showed that the roughness parameters are the key source of errors in input aggregation for the SEBS model. Sources of uncertainties in roughness estimation encompass the errors in estimation of the vegetation phenological metrics like leaf area index (LAI), fractional vegetation cover (f_c) and vegetation height (h_c). For metrics like LAI and f_c , current parameterizations are often developed based on data with specific spatial resolutions (Ross 1976a; Jiménez-Muñoz et al. 2009) and their application with different resolutions cause uncertainties. Developing resolution

invariant or extending the current parameterizations to a broader range of resolutions requires future research.

For vegetation height, the current state of data product choice is slim, with the best available global product being the one developed by [Simard et al. \(2011\)](#) at 1 km resolution. Unfortunately, the product is lacking reliable values over short vegetation and is static (i.e. lacking seasonal dynamics of h_c). Hence, vegetation height for aerodynamic parameterization of models like SEBS are often loosely estimated by field survey, or approximated from vegetation indices ([Su 2001b](#); [van der Kwast et al. 2009](#)). A needed effort for future research is improving the parameterization of vegetation height using joint application of available LIDAR data and optical imagery.

Assessing temporal scaling impacts on ET modeling

The focus of this thesis was on hourly and half-hourly data, mainly because ET models are strictly valid only in steady state conditions (i.e. ≤ 1 hour) ([Brutsaert 1982](#); [Katerji et al. 2010](#)). Similar to the ‘input’ and ‘flux’ aggregation procedures of **Chapter 4**, an assessment of temporal aggregation effects on both input variables and the flux products can be recommended. Such analysis is important as many studies used aggregation to daily and monthly, without assessing their inherent uncertainties ([Crago and Brutsaert 1992](#); [Xu and Chen 2005](#); [Schneider et al. 2007](#); [Vinukollu et al. 2011c](#)).

Developing scale-invariant resistance parameterizations

The lower efficiency of the PM models in **Chapter 3** (compared to similar previous studies) was partly related to the coarse (250 m) resolution of the remote sensing data used for parameterization of the resistances. The issue is related to the limited capacity of the coarse resolution remote sensing data in capturing the sub-pixel variability and dynamics of vegetation phenology, which results in uncertainties in estimating vegetation metrics like leaf area index and fractional vegetation cover. Understanding the influence of resolution-induced uncertainties and providing appropriate techniques to either enhance the spatial quality of the images (e.g. sharpening), or adjust the resistance parameterizations to work with coarse data are important future investigations.

6.2.3 Uncertainty

The Bayesian uncertainty assessments of **Chapter 5** could be further developed in future research, with recommendations provided as following:

Examining the integrated uncertainty at sites with advection

Advection is dominant at active evaporating patches located in the vicinity of large barren surfaces. However, the MOST theory has no capacity to effectively address the advection mechanism. Establishment of new multi-tower field campaigns in water-limited regions with large advections (e.g. BEAREX08; [Evelt et al. 2012](#)) is inspirational

for future research, and the Bayesian method of **Chapter 5** has theoretical capacity for handling such datasets.

Extending the Bayesian uncertainty assessments to other ET approaches

Results from **Chapter 2** and **Chapter 3** suggested that fundamental ET approaches have differing sensitivities to data and parameterization uncertainties. Joint Bayesian uncertainty assessment of the approaches would provide a basis for application and development of the models to error-prone datasets or data-scarce regions: an immediate requirement for large scale hydrological evaluations.

Extending the Bayesian analysis to FLUXNET towers

The uncertainty assessments performed in **Chapter 5** are limited to soybean and corn and also to a relatively short period of tower data, which are not enough to capture the realistic land surface hydrological variability. FLUXNET provides a capacity for heat flux uncertainty assessment across diverse land surface conditions. However, uncertainty assessment of a single-tower requires further development of the Bayesian method. In particular, more research is necessary for developing reliable prior distributions for input data. Also, further development of the Bayesian inference technique is necessary to effectively handle all sources of uncertainty, including those caused by model structure and parameterization. In a broader view, the uncertainties assessments could include those originating from resistance parameterization of the models, as well as ones caused by non-closure of energy sources (as response errors).

6.2 Concluding Remarks

The main contributions of the current research can be summarized as: i) assessing the behaviour and performance of the models, including evaluating the significance of model structure and parameterizations across a range of land surfaces to address the application challenges; ii) multi-scale diagnosis of aggregation errors in heat flux estimation to address scaling challenges; and iii) quantifying errors in heat flux estimation via a Bayesian inference technique to address uncertainty challenges. The findings are important in better understanding the evaporative process in land-atmosphere feedback mechanisms, as well as in field to global scale application of the models for reliable ET estimation in hydrological and water resources studies. Indeed, the insights attained from the research shed light on some of the underlying issues in the estimation of evapotranspiration.

Future collaborative international research is essential to remove barriers impeding progress towards reliable ET estimation at multiple spatio-temporal scales. Such contributions are essential to support further insights into the evaporative process. Ultimately, such improvements will play a role in directly addressing some grand Earth science challenges (Reid et al. 2010) that include sustainable development and management of water resources, food security and understanding and mitigation of the global climate change.

References

- Agam, N., Kustas, W.P., Anderson, M.C., Li, F., & Neale, C.M.U. (2007). A vegetation index based technique for spatial sharpening of thermal imagery. *Remote Sensing of Environment*, 107, 545-558
- Agarwal, D.A., Humphrey, M., Beekwilder, N.F., Jackson, K.R., Goode, M.M., & van Ingen, C. (2010). A data-centered collaboration portal to support global carbon-flux analysis. *Concurrency and Computation: Practice and Experience*, 22, 2323-2334
- Ali, M.F., & Mawdsley, J.A. (1987). Comparison of two recent models for estimating actual evapotranspiration using only regularly recorded data. *Journal of Hydrology*, 93, 257-276
- Allen, R., Pereira, L., Smith, M., Raes, D., & Wright, J. (2005). FAO-56 Dual Crop Coefficient Method for Estimating Evaporation from Soil and Application Extensions. *Journal of Irrigation and Drainage Engineering*, 131, 2-13
- Allen, R.G. (2000). Using the FAO-56 dual crop coefficient method over an irrigated region as part of an evapotranspiration intercomparison study. *Journal of Hydrology*, 229, 27-41
- Allen, R.G., Pereira, L.S., Howell, T.A., & Jensen, M.E. (2011a). Evapotranspiration information reporting: I. Factors governing measurement accuracy. *Agricultural Water Management*, 98, 899-920
- Allen, R.G., Pereira, L.S., Howell, T.A., & Jensen, M.E. (2011b). Evapotranspiration information reporting: II. Recommended documentation. *Agricultural Water Management*, 98, 921-929
- Allen, R.G., Perista, L.S., Raes, D., & Smith, M. (1998). Crop evapotranspiration - Guidelines for computing crop water requirements; FAO Irrigation and Drainage Papers - 56. In. Rome: FAO - Food and Agriculture Organization of the United Nations
- Allen, R.G., Tasumi, M., Morse, A., Trezza, R., Wright, J.L., Bastiaanssen, W., Kramber, W., Lorite, I., & Robison, C.W. (2007a). Satellite-Based Energy Balance for Mapping Evapotranspiration with Internalized Calibration (METRIC)-Applications. *Journal of Irrigation and Drainage Engineering*, 133, 395-406
- Allen, R.G., Tasumi, M., & Trezza, R. (2007b). Satellite-Based Energy Balance for Mapping Evapotranspiration with Internalized Calibration (METRIC)-Model. *Journal of Irrigation and Drainage Engineering*, 133, 380-394
- Alves, I., Perrier, A., & Pereira, L.S. (1998). Aerodynamic and surface resistances of complete cover crops: How good is the big leaf? *Transactions of the ASAE*, 41, 345-351
- Alves, I., & Santos Pereira, L. (2000). Modelling surface resistance from climatic variables? *Agricultural Water Management*, 42, 371-385

References

- Anderson, M. (2003). SMEX02 Watershed Vegetation Sampling Data, Walnut Creek, Iowa. In: Boulder, CO: National Snow and Ice Data Center. Digital media.
- Anderson, M.C., Kustas, W.P., & Norman, J.M. (2003). Upscaling and Downscaling-A Regional View of the Soil-Plant-Atmosphere Continuum. *Agronomy Journal*, 95, 1408-1423
- Anderson, M.C., Kustas, W.P., & Norman, J.M. (2007). Upscaling Flux Observations from Local to Continental Scales Using Thermal Remote Sensing. *Agronomy Journal*, 99, 240-254
- Anderson, M.C., Kustas, W.P., Norman, J.M., Hain, C.R., Mecikalski, J.R., Schultz, L., Gonzalez-Dugo, M.P., Cammalleri, C., d'Urso, G., Pimstein, A., & Gao, F. (2011). Mapping daily evapotranspiration at field to continental scales using geostationary and polar orbiting satellite imagery. *Hydrol. Earth Syst. Sci.*, 15, 223-239
- Anderson, M.C., Neale, C.M.U., Li, F., Norman, J.M., Kustas, W.P., Jayanthi, H., & Chavez, J. (2004a). Upscaling ground observations of vegetation water content, canopy height, and leaf area index during SMEX02 using aircraft and Landsat imagery. *Remote Sensing of Environment*, 92, 447-464
- Anderson, M.C., Norman, J.M., Kustas, W.P., Li, F., Prueger, J.H., & Mecikalski, J.R. (2005). Effects of Vegetation Clumping on Two-Source Model Estimates of Surface Energy Fluxes from an Agricultural Landscape during SMACEX. *Journal of Hydrometeorology*, 6, 892-909
- Anderson, M.C., Norman, J.M., Mecikalski, J.R., Torn, R.D., Kustas, W.P., & Basara, J.B. (2004b). A Multiscale Remote Sensing Model for Disaggregating Regional Fluxes to Micrometeorological Scales. *Journal of Hydrometeorology*, 5, 343-363
- Aubinet, M., Vesala, T., & Papale, D. (2012). *Eddy covariance: a practical guide to measurement and data analysis*: Springer
- Avissar, R., & Pielke, R.A. (1989). A Parameterization of Heterogeneous Land Surfaces for Atmospheric Numerical Models and Its Impact on Regional Meteorology. *Monthly Weather Review*, 117, 2113-2136
- Bailey, W.G., & Davies, J.A. (1981). The effect of uncertainty in aerodynamic resistance on evaporation estimates from the combination model. *Boundary-Layer Meteorology*, 20, 187-199
- Baldocchi, D., Falge, E., Gu, L., Olson, R., Hollinger, D., Running, S., Anthoni, P., Bernhofer, C., Davis, K., Evans, R., Fuentes, J., Goldstein, A., Katul, G., Law, B., Lee, X., Malhi, Y., Meyers, T., Munger, W., Oechel, W., Paw, K.T., Pilegaard, K., Schmid, H.P., Valentini, R., Verma, S., Vesala, T., Wilson, K., & Wofsy, S. (2001). FLUXNET: A New Tool to Study the Temporal and Spatial Variability of Ecosystem-Scale Carbon Dioxide, Water Vapor, and Energy Flux Densities. *Bulletin of the American Meteorological Society*, 82, 2415-2434
- Ball, J. (1987). A model predicting stomatal conductance and its contribution to the control of photosynthesis under different environmental conditions. In, *Prog.*

- Photosynthesis Res. Proc. Int. Congress 7th, Providence. 10-15 Aug 1986. Vol4. Kluwer, Boston.* (pp. 221-224)
- Barr, A.G., Morgenstern, K., Black, T.A., McCaughey, J.H., & Nesic, Z. (2006). Surface energy balance closure by the eddy-covariance method above three boreal forest stands and implications for the measurement of the CO₂ flux. *Agricultural and Forest Meteorology*, 140, 322-337
- Bastiaanssen, W.G.M., Menenti, M., Feddes, R.A., & Holtslag, A.A.M. (1998a). A remote sensing surface energy balance algorithm for land (SEBAL). 1. Formulation. *Journal of Hydrology*, 212-213, 198-212
- Bastiaanssen, W.G.M., Pelgrum, H., Wang, J., Ma, Y., Moreno, J.F., Roerink, G.J., & van der Wal, T. (1998b). A remote sensing surface energy balance algorithm for land (SEBAL). 2. Validation. *Journal of Hydrology*, 212-213, 213-229
- Becker, F., & Li, Z.L. (1995). Surface temperature and emissivity at various scales: Definition, measurement and related problems. *Remote Sensing Reviews*, 12, 225-253
- Beljaars, A.C.M., & Holtslag, A.A.M. (1991). Flux Parameterization over Land Surfaces for Atmospheric Models. *Journal of Applied Meteorology*, 30, 327-341
- Berk, A., Anderson, G.P., Acharya, P.K., & Shettle, E.P. (2008). MODTRAN®5.2.0.0 User's Manual. In (p. 98): SPECTRAL SCIENCES, INC.
- Bertoldi, G., Kustas, W.P., & Albertson, J.D. (2008). Estimating Spatial Variability in Atmospheric Properties over Remotely Sensed Land Surface Conditions. *Journal of Applied Meteorology and Climatology*, 47, 2147-2165
- Beven, K. (1979). A sensitivity analysis of the Penman-Monteith actual evapotranspiration estimates. *Journal of Hydrology*, 44, 169-190
- Beven, K. (1989). Changing ideas in hydrology – The case of physically-based models. *Journal of Hydrology*, 105, 157-172
- Beven, K. (2006). A manifesto for the equifinality thesis. *Journal of Hydrology*, 320, 18-36
- Beven, K., & Freer, J. (2001). Equifinality, data assimilation, and uncertainty estimation in mechanistic modelling of complex environmental systems using the GLUE methodology. *Journal of Hydrology*, 249, 11-29
- Biswas, A.K. (2004). Integrated Water Resources Management: A Reassessment. *Water International*, 29, 248-256
- Bormann, H. (2011). Sensitivity analysis of 18 different potential evapotranspiration models to observed climatic change at German climate stations. *Climatic Change*, 104, 729-753
- Bos, M.G., Kselik, R.A.L., Allen, R.G., & Molden, D.J. (2008). *Water Requirements for Irrigation and the Environment*. Dordrecht: Springer

- Bouchet, R.J. (1963a). Evapotranspiration réelle et potentielle, signification climatique. In, *General Assembly Berkeley, International Association for Hydrological Sciences* (pp. 134-142). Gentbrugge, Belgium
- Bouchet, R.J. (1963b). Evapotranspiration réelle, evapotranspiration potentielle, et production agricole. *Ann Agron*, 14, 743-824
- Bowen, I.S. (1926). The Ratio of Heat Losses by Conduction and by Evaporation from any Water Surface. *Physical Review*, 27, 779-787
- Brenner, A.J., & Incoll, L.D. (1997). The effect of clumping and stomatal response on evaporation from sparsely vegetated shrublands. *Agricultural and Forest Meteorology*, 84, 187-205
- Brooks, S.P., & Gelman, A. (1998). General Methods for Monitoring Convergence of Iterative Simulations. *Journal of Computational and Graphical Statistics*, 7, 434-455
- Brunsell, N.A., & Anderson, M.C. (2011). Characterizing the multi-scale spatial structure of remotely sensed evapotranspiration with information theory. *Biogeosciences*, 8, 2269-2280
- Brunsell, N.A., & Gillies, R.R. (2003). Scale issues in land-atmosphere interactions: implications for remote sensing of the surface energy balance. *Agricultural and Forest Meteorology*, 117, 203-221
- Brunsell, N.A., Ham, J.M., & Owensby, C.E. (2008). Assessing the multi-resolution information content of remotely sensed variables and elevation for evapotranspiration in a tall-grass prairie environment. *Remote Sensing of Environment*, 112, 2977-2987
- Brutsaert, W. (1982). *Evaporation Into the Atmosphere : theory, history, and applications*. Dordrecht etc.: Reidel Publishing
- Brutsaert, W. (1999). Aspects of Bulk Atmospheric Boundary Layer Similarity Under Free-Convective Conditions. *Rev. Geophys.*, 37
- Brutsaert, W. (2005). *Hydrology : An Introduction*. Cambridge: Cambridge University Press
- Brutsaert, W., & Stricker, H. (1979). An advection-aridity approach to estimate actual regional evapotranspiration. *Water Resour. Res.*, 15, 443-450
- Buizza, R., Milleer, M., & Palmer, T.N. (1999). Stochastic representation of model uncertainties in the ECMWF ensemble prediction system. *Quarterly Journal of the Royal Meteorological Society*, 125, 2887-2908
- Burba, G.G., & Verma, S.B. (2005). Seasonal and interannual variability in evapotranspiration of native tallgrass prairie and cultivated wheat ecosystems. *Agricultural and Forest Meteorology*, 135, 190-201

- Calvet, J.C., Noilhan, J., & Bessemoulin, P. (1998). Retrieving the root-zone soil moisture from surface soil moisture or temperature estimates: A feasibility study based on field measurements. *Journal of Applied Meteorology*, 37, 371-386
- Campbell, G.S., & Norman, J.M. (1998). *An Introduction to Environmental Biophysics*. New York: Springer-Verlag
- Carlson, T. (2007). An Overview of the "Triangle Method" for Estimating Surface Evapotranspiration and Soil Moisture from Satellite Imagery. *Sensors*, 7, 1612-1629
- Castelletti, A., & Soncini-Sessa, R. (2007). Bayesian Networks and participatory modelling in water resource management. *Environmental Modelling & Software*, 22, 1075-1088
- Cavanaugh, M.L., Kurc, S.A., & Scott, R.L. (2011). Evapotranspiration partitioning in semiarid shrubland ecosystems: a two-site evaluation of soil moisture control on transpiration. *Ecology*, 92, 671-681
- Chander, G., & Markham, B. (2003). Revised Landsat-5 TM radiometric calibration procedures and postcalibration dynamic ranges. *IEEE Transactions on Geoscience and Remote Sensing*, 41, 2674-2677
- Chander, G., Markham, B.L., & Barsi, J.A. (2007). Revised Landsat-5 Thematic Mapper Radiometric Calibration. *Geoscience and Remote Sensing Letters, IEEE*, 4, 490-494
- Chen, F., & Dudhia, J. (2001). Coupling an Advanced Land Surface-Hydrology Model with the Penn State-NCAR MM5 Modeling System. Part I: Model Implementation and Sensitivity. *Monthly Weather Review*, 129, 569-585
- Chen, F., Janjić, Z., & Mitchell, K. (1997). Impact of Atmospheric Surface-layer Parameterizations in the new Land-surface Scheme of the NCEP Mesoscale Eta Model. *Boundary-Layer Meteorology*, 85, 391-421
- Chen, F., Zhao, X., & Ye, H. (2012). Making Use of the Landsat 7 SLC-off ETM+ Image Through Different Recovering Approaches
- Choi, M., Kustas, W.P., Anderson, M.C., Allen, R.G., Li, F., & Kjaersgaard, J.H. (2009). An intercomparison of three remote sensing-based surface energy balance algorithms over a corn and soybean production region (Iowa, U.S.) during SMACEX. *Agricultural and Forest Meteorology*, In Press, Corrected Proof
- Choudhury, B.J., & Monteith, J.L. (1988). A four-layer model for the heat budget of homogeneous land surfaces. *Quarterly Journal of the Royal Meteorological Society*, 114, 373-398
- Christensen, N., & Lettenmaier, D.P. (2006). A multimodel ensemble approach to assessment of climate change impacts on the hydrology and water resources of the Colorado River basin. *Hydrol. Earth Syst. Sci. Discuss.*, 3, 3727-3770

- Cleugh, H.A., Leuning, R., Mu, Q., & Running, S.W. (2007). Regional evaporation estimates from flux tower and MODIS satellite data. *Remote Sensing of Environment*, 106, 285-304
- Crago, R., & Crowley, R. (2005). Complementary relationships for near-instantaneous evaporation. *Journal of Hydrology*, 300, 199-211
- Crago, R., Hervol, N., & Crowley, R. (2005). A complementary evaporation approach to the scalar roughness length. *Water Resour. Res.*, 41, W06017
- Crago, R.D., & Brutsaert, W. (1992). A comparison of several evaporation equations. *Water Resour. Res.*, 28, 951-954
- Curtis, P.S., Hanson, P.J., Bolstad, P., Barford, C., Randolph, J.C., Schmid, H.P., & Wilson, K.B. (2002). Biometric and eddy-covariance based estimates of annual carbon storage in five eastern North American deciduous forests. *Agricultural and Forest Meteorology*, 113, 3-19
- Daamen, C.C. (1997). Two source model of surface fluxes for millet fields in Niger. *Agricultural and Forest Meteorology*, 83, 205-230
- Dagan, G. (1985). Stochastic Modeling of Groundwater Flow by Unconditional and Conditional Probabilities: The Inverse Problem. *Water Resour. Res.*, 21, 65-72
- Dalton, J. (1802). *Experiments and Observations to Determine Whether the Quantity of Rain and Dew is Equal to the Quantity of Water Carried Off by the Rivers and Raised by Evaporation: With an Enquiry Into the Origin of Springs*
- De Bruin, H.A.R., & Keijman, J.Q. (1979). The Priestley-Taylor Evaporation Model Applied to a Large, Shallow Lake in the Netherlands. *Journal of Applied Meteorology*, 18, 898-903
- Delpierre, N., Soudani, K., Francois, C., Köstner, B., Pontailler, J.Y., Nikinmaa, E., Misson, L., Aubinet, M., Bernhofer, C., & Granier, A. (2009). Exceptional carbon uptake in European forests during the warm spring of 2007: a data-model analysis. *Global Change Biology*, 15, 1455-1474
- Dickinson, R.E., Henderson-Sellers, A., Rosenzweig, C., & Sellers, P.J. (1991). Evapotranspiration models with canopy resistance for use in climate models, a review. *Agricultural and Forest Meteorology*, 54, 373-388
- Dolman, A.J. (1993). A multiple-source land surface energy balance model for use in general circulation models. *Agricultural and Forest Meteorology*, 65, 21-45
- Domingo, F., Villagarcía, L., Brenner, A.J., & Puigdefábregas, J. (1999). Evapotranspiration model for semi-arid shrub-lands tested against data from SE Spain. *Agricultural and Forest Meteorology*, 95, 67-84
- Doorenbos, J., & Pruitt, W.O. (1975). Guidelines for predicting crop water requirements. *Irrigation and drainage paper*

- Dragoni, D., Schmid, H.P., Wayson, C.A., Potter, H., Grimmond, C.S.B., & Randolph, J.C. (2011). Evidence of increased net ecosystem productivity associated with a longer vegetated season in a deciduous forest in south-central Indiana, USA. *Global Change Biology*, 17, 886-897
- Droogers, P., Immerzeel, W.W., Terink, W., Hoogeveen, J., Bierkens, M.F.P., van Beek, L.P.H., & Debele, B. (2012). Water resources trends in Middle East and North Africa towards 2050. *Hydrol. Earth Syst. Sci.*, 16, 3101-3114
- Duan, Q., Ajami, N.K., Gao, X., & Sorooshian, S. (2007). Multi-model ensemble hydrologic prediction using Bayesian model averaging. *Advances in Water Resources*, 30, 1371-1386
- Dunin, F.X., & Aston, A.R. (1984). The development and proving of models of large scale evapotranspiration: An Australian study. *Agricultural Water Management*, 8, 305-323
- Eichinger, W.E., Parlange, M.B., & Stricker, H. (1996). On the Concept of Equilibrium Evaporation and the Value of the Priestley-Taylor Coefficient. *Water Resour. Res.*, 32, 161-164
- Ek, M.B., Mitchell, K.E., Lin, Y., Rogers, E., Grunmann, P., Koren, V., Gayno, G., & Tarpley, J.D. (2003). Implementation of Noah land surface model advances in the National Centers for Environmental Prediction operational mesoscale Eta model. *J. Geophys. Res.*, 108, 8851
- El Tahir, M., Wenzhong, W., Xu, C., Youjing, Z., & Singh, V. (2011). Comparison of Methods for Estimation of Regional Actual Evapotranspiration in Data Scarce Regions: Blue Nile Region, Eastern Sudan. *Journal of Hydrologic Engineering*, 17, 578-589
- Elhag, M., Psilovikos, A., Manakos, I., & Perakis, K. (2011). Application of the SEBS Water Balance Model in Estimating Daily Evapotranspiration and Evaporative Fraction from Remote Sensing Data Over the Nile Delta. *Water Resources Management*, 25, 2731-2742
- Entekhabi, D., & Eagleson, P.S. (1989). Land Surface Hydrology Parameterization for Atmospheric General Circulation models Including Subgrid Scale Spatial Variability. *Journal of Climate*, 2, 816-831
- Er-Raki, S., Chehbouni, A., Guemouria, N., Duchemin, B., Ezzahar, J., & Hadria, R. (2007). Combining FAO-56 model and ground-based remote sensing to estimate water consumptions of wheat crops in a semi-arid region. *Agricultural Water Management*, 87, 41-54
- Ershadi, A., McCabe, M.F., Evans, J.P., Chaney, N.W., & Wood, E. (In review-a). Multi-site evaluation of terrestrial evapotranspiration models using globally distributed FLUXNET data. *Agricultural and Forest Meteorology*
- Ershadi, A., McCabe, M.F., Evans, J.P., Chaney, N.W., & Wood, E.F. (In Review-b). Significance of model structure and parameterization on Penman-Monteith type evapotranspiration models. *Journal of Hydrology*

References

- Ershadi, A., McCabe, M.F., Evans, J.P., Mariethoz, G., & Kavetski, D. (2013a). A Bayesian analysis of sensible heat flux estimation: Quantifying uncertainty in meteorological forcing to improve model prediction. *Water Resources Research*, 49, 2343-2358
- Ershadi, A., McCabe, M.F., Evans, J.P., & Walker, J.P. (2013b). Effects of spatial aggregation on the multi-scale estimation of evapotranspiration. *Remote Sensing of Environment*, 131, 51-62
- Evans, J.P., & McCabe, M.F. (2010). Regional climate simulation over Australia's Murray-Darling basin: A multitemporal assessment. *J. Geophys. Res.*, 115, D14114
- Evetts, S.R., Kustas, W.P., Gowda, P.H., Anderson, M.C., Prueger, J.H., & Howell, T.A. (2012). Overview of the Bushland Evapotranspiration and Agricultural Remote sensing EXperiment 2008 (BEAREX08): A field experiment evaluating methods for quantifying ET at multiple scales. *Advances in Water Resources*
- Famiglietti, J.S., & Wood, E.F. (1994). Application of multiscale water and energy balance models on a tallgrass prairie. *Water Resour. Res.*, 30, 3079-3093
- Farahani, H.J., & Ahuja, L.R. (1996). *Evapotranspiration modeling of partial canopy/residue-covered fields*. St. Joseph, MI, ETATS-UNIS: American Society of Agricultural Engineers
- Farahani, H.J., & Bausch, W.C. (1995). Performance of evapotranspiration models for maize—bare soil to closed canopy. *Transactions of the ASAE*, 38, 1049-1059
- Farahani, H.J., Howell, T.A., Shuttleworth, W.J., & Bausch, W.C. (2007). Evapotranspiration: progress in measurement and modeling in agriculture. *Trans. Asabe*, 50, 1627-1638
- Ferguson, C.R., Sheffield, J., Wood, E.F., & Gao, H. (2010). Quantifying uncertainty in a remote sensing-based estimate of evapotranspiration over continental USA. *International Journal of Remote Sensing*, 31, 3821-3865
- Ferguson, C.R., Wood, E.F., & Vinukollu, R.K. (2012). A Global Intercomparison of Modeled and Observed Land-Atmosphere Coupling*. *Journal of Hydrometeorology*, 13, 749-784
- Finnigan, J.J., Clement, R., Malhi, Y., Leuning, R., & Cleugh, H.A. (2003). A re-evaluation of long-term flux measurement techniques - Part I: Averaging and coordinate rotation. *Boundary-Layer Meteorology*, 107, 1-48
- Fisher, J.B., DeBiase, T.A., Qi, Y., Xu, M., & Goldstein, A.H. (2005). Evapotranspiration models compared on a Sierra Nevada forest ecosystem. *Environmental Modelling & Software*, 20, 783-796
- Fisher, J.B., Tu, K.P., & Baldocchi, D.D. (2008). Global estimates of the land-atmosphere water flux based on monthly AVHRR and ISLSCP-II data, validated at 16 FLUXNET sites. *Remote Sensing of Environment*, 112, 901-919

References

- Fisher, J.B., Whittaker, R.J., & Malhi, Y. (2011). ET come home: potential evapotranspiration in geographical ecology. *Global Ecology and Biogeography*, 20, 1-18
- Flint, A.L., & Childs, S.W. (1991). Use of the Priestley-Taylor evaporation equation for soil water limited conditions in a small forest clearcut. *Agricultural and Forest Meteorology*, 56, 247-260
- Foken, T. (2008). The energy balance closure problem: An overview. *Ecological Applications*, 18, 1351-1367
- Foken, T., Aubinet, M., Finnigan, J.J., Leclerc, M.Y., Mauder, M., & PawU, K.T. (2011). Results of a panel discussion about the energy balance closure correction for trace gases. *Bulletin of the American Meteorological Society*, 92
- Foken, T., Leuning, R., Oncley, S.R., Mauder, M., & Aubinet, M. (2012). Corrections and Data Quality Control. In M. Aubinet, T. Vesala & D. Papale (Eds.), *Eddy Covariance, A Practical Guide to Measurement and Data Analysis*: Springer
- Franssen, H.J.H., Stöckli, R., Lehner, I., Rotenberg, E., & Seneviratne, S.I. (2010). Energy balance closure of eddy-covariance data: A multisite analysis for European FLUXNET stations. *Agricultural and Forest Meteorology*, 150, 1553-1567
- Furon, A.C., Warland, J.S., & Wagner-Riddle, C. (2007). Analysis of Scaling-Up Resistances from Leaf to Canopy Using Numerical Simulations. *Agron. J.*, 99, 1483-1491
- García, M., Sandholt, I., Ceccato, P., Ridler, M., Mougín, E., Kergoat, L., Morillas, L., Timouk, F., Fensholt, R., & Domingo, F. (2013). Actual evapotranspiration in drylands derived from in-situ and satellite data: Assessing biophysical constraints. *Remote Sensing of Environment*, 131, 103-118
- Gebremichael, M., Wang, J., & Sammis, T.W. (2010). Dependence of remote sensing evapotranspiration algorithm on spatial resolution. *Atmospheric Research*, 96, 489-495
- Gelman, A., & Rubin, D.B. (1992). Inference from Iterative Simulation Using Multiple Sequences. *Statistical Science*, 7, 457-472
- Gibson, L.A., Münch, Z., & Engelbrecht, J. (2011). Particular uncertainties encountered in using a pre-packaged SEBS model to derive evapotranspiration in a heterogeneous study area in South Africa. *Hydrol. Earth Syst. Sci.*, 15, 295-310
- Gilmanov, T.G., Soussana, J.F., Aires, L., Allard, V., Ammann, C., Balzarolo, M., Barcza, Z., Bernhofer, C., Campbell, C.L., & Cernusca, A. (2007). Partitioning European grassland net ecosystem CO₂ exchange into gross primary productivity and ecosystem respiration using light response function analysis. *Agriculture, ecosystems & environment*, 121, 93-120
- Gokmen, M., Vekerdy, Z., Verhoef, A., Verhoef, W., Batelaan, O., & van der Tol, C. (2012). Integration of soil moisture in SEBS for improving evapotranspiration estimation under water stress conditions. *Remote Sensing of Environment*, 121, 261-274

References

- Goss, M.J., & Ehlers, W. (2009). The role of lysimeters in the development of our understanding of soil water and nutrient dynamics in ecosystems. *Soil Use and Management*, 25, 213-223
- Graham, L.P., Andréasson, J., & Carlsson, B. (2007). Assessing climate change impacts on hydrology from an ensemble of regional climate models, model scales and linking methods – a case study on the Lule River basin. *Climatic Change*, 81, 293-307
- Granger, R.J., & Gray, D.M. (1989). Evaporation from natural nonsaturated surfaces. *Journal of Hydrology*, 111, 21-29
- Granier, A., Huc, R., & Barigah, S.T. (1996). Transpiration of natural rain forest and its dependence on climatic factors. *Agricultural and Forest Meteorology*, 78, 19-29
- Guo, Z., Dirmeyer, P.A., Gao, X., & Zhao, M. (2007). Improving the quality of simulated soil moisture with a multi-model ensemble approach. *Quarterly Journal of the Royal Meteorological Society*, 133, 731-747
- Han, S., Hu, H., Yang, D., & Tian, F. (2011). A complementary relationship evaporation model referring to the Granger model and the advection–aridity model. *Hydrological Processes*, 25, 2094-2101
- Harman, I. (2012). The Role of Roughness Sublayer Dynamics Within Surface Exchange Schemes. *Boundary-Layer Meteorology*, 142, 1-20
- Harman, I., & Finnigan, J. (2007). A simple unified theory for flow in the canopy and roughness sublayer. *Boundary-Layer Meteorology*, 123, 339-363
- Hatfield, J.L., Prueger, J.H., & Meek, D.W. (1999). Spatial Variation of Rainfall over a Large Watershed in Central Iowa. *Theoretical and Applied Climatology*, 64, 49-60
- Haverd, V., Cuntz, M., Leuning, R., & Keith, H. (2007). Air and biomass heat storage fluxes in a forest canopy: Calculation within a soil vegetation atmosphere transfer model. *Agricultural and Forest Meteorology*, 147, 125-139
- Helgason, W., & Pomeroy, J.W. (2011). Characteristics of the Near-Surface Boundary Layer within a Mountain Valley during Winter. *Journal of Applied Meteorology and Climatology*, 51, 583-597
- Hobbins, M.T., Ramírez, J.A., & Brown, T.C. (2001). The complementary relationship in estimation of regional evapotranspiration: An enhanced advection-aridity model. *Water Resour. Res.*, 37, 1389-1403
- Hollinger, D.Y., Ollinger, S.V., Richardson, A.D., Meyers, T.P., Dail, D.B., Martin, M.E., Scott, N.A., Arkebauer, T.J., Baldocchi, D.D., & Clark, K.L. (2010). Albedo estimates for land surface models and support for a new paradigm based on foliage nitrogen concentration. *Global Change Biology*, 16, 696-710
- Hollinger, D.Y., & Richardson, A.D. (2005). Uncertainty in eddy covariance measurements and its application to physiological models. *Tree Physiology*, 25, 873-885

- Holmes, J.W. (1984). Measuring evapotranspiration by hydrological methods. *Agricultural Water Management*, 8, 29-40
- Hong, S.-h., Hendrickx, J.M.H., & Borchers, B. (2009). Up-scaling of SEBAL derived evapotranspiration maps from Landsat (30 m) to MODIS (250 m) scale. *Journal of Hydrology*, 370, 122-138
- Horn, J.E., & Schulz, K. (2011). Identification of a general light use efficiency model for gross primary production. *Biogeosciences*, 8, 999 - 1021
- Hu, Z., Yu, G., Zhou, Y., Sun, X., Li, Y., Shi, P., Wang, Y., Song, X., Zheng, Z., Zhang, L., & Li, S. (2009). Partitioning of evapotranspiration and its controls in four grassland ecosystems: Application of a two-source model. *Agricultural and Forest Meteorology*, 149, 1410-1420
- Huard, D., & Mailhot, A. (2006). A Bayesian perspective on input uncertainty in model calibration: Application to hydrological model "abc". *Water Resour. Res.*, 42, W07416
- Huntingford, C., Allen, S.J., & Harding, R.J. (1995). An intercomparison of single and dual-source vegetation-atmosphere transfer models applied to transpiration from sahelian savannah. *Boundary-Layer Meteorology*, 74, 397-418
- Huntington, J.L., Szilagyi, J., Tyler, S.W., & Pohl, G.M. (2011). Evaluating the complementary relationship for estimating evapotranspiration from arid shrublands. *Water Resour. Res.*, 47, W05533
- Hutley, L.B., Leuning, R., Beringer, J., & Cleugh, H.A. (2005). The utility of the eddy covariance techniques as a tool in carbon accounting: tropical savanna as a case study. *Australian Journal of Botany*, 53, 663-675
- Immerzeel, W.W., & Droogers, P. (2008). Calibration of a distributed hydrological model based on satellite evapotranspiration. *Journal of Hydrology*, 349, 411-424
- Inamdar, A.K., & French, A. (2009). Disaggregation of GOES land surface temperatures using surface emissivity. *Geophysical Research Letters*, 36, L02408
- Inclán, M.G., & Forkel, R. (1995). Comparison of energy fluxes calculated with the Penman-Monteith equation and the vegetation models SiB and Cupid. *Journal of Hydrology*, 166, 193-211
- Iritz, Z., Lindroth, A., Heikinheimo, M., Grelle, A., & Kellner, E. (1999). Test of a modified Shuttleworth-Wallace estimate of boreal forest evaporation. *Agricultural and Forest Meteorology*, 98-99, 605-619
- Irmak, A. (2011). *Evapotranspiration - Remote Sensing and Modeling*. Croatia: InTech
- Irmak, S., & Haman, D.Z. (2003). Evapotranspiration: potential or reference. *Agricultural Engineering, Florida Cooperative Extension Service, Institute of Food and Agricultural Sciences, University of Florida, ABE*, 343

- Irmak, S., & Mutiibwa, D. (2010). On the dynamics of canopy resistance: Generalized linear estimation and relationships with primary micrometeorological variables. *Water Resour. Res.*, *46*, W08526
- Irons, J.R., Dwyer, J.L., & Barsi, J.A. (2012). The next Landsat satellite: The Landsat Data Continuity Mission. *Remote Sensing of Environment*, *122*, 11-21
- Jabloun, M., & Sahli, A. (2008). Evaluation of FAO-56 methodology for estimating reference evapotranspiration using limited climatic data: Application to Tunisia. *Agricultural Water Management*, *95*, 707-715
- Jacquemin, B., & Noilhan, J. (1990). Sensitivity study and validation of a land surface parameterization using the HAPEX-MOBILHY data set. *Boundary-Layer Meteorology*, *52*, 93-134
- Jia, L., Su, Z., van den Hurk, B., Menenti, M., Moene, A., De Bruin, H.A.R., Yrisarry, J.J.B., Ibanez, M., & Cuesta, A. (2003). Estimation of sensible heat flux using the Surface Energy Balance System (SEBS) and ATSR measurements. *Physics and Chemistry of the Earth, Parts A/B/C*, *28*, 75-88
- Jiang, L., & Islam, S. (1999). A methodology for estimation of surface evapotranspiration over large areas using remote sensing observations. *Geophys. Res. Lett.*, *26*, 2773-2776
- Jiménez-Muñoz, J., Sobrino, J., Plaza, A., Guanter, L., Moreno, J., & Martínez, P. (2009). Comparison Between Fractional Vegetation Cover Retrievals from Vegetation Indices and Spectral Mixture Analysis: Case Study of PROBA/CHRIS Data Over an Agricultural Area. *Sensors*, *9*, 768-793
- Jiménez, C., Prigent, C., Mueller, B., Seneviratne, S.I., McCabe, M.F., Wood, E.F., Rossow, W.B., Balsamo, G., Betts, A.K., Dirmeyer, P.A., Fisher, J.B., Jung, M., Kanamitsu, M., Reichle, R.H., Reichstein, M., Rodell, M., Sheffield, J., Tu, K., & Wang, K. (2011a). Global intercomparison of 12 land surface heat flux estimates. *J. Geophys. Res.*, *116*, D02102
- Jiménez, C., Prigent, C., Mueller, B., Seneviratne, S.I., McCabe, M.F., Wood, E.F., Rossow, W.B., Balsamo, G., Betts, A.K., Dirmeyer, P.A., Fisher, J.B., Jung, M., Kanamitsu, M., Reichle, R.H., Reichstein, M., Rodell, M., Sheffield, J., Tu, K., & Wang, K. (2011b). Global intercomparison of 12 land surface heat flux estimates. *Journal of Geophysical Research D: Atmospheres*, *116*
- Jung, M., Reichstein, M., & Bondeau, A. (2009). Towards global empirical upscaling of FLUXNET eddy covariance observations: validation of a model tree ensemble approach using a biosphere model. *Biogeosciences*, *6*, 2001-2013
- Jung, M., Reichstein, M., Ciais, P., Seneviratne, S.I., Sheffield, J., Goulden, M.L., Bonan, G., Cescatti, A., Chen, J., & de Jeu, R. (2010). Recent decline in the global land evapotranspiration trend due to limited moisture supply. *Nature*, *467*, 951-954

- Kalma, J., McVicar, T., & McCabe, M. (2008). Estimating Land Surface Evaporation: A Review of Methods Using Remotely Sensed Surface Temperature Data. *Surveys in Geophysics*, 29, 421-469
- Kalma, J.D., & Jupp, D.L.B. (1990). Estimating evaporation from pasture using infrared thermometry: evaluation of a one-layer resistance model. *Agricultural and Forest Meteorology*, 51, 223-246
- Karnieli, A., Agam, N., Pinker, R.T., Anderson, M., Imhoff, M.L., Gutman, G.G., Panov, N., & Goldberg, A. (2010). Use of NDVI and Land Surface Temperature for Drought Assessment: Merits and Limitations. *Journal of Climate*, 23, 618-633
- Kass, R.E., Carlin, B.P., Gelman, A., & Neal, R.M. (1998). Markov Chain Monte Carlo in Practice: A Roundtable Discussion. *The American Statistician*, 52, 93-100
- Katerji, N., Rana, G., & Fahed, S. (2010). Parameterizing canopy resistance using mechanistic and semi-empirical estimates of hourly evapotranspiration: critical evaluation for irrigated crops in the Mediterranean. *Hydrological Processes*, 25, 117-129
- Katul, G., Goltz, S., Hsieh, C.-I., Cheng, Y., Mowry, F., & Sigmon, J. (1995). Estimation of surface heat and momentum fluxes using the flux-variance method above uniform and non-uniform terrain. *Boundary-Layer Meteorology*, 74, 237-260
- Katul, G., Hsieh, C.-I., Bowling, D., Clark, K., Shurpali, N., Turnipseed, A., Albertson, J., Tu, K., Hollinger, D., Evans, B., Offerle, B., Anderson, D., Ellsworth, D., Vogel, C., & Oren, R. (1999). Spatial Variability of Turbulent Fluxes in the Roughness Sublayer of an Even-Aged Pine Forest. *Boundary-Layer Meteorology*, 93, 1-28
- Kavetski, D., Franks, S.W., & Kuczera, G. (2003). Confronting input uncertainty in environmental modelling. In Q. Duan, H.V. Gupta, S. Sorooshian, A.N. Rousseau & R. Turcotte (Eds.), *Calibration of Watershed Models, Water Science and Applications Series 6* (pp. 49-68). Washington, D. C.: American Geophysical Union
- Kavetski, D., Kuczera, G., & Franks, S.W. (2006a). Bayesian analysis of input uncertainty in hydrological modeling: 1. Theory. *Water Resour. Res.*, 42, W03407
- Kavetski, D., Kuczera, G., & Franks, S.W. (2006b). Bayesian analysis of input uncertainty in hydrological modeling: 2. Application. *Water Resour. Res.*, 42, W03408
- Kelliher, F., Black, T., & Price, D. (1986). Estimating the effects of understory removal from a Douglas fir forest using a two-layer canopy evapotranspiration model. *Water Resour. Res.*, 22, 1891-1899
- Kljun, N., Calanca, P., Rotach, M., & Schmid, H. (2004). A Simple Parameterisation for Flux Footprint Predictions. *Boundary-Layer Meteorology*, 112, 503-523
- Kracher, D., Mengelkamp, H.-T., & Foken, T. (2009). The residual of the energy balance closure and its influence on the results of three SVAT models. *Meteorologische Zeitschrift*, 18, 647-661

References

- Kuczera, G., Kavetski, D., Franks, S., & Thyer, M. (2006). Towards a Bayesian total error analysis of conceptual rainfall-runoff models: Characterising model error using storm-dependent parameters. *Journal of Hydrology*, 331, 161-177
- Kuczera, G., Kavetski, D., Renard, B., & Thyer, M. (2010). A limited-memory acceleration strategy for MCMC sampling in hierarchical Bayesian calibration of hydrological models. *Water Resour. Res.*, 46, W07602
- Kumar, A., Chen, F., Niyogi, D., Alfieri, J., Ek, M., & Mitchell, K. (2011). Evaluation of a Photosynthesis-Based Canopy Resistance Formulation in the Noah Land-Surface Model. *Boundary-Layer Meteorology*, 138, 263-284
- Kustas, W., & Anderson, M. (2009). Advances in thermal infrared remote sensing for land surface modeling. *Agricultural and Forest Meteorology*, 149, 2071-2081
- Kustas, W.P. (1990). Estimates of evapotranspiration with a one-and two-layer model of heat transfer over partial canopy cover. *Journal of Applied Meteorology*, 29, 704-715
- Kustas, W.P., & Albertson, J.D. (2003). Effects of surface temperature contrast on land-atmosphere exchange: A case study from Monsoon 90. *Water Resources Research*, 39, 1159
- Kustas, W.P., Anderson, M.C., French, A.N., & Vickers, D. (2006). Using a remote sensing field experiment to investigate flux-footprint relations and flux sampling distributions for tower and aircraft-based observations. *Advances in Water Resources*, 29, 355-368
- Kustas, W.P., & Brutsaert, W. (1987). Budgets of Water Vapor in the Unstable Boundary Layer over Rugged Terrain. *Journal of Climate and Applied Meteorology*, 26, 607-620
- Kustas, W.P., & Daughtry, C.S.T. (1990). Estimation of the soil heat flux/net radiation ratio from spectral data. *Agricultural and Forest Meteorology*, 49, 205-223
- Kustas, W.P., Hatfield, J.L., & Prueger, J.H. (2005). The Soil Moisture-Atmosphere Coupling Experiment (SMACEX): Background, Hydrometeorological Conditions, and Preliminary Findings. *Journal of Hydrometeorology*, 6, 791-804
- Kustas, W.P., Li, F., Jackson, T.J., Prueger, J.H., MacPherson, J.I., & Wolde, M. (2004). Effects of remote sensing pixel resolution on modeled energy flux variability of croplands in Iowa. *Remote Sensing of Environment*, 92, 535-547
- Kustas, W.P., & Norman, J.M. (1996). Use of remote sensing for evapotranspiration monitoring over land surfaces. *Hydrological sciences journal*, 41, 495-516
- Kustas, W.P., & Norman, J.M. (2000). Evaluating the effects of subpixel heterogeneity on pixel average fluxes. *Remote Sensing of Environment*, 74, 327-342
- Kustas, W.P., Norman, J.M., Anderson, M.C., & French, A.N. (2003). Estimating subpixel surface temperatures and energy fluxes from the vegetation index-radiometric temperature relationship. *Remote Sensing of Environment*, 85, 429-440

- Ladson, T., Lander, J., Western, A., Grayson, R., & Zhang, L. (2004). *Estimating extractable soil moisture content for Australian soils*: CRC for Catchment Hydrology
- Lagos, L., Martin, D., Verma, S., Suyker, A., & Irmak, S. (2009). Surface energy balance model of transpiration from variable canopy cover and evaporation from residue-covered or bare-soil systems. *Irrigation Science*, 28, 51-64
- Leclerc, M.Y., & Thurtell, G.W. (1990). Footprint prediction of scalar fluxes using a Markovian analysis. *Boundary-Layer Meteorology*, 52, 247-258
- Leuning, R., Zhang, Y.Q., Rajaud, A., Cleugh, H., & Tu, K. (2008). A simple surface conductance model to estimate regional evaporation using MODIS leaf area index and the Penman-Monteith equation. *Water Resour. Res.*, 44, W10419
- Lhomme, J.P., Montes, C., Jacob, F., & Prévot, L. (2012). Evaporation from Heterogeneous and Sparse Canopies: On the Formulations Related to Multi-Source Representations. *Boundary-Layer Meteorology*, 144, 243-262
- Li, F., Jackson, T.J., Kustas, W.P., Schmugge, T.J., French, A.N., Cosh, M.H., & Bindlish, R. (2004). Deriving land surface temperature from Landsat 5 and 7 during SMEX02/SMACEX. *Remote Sensing of Environment*, 92, 521-534
- Li, F., Kustas, W.P., Anderson, M.C., Prueger, J.H., & Scott, R.L. (2008). Effect of remote sensing spatial resolution on interpreting tower-based flux observations. *Remote Sensing of Environment*, 112, 337-349
- Li, L., Luo, G., Chen, X., Li, Y., Xu, G., Xu, H., & Bai, J. (2011). Modelling evapotranspiration in a Central Asian desert ecosystem. *Ecological Modelling*, 222, 3680-3691
- Li, X., Yang, P., Ren, S., Li, Y., Liu, H., Du, J., Li, P., Wang, C., & Ren, L. (2010a). Modeling cherry orchard evapotranspiration based on an improved dual-source model. *Agricultural Water Management*, 98, 12-18
- Li, X., Yang, P., Ren, S., Li, Y., Xu, T., Ren, L., & Wang, C. (2010b). An improved canopy transpiration model and parameter uncertainty analysis by Bayesian approach. *Mathematical and Computer Modelling*, 51, 1368-1374
- Liu, G., Liu, Y., Hafeez, M., Xu, D., & Vote, C. (2012). Comparison of two methods to derive time series of actual evapotranspiration using eddy covariance measurements in the southeastern Australia. *Journal of Hydrology*, 454-455, 1-6
- Liu, Y., Zhuang, Q., Chen, M., Pan, Z., Tchebakova, N., Sokolov, A., Kicklighter, D., Melillo, J., Sirin, A., Zhou, G., He, Y., Chen, J., Bowling, L., Miralles, D., & Parfenova, E. (2013). Response of evapotranspiration and water availability to changing climate and land cover on the Mongolian Plateau during the 21st century. *Global and Planetary Change*, 108, 85-99
- Lokupitiya, E., Denning, S., Paustian, K., Baker, I., Schaefer, K., VERMA, S., MEYERS, T., Bernacchi, C.J., SUYKER, A., & Fischer, M. (2009). Incorporation of crop phenology

- in Simple Biosphere Model (SiBcrop) to improve land-atmosphere carbon exchanges from croplands. *Biogeosciences*, 6, 1103 - 1103
- Long, D., Singh, V.P., & Li, Z.L. (2011). How sensitive is SEBAL to changes in input variables, domain size and satellite sensor? *Journal of Geophysical Research D: Atmospheres*, 116
- Lu, H., Raupach, M.R., McVicar, T.R., & Barrett, D.J. (2003). Decomposition of vegetation cover into woody and herbaceous components using AVHRR NDVI time series. *Remote Sensing of Environment*, 86, 1-18
- Lu, J., Sun, G., McNulty, S.G., & Amatya, D.M. (2005). A comparison of six potential evapotranspiration methods for regional use in the southeastern United States. *JAWRA Journal of the American Water Resources Association*, 41, 621-633
- Luo, L., Wood, E.F., & Pan, M. (2007). Bayesian merging of multiple climate model forecasts for seasonal hydrological predictions. *J. Geophys. Res.*, 112, D10102
- Mackay, D.S., Ewers, B.E., Loranty, M.M., Kruger, E.L., & Samanta, S. (2012). Bayesian analysis of canopy transpiration models: A test of posterior parameter means against measurements. *Journal of Hydrology*, 432-433, 75-83
- Mahrt, L. (2010). Computing turbulent fluxes near the surface: Needed improvements. *Agricultural and Forest Meteorology*, 150, 501-509
- Mahrt, L., & Ek, M. (1984). The Influence of Atmospheric Stability on Potential Evaporation. *Journal of Climate and Applied Meteorology*, 23, 222-234
- Maidment, D.R. (1992). *Handbook of hydrology*: McGraw-Hill Inc.
- Markham, B.L., Storey, J.C., Williams, D.L., & Irons, J.R. (2004). Landsat sensor performance: history and current status. *Geoscience and Remote Sensing, IEEE Transactions on*, 42, 2691-2694
- Massman, W.J., & Lee, X. (2002). Eddy covariance flux corrections and uncertainties in long-term studies of carbon and energy exchanges. *Agricultural and Forest Meteorology*, 113, 121-144
- Mauder, M., & Foken, T. (2006). Impact of post-field data processing on eddy covariance flux estimates and energy balance closure. *Meteorologische Zeitschrift*, 15, 597-609
- Mauder, M., Foken, T., Clement, R., Elbers, J.A., Eugster, W., Grünwald, T., Heusinkveld, B., & Kolle, O. (2008). Quality control of CarboEurope flux data - Part 2: Inter-comparison of eddy-covariance software. *Biogeosciences*, 5, 451-462
- McCabe, M., Ershadi, A., Chaney, N., Jimenez, C., Miralles, D., Mueller, B., Seneviratne, S., & Wood, E. (2013). Global estimation of evapotranspiration from the GEWEX LandFlux Initiative: model intercomparison and evaluation at the tower scale. In, *EGU General Assembly Conference* (p. 6439)

References

- McCabe, M.F., Balick, L.K., Theiler, J., Gillespie, A.R., & Mushkin, A. (2008). Linear mixing in thermal infrared temperature retrieval. *International Journal of Remote Sensing*, 29, 5047-5061
- McCabe, M.F., Kalma, J.D., & Franks, S.W. (2005). Spatial and temporal patterns of land surface fluxes from remotely sensed surface temperatures within an uncertainty modelling framework. *Hydrol. Earth Syst. Sci.*, 9, 467-480
- McCabe, M.F., & Wood, E.F. (2006). Scale influences on the remote estimation of evapotranspiration using multiple satellite sensors. *Remote Sensing of Environment*, 105, 271-285
- Meijninger, W.M.L., Hartogensis, O.K., Kohsiek, W., Hoedjes, J.C.B., Zuurbier, R.M., & De Bruin, H.A.R. (2002). Determination of Area-Averaged Sensible Heat Fluxes with a Large Aperture Scintillometer over a Heterogeneous Surface – Flevoland Field Experiment. *Boundary-Layer Meteorology*, 105, 37-62
- Meyers, T.P., & Baldocchi, D.D. (2005). Current micrometeorological flux methodologies with applications in agriculture. *Micrometeorology in Agricultural Systems*, 381-396
- Miralles, D.G., Holmes, T.R.H., De Jeu, R.A.M., Gash, J.H., Meesters, A.G.C.A., & Dolman, A.J. (2011). Global land-surface evaporation estimated from satellite-based observations. *Hydrol. Earth Syst. Sci.*, 15, 453-469
- Mo, X., & Beven, K. (2004). Multi-objective parameter conditioning of a three-source wheat canopy model. *Agricultural and Forest Meteorology*, 122, 39-63
- Moffett, K.B., & Gorelick, S.M. (2012). A method to calculate heterogeneous evapotranspiration using submeter thermal infrared imagery coupled to a stomatal resistance submodel. *Water Resour. Res.*, 48, W01545
- Monin, A.S., & Obukhov, A.M. (1945). Basic laws of turbulent mixing in the surface layer of the atmosphere. *Tr. Akad. Nauk SSSR Geophys. Inst.*, 24, 163-187
- Montandon, L.M., & Small, E.E. (2008). The impact of soil reflectance on the quantification of the green vegetation fraction from NDVI. *Remote Sensing of Environment*, 112, 1835-1845
- Monteith, J.L. (1965). Evaporation and environment. *Symp. Soc. Exp. Biol.*, 19, 205-234
- Monteith, J.L. (1973). *Principles of Environmental Physics*: Edward Arnold Press
- Moore, D.S., McCabe, G.P., & Craig, B.A. (2009). Introduction to the Practice of Statistics
- Moran, S.M., Humes, K.S., & Pinter Jr, P.J. (1997). The scaling characteristics of remotely-sensed variables for sparsely-vegetated heterogeneous landscapes. *Journal of Hydrology*, 190, 337-362

- Moriasi, N., D., Arnold, G., J., Liew, V., W., M., Binger, L., R., Harmel, D., R., Veith, & L., T. (2007). *Model evaluation guidelines for systematic quantification of accuracy in watershed simulations*. St. Joseph, MI, ETATS-UNIS: American Society of Agricultural Engineers
- Mu, Q., Heinsch, F.A., Zhao, M., & Running, S.W. (2007). Development of a global evapotranspiration algorithm based on MODIS and global meteorology data. *Remote Sensing of Environment*, 111, 519-536
- Mu, Q., Zhao, M., & Running, S.W. (2011). Improvements to a MODIS global terrestrial evapotranspiration algorithm. *Remote Sensing of Environment*, 115, 1781-1800
- Mueller, B., Hirschi, M., Jimenez, C., Ciais, P., Dirmeyer, P.A., Dolman, A.J., Fisher, J.B., Jung, M., Ludwig, F., Maignan, F., Miralles, D., McCabe, M.F., Reichstein, M., Sheffield, J., Wang, K.C., Wood, E.F., Zhang, Y., & Seneviratne, S.I. (2013). Benchmark products for land evapotranspiration: LandFlux-EVAL multi-dataset synthesis. *Hydrol. Earth Syst. Sci. Discuss.*, 10, 769-805
- Mueller, B., Seneviratne, S.I., Jimenez, C., Corti, T., Hirschi, M., Balsamo, G., Ciais, P., Dirmeyer, P., Fisher, J.B., Guo, Z., Jung, M., Maignan, F., McCabe, M.F., Reichle, R., Reichstein, M., Rodell, M., Sheffield, J., Teuling, A.J., Wang, K., Wood, E.F., & Zhang, Y. (2011a). Evaluation of global observations-based evapotranspiration datasets and IPCC AR4 simulations. *Geophys. Res. Lett.*, 38, L06402
- Mueller, B., Seneviratne, S.I., Jimenez, C., Corti, T., Hirschi, M., Balsamo, G., Ciais, P., Dirmeyer, P., Fisher, J.B., Guo, Z., Jung, M., Maignan, F., McCabe, M.F., Reichle, R., Reichstein, M., Rodell, M., Sheffield, J., Teuling, A.J., Wang, K., Wood, E.F., & Zhang, Y. (2011b). Evaluation of global observations-based evapotranspiration datasets and IPCC AR4 simulations. *Geophysical Research Letters*, 38
- Nagler, P.L., Cleverly, J., Glenn, E., Lampkin, D., Huete, A., & Wan, Z. (2005a). Predicting riparian evapotranspiration from MODIS vegetation indices and meteorological data. *Remote Sensing of Environment*, 94, 17-30
- Nagler, P.L., Scott, R.L., Westenburg, C., Cleverly, J.R., Glenn, E.P., & Huete, A.R. (2005b). Evapotranspiration on western U.S. rivers estimated using the Enhanced Vegetation Index from MODIS and data from eddy covariance and Bowen ratio flux towers. *Remote Sensing of Environment*, 97, 337-351
- Nakaegawa, T., Oki, T., & Musiake, K. (2001). Aggregation criteria for surface heat balances in a heterogeneous area based on a linear model. *Advances in Water Resources*, 24, 1159-1171
- Nash, J.E., & Sutcliffe, J.V. (1970). River flow forecasting through conceptual models part I – A discussion of principles. *Journal of Hydrology*, 10, 282-290
- Neal, R.M. (2003). Slice Sampling. *Annals of Statistics*, 31, 705-767
- Neuman, S.P. (2003). Maximum likelihood Bayesian averaging of uncertain model predictions. *Stochastic Environmental Research and Risk Assessment*, 17, 291-305

References

- Nijssen, B., Schnur, R., & Lettenmaier, D.P. (2001). Global Retrospective Estimation of Soil Moisture Using the Variable Infiltration Capacity Land Surface Model, 1980–93. *Journal of Climate*, 14, 1790-1808
- Noh, Y., Choi, K., & Lee, I. (2010). Comparison study between MCMC-based and weight-based Bayesian methods for identification of joint distribution. *Structural and Multidisciplinary Optimization*, 42, 823-833
- Noilhan, J., & Planton, S. (1989). A Simple Parameterization of Land Surface Processes for Meteorological Models. *Monthly Weather Review*, 117, 536-549
- Norman, J.M., Anderson, M.C., Kustas, W.P., French, A.N., Mecikalski, J., Torn, R., Diak, G.R., Schmugge, T.J., & Tanner, B.C.W. (2003). Remote sensing of surface energy fluxes at 10¹-m pixel resolutions. *Water Resour. Res.*, 39
- Norman, J.M., Kustas, W.P., & Humes, K.S. (1995). Source approach for estimating soil and vegetation energy fluxes in observations of directional radiometric surface temperature. *Agricultural and Forest Meteorology*, 77, 263-293
- Norman, J.M., Kustas, W.P., Prueger, J.H., & Diak, G.R. (2000). Surface flux estimation using radiometric temperature: A dual-temperature-difference method to minimize measurement errors. *Water Resour. Res.*, 36
- Odhiambo, L., & Irmak, S. (2011). Performance of extended Shuttleworth-Wallace model for estimating and partitioning of evapotranspiration in a partial residue-covered subsurface drip-irrigated soybean field. *Transactions of the ASABE*, 54, 915-930
- Ortega-Farias, S., Poblete-Echeverría, C., & Brisson, N. (2010). Parameterization of a two-layer model for estimating vineyard evapotranspiration using meteorological measurements. *Agricultural and Forest Meteorology*, 150, 276-286
- Pan, M., Wood, E.F., Wójcik, R., & McCabe, M.F. (2008). Estimation of regional terrestrial water cycle using multi-sensor remote sensing observations and data assimilation. *Remote Sensing of Environment*, 112, 1282-1294
- Parlange, M.B., & Katul, G.G. (1992). An advection-aridity evaporation model. *Water Resour. Res.*, 28, 127-132
- Parry, M., Rosenzweig, C., Iglesias, A., Fischer, G., & Livermore, M. (1999). Climate change and world food security: a new assessment. *Global Environmental Change*, 9, Supplement 1, S51-S67
- Pauwels, V.R.N., & Samson, R. (2006). Comparison of different methods to measure and model actual evapotranspiration rates for a wet sloping grassland. *Agricultural Water Management*, 82, 1-24
- Penman, H.L. (1948). Natural Evaporation from Open Water, Bare Soil and Grass. *Proceedings of the Royal Society of London. Series A. Mathematical and Physical Sciences*, 193, 120-145

References

- Pereira, A.R., & Villa Nova, N.A. (1992). Analysis of the Priestley-Taylor parameter. *Agricultural and Forest Meteorology*, 61, 1-9
- Peters-Lidard, C.D., Kumar, S.V., Mocko, D.M., & Tian, Y. (2011). Estimating evapotranspiration with land data assimilation systems. *Hydrological Processes*, 25, 3979-3992
- Petropoulos, G., Carlson, T.N., Wooster, M.J., & Islam, S. (2009). A review of Ts/VI remote sensing based methods for the retrieval of land surface energy fluxes and soil surface moisture. *Progress in Physical Geography*, 33, 224-250
- Polhamus, A., Fisher, J.B., & Tu, K.P. (2013). What controls the error structure in evapotranspiration models? *Agricultural and Forest Meteorology*, 169, 12-24
- Price, J.C. (1982). Estimation of Regional Scale Evapotranspiration Through Analysis of Satellite Thermal-infrared Data. *Geoscience and Remote Sensing, IEEE Transactions on, GE-20*, 286-292
- Priestley, C.H.B., & Taylor, R.J. (1972). On the Assessment of Surface Heat Flux and Evaporation Using Large-Scale Parameters. *Monthly Weather Review*, 100, 81-92
- Prueger, J.H., Hatfield, J.L., Albertson, J.D., Cahill, T., Cooper, D., Eichinger, B., Hipps, L., Kustas, W.P., & Norman, J.M. (2009). SMEX02 SMACEX Tower Meteorological/Flux Data. In. Boulder, Colorado USA: National Snow and Ice Data Center
- Prueger, J.H., Hatfield, J.L., Kustas, W.P., Hipps, L.E., MacPherson, J.I., Neale, C.M.U., Eichinger, W.E., Cooper, D.I., & Parkin, T.B. (2005). Tower and Aircraft Eddy Covariance Measurements of Water Vapor, Energy, and Carbon Dioxide Fluxes during SMACEX. *Journal of Hydrometeorology*, 6, 954-960
- Qualls, R.J., & Gultekin, H. (1997). Influence of components of the advection-aridity approach on evapotranspiration estimation. *Journal of Hydrology*, 199, 3-12
- Räisänen, J., & Palmer, T.N. (2001). A Probability and Decision-Model Analysis of a Multimodel Ensemble of Climate Change Simulations. *Journal of Climate*, 14, 3212-3226
- Rana, G., & Katerji, N. (1998). A Measurement Based Sensitivity Analysis of the Penman-Monteith Actual Evapotranspiration Model for Crops of Different Height and in Contrasting Water Status. *Theoretical and Applied Climatology*, 60, 141-149
- Rana, G., & Katerji, N. (2000). Measurement and estimation of actual evapotranspiration in the field under Mediterranean climate: a review. *European Journal of Agronomy*, 13, 125-153
- Raupach, M., & Finnigan, J. (1988). 'Single-layer models of evaporation from plant canopies are incorrect but useful, whereas multilayer models are correct but useless': Discuss. *Functional Plant Biology*, 15, 705-716
- Raupach, M.R. (1995). Vegetation-atmosphere interaction and surface conductance at leaf, canopy and regional scales. *Agricultural and Forest Meteorology*, 73, 151-179

- Raupach, M.R., & Finnigan, J.J. (1995). Scale issues in boundary-layer meteorology: Surface energy balances in heterogeneous terrain. *Hydrological Processes*, 9, 589-612
- Raupach, M.R., Rayner, P.J., Barrett, D.J., DeFries, R.S., Heimann, M., Ojima, D.S., Quegan, S., & Schmullius, C.C. (2005). Model-data synthesis in terrestrial carbon observation: methods, data requirements and data uncertainty specifications. *Global Change Biology*, 11, 378-397
- Reba, M.L., Pomeroy, J., Marks, D., & Link, T.E. (2012). Estimating surface sublimation losses from snowpacks in a mountain catchment using eddy covariance and turbulent transfer calculations. *Hydrological Processes*, 26, 3699-3711
- Rebmann, C., Göckede, M., Foken, T., Aubinet, M., Aurela, M., Berbigier, P., Bernhofer, C., Buchmann, N., Carrara, A., & Cescatti, A. (2005). Quality analysis applied on eddy covariance measurements at complex forest sites using footprint modelling. *Theoretical and Applied Climatology*, 80, 121-141
- Reid, W.V., Chen, D., Goldfarb, L., Hackmann, H., Lee, Y.T., Mokhele, K., Ostrom, E., Raivio, K., Rockström, J., Schellnhuber, H.J., & Whyte, A. (2010). Earth System Science for Global Sustainability: Grand Challenges. *Science*, 330, 916-917
- Renard, B., Kavetski, D., Kuczera, G., Thyer, M., & Franks, S.W. (2010). Understanding predictive uncertainty in hydrologic modeling: The challenge of identifying input and structural errors. *Water Resour. Res.*, 46, W05521
- Renard, B., Kavetski, D., Leblois, E., Thyer, M., Kuczera, G., & Franks, S.W. (2011). Toward a reliable decomposition of predictive uncertainty in hydrological modeling: Characterizing rainfall errors using conditional simulation. *Water Resour. Res.*, 47, W11516
- Richardson, A.D., Aubinet, M., Barr, A.G., Hollinger, D.Y., Ibrom, A., Lasslop, G., & Reichstein, M. (2012). Uncertainty quantification. In M. Aubinet, T. Vesala & D. Papale (Eds.), *Eddy Covariance* (pp. 173-209): Springer
- Richardson, A.D., Hollinger, D.Y., Burba, G.G., Davis, K.J., Flanagan, L.B., Katul, G.G., William Munger, J., Ricciuto, D.M., Stoy, P.C., Suyker, A.E., Verma, S.B., & Wofsy, S.C. (2006). A multi-site analysis of random error in tower-based measurements of carbon and energy fluxes. *Agricultural and Forest Meteorology*, 136, 1-18
- Rienecker, M.M., Suarez, M.J., Gelaro, R., Todling, R., Bacmeister, J., Liu, E., Bosilovich, M.G., Schubert, S.D., Takacs, L., Kim, G.-K., Bloom, S., Chen, J., Collins, D., Conaty, A., da Silva, A., Gu, W., Joiner, J., Koster, R.D., Lucchesi, R., Molod, A., Owens, T., Pawson, S., Pegion, P., Redder, C.R., Reichle, R., Robertson, F.R., Ruddick, A.G., Sienkiewicz, M., & Woollen, J. (2011). MERRA: NASA's Modern-Era Retrospective Analysis for Research and Applications. *Journal of Climate*, 24, 3624-3648
- Román, M.O., Schaaf, C.B., Woodcock, C.E., Strahler, A.H., Yang, X., Braswell, R.H., Curtis, P.S., Davis, K.J., Dragoni, D., & Goulden, M.L. (2009). The MODIS (Collection V005) BRDF/albedo product: Assessment of spatial representativeness over forested landscapes. *Remote Sensing of Environment*, 113, 2476-2498

References

- Ross, J. (1976a). Radiative transfer in plant communities. In J.L. Monteith (Ed.), *Vegetation and the atmosphere* (pp. 13-56). London: Academic Press
- Ross, J. (1976b). Radiative transfer in plant communities. In J.L. Monteith (Ed.), *Vegetation and the atmosphere* (pp. 13-56). London: Academic Press
- Running, S.W., Nemani, R.R., & Hungerford, R.D. (1987). Extrapolation of synoptic meteorological data in mountainous terrain and its use for simulating forest evapotranspiration and photosynthesis. *Canadian Journal of Forest Research*, 17, 472-483
- Ruppert, J., Thomas, C., & Foken, T. (2006). Scalar Similarity for Relaxed Eddy Accumulation Methods. *Boundary-Layer Meteorology*, 120, 39-63
- Samanta, S., Clayton, M.K., Mackay, D.S., Kruger, E.L., & Ewers, B.E. (2008). Quantitative comparison of canopy conductance models using a Bayesian approach. *Water Resour. Res.*, 44, W09431
- Samanta, S., Mackay, D.S., Clayton, M.K., Kruger, E.L., & Ewers, B.E. (2007). Bayesian analysis for uncertainty estimation of a canopy transpiration model. *Water Resour. Res.*, 43, W04424
- Schmid, H.P. (2002). Footprint modeling for vegetation atmosphere exchange studies: a review and perspective. *Agricultural and Forest Meteorology*, 113, 159-183
- Schmugge, T.J., Kustas, W.P., Ritchie, J.C., Jackson, T.J., & Rango, A. (2002). Remote sensing in hydrology. *Advances in Water Resources*, 25, 1367-1385
- Schneider, K., Ketzer, B., Breuer, L., Vaché, K.B., Bernhofer, C., & Frede, H.G. (2007). Evaluation of evapotranspiration methods for model validation in a semi-arid watershed in northern China. *Adv. Geosci.*, 11, 37-42
- Schuepp, P.H., Leclerc, M.Y., MacPherson, J.I., & Desjardins, R.L. (1990). Footprint prediction of scalar fluxes from analytical solutions of the diffusion equation. *Boundary-Layer Meteorology*, 50, 355-373
- Selker, J.S., Thévenaz, L., Huwald, H., Mallet, A., Luxemburg, W., van de Giesen, N., Stejskal, M., Zeman, J., Westhoff, M., & Parlange, M.B. (2006). Distributed fiber-optic temperature sensing for hydrologic systems. *Water Resources Research*, 42, W12202
- Sellers, P.J., Dickinson, R.E., Randall, D.A., Betts, A.K., Hall, F.G., Berry, J.A., Collatz, G.J., Denning, A.S., Mooney, H.A., Nobre, C.A., Sato, N., Field, C.B., & Henderson-Sellers, A. (1997). Modeling the Exchanges of Energy, Water, and Carbon Between Continents and the Atmosphere. *Science*, 275, 502-509
- Senay, G., Budde, M., Verdin, J., & Melesse, A. (2007). A Coupled Remote Sensing and Simplified Surface Energy Balance Approach to Estimate Actual Evapotranspiration from Irrigated Fields. *Sensors*, 7, 979-1000
- Seneviratne, S.I., Lüthi, D., Litschi, M., & Schär, C. (2006). Land-atmosphere coupling and climate change in Europe. *Nature*, 443, 205-209

- Settle, J.J., & Drake, N.A. (1993). Linear mixing and the estimation of ground cover proportions. *International Journal of Remote Sensing*, 14, 1159-1177
- Sheffield, J., Goteti, G., & Wood, E.F. (2006). Development of a 50-year high-resolution global dataset of meteorological forcings for land surface modeling. *Journal of Climate*, 19, 3088-3111
- Sheffield, J., & Wood, E. (2008). Projected changes in drought occurrence under future global warming from multi-model, multi-scenario, IPCC AR4 simulations. *Climate Dynamics*, 31, 79-105
- Sheffield, J., & Wood, E.F. (2007). Characteristics of global and regional drought, 1950-2000: Analysis of soil moisture data from off-line simulation of the terrestrial hydrologic cycle. *Journal of Geophysical Research: Atmospheres*, 112, D17115
- Sheffield, J., Wood, E.F., & Munoz-Arriola, F. (2009). Long-Term Regional Estimates of Evapotranspiration for Mexico Based on Downscaled ISCCP Data. *Journal of Hydrometeorology*, 11, 253-275
- Shi, T., Guan, D., Wang, A., Wu, J., Jin, C., & Han, S. (2008). Comparison of three models to estimate evapotranspiration for a temperate mixed forest. *Hydrological Processes*, 22, 3431-3443
- Shu, Y., Stisen, S., Jensen, K.H., & Sandholt, I. (2011). Estimation of regional evapotranspiration over the North China Plain using geostationary satellite data. *International Journal of Applied Earth Observation and Geoinformation*, 13, 192-206
- Shuttleworth, W.J., & Gurney, R.J. (1990). The theoretical relationship between foliage temperature and canopy resistance in sparse crops. *Quarterly Journal of the Royal Meteorological Society*, 116, 497-519
- Shuttleworth, W.J., & Wallace, J.S. (1985). Evaporation from sparse crops-an energy combination theory. *Quarterly Journal of the Royal Meteorological Society*, 111, 839-855
- Simard, M., Pinto, N., Fisher, J.B., & Baccini, A. (2011). Mapping forest canopy height globally with spaceborne lidar. *Journal of Geophysical Research: Biogeosciences*, 116, G04021
- Simpson, I.J., Thurtell, G.W., Neumann, H.H., Den Hartog, G., & Edwards, G.C. (1998). The Validity of Similarity Theory in the Roughness Sublayer Above Forests. *Boundary-Layer Meteorology*, 87, 69-99
- Sobrino, J.A., Jiménez-Muñoz, J.C., & Paolini, L. (2004). Land surface temperature retrieval from LANDSAT TM 5. *Remote Sensing of Environment*, 90, 434-440
- Solano, R., Didan, K., Jacobson, A., & Huete, A. (2010). MODIS Vegetation Index User's Guide. In: *Vegetation Index and Phenology Lab*, The University of Arizona
- Sorooshian, S., Duan, Q., & Gupta, V.K. (1993). Calibration of rainfall-runoff models: Application of global optimization to the Sacramento Soil Moisture Accounting Model. *Water Resources Research*, 29, 1185-1194

- Sridhar, V., Elliott, R.L., & Chen, F. (2003). Scaling effects on modeled surface energy-balance components using the NOAH-OSU land surface model. *Journal of Hydrology*, 280, 105-123
- Stannard, D.I. (1993). Comparison of Penman-Monteith, Shuttleworth-Wallace, and Modified Priestley-Taylor Evapotranspiration Models for wildland vegetation in semiarid rangeland. *Water Resour. Res.*, 29, 1379-1392
- Stott, P., Paruelo, J.M., & Lauenroth, W.K. (1998). Interannual variability of NDVI and its relationship to climate for North American shrublands and grasslands. *Journal of Biogeography*, 25, 721-733
- Stull, R.B. (1988). *Introduction to Boundary Layer Meteorology*. Vancouver: Springer
- Su, B. (2001a). A Surface Energy Balance System (SEBS) for estimation of turbulent heat fluxes from point to continental scale. In *Publications of the National Remote Sensing Board (BCRS)*
- Su, H., McCabe, M.F., Wood, E.F., Su, Z., & Prueger, J.H. (2005). Modeling Evapotranspiration during SMACEX: Comparing Two Approaches for Local- and Regional-Scale Prediction. *Journal of Hydrometeorology*, 6, 910-922
- Su, Z. (2002). The Surface Energy Balance System (SEBS) for estimation of turbulent heat fluxes. *Hydrol. Earth Syst. Sci.*, 6, 85-100
- Su, Z., Pelgrum, H., & Menenti, M. (1999). Aggregation effects of surface heterogeneity in land surface processes. *Hydrol. Earth Syst. Sci.*, 3, 549-563
- Su, Z., Schmugge, T., Kustas, W.P., & Massman, W.J. (2001). An Evaluation of Two Models for Estimation of the Roughness Height for Heat Transfer between the Land Surface and the Atmosphere. *Journal of Applied Meteorology*, 40, 1933-1951
- Su, Z.B. (2001b). A Surface Energy Balance System (SEBS) for estimation of turbulent heat fluxes from point to continental scale. In (p. 23)
- Sulkava, M., LUYSSAERT, S., ZAEHLE, S., & Papale, D. (2011). Assessing and improving the representativeness of monitoring networks: The European flux tower network example. *Journal of Geophysical Research*, 116
- Sumner, D.M., & Jacobs, J.M. (2005). Utility of Penman-Monteith, Priestley-Taylor, reference evapotranspiration, and pan evaporation methods to estimate pasture evapotranspiration. *Journal of Hydrology*, 308, 81-104
- Szilagyi, J., Hobbins, M., & Jozsa, J. (2009). Modified Advection-Aridity Model of Evapotranspiration. *Journal of Hydrologic Engineering*, 14, 569-574
- Tang, Q., Vivoni, E.R., Muñoz-Arriola, F., & Lettenmaier, D.P. (2011). Predictability of Evapotranspiration Patterns Using Remotely Sensed Vegetation Dynamics during the North American Monsoon. *Journal of Hydrometeorology*, 13, 103-121

- Tanner, C.B. (1967). Measurement of evapotranspiration. *Irrigation of agricultural lands*, 534-574
- Tasumi, M., & Allen, R.G. (2007). Satellite-based ET mapping to assess variation in ET with timing of crop development. *Agricultural Water Management*, 88, 54-62
- Tebaldi, C., & Knutti, R. (2007). The use of the multi-model ensemble in probabilistic climate projections. *Philosophical Transactions of the Royal Society A: Mathematical, Physical and Engineering Sciences*, 365, 2053-2075
- Thom, A.S. (1975). Momentum, mass and heat exchange of the plant communities. In J.L. Monteith (Ed.), *Vegetation and Atmosphere* (pp. 57-109). London: Academic Press
- Thom, A.S., Stewart, J.B., Oliver, H.R., & Gash, J.H.C. (1975). Comparison of aerodynamic and energy budget estimates of fluxes over a pine forest. *Quarterly Journal of the Royal Meteorological Society*, 101, 93-105
- Thorne, P.W., Parker, D.E., Christy, J.R., & Mears, C.A. (2005). UNCERTAINTIES IN CLIMATE TRENDS: Lessons from Upper-Air Temperature Records. *Bulletin of the American Meteorological Society*, 86, 1437-1442
- Thornthwaite, C.W., & Holzman, B. (1939). The determination of evaporation from land and water surfaces. *Monthly Weather Review*, 67, 4
- Thornton, P.E. (1998). Regional ecosystem simulation: Combining surface- and satellite-based observations to study linkages between terrestrial energy and mass budgets. In (pp. 280-280 p.). United States -- Montana: University of Montana
- Tian, H., Wen, J., Wang, C.-h., Liu, R., & Lu, D.-r. (2012). Effect of pixel scale on evapotranspiration estimation by remote sensing over oasis areas in north-western China. *Environmental Earth Sciences*, 1-13
- Timmermans, J., Su, Z., van der Tol, C., Verhoef, A., & Verhoef, W. (2013). Quantifying the uncertainty in estimates of surface-atmosphere fluxes through joint evaluation of the SEBS and SCOPE models. *Hydrol. Earth Syst. Sci.*, 17, 1561-1573
- Timmermans, J., van der Tol, C., Verhoef, A., Verhoef, W., Su, Z., van Helvoirt, M., & Wang, L. (2011). Quantifying the uncertainty in estimates of surface- atmosphere fluxes through joint evaluation of the SEBS and SCOPE models. *Hydrol. Earth Syst. Sci. Discuss.*, 8, 2861-2893
- Timmermans, W.J., Kustas, W.P., Anderson, M.C., & French, A.N. (2007). An intercomparison of the Surface Energy Balance Algorithm for Land (SEBAL) and the Two-Source Energy Balance (TSEB) modeling schemes. *Remote Sensing of Environment*, 108, 369-384
- Timmermans, W.J., Su, Z., & Olioso, A. (2009). Footprint issues in scintillometry over heterogeneous landscapes. *Hydrol. Earth Syst. Sci. Discuss.*, 6, 2099-2127

References

- Todd, R.W., Evett, S.R., & Howell, T.A. (2000). The Bowen ratio-energy balance method for estimating latent heat flux of irrigated alfalfa evaluated in a semi-arid, advective environment. *Agricultural and Forest Meteorology*, 103, 335-348
- Todorovic, M. (1999). Single-layer evapotranspiration model with variable canopy resistance. *Journal of Irrigation and Drainage Engineering*, 125, 235-245
- Tourula, T., & Heikinheimo, M. (1998). Modelling evapotranspiration from a barley field over the growing season. *Agricultural and Forest Meteorology*, 91, 237-250
- Trambouze, W., Bertuzzi, P., & Voltz, M. (1998). Comparison of methods for estimating actual evapotranspiration in a row-cropped vineyard. *Agricultural and Forest Meteorology*, 91, 193-208
- Twine, T.E., Kustas, W.P., Norman, J.M., Cook, D.R., Houser, P.R., Meyers, T.P., Prueger, J.H., Starks, P.J., & Wesely, M.L. (2000). Correcting eddy-covariance flux underestimates over a grassland. *Agricultural and Forest Meteorology*, 103, 279-300
- van Bavel, C.H.M., & Hillel, D.I. (1976). Calculating potential and actual evaporation from a bare soil surface by simulation of concurrent flow of water and heat. *Agricultural Meteorology*, 17, 453-476
- van Bussel, L.G.J., Müller, C., van Keulen, H., Ewert, F., & Leffelaar, P.A. (2011). The effect of temporal aggregation of weather input data on crop growth models' results. *Agricultural and Forest Meteorology*, 151, 607-619
- van der Kwast, J., Timmermans, W., Gieske, A., Su, Z., Oliso, A., Jia, L., Elbers, J., Karssenber, D., & de Jong, S. (2009). Evaluation of the Surface Energy Balance System (SEBS) applied to ASTER imagery with flux-measurements at the SPARC 2004 site (Barrax, Spain). *Hydrol. Earth Syst. Sci.*, 13, 1337-1347
- van der Tol, C., van der Tol, S., Verhoef, A., Su, B., Timmermans, J., Houldcroft, C., & Gieske, A. (2009). A Bayesian approach to estimate sensible and latent heat over vegetated land surface. *Hydrol. Earth Syst. Sci.*, 13, 749-758
- Veenendaal, E.M., Kolle, O., & Lloyd, J. (2004). Seasonal variation in energy fluxes and carbon dioxide exchange for a broad-leaved semi-arid savanna (Mopane woodland) in Southern Africa. *Global Change Biology*, 10, 318-328
- Venturini, V., Krepper, C., & Rodriguez, L. (2012). Evapotranspiration Estimation Based on the Complementary Relationships. *Evapotranspiration-Remote Sensing and Modeling*, Irmak A (ed.). Intechweb.org: Rijeka, Croatia, 19-40
- Verma, S.B. (1989). Aerodynamic Resistance to Transfers of Heat, Mass and Momentum. In, *Workshop on Estimation of Areal Evapotranspiration*. Vancouver, Canada
- Verstraeten, W., Veroustraete, F., & Feyen, J. (2008). Assessment of Evapotranspiration and Soil Moisture Content Across Different Scales of Observation. *Sensors*, 8, 70-117
- Vickers, D., Göckede, M., & Law, B.E. (2010). Uncertainty estimates for 1-h averaged turbulence fluxes of carbon dioxide, latent heat and sensible heat. *Tellus B*, 62, 87-99

- Villagarcía, L., Were, A., García, M., & Domingo, F. (2010). Sensitivity of a clumped model of evapotranspiration to surface resistance parameterisations: Application in a semi-arid environment. *Agricultural and Forest Meteorology*, 150, 1065-1078
- Vinukollu, R.K., Meynadier, R., Sheffield, J., & Wood, E.F. (2011a). Multi-model, multi-sensor estimates of global evapotranspiration: climatology, uncertainties and trends. *Hydrological Processes*, 25, 3993-4010
- Vinukollu, R.K., Sheffield, J., Wood, E.F., Bosilovich, M.G., & Mocko, D. (2011b). Multimodel Analysis of Energy and Water Fluxes: Intercomparisons between Operational Analyses, a Land Surface Model, and Remote Sensing. *Journal of Hydrometeorology*, 13, 3-26
- Vinukollu, R.K., Wood, E.F., Ferguson, C.R., & Fisher, J.B. (2011c). Global estimates of evapotranspiration for climate studies using multi-sensor remote sensing data: Evaluation of three process-based approaches. *Remote Sensing of Environment*, 115, 801-823
- Wallace, J.S. (1995). Calculating evaporation: resistance to factors. *Agricultural and Forest Meteorology*, 73, 353-366
- Wallace, J.S., Roberts, J.M., & Sivakumar, M.V.K. (1990). The estimation of transpiration from sparse dryland millet using stomatal conductance and vegetation area indices. *Agricultural and Forest Meteorology*, 51, 35-49
- Wang, J., & Currit, N. (2011). Uncertainty with the scaling-up of remotely sensed evapotranspiration estimation. In, *Proceedings of the 2nd ACM SIGSPATIAL International Workshop on Querying and Mining Uncertain Spatio-Temporal Data* (pp. 3-7). Chicago, Illinois: ACM
- Wang, K., Augustine, J., & Dickinson, R.E. (2012a). Critical assessment of surface incident solar radiation observations collected by SURFRAD, USCRN and AmeriFlux networks from 1995 to 2011. *Journal of Geophysical Research: Atmospheres*, 117, D23105
- Wang, K., & Dickinson, R.E. (2012). A review of global terrestrial evapotranspiration: Observation, modeling, climatology, and climatic variability. *Rev. Geophys.*, 50, RG2005
- Wang, K., & Dickinson, R.E. (2013). Global atmospheric downward longwave radiation at the surface from ground-based observations, satellite retrievals, and reanalyses. *Reviews of Geophysics*, 51, 150-185
- Wang, L., D'Odorico, P., Evans, J.P., Eldridge, D.J., McCabe, M.F., Caylor, K.K., & King, E.G. (2012b). Dryland ecohydrology and climate change: critical issues and technical advances. *Hydrol. Earth Syst. Sci.*, 16, 2585-2603
- Wang, P., & Yamanaka, T. (2012). Application of a two-source model for partitioning evapotranspiration and assessing its controls in temperate grasslands in central Japan. *Ecohydrology*, n/a-n/a
- Ward, R.C. (1971). Measuring evapotranspiration; a review. *Journal of Hydrology*, 13, 1-21

References

- Weligepolage, K., Gieske, A.S.M., van der Tol, C., Timmermans, J., & Su, Z. (2012). Effect of sub-layer corrections on the roughness parameterization of a Douglas fir forest. *Agricultural and Forest Meteorology*, 162–163, 115-126
- Wever, L.A., Flanagan, L.B., & Carlson, P.J. (2002). Seasonal and interannual variation in evapotranspiration, energy balance and surface conductance in a northern temperate grassland. *Agricultural and Forest Meteorology*, 112, 31-49
- Wharton, S., Schroeder, M., Paw U, K.T., Falk, M., & Bible, K. (2009). Turbulence considerations for comparing ecosystem exchange over old-growth and clear-cut stands for limited fetch and complex canopy flow conditions. *Agricultural and Forest Meteorology*, 149, 1477-1490
- Williams, M., Richardson, A.D., Reichstein, M., Stoy, P.C., Peylin, P., Verbeeck, H., Carvalhais, N., Jung, M., Hollinger, D.Y., Kattge, J., Leuning, R., Luo, Y., Tomelleri, E., Trudinger, C.M., & Wang, Y.P. (2009). Improving land surface models with FLUXNET data. *Biogeosciences*, 6, 1341-1359
- Willmott, C.J. (1982). Some Comments on the Evaluation of Model Performance. *Bulletin of the American Meteorological Society*, 63, 1309-1313
- Wilson, K., Goldstein, A., Falge, E., Aubinet, M., Baldocchi, D., Berbigier, P., Bernhofer, C., Ceulemans, R., Dolman, H., Field, C., Grelle, A., Ibrom, A., Law, B.E., Kowalski, A., Meyers, T., Moncrieff, J., Monson, R., Oechel, W., Tenhunen, J., Valentini, R., & Verma, S. (2002). Energy balance closure at FLUXNET sites. *Agricultural and Forest Meteorology*, 113, 223-243
- Wilson, K.B., Hanson, P.J., Mulholland, P.J., Baldocchi, D.D., & Wullschleger, S.D. (2001). A comparison of methods for determining forest evapotranspiration and its components: sap-flow, soil water budget, eddy covariance and catchment water balance. *Agricultural and Forest Meteorology*, 106, 153-168
- Wood, E.F., & Rodríguez-Iturbe, I. (1975). A Bayesian approach to analyzing uncertainty among flood frequency models. *Water Resources Research*, 11, 839-843
- Xiao, X., Hollinger, D., Aber, J., Goltz, M., Davidson, E.A., Zhang, Q., & Moore Iii, B. (2004). Satellite-based modeling of gross primary production in an evergreen needleleaf forest. *Remote Sensing of Environment*, 89, 519-534
- Xu, C.Y., & Chen, D. (2005). Comparison of seven models for estimation of evapotranspiration and groundwater recharge using lysimeter measurement data in Germany. *Hydrological Processes*, 19, 3717-3734
- Xu, C.Y., & Singh, V.P. (2002). Cross Comparison of Empirical Equations for Calculating Potential Evapotranspiration with Data from Switzerland. *Water Resources Management*, 16, 197-219
- Xystrakis, F., & Matzarakis, A. (2011). Evaluation of 13 Empirical Reference Potential Evapotranspiration Equations on the Island of Crete in Southern Greece. *Journal of Irrigation and Drainage Engineering*, 137, 211-222

References

- Yan, H., Wang, S.Q., Billesbach, D., Oechel, W., Zhang, J.H., Meyers, T., Martin, T.A., Matamala, R., Baldocchi, D., Bohrer, G., Dragoni, D., & Scott, R. (2012). Global estimation of evapotranspiration using a leaf area index-based surface energy and water balance model. *Remote Sensing of Environment*, 124, 581-595
- Yang, H., Yang, D., & Lei, Z. (2012). Seasonal variability of the complementary relationship in the Asian monsoon region. *Hydrological Processes*, n/a-n/a
- Zhang, B., Kang, S., Li, F., & Zhang, L. (2008). Comparison of three evapotranspiration models to Bowen ratio-energy balance method for a vineyard in an arid desert region of northwest China. *Agricultural and Forest Meteorology*, 148, 1629-1640
- Zhang, Q., Xu, C.-Y., Chen, Y., & Ren, L. (2011). Comparison of evapotranspiration variations between the Yellow River and Pearl River basin, China. *Stochastic Environmental Research and Risk Assessment*, 25, 139-150
- Zhang, X., Jia, X., Yang, J., & Hu, L. (2010a). Evaluation of MOST functions and roughness length parameterization on sensible heat flux measured by large aperture scintillometer over a corn field. *Agricultural and Forest Meteorology*, 150, 1182-1191
- Zhang, Y., Leuning, R., Hutley, L.B., Beringer, J., McHugh, I., & Walker, J.P. (2010b). Using long-term water balances to parameterize surface conductances and calculate evaporation at 0.05° spatial resolution. *Water Resources Research*, 46, W05512
- Zhao, M., Heinsch, F.A., Nemani, R.R., & Running, S.W. (2005). Improvements of the MODIS terrestrial gross and net primary production global data set. *Remote Sensing of Environment*, 95, 164-176
- Zhao, W., Hidenori, T., & Zhao, H. (1997). Estimation of vegetative surface albedo in the Kushiro Mire with Landsat TM data. *Chinese Geographical Science*, 7, 278-288
- Zhou, M.C., Ishidaira, H., Hapuarachchi, H.P., Magome, J., Kiem, A.S., & Takeuchi, K. (2006). Estimating potential evapotranspiration using Shuttleworth-Wallace model and NOAA-AVHRR NDVI data to feed a distributed hydrological model over the Mekong River basin. *Journal of Hydrology*, 327, 151-173
- Zotarelli, L., Dukes, M.D., & Morgan, K.T. (2010). Interpretation of Soil Moisture Content to Determine Soil Field Capacity and Avoid Over-Irrigating Sandy Soils Using Soil Moisture Sensors
- Zwart, S.J., & Bastiaanssen, W.G.M. (2007). SEBAL for detecting spatial variation of water productivity and scope for improvement in eight irrigated wheat systems. *Agricultural Water Management*, 89, 287-296

Appendix A – Supplementary materials for Chapter 2

The following are supplementary materials which provide additional details on the performance of the evapotranspiration models (**Chapter 2**), including scatterplots and summary of statistics.

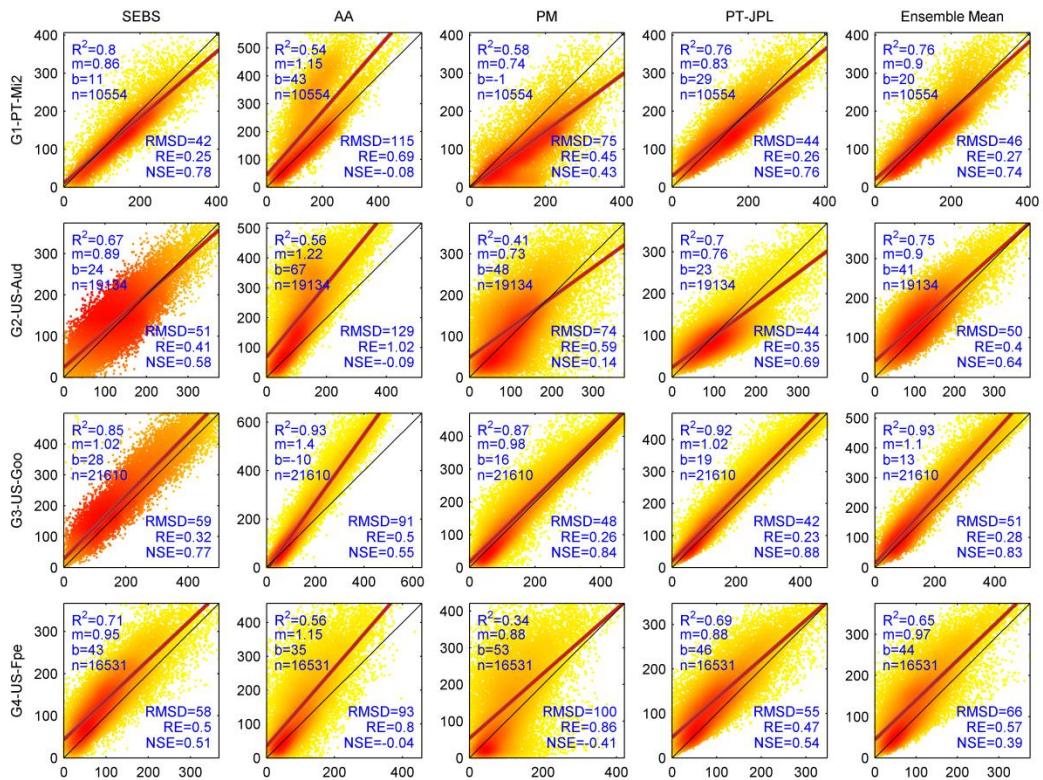


Figure A1: Scatterplots of observed (x-axis) versus simulated (y-axis) latent heat flux ($W \cdot m^{-2}$) for grassland sites. The statistics on the graphs are R^2 , slope (m), y-intercept (b), number of data records (n), the root-mean-squared difference ($RMSD$), relative error (RE) and the Nash-Sutcliffe Efficiency coefficient (NSE). The thick gray line is the linear regression and the thin gray line is the 1:1 line. The color of the points in the scatterplot is indicative of the density from low (yellow) to high (red).

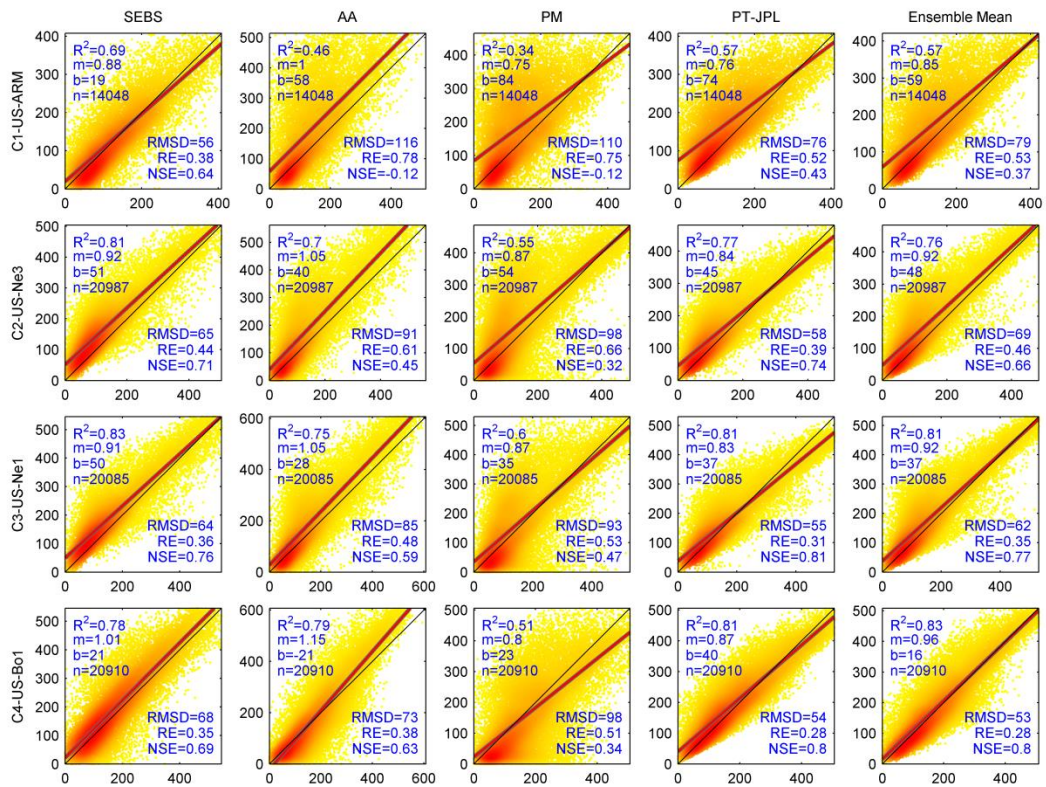


Figure A2: Scatterplots of observed (x-axis) versus simulated (y-axis) latent heat flux ($W.m^{-2}$) for cropland sites. The statistics on the graphs are R^2 , slope (m), y-intercept (b), number of data records (n), the root-mean-squared difference ($RMSD$), relative error (RE) and the Nash-Sutcliffe Efficiency coefficient (NSE). The thick gray line is the linear regression and the thin gray line is the 1:1 line. The color of the points in the scatterplot is indicative of the density from low (yellow) to high (red).

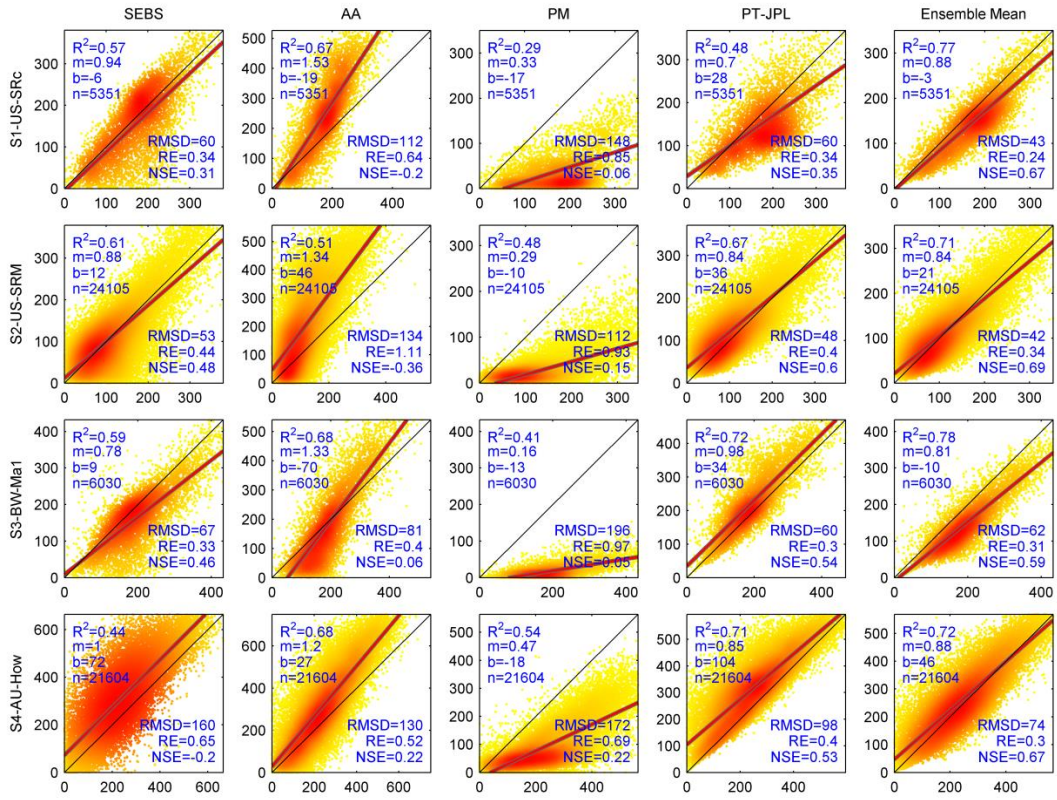


Figure A3: Scatterplots of observed (x-axis) versus simulated (y-axis) latent heat flux ($W.m^{-2}$) for shrubland sites. The statistics on the graphs are R^2 , slope (m), y-intercept (b), number of data records (n), the root-mean-squared difference ($RMSD$), relative error (RE) and the Nash-Sutcliffe Efficiency coefficient (NSE). The thick gray line is the linear regression and the thin gray line is the 1:1 line. The color of the points in the scatterplot is indicative of the density from low (yellow) to high (red).

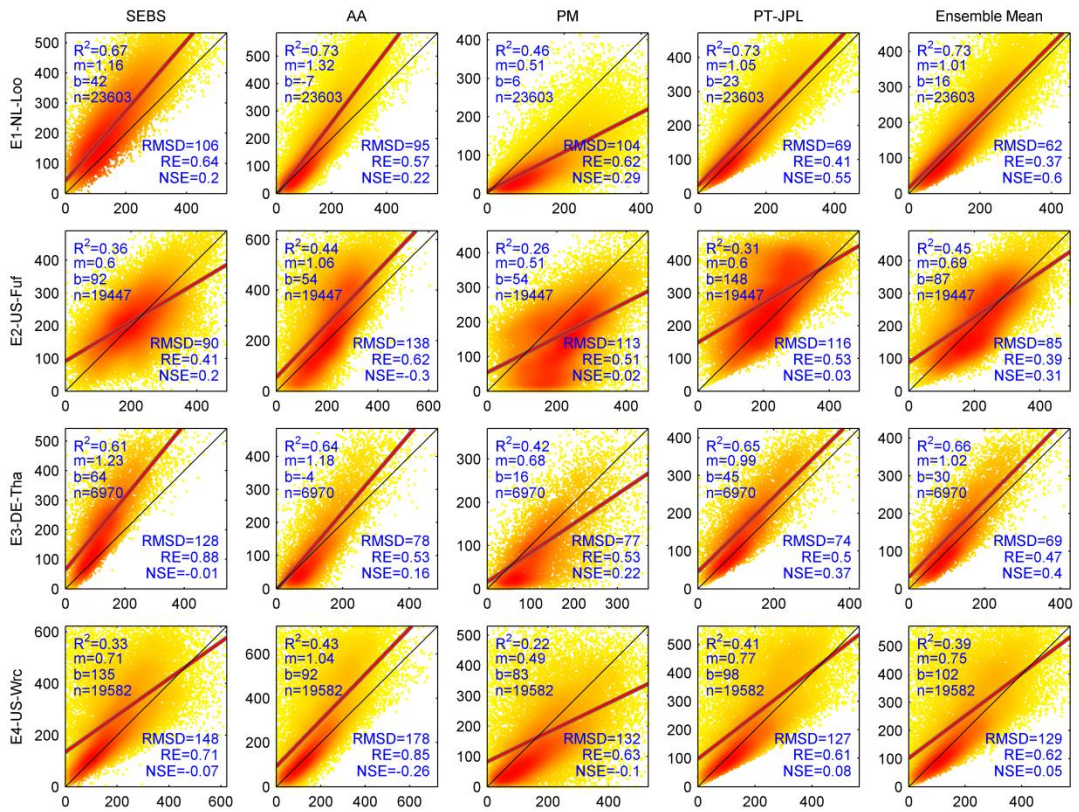


Figure A4: Scatterplots of observed (x-axis) versus simulated (y-axis) latent heat flux ($W.m^{-2}$) for evergreen needleleaf forest sites. The statistics on the graphs are R^2 , slope (m), y-intercept (b), number of data records (n), the root-mean-squared difference ($RMSD$), relative error (RE) and the Nash-Sutcliffe Efficiency coefficient (NSE). The thick gray line is the linear regression and the thin gray line is the 1:1 line. The color of the points in the scatterplot is indicative of the density from low (yellow) to high (red).

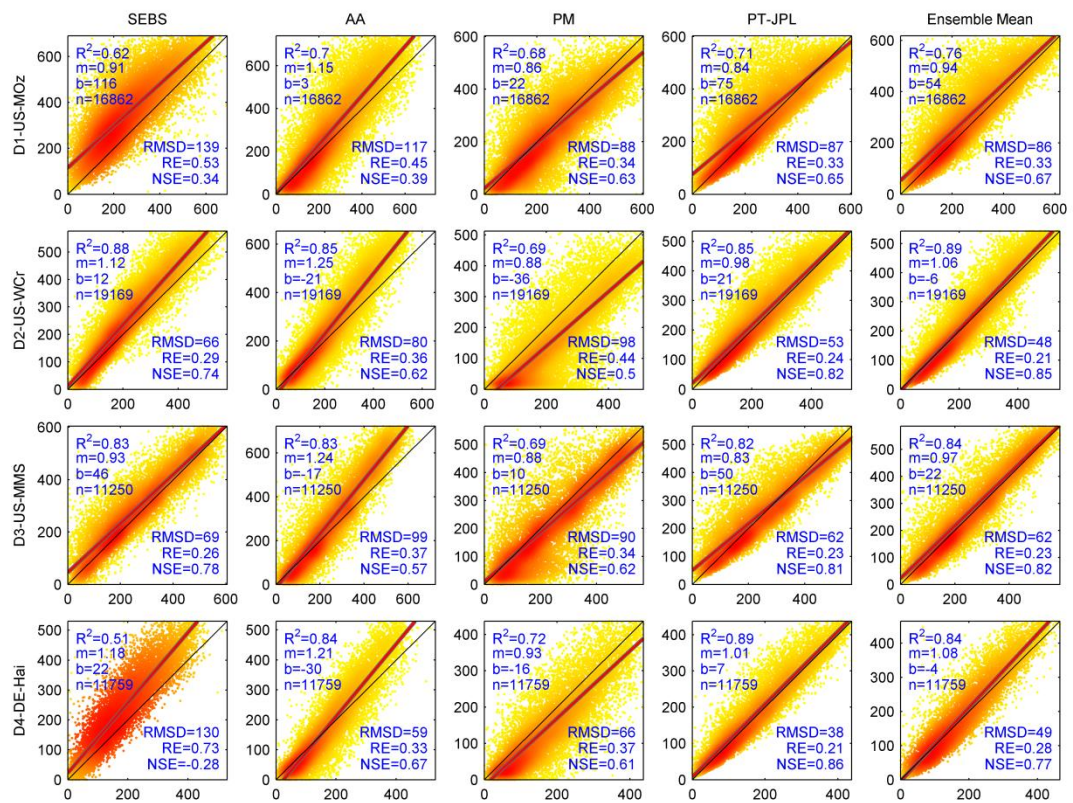


Figure A5: Scatterplots of observed (x-axis) versus simulated (y-axis) latent heat flux ($W.m^{-2}$) for deciduous broadleaf forest sites. The statistics on the graphs are R^2 , slope (m), y-intercept (b), number of data records (n), the root-mean-squared difference (RMSD), relative error (RE) and the Nash-Sutcliffe Efficiency coefficient (NSE). The thick gray line is the linear regression and the thin gray line is the 1:1 line. The color of the points in the scatterplot is indicative of the density from low (yellow) to high (red).

Appendices

Table A1: Summary of the statistical performance of the models over different biomes.

Biome	Tower	SEBS						Advection-Aridity						Penman-Monteith					
		R ²	slope	y-intercept	NSE	RE	RMSD	R ²	Slope	y-intercept	NSE	RE	RMSD	R ²	slope	y-intercept	NSE	RE	RMSD
Grassland	G1	0.80	0.9	11	0.78	0.25	42	0.54	1.15	43	-0.08	0.69	115	0.58	0.7	-1	0.43	0.45	75
	G2	0.67	0.9	24	0.58	0.41	51	0.56	1.22	67	-0.09	1.02	129	0.41	0.7	48	0.14	0.59	74
	G3	0.85	1.0	28	0.77	0.32	59	0.93	1.40	-10	0.55	0.50	91	0.87	1.0	16	0.84	0.26	48
	G4	0.71	0.9	43	0.51	0.50	58	0.56	1.15	35	-0.04	0.80	93	0.34	0.9	53	-0.41	0.86	100
Cropland	C1	0.69	0.9	19	0.64	0.38	56	0.46	1.00	58	-0.12	0.78	116	0.34	0.7	84	-0.12	0.75	110
	C2	0.81	0.9	51	0.71	0.44	65	0.70	1.05	40	0.45	0.61	91	0.55	0.9	54	0.32	0.66	98
	C3	0.83	0.9	50	0.76	0.36	64	0.75	1.05	28	0.59	0.48	85	0.60	0.9	35	0.47	0.53	93
	C4	0.78	1.0	21	0.69	0.35	68	0.79	1.15	-21	0.63	0.38	73	0.51	0.8	23	0.34	0.51	98
Shrubland	S1	0.57	0.9	-6	0.31	0.34	60	0.67	1.53	-19	-0.20	0.64	112	0.29	0.3	-17	0.06	0.85	148
	S2	0.61	0.9	12	0.48	0.44	53	0.51	1.34	46	-0.36	1.11	134	0.48	0.3	-10	0.15	0.93	112
	S3	0.59	0.8	9	0.46	0.33	67	0.68	1.33	-70	0.06	0.40	81	0.41	0.2	-13	0.05	0.97	196
	S4	0.44	1.0	72	-0.20	0.65	160	0.68	1.20	27	0.22	0.52	130	0.54	0.5	-18	0.22	0.69	172
ENF	E1	0.67	1.2	42	0.20	0.64	106	0.73	1.32	-7	0.22	0.57	95	0.46	0.5	6	0.29	0.62	104
	E2	0.36	0.6	92	0.20	0.41	90	0.44	1.06	54	-0.30	0.62	138	0.26	0.5	54	0.02	0.51	113
	E3	0.61	1.2	64	-0.01	0.88	128	0.64	1.18	-4	0.16	0.53	78	0.42	0.7	16	0.22	0.53	77
	E4	0.33	0.7	135	-0.07	0.71	148	0.43	1.04	92	-0.26	0.85	178	0.22	0.5	83	-0.10	0.63	132
DBF	D1	0.62	0.9	116	0.34	0.53	139	0.70	1.15	3	0.39	0.45	117	0.68	0.9	22	0.63	0.34	88
	D2	0.88	1.1	12	0.74	0.29	66	0.85	1.25	-21	0.62	0.36	80	0.69	0.9	-36	0.50	0.44	98
	D3	0.83	0.9	46	0.78	0.26	69	0.83	1.24	-17	0.57	0.37	99	0.69	0.9	10	0.62	0.34	90
	D4	0.51	1.2	22	-0.28	0.73	130	0.84	1.21	-30	0.67	0.33	59	0.72	0.9	-16	0.61	0.37	66

Appendices

Table A1 (continue): Summary of the statistical performance of the models over different biomes.

Biome	Tower	Priestley-Taylor JPL						Ensemble Mean					
		R^2	slope	y-intercept	NSE	RE	<i>RM</i> SD	R^2	Slope	y-intercept	NSE	RE	<i>RM</i> SD
Grassland	G1	0.76	0.8	29	0.76	0.26	44	0.76	0.9	20	0.74	0.27	46
	G2	0.70	0.8	23	0.69	0.35	44	0.75	0.9	41	0.64	0.40	50
	G3	0.92	1.0	19	0.88	0.23	42	0.93	1.1	13	0.83	0.28	51
	G4	0.69	0.9	46	0.54	0.47	55	0.65	1.0	44	0.39	0.57	66
Cropland	C1	0.57	0.8	74	0.43	0.52	76	0.57	0.8	59	0.37	0.53	79
	C2	0.77	0.8	45	0.74	0.39	58	0.76	0.9	48	0.66	0.46	69
	C3	0.81	0.8	37	0.81	0.31	55	0.81	0.9	37	0.77	0.35	62
	C4	0.81	0.9	40	0.80	0.28	54	0.83	1.0	16	0.80	0.28	53
Shrubland	S1	0.48	0.7	28	0.35	0.34	60	0.77	0.9	-3	0.67	0.24	43
	S2	0.67	0.8	36	0.60	0.40	48	0.71	0.8	21	0.69	0.34	42
	S3	0.72	1.0	34	0.54	0.30	60	0.78	0.8	-10	0.59	0.31	62
	S4	0.71	0.9	104	0.53	0.40	98	0.72	0.9	46	0.67	0.30	74
ENF	E1	0.73	1.0	23	0.55	0.41	69	0.73	1.0	16	0.60	0.37	62
	E2	0.31	0.6	148	0.03	0.53	116	0.45	0.7	87	0.31	0.39	85
	E3	0.65	1.0	45	0.37	0.50	74	0.66	1.0	30	0.40	0.47	69
	E4	0.41	0.8	98	0.08	0.61	127	0.39	0.8	102	0.05	0.62	129
DBF	D1	0.71	0.8	75	0.65	0.33	87	0.76	0.9	54	0.67	0.33	86
	D2	0.85	1.0	21	0.82	0.24	53	0.89	1.1	-6	0.85	0.21	48
	D3	0.82	0.8	50	0.81	0.23	62	0.84	1.0	22	0.82	0.23	62
	D4	0.89	1.0	7	0.86	0.21	38	0.84	1.1	-4	0.77	0.28	49

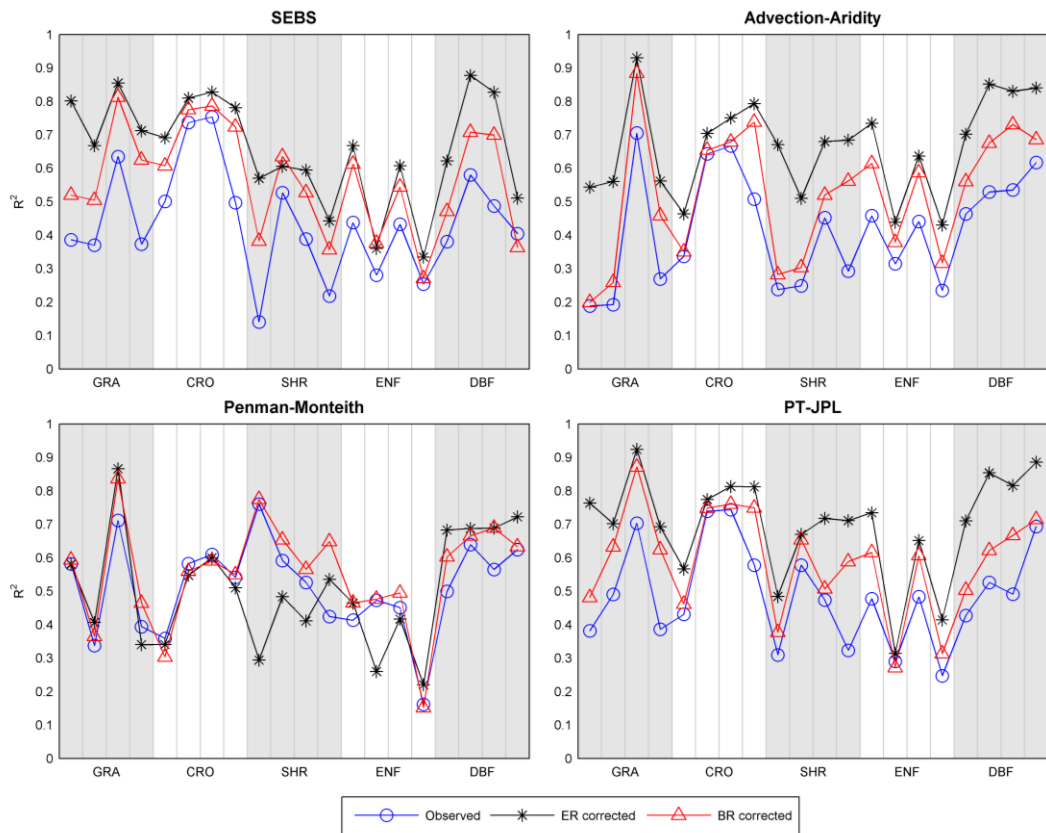


Figure A6: Comparison of R^2 calculated for simulated latent heat flux versus observed, energy residual (ER) corrected and Bowen ratio (BR) corrected ones. GRA=Grassland, CRO=Cropland, SHR=Shrubland, ENF=Evergreen Needleleaf Forest, DBF=Deciduous Broadleaf Forest

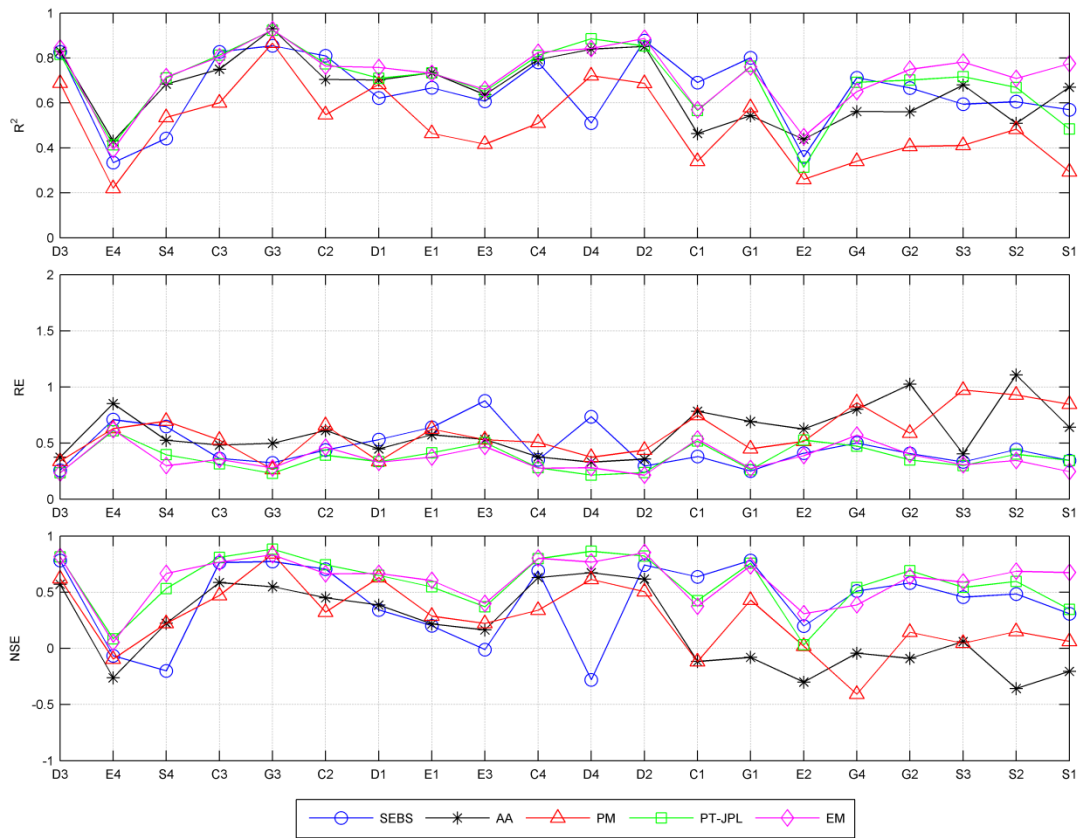


Figure A7: Comparison of the efficiency of the evapotranspiration models. RE is relative error (lower is better) and NSE is the Nash-Sutcliffe Efficiency coefficient (higher is better). Towers are sorted from left to right based on total mean rainfall. The figure shows water availability alone does not significantly influence the performance of the models.

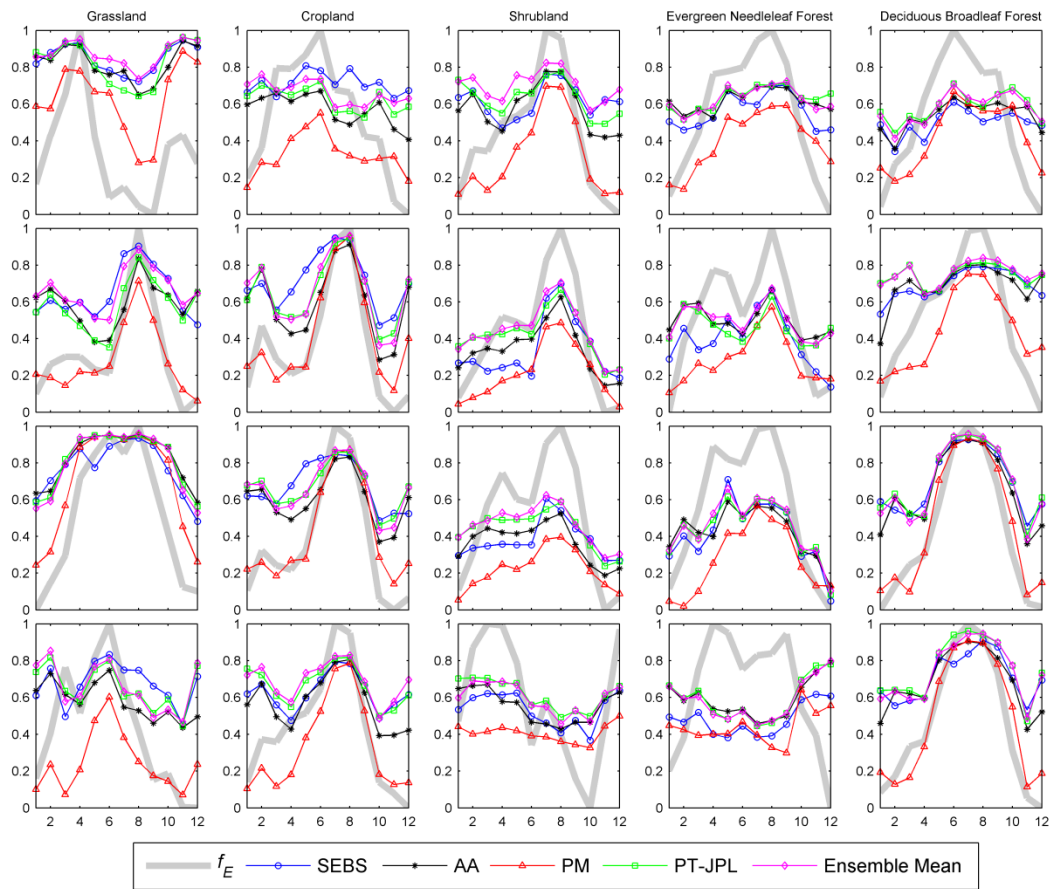


Figure A8: Mean per-month values of the R^2 calculated for each of the four studied models at each of the 20 tower locations. The x-axis represents month of the year, while each point on the graph represents the temporally averaged per-month R^2 calculated for all available tower record years (see Table 2-1 for details on individual tower data length). Note that the per-month R^2 values are for half-hourly or hourly scale ET data, not in monthly scale. f_E is normalized fraction of monthly observed evaporation.

Appendix B – Supplementary materials for Chapter 3

The following are supplementary non-print materials which provide additional details on the performance of the Penman-Monteith scenarios (**Chapter 3**), including scatterplots and summary of statistics.

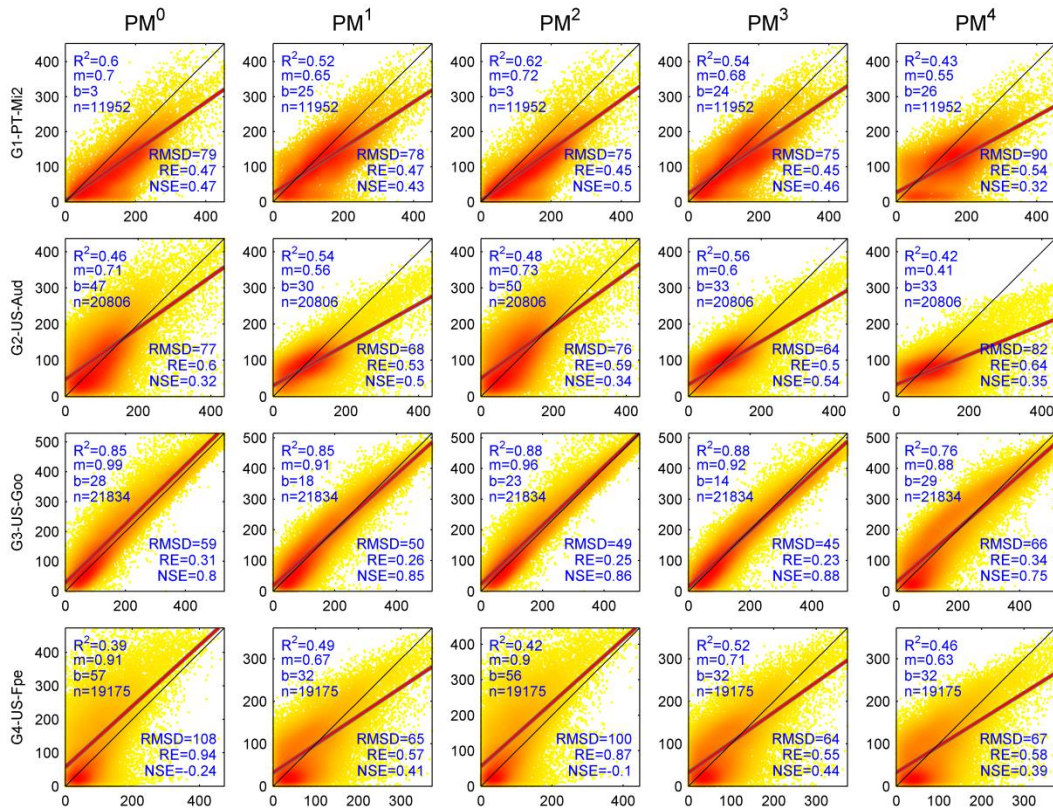


Figure B1: Scatterplots of observed (x-axis) versus simulated (y-axis) latent heat flux ($W.m^{-2}$) for **PM** scenarios across **grassland** sites. The statistics on the graphs are R^2 , slope (m), y-intercept (b), number of data records (n), the root-mean-squared difference (*RMSD*), relative error (*RE*) and the Nash-Sutcliffe Efficiency coefficient (*NSE*). The thick gray line is the linear regression and the thin gray line is the 1:1 line. The color of the points in the scatterplot is indicative of the density from low (yellow) to high (red).

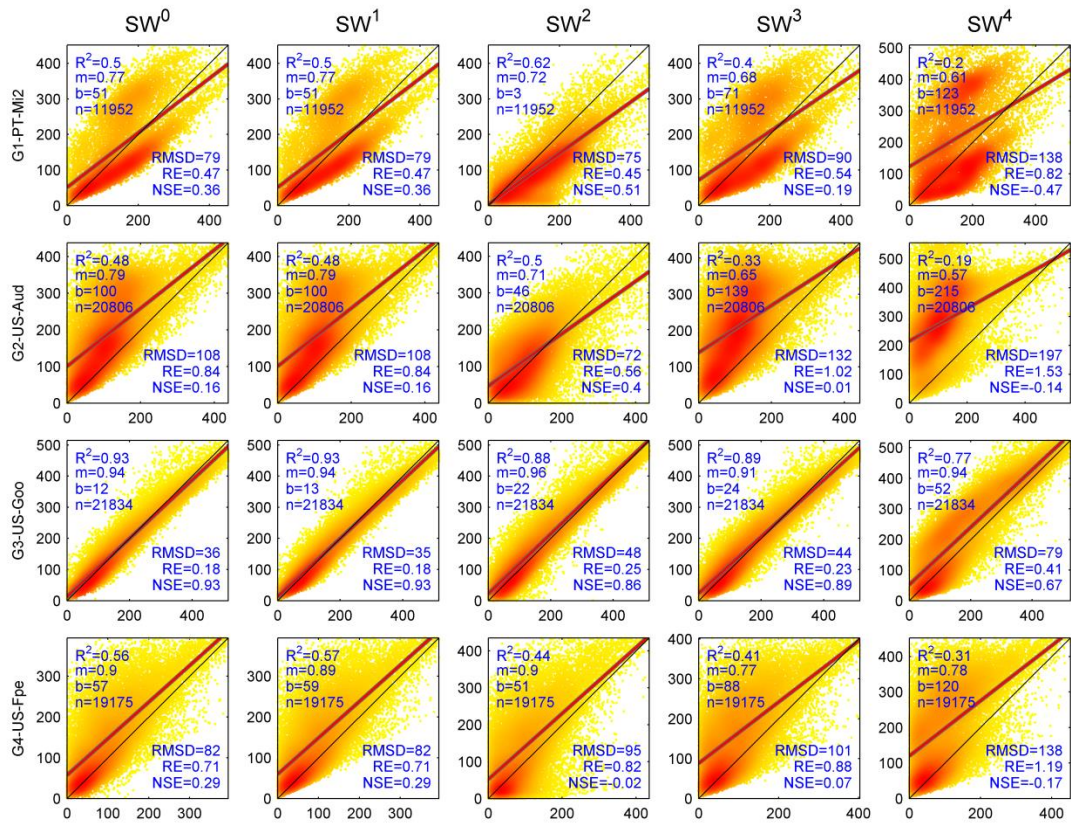


Figure B2: Scatterplots of observed (x-axis) versus simulated (y-axis) latent heat flux ($W.m^{-2}$) for SW scenarios across grassland sites. The statistics on the graphs are R^2 , slope (m), y-intercept (b), number of data records (n), the root-mean-squared difference ($RMSD$), relative error (RE) and the Nash-Sutcliffe Efficiency coefficient (NSE). The thick gray line is the linear regression and the thin gray line is the 1:1 line. The color of the points in the scatterplot is indicative of the density from low (yellow) to high (red).

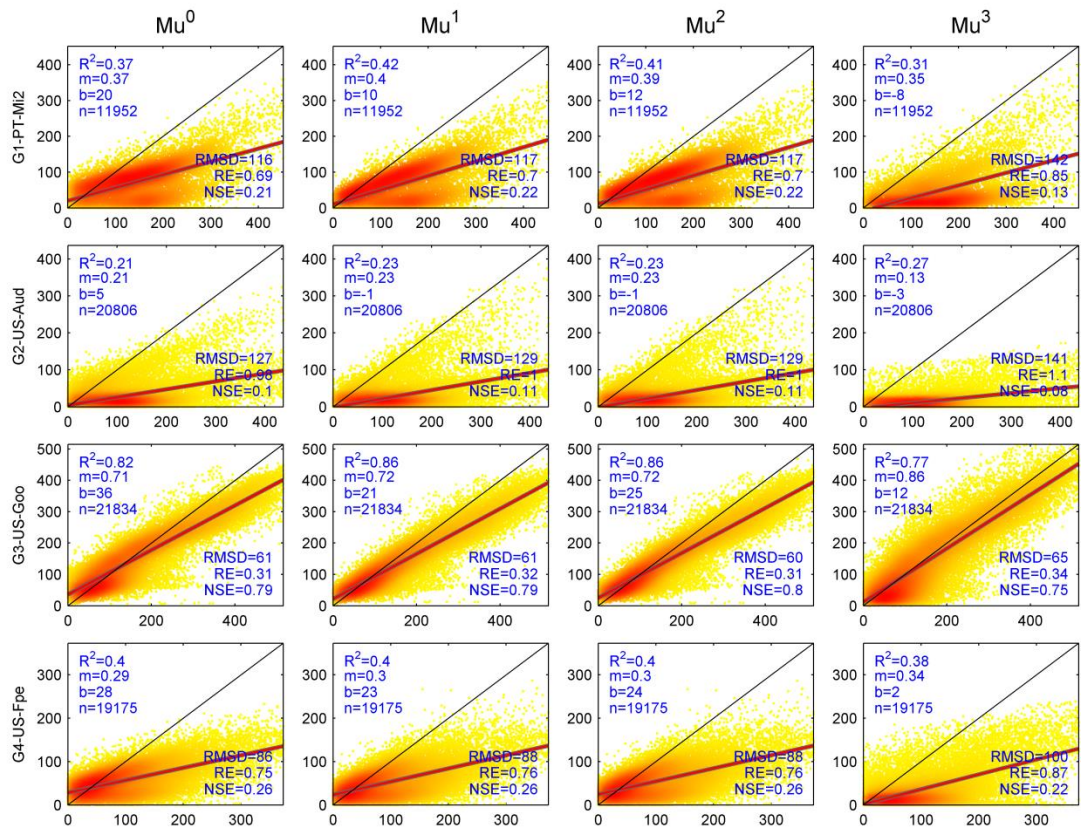


Figure B3: Scatterplots of observed (x-axis) versus simulated (y-axis) latent heat flux ($W.m^{-2}$) for **Mu** scenarios across **grassland** sites. The statistics on the graphs are R^2 , slope (m), y-intercept (b), number of data records (n), the root-mean-squared difference ($RMSD$), relative error (RE) and the Nash-Sutcliffe Efficiency coefficient (NSE). The thick gray line is the linear regression and the thin gray line is the 1:1 line. The color of the points in the scatterplot is indicative of the density from low (yellow) to high (red).

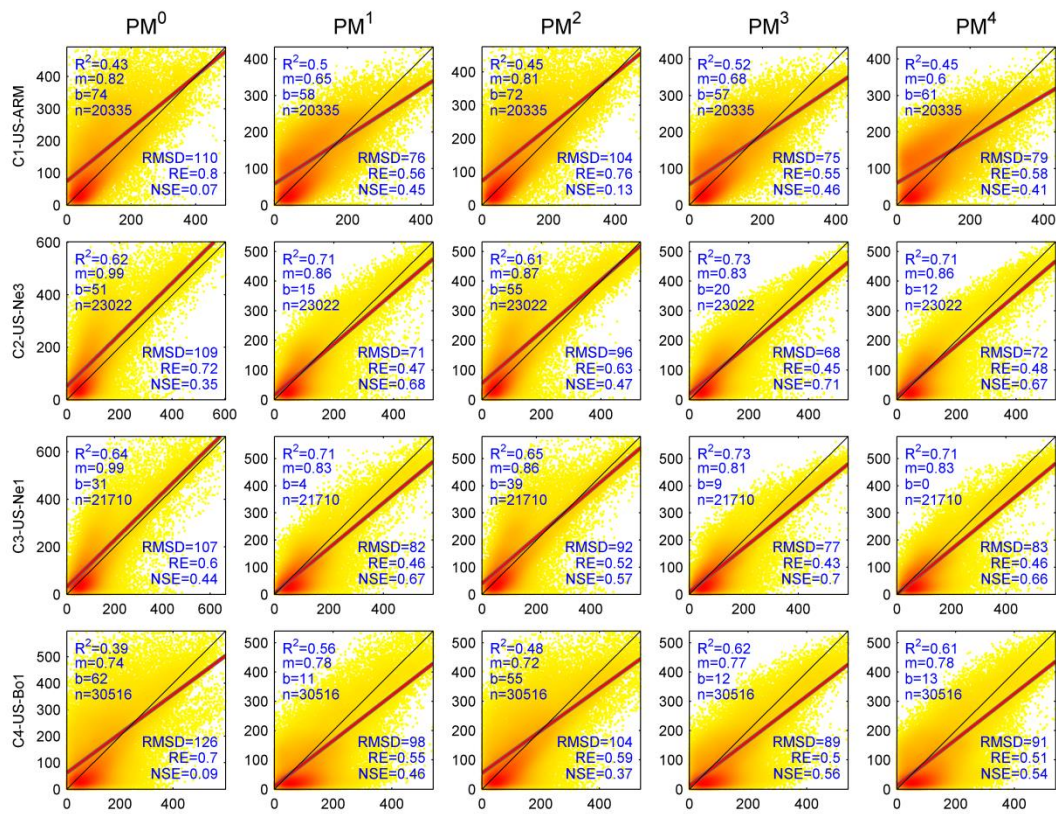


Figure B4: Scatterplots of observed (x-axis) versus simulated (y-axis) latent heat flux ($W.m^{-2}$) for PM scenarios across cropland sites. The statistics on the graphs are R^2 , slope (m), y-intercept (b), number of data records (n), the root-mean-squared difference (RMSD), relative error (RE) and the Nash-Sutcliffe Efficiency coefficient (NSE). The thick gray line is the linear regression and the thin gray line is the 1:1 line. The color of the points in the scatterplot is indicative of the density from low (yellow) to high (red).

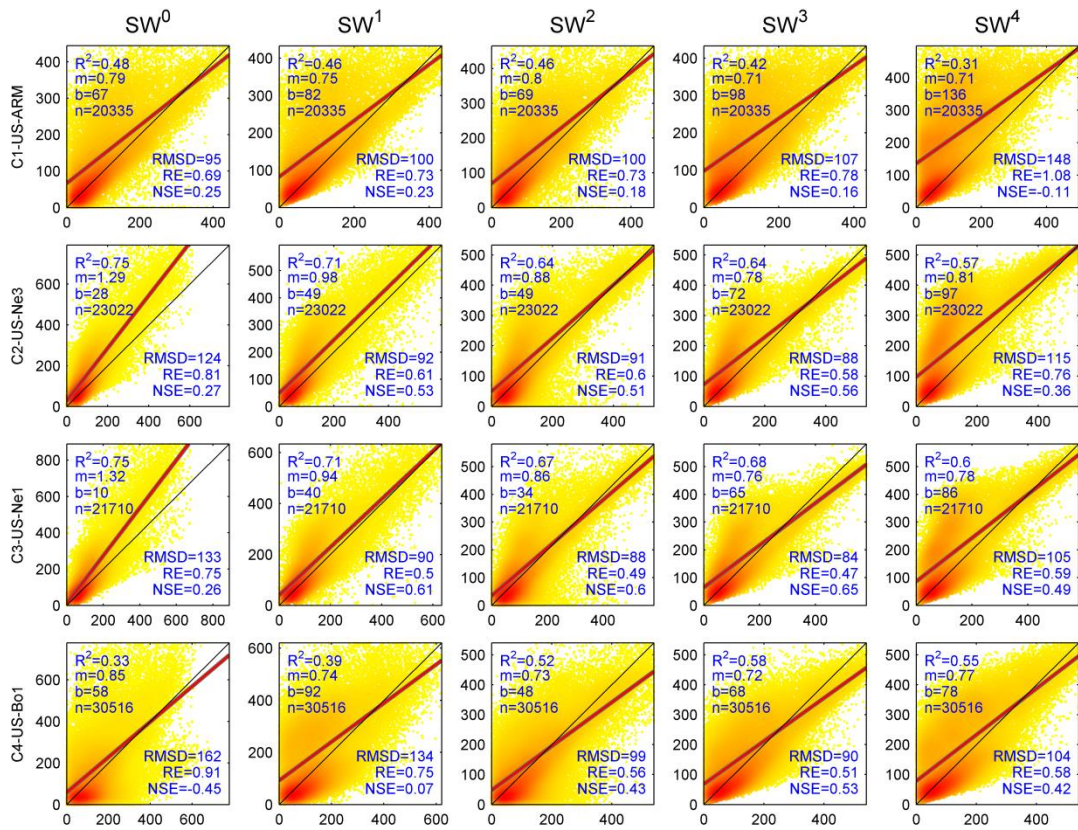


Figure B5: Scatterplots of observed (x-axis) versus simulated (y-axis) latent heat flux ($W.m^{-2}$) for **SW** scenarios across **cropland** sites. The statistics on the graphs are R^2 , slope (m), y-intercept (b), number of data records (n), the root-mean-squared difference ($RMSD$), relative error (RE) and the Nash-Sutcliffe Efficiency coefficient (NSE). The thick gray line is the linear regression and the thin gray line is the 1:1 line. The color of the points in the scatterplot is indicative of the density from low (yellow) to high (red).

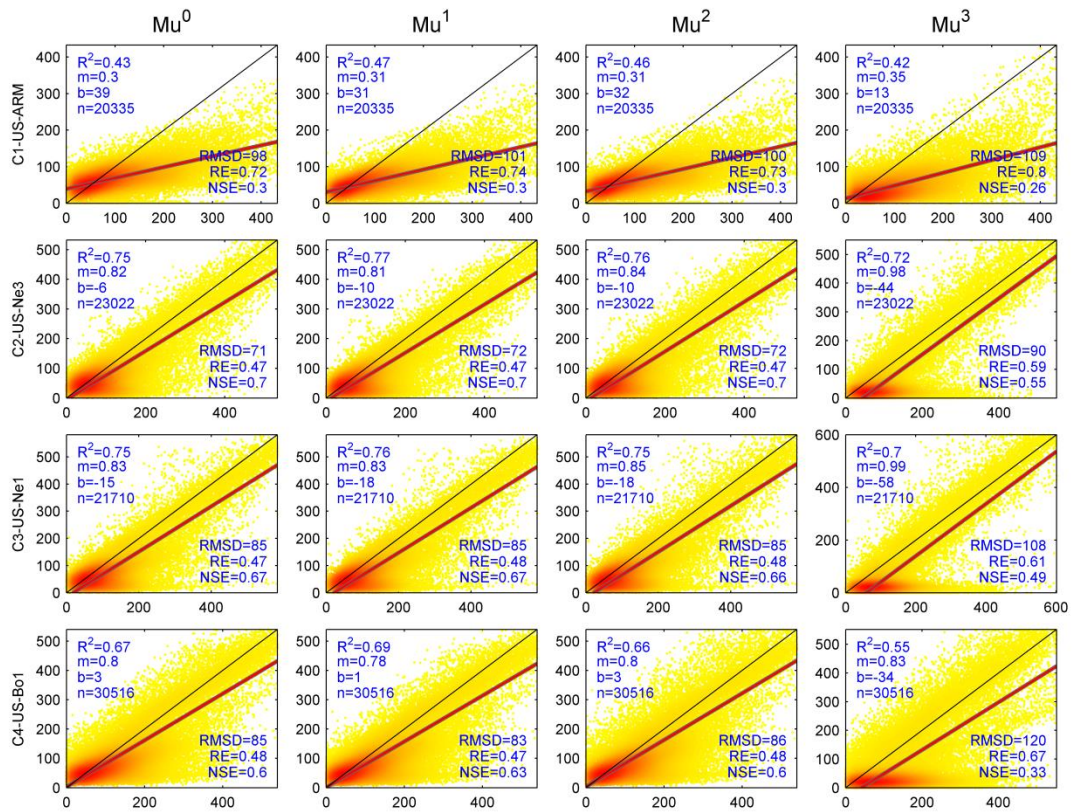


Figure B6: Scatterplots of observed (x-axis) versus simulated (y-axis) latent heat flux ($W.m^{-2}$) for **Mu** scenarios across **cropland** sites. The statistics on the graphs are R^2 , slope (m), y-intercept (b), number of data records (n), the root-mean-squared difference ($RMSD$), relative error (RE) and the Nash-Sutcliffe Efficiency coefficient (NSE). The thick gray line is the linear regression and the thin gray line is the 1:1 line. The color of the points in the scatterplot is indicative of the density from low (yellow) to high (red).

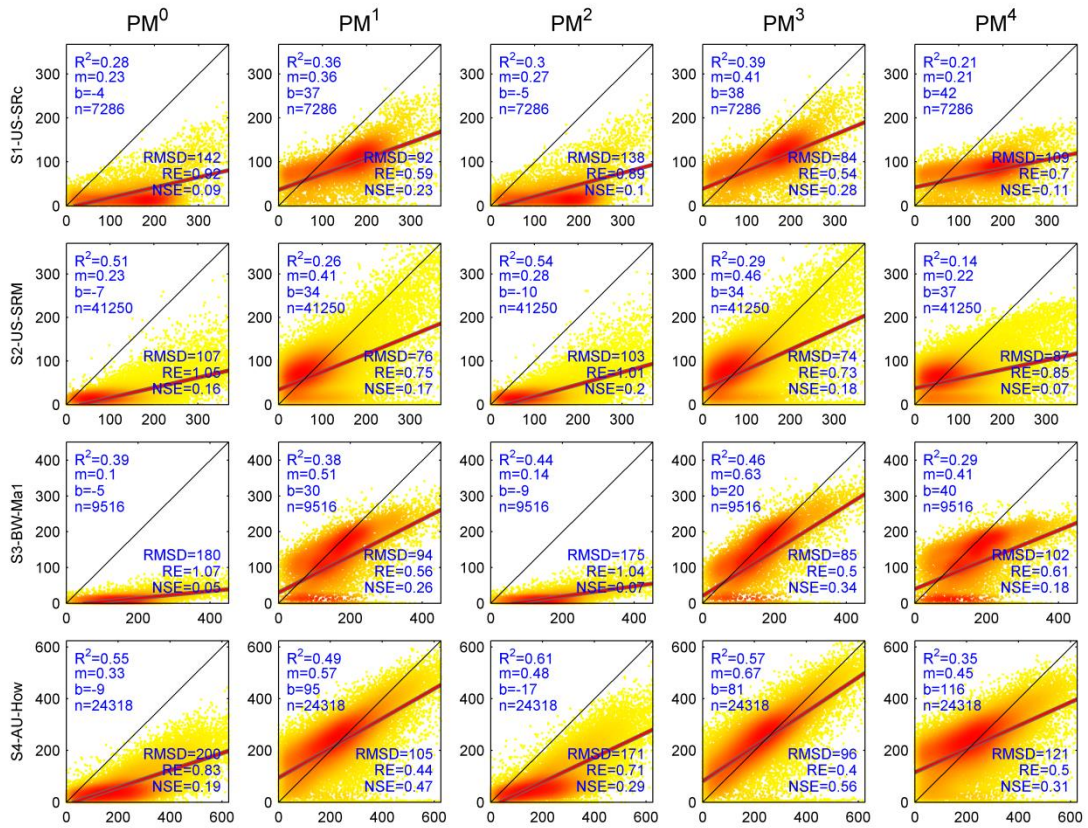


Figure B7: Scatterplots of observed (x-axis) versus simulated (y-axis) latent heat flux (W.m⁻²) for PM scenarios across **shrubland** sites. The statistics on the graphs are R^2 , slope (m), y-intercept (b), number of data records (n), the root-mean-squared difference (RMSD), relative error (RE) and the Nash-Sutcliffe Efficiency coefficient (NSE). The thick gray line is the linear regression and the thin gray line is the 1:1 line. The color of the points in the scatterplot is indicative of the density from low (yellow) to high (red).

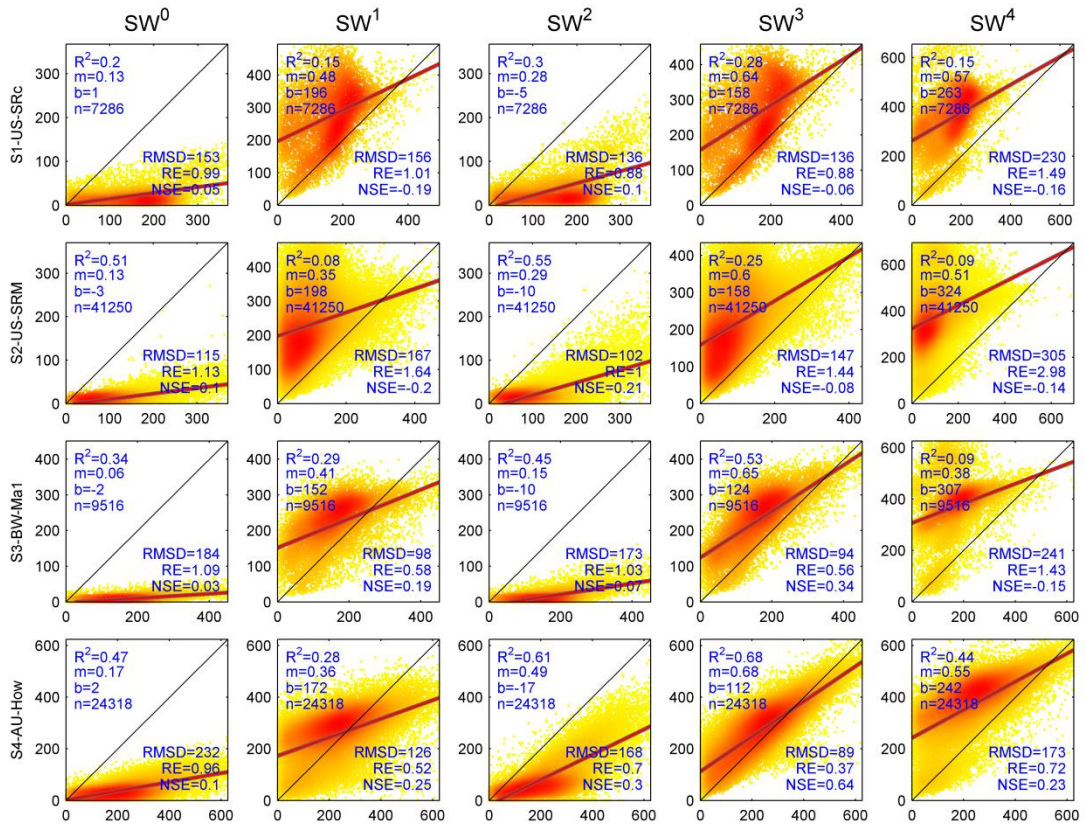


Figure B8: Scatterplots of observed (x-axis) versus simulated (y-axis) latent heat flux ($W.m^{-2}$) for SW scenarios across shrubland sites. The statistics on the graphs are R^2 , slope (m), y-intercept (b), number of data records (n), the root-mean-squared difference (RMSD), relative error (RE) and the Nash-Sutcliffe Efficiency coefficient (NSE). The thick gray line is the linear regression and the thin gray line is the 1:1 line. The color of the points in the scatterplot is indicative of the density from low (yellow) to high (red).

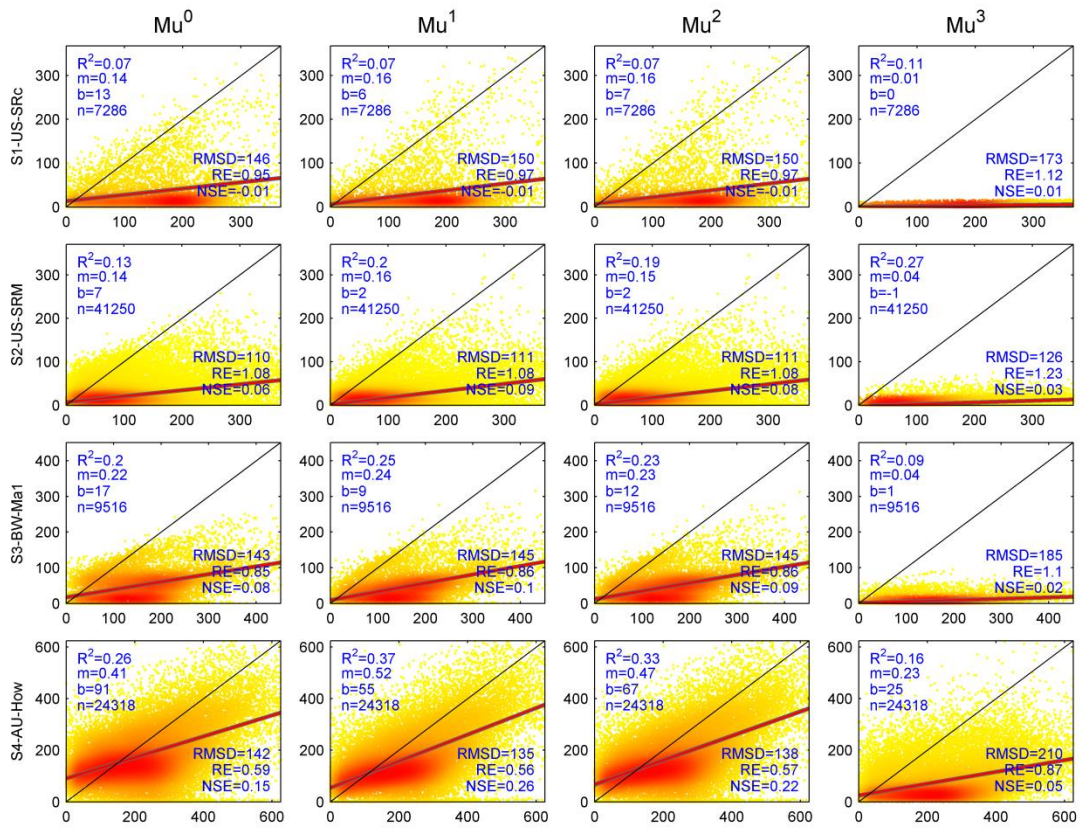


Figure B9: Scatterplots of observed (x-axis) versus simulated (y-axis) latent heat flux (W.m⁻²) for Mu scenarios across shrubland sites. The statistics on the graphs are R^2 , slope (m), y-intercept (b), number of data records (n), the root-mean-squared difference (RMSD), relative error (RE) and the Nash-Sutcliffe Efficiency coefficient (NSE). The thick gray line is the linear regression and the thin gray line is the 1:1 line. The color of the points in the scatterplot is indicative of the density from low (yellow) to high (red).

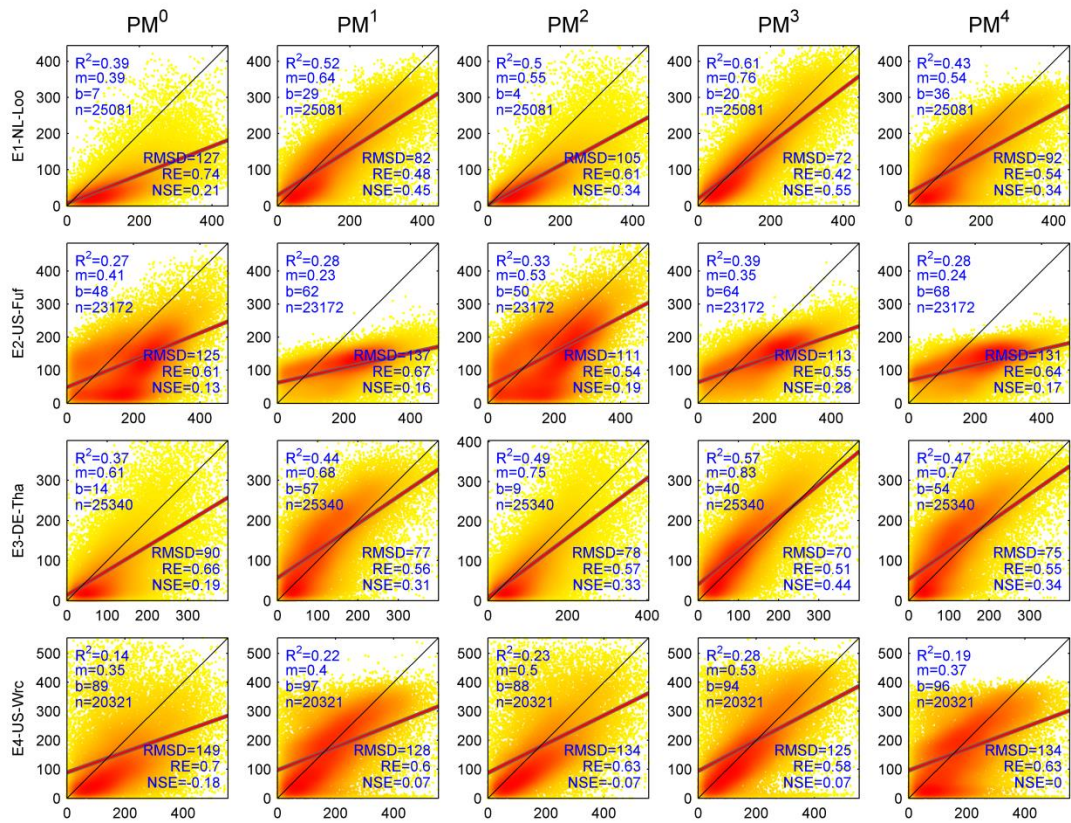


Figure B10 : Scatterplots of observed (x-axis) versus simulated (y-axis) latent heat flux ($W.m^{-2}$) for PM scenarios across evergreen needleleaf forest sites. The statistics on the graphs are R^2 , slope (m), y-intercept (b), number of data records (n), the root-mean-squared difference (RMSD), relative error (RE) and the Nash-Sutcliffe Efficiency coefficient (NSE). The thick gray line is the linear regression and the thin gray line is the 1:1 line. The color of the points in the scatterplot is indicative of the density from low (yellow) to high (red).

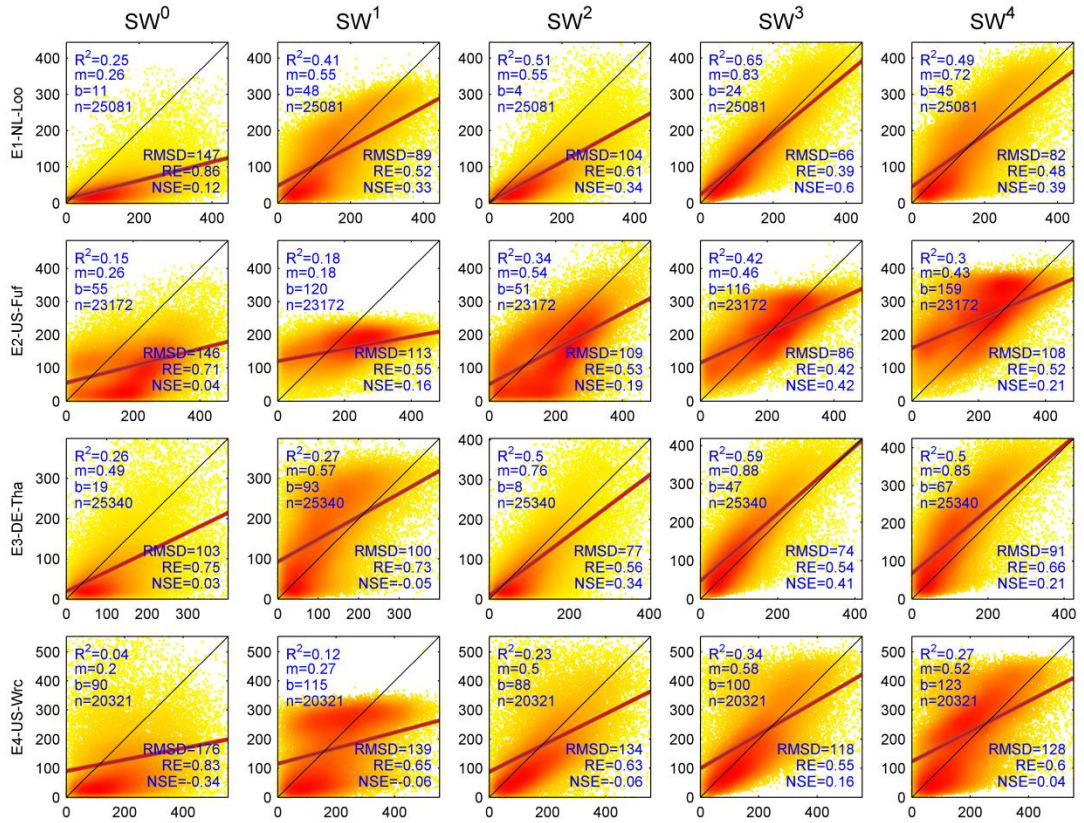


Figure B11: Scatterplots of observed (x-axis) versus simulated (y-axis) latent heat flux ($W \cdot m^{-2}$) for SW scenarios across evergreen needleleaf forest sites. The statistics on the graphs are R^2 , slope (m), y-intercept (b), number of data records (n), the root-mean-squared difference ($RMSD$), relative error (RE) and the Nash-Sutcliffe Efficiency coefficient (NSE). The thick gray line is the linear regression and the thin gray line is the 1:1 line. The color of the points in the scatterplot is indicative of the density from low (yellow) to high (red).

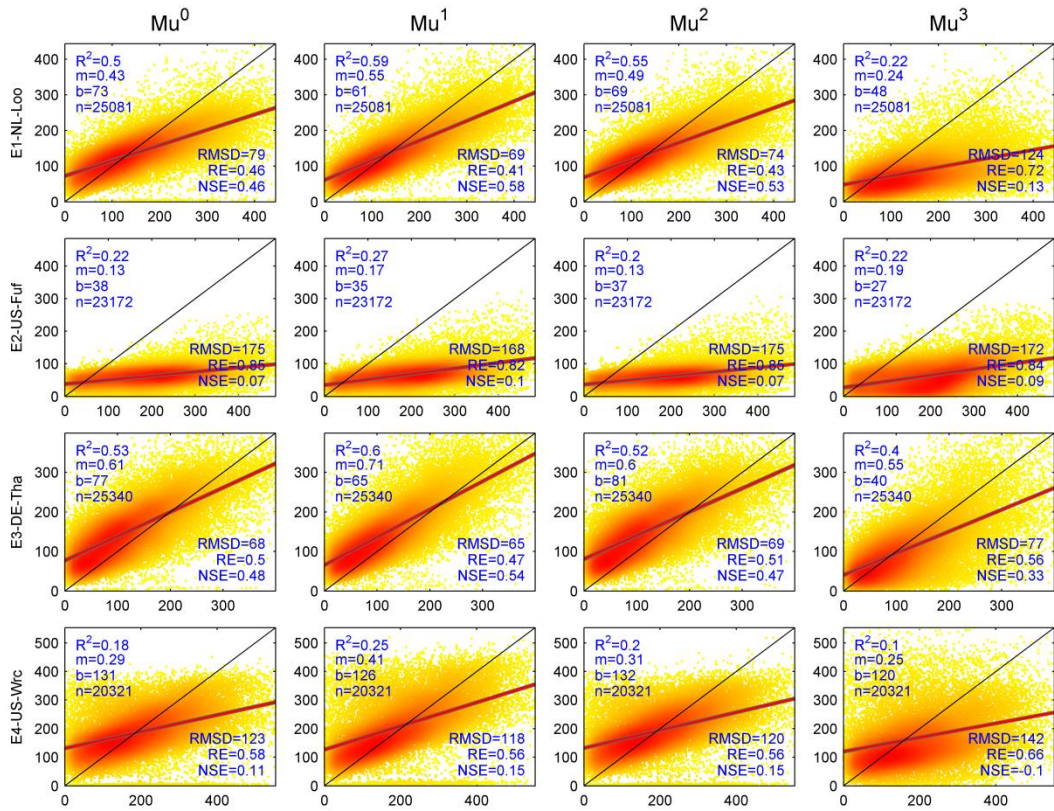


Figure B12: Scatterplots of observed (x-axis) versus simulated (y-axis) latent heat flux ($\text{W}\cdot\text{m}^{-2}$) for **Mu** scenarios across **evergreen needleleaf forest** sites. The statistics on the graphs are R^2 , slope (m), y-intercept (b), number of data records (n), the root-mean-squared difference (RMSD), relative error (RE) and the Nash-Sutcliffe Efficiency coefficient (NSE). The thick gray line is the linear regression and the thin gray line is the 1:1 line. The color of the points in the scatterplot is indicative of the density from low (yellow) to high (red).

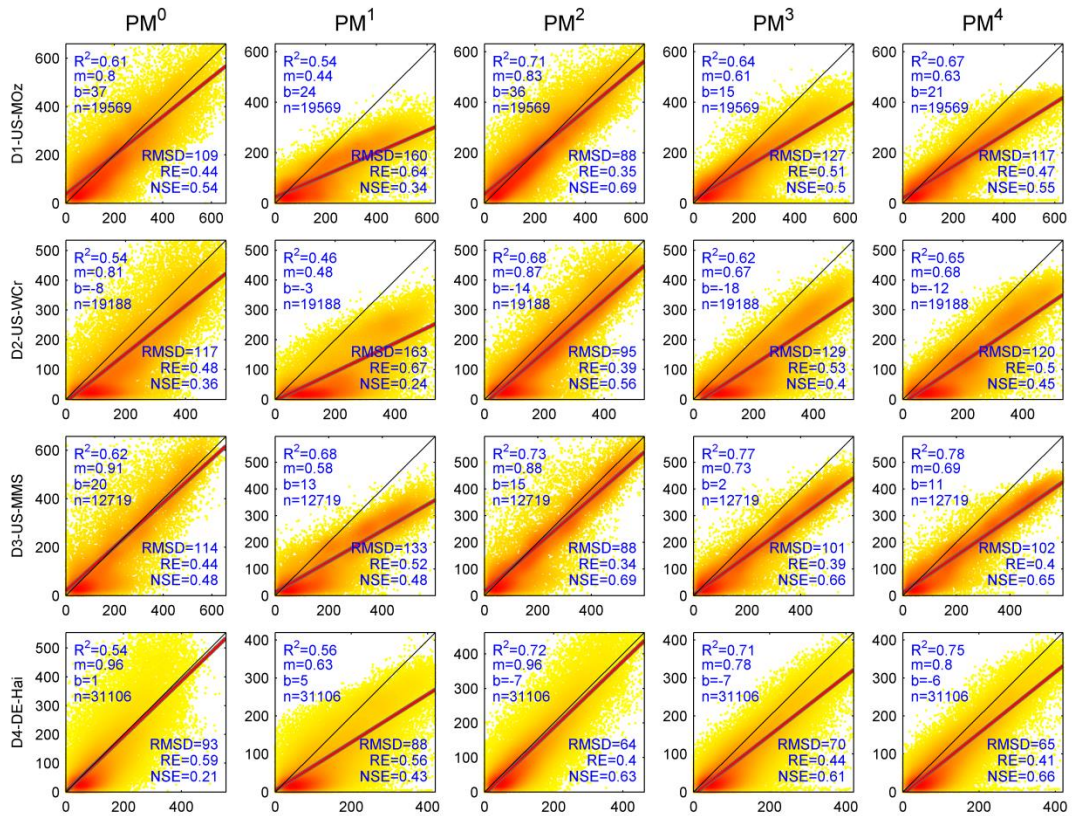


Figure B13: Scatterplots of observed (x-axis) versus simulated (y-axis) latent heat flux ($\text{W}\cdot\text{m}^{-2}$) for PM scenarios across deciduous broadleaf forest sites. The statistics on the graphs are R^2 , slope (m), y-intercept (b), number of data records (n), the root-mean-squared difference (RMSD), relative error (RE) and the Nash-Sutcliffe Efficiency coefficient (NSE). The thick gray line is the linear regression and the thin gray line is the 1:1 line. The color of the points in the scatterplot is indicative of the density from low (yellow) to high (red).

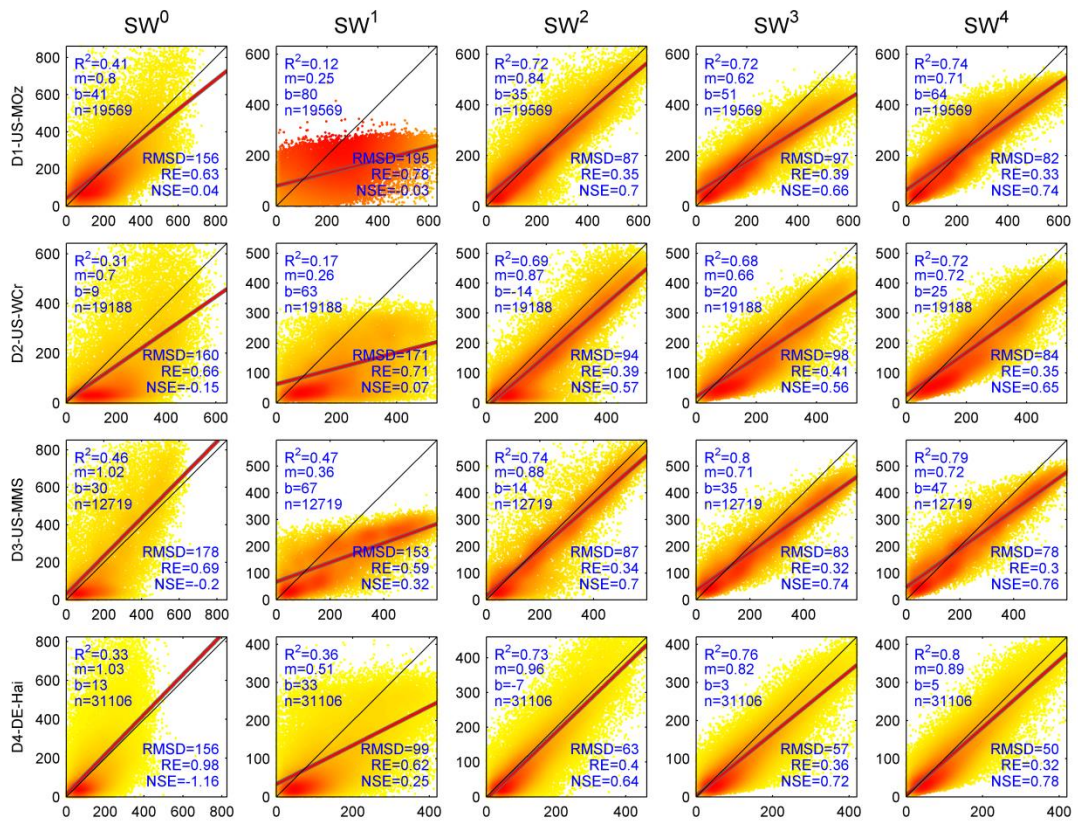


Figure B14: Scatterplots of observed (x-axis) versus simulated (y-axis) latent heat flux ($\text{W}\cdot\text{m}^{-2}$) for **SW** scenarios across **deciduous broadleaf forest** sites. The statistics on the graphs are R^2 , slope (m), y-intercept (b), number of data records (n), the root-mean-squared difference ($RMSD$), relative error (RE) and the Nash-Sutcliffe Efficiency coefficient (NSE). The thick gray line is the linear regression and the thin gray line is the 1:1 line. The color of the points in the scatterplot is indicative of the density from low (yellow) to high (red).

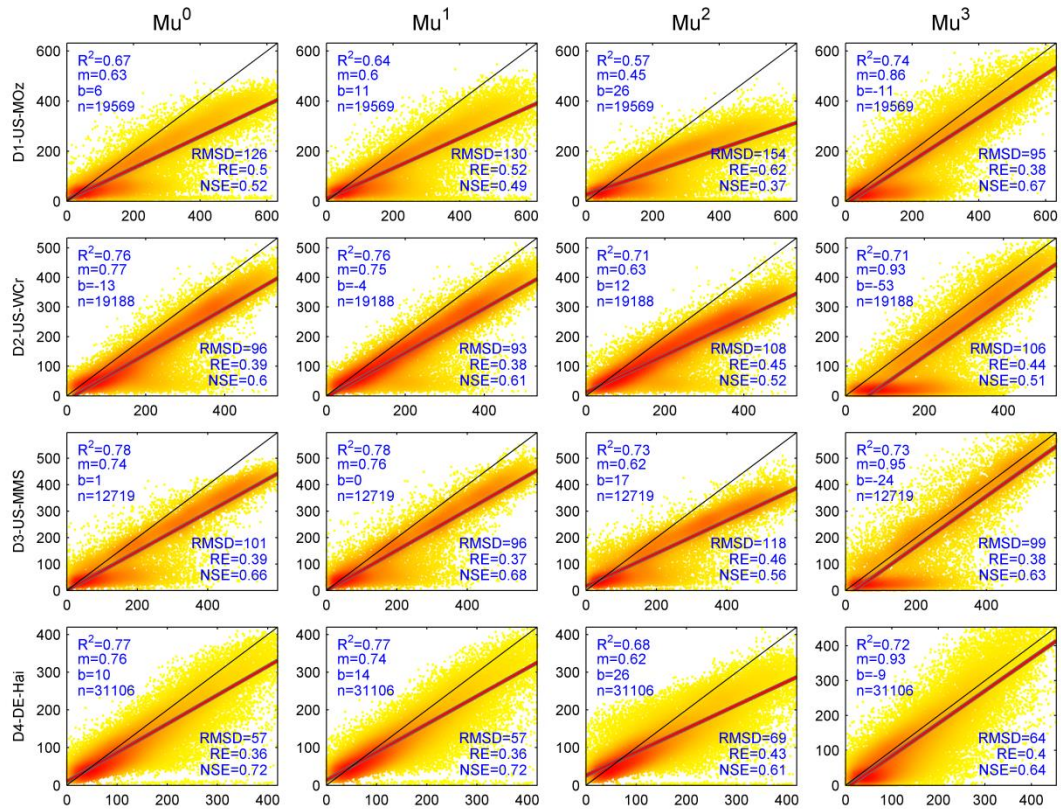


Figure B15: Scatterplots of observed (x-axis) versus simulated (y-axis) latent heat flux ($W \cdot m^{-2}$) for **Mu** scenarios across **deciduous broadleaf forest** sites. The statistics on the graphs are R^2 , slope (m), y-intercept (b), number of data records (n), the root-mean-squared difference ($RMSD$), relative error (RE) and the Nash-Sutcliffe Efficiency coefficient (NSE). The thick gray line is the linear regression and the thin gray line is the 1:1 line. The color of the points in the scatterplot is indicative of the density from low (yellow) to high (red).

Appendix C – Supplementary materials for Chapter 5

The following are supplementary materials which provide additional details on the performance of the Bayesian uncertainty analysis (**Chapter 5**).

C.1 Evaluation of the Response Error Parameter r

The standard deviation (σ_H) of the prior PDF for the response variable (sensible heat flux, H) is expressed as a fraction (r) of the observed sensible heat flux, $\sigma_H = r \times H_o$. The choice of σ_H has a direct influence on the inference of the input variables. The influence of a change in r on the inference of input variables is evaluated as a criterion for the choice of r . One criterion for evaluation of the Bayesian inference is to calculate the root mean squared difference ($RMSD$) of the observed and inferred values of T_s , T_a or u_a . Results for $r\{0.05,0.10,0.15\}$ are shown in Figure C1 and indicate that in all three cases of r , the relative variation in the range and magnitude of $RMSD$ for T_s , T_a and u_a are similar. Also, by reducing r parameters, the $RMSD$ of H (the response variable) decreased, but the $RMSD$ of inference for input variables increased.

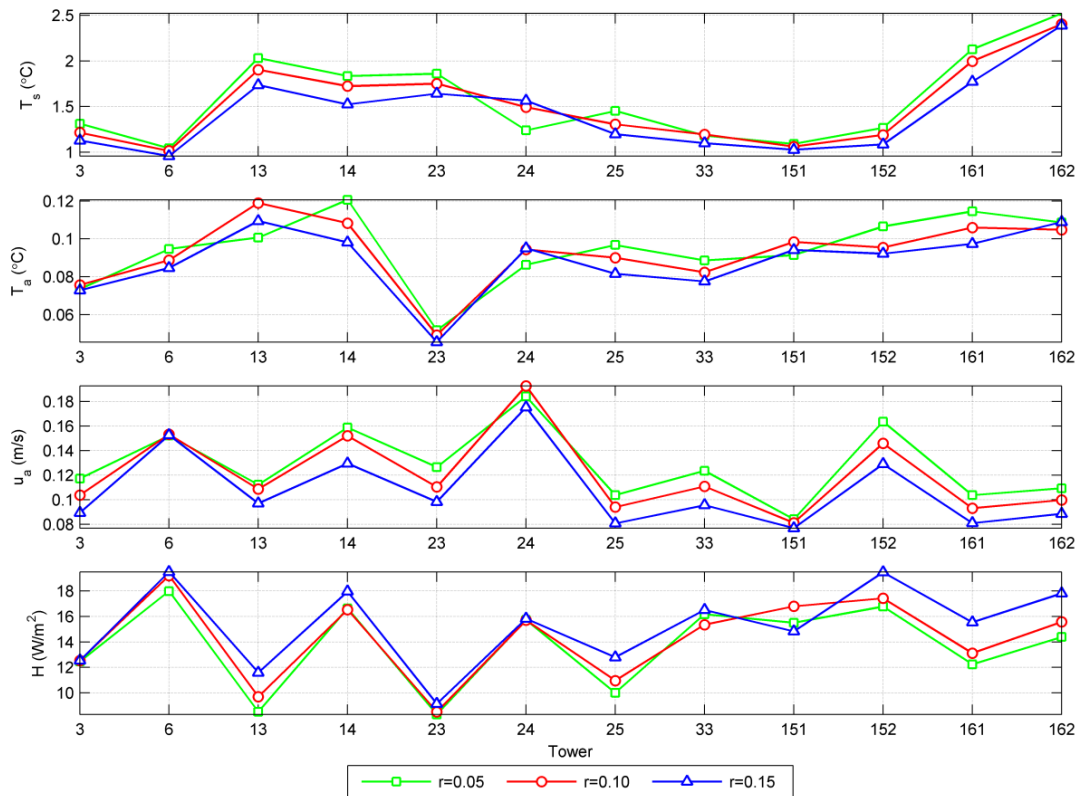


Figure C1: Sensitivity of Bayesian inference to selected values of r parameter. Variations of $RMSD$ of the observed and inferred values of T_s , T_a and u_a are shown in the three first rows.

The last row shows the *RMSD* of observed and stochastic estimated sensible heat flux. X-axis shows the tower number (12 towers in total).

C.2 Evaluation of the Significance of the Choice of Priors

To show the importance of the choice of priors, we simulated BIT-SEBS for tower WC13 (soybean) considering the same (larger) values of standard deviations (equal to that of T_s) for all input variables. Results of this analysis are shown in Figure C2 below. As in this case the priors for T_a and u_a are not informative, the efficiency in stochastic sensible heat flux production is greatly reduced. Also, the differences between inferred and observed values for all three variables are approximately in the same range. These results show the importance of the correct definition of the priors in Bayesian inference.

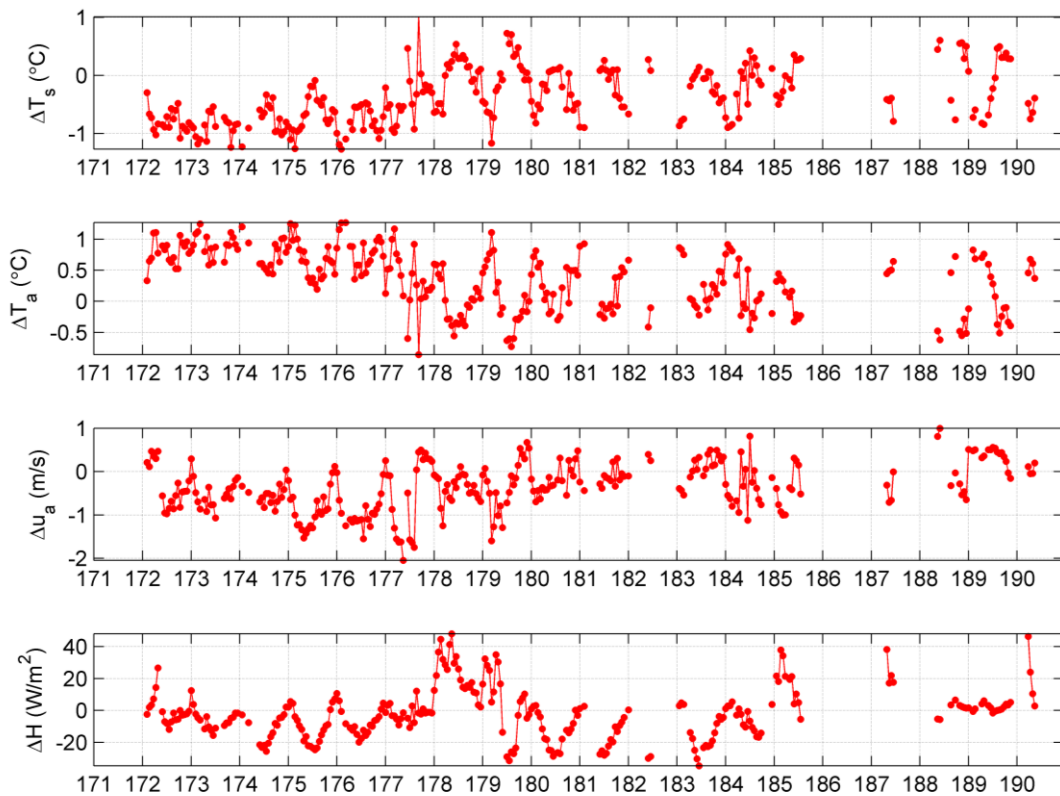


Figure C2: Difference in inferred and observed input variables (3 top panels) and difference in stochastic simulated and observed sensible heat flux (bottom panel) for tower WC13 (soybean). The standard deviations in prior PDF of T_a and u_a are assumed equal to those of T_s . X-axis is day-of-year.